National Library
of Canada

Acquisitions and
Bibliographic Services Branch

395 Wellington Street
Ottawa, Ontario
K1A 0N4

Bibliothèque nationale
du Canada

Direction des acquisitions et
des services bibliographiques

395, rue Wellington
Ottawa (Ontario)
K1A 0N4

Your file Votre référence

Our file Notre référence

NOTICE

The quality of this microform is heavily dependent upon the quality of the original thesis submitted for microfilming. Every effort has been made to ensure the highest quality of reproduction possible.

If pages are missing, contact the university which granted the degree.

Some pages may have indistinct print especially if the original pages were typed with a poor typewriter ribbon or if the university sent us an inferior photocopy.

Reproduction in full or in part of this microform is governed by the Canadian Copyright Act, R.S.C. 1970, c. C-30, and subsequent amendments.

AVIS

La qualité de cette microforme dépend grandement de la qualité de la thèse soumise au microfilmage. Nous avons tout fait pour assurer une qualité supérieure de reproduction.

S'il manque des pages, veuillez communiquer avec l'université qui a conféré le grade.

La qualité d'impression de certaines pages peut laisser à désirer, surtout si les pages originales ont été dactylographiées à l'aide d'un ruban usé ou si l'université nous a fait parvenir une photocopie de qualité inférieure.

La reproduction, même partielle, de cette microforme est soumise à la Loi canadienne sur le droit d'auteur, SRC 1970, c. C-30, et ses amendements subséquents.

Canada

UNIVERSITY OF ALBERTA

Numerical Simulation of Sand Deposition and Accumulation in a Horizontal Well

by

Quang T. Doan ©

A THESIS
SUBMITTED TO THE FACULTY OF GRADUATE STUDIES AND RESEARCH
IN PARTIAL FULFILMENT OF THE REQUIREMENTS FOR THE DEGREE OF

Doctor of Philosophy

IN

Petroleum Engineering

Department of Mining, Metallurgical and Petroleum Engineering

Edmonton, Alberta
Fall 1995

National Library
of Canada

Acquisitions and
Bibliographic Services Branch

395 Wellington Street
Ottawa, Ontario
K1A 0N4

Bibliothèque nationale
du Canada

Direction des acquisitions et
des services bibliographiques

395, rue Wellington
Ottawa (Ontario)
K1A 0N4

Your file Votre référence

Our file Notre référence

THE AUTHOR HAS GRANTED AN IRREVOCABLE NON-EXCLUSIVE LICENCE ALLOWING THE NATIONAL LIBRARY OF CANADA TO REPRODUCE, LOAN, DISTRIBUTE OR SELL COPIES OF HIS/HER THESIS BY ANY MEANS AND IN ANY FORM OR FORMAT, MAKING THIS THESIS AVAILABLE TO INTERESTED PERSONS.

L'AUTEUR A ACCORDE UNE LICENCE IRREVOCABLE ET NON EXCLUSIVE PERMETTANT A LA BIBLIOTHEQUE NATIONALE DU CANADA DE REPRODUIRE, PRETER, DISTRIBUER OU VENDRE DES COPIES DE SA THESE DE QUELQUE MANIERE ET SOUS QUELQUE FORME QUE CE SOIT POUR METTRE DES EXEMPLAIRES DE CETTE THESE A LA DISPOSITION DES PERSONNE INTERESSEES.

THE AUTHOR RETAINS OWNERSHIP OF THE COPYRIGHT IN HIS/HER THESIS. NEITHER THE THESIS NOR SUBSTANTIAL EXTRACTS FROM IT MAY BE PRINTED OR OTHERWISE REPRODUCED WITHOUT HIS/HER PERMISSION.

L'AUTEUR CONSERVE LA PROPRIETE DU DROIT D'AUTEUR QUI PROTEGE SA THESE. NI LA THESE NI DES EXTRAITS SUBSTANTIELS DE CELLE-CI NE DOIVENT ETRE IMPRIMES OU AUTREMENT REPRODUITS SANS SON AUTORISATION.

ISBN 0-612-06203-1

Canada

UNIVERSITY OF ALBERTA

LIBRARY RELEASE FORM

NAME OF AUTHOR Quang T. Doan

TITLE OF THESIS Numerical Simulation of Sand Deposition and Accumulation in a Horizontal Well

DEGREE FOR WHICH THESIS WAS PRESENTED Doctor of Philosophy

YEAR THIS DEGREE GRANTED 1995

Permission is hereby granted to THE UNIVERSITY OF ALBERTA LIBRARY to reproduce single copies of this thesis and to lend or sell such copies for private, scholarly or scientific research purposes only.

The author reserves other publication rights, and neither the thesis nor extensive extracts from it may be printed or otherwise reproduced without the author' s written permission.

(SIGNED)

PERMANENT ADDRESS:
2933 - 111B STREET
EDMONTON, ALBERTA
CANADA T6J 4R5

DATED OCTOBER 05, 1995

UNIVERSITY OF ALBERTA

FACULTY OF GRADUATE STUDIES AND RESEARCH

The undersigned certify that they have read, and recommend to the Faculty of Graduate Studies and Research, for acceptance, a thesis entitled Numerical Simulation of Sand Deposition and Accumulation in a Horizontal Well submitted by Quang T. Doan in partial fulfillment of the requirements for the degree of Doctor of Philosophy in Petroleum Engineering.

Professor S.M. Farouq Ali (Supervisor)

Ramon Bentsen

Professor R.G. Bentsen

N Rajaratnam

Professor N. Rajaratnam

Professor J. Szymanski

WS Tortike

Professor W.S. Tortike

R G Moore.

Professor R.G. Moore (External Examiner)

Date Sept 28, 95

CÔNG CHA NHƯ NÚI THÁI SƠN,
NGHĨA MẸ NHƯ NƯỚC TRONG NGUỒN CHẢY RA,
MỘT LÒNG THỜ MẸ KÍNH CHA,
CHO TRÒN CHỮ HIẾU MỚI LÀ ĐẠO CON

CA DAO TỤC NGỮ VIỆT NAM

Abstract

Horizontal wells are currently finding ever-increasing application to recover oil and gas worldwide. In Canada, one of the main applications of a horizontal well is to recover heavy oil in Saskatchewan and Alberta. These reservoirs are predominantly marginal, having thin pay and bottom water. They are, in addition, poorly consolidated; as a result, recovery operations in these reservoirs are often susceptible to sand production. Sand production, deposition, and accumulation in a horizontal wellbore is a serious problem, as it plugs and partitions the horizontal well into sections – thus negating the principal advantage of a larger reservoir-wellbore contact area for horizontal wells. Despite the significant impairment to well productivity, particularly in the case of horizontal wells, the mathematical treatment of this complex transport process has been outside the realm of conventional petroleum engineering. The present work is a systematic examination of this complex flow problem.

Of the 145 references cited in this study less than one-third are from petroleum engineering publications, many of these being experimental investigations of cuttings transport and settling velocity of fracture proppants. None of the published papers gives a satisfactory treatment of the transport and deposition of sand in a horizontal well. Nor is there any experimental data available in the literature to test a given mathematical model. Only one paper – discussed in depth in this work – touches upon the problem of suspension transport in a different context (fill-up of a fracture). This is shown to be inadequate for the problem at hand – sand deposition and accumulation in a horizontal well. Instead, a new mathematical model is developed and solved numerically. This model takes into account the buildup of the sand deposit inside a horizontal well as a function of oil viscosity, particle size, flow velocity, and other parameters. Limited (storage) memory capacity of the computer used in this study (Macintosh Quadra 800) results in the simulation of only the early stage of the deposition and solid bed expansion processes.

The numerical model is tested using field data including oil viscosity, flow rate and well diameter. The particle size is magnified, but still within a reasonable sand size range, to enable certain basic transport phenomena to be observed. Simulation runs are performed to evaluate the influence of key variables on the deposition and deposit bed expansion processes. The numerical results agree with experimental observation for the formation of sand ripples in a shallow-water environment, and make intuitive sense. Implications of the simulation results for field conditions are discussed. Scaling criteria for the transport process are also derived for possible use in future experimental studies, as well as selected simulation studies.

Acknowledgements

The author wishes to express his sincere appreciation and gratitude to Dr. S.M. Farouq Ali for the constant encouragement, guidance, and support throughout the course of this study. Without Dr. Farouq Ali' s guidance and support this study would have certainly taken longer to complete.

The author also wishes to thank Mr. Mustafa Oguztoreli for his considerable help and many discussions in the later stage of this study.

The generous financial support provided for this research by Energy Research Laboratories (ERL) of CANMET – Energy, Mines and Resources Canada is greatly appreciated. The author wishes to thank Dr. Albert E. George, in particular, and Dr. K. Jha for their keen interest, support and input into this research work.

Table of Contents

ABSTRACT ---------- V

ACKNOWLEDGEMENTS ---------- VI

LIST OF TABLES ---------- X

LIST OF FIGURES ---------- XII

NOMENCLATURE ---------- XVII

CHAPTER 1. INTRODUCTION ---------- 1

CHAPTER 2. SURVEY OF THE LITERATURE ---------- 2

2.1. MOTION OF A SOLID PARTICLE IN A FLUID ---------- 2
  2.1.1. Fundamentals ---------- 2
    2.1.1.1. Drag Force ---------- 2
    2.1.1.2. Lift Force ---------- 4
  2.1.2. Effect of Particle Shape ---------- 7
  2.1.3. Effect of non-Newtonian Fluid Rheology ---------- 8
2.2. MOTION OF PARTICLE CLOUDS IN A FLUID ---------- 10
  2.2.1. Fluidization and Sedimentation ---------- 10
  2.2.2. Saltation ---------- 14
2.3. FLOW OF SUSPENSIONS ---------- 15
  2.3.1. Rheology of Suspensions ---------- 15
  2.3.2. Experimental Studies ---------- 16
    2.3.2.1. Suspension Flow ---------- 16
      2.3.2.1.1. Sediment Transport ---------- 16
      2.3.2.1.2. Flow of Suspensions in Pipes ---------- 17
    2.3.2.2. Gravity Settling of Aerosols ---------- 27
    2.3.2.3. Drill Cuttings Transport ---------- 27
  2.3.3. Theoretical Studies ---------- 29
  2.3.4. Numerical Studies ---------- 31
    2.3.4.1. Homogeneous Suspensions ---------- 31
    2.3.4.2. Heterogeneous Suspensions ---------- 33

CHAPTER 3. STATEMENT OF THE PROBLEM ---------- 36

CHAPTER 4. DEVELOPMENT OF MATHEMATICAL MODELS ---------- 37

4.1. INTRODUCTION ---------- 37
4.2. REVIEW OF AVAILABLE MATHEMATICAL MODELS FOR SOLID-FLUID MULTIPHASE FLOW ---------- 38
  4.2.1. Pseudo Single-phase Fluid ---------- 38
  4.2.2. Two-phase Flow with One Pressure ---------- 38
  4.2.3. Two-phase Flow with Two Distinct Pressures (One for Each Phase) ---------- 43
4.3. DEVELOPMENT OF MATHEMATICAL MODELS ---------- 47
  4.3.1. Formulation of a Two-dimensional Model ---------- 47
  4.3.2. Formulation of One-dimensional Models ---------- 61

- 4.3.2.1. Givler & Mikatarian' s Constriction Model ---------- 63
- 4.3.2.2. Gravity Deposition Model ---------- 66
- 4.4. Initial Conditions and Boundary Conditions ---------- 71
  - 4.4.1. Initial and Boundary Conditions for Multiphase Flow Modelling ---------- 71
  - 4.4.2. Initial & Boundary Conditions for Givler & Mikatarian' s Constriction Model ---------- 72
  - 4.4.3. Initial and Boundary Conditions for Gravity Deposition Model ---------- 73
- 4.5. Numerical Solution Procedures ---------- 73
  - 4.5.1. Discretization ---------- 73
  - 4.5.2. Solution Procedure ---------- 74
  - 4.5.3. Stability Considerations ---------- 77

CHAPTER 5. DEVELOPMENT OF SCALING CRITERIA ---------- 78

- 5.1. Introduction ---------- 78
- 5.2. Two-dimensional Model ---------- 79
  - 5.2.1. Inspectional Analysis ---------- 79
  - 5.2.2. Dimensional Analysis ---------- 86
- 5.3. One-dimensional Models ---------- 93
  - 5.3.1. Givler & Mikatarian' s Constriction Model ---------- 93
  - 5.3.2. Gravity Deposition Model ---------- 94
- 5.4. Concluding Remarks ---------- 95

CHAPTER 6. DISCUSSION OF RESULTS ---------- 97

- 6.1. Introduction ---------- 97
- 6.2. Givler and Mikatarian' s Constriction Model ---------- 97
  - 6.2.1. Constriction Model – Flow Dominated by Pressure Forces ---------- 99
  - 6.2.2. Constriction Model – Flow Dominated by Interfacial Drag Force ---------- 108
  - 6.2.3. Applicability of the Constriction Model ---------- 123
- 6.3. Gravity Deposition Model ---------- 124
  - 6.3.1. Gravity Deposition Model – Input Data ---------- 125
  - 6.3.2. Gravity Deposition Model – Results of "Representative" Case ---------- 127
- 6.4. Gravity Deposition Model – Effects of Hydrodynamic Variables ---------- 135
  - 6.4.1. Light Oil ---------- 136
    - 6.4.1.1. Effect of Oil Viscosity ---------- 136
    - 6.4.1.2. Effect of Velocity ---------- 147
    - 6.4.1.3. Effect of Particle Size ---------- 154
  - 6.4.2. Heavy Oil ---------- 165
    - 6.4.2.1. Effect of Oil Viscosity ---------- 165
    - 6.4.2.2. Effect of Velocity ---------- 169
    - 6.4.2.3. Effect of Particle Size ---------- 177
- 6.5. Implication of Simulation Results for Field Conditions ---------- 182
- 6.6. Concluding Remarks ---------- 185

CHAPTER 7. CONCLUSIONS ---------- 187

CHAPTER 8. RECOMMENDATIONS ---------- 189

REFERENCES ---------- 190

APPENDIX A ---------- 200

APPENDIX B ---------- 203

APPENDIX C ---------- 208

APPENDIX D--212

APPENDIX E--219

List of Tables

Table 4.1: Values of constant and exponents for lift coefficient (after Reference 81) 54

Table 4.2: The function $h(\phi)$ versus ϕ (after Reference 114) 56

Table 5.1: Dimensionless Similarity Groups from Inspectional Analysis for the Two-dimensional Model. 86

Table 5.2: Dimensionless Similarity Groups from Dimensional Analysis for the Two-dimensional Model. 88

Table 5.3: Physical Meaning of Scaling Criteria for the Two-dimensional Model. 89

Table 5.4: Dimensionless Similarity Groups from Inspectional Analysis for the One-dimensional Constriction Model. 93

Table 5.5: Dimensionless Similarity Groups from Dimensional Analysis for the One-dimensional Constriction Model. 94

Table 5.6: Dimensionless Similarity Groups from Inspectional Analysis for the One-dimensional Gravity Deposition Model. 94

Table 5.7: Dimensionless Similarity Groups from Dimensional Analysis for the One-dimensional Gravity Deposition Model. 95

Table 6.1: Data used in simulation runs for Constriction Model. 99

Table 6.2: Slip velocity for Case 1 and Case 2 at different times, Constriction Model. 122

Table 6.3: Some data used in runs for the Gravity Deposition Model. 125

Table 6.4: Summary of simulation runs with the Gravity Deposition Model. 126

Table 6.5: Values of height of deposit bed at different positions, Run L 01 vs Run L 02 vs Run L 03, Gravity Deposition Model. 149

Table 6.6: Values of height of deposit bed at different positions, Run L 04 vs Run L 05 vs Run L 06, Gravity Deposition Model. 151

Table 6.7: Values of height of deposit bed at different positions, Run L 07 vs Run L 08 vs Run L 09, Gravity Deposition Model. 153

Table 6.8: Values of height of deposit bed at different positions, Run L 10 vs Run L 11 vs Run L 12, Gravity Deposition Model. 154

Table 6.9: Values of height of deposit bed at different positions, Run H 01 vs Run H 02 vs Run H 03, Gravity Deposition Model. 174

Table B.1: Dimensionless Similarity Groups for Flow of Dilute Suspensions ______________205

Table B.2: Dimensionless Groups Characterizing Flow of Dilute Suspensions ____________206

List of Figures

Figure 2.1: Organization of Chapter 2 – Survey of Multiphase Flow Literature. ____________3

Figure 2.2: Drag coefficient for a single solid sphere. ____________5

Figure 4.1: Control volume element for flow inside a horizontal well. ____________48

Figure 4.2: Schematic drawing of flow geometry for Constriction Model. ____________64

Figure 4.3: Plane of symmetry assumed for Gravity Deposition Model.____________67

Figure 4.4: Schematic drawing of staggered mesh for 2-D model. ____________75

Figure 4.5: Schematic drawing of staggered mesh for Gravity Deposition Model. ____________76

Figure 6.1: Organization of Chapter 6 – Discussion of Results. ____________98

Figure 6.2: Constriction Model – Solid Phase Pressure Profile at different times for Case 1 (transport process dominated by Pressure Forces). ____________100

Figure 6.3: Constriction Model – Fluid Phase Pressure Profile at different times for Case 1 (transport process dominated by Pressure Forces). ____________101

Figure 6.4: Constriction Model – Kinematic Pressure Profile at different times for Case 1 (transport process dominated by Pressure Forces). ____________102

Figure 6.5: Constriction Model –Solid Phase Concentration Profile at different times for Case 1 (transport process dominated by Pressure Forces). ____________103

Figure 6.6: Constriction Model – Solid Phase Velocity Profile at different times for Case 1 (transport process dominated by Pressure Forces). ____________104

Figure 6.7: Constriction Model – Fluid Phase Velocity Profile at different times for Case 1 (transport process dominated by Pressure Forces). ____________105

Figure 6.8: Constriction Model – Solid Phase Pressure Profile at different times for Case 2(transport process dominated by Drag Force).____________108

Figure 6.9: Constriction Model – Fluid Phase Pressure Profile at different times for Case 2(transport process dominated by Drag Force).____________110

Figure 6.10: Constriction Model – Kinematic Pressure Profile at different times for Case 2(transport process dominated by Drag Force).____________111

Figure 6.11: Constriction Model – Solid Phase Concentration Profile at different times for Case 2(transport process dominated by Drag Force).____________112

Figure 6.12: Constriction Model – Solid Phase Velocity Profile at different times for Case 2(transport process dominated by Drag Force).____________113

Figure 6.13: Constriction Model – Fluid Phase Velocity Profile at different times for Case 2(transport process dominated by Drag Force). 114

Figure 6.14: Constriction Model – Profile of Solid Phase Pressure at different times for Case 1 (Pressure Forces Dominating Process) vs Case 2 (Interfacial Drag Force Dominating Process). 116

Figure 6.15: Constriction Model – Profile of Fluid Phase Pressure at different times for Case 1 (Pressure Forces Dominating Process) vs Case 2 (Interfacial Drag Force Dominating Process). 117

Figure 6.16: Constriction Model – Profile of Kinematic Pressure at different times for Case 1 (Pressure Forces Dominating Process) vs Case 2 (Interfacial Drag Force Dominating Process). 118

Figure 6.17: Constriction Model – Profile of Solid Phase Concentration at different times for Case 1 (Pressure Forces Dominating Process) vs Case 2 (Interfacial Drag Force Dominating Process). 119

Figure 6.18: Constriction Model – Profile of Solid Phase Velocity at different times for Case 1 (Pressure Forces Dominating Process) vs Case 2 (Interfacial Drag Force Dominating Process). 120

Figure 6.19: Constriction Model – Profile of Fluid Phase Velocity at different times for Case 1 (Pressure Forces Dominating Process) vs Case 2 (Interfacial Drag Force Dominating Process). 121

Figure 6.20: Gravity Deposition Model – Solid Phase Pressure Profile for a light oil, Run L 13 (μ = 25 mPa.s, W_f = 13.65 cm/s, d = 0.5 cm) . 128

Figure 6.21: Gravity Deposition Model – Kinematic Pressure Profile for a light oil, Run L 13 (μ = 25 mPa.s, W_f = 13.65 cm/s, d = 0.5 cm) . 129

Figure 6.22: Gravity Deposition Model – Fluid Phase Concentration Profile for a light oil, Run L 13 (μ = 25 mPa.s, W_f = 13.65 cm/s, d = 0.5 cm) . 130

Figure 6.23: Gravity Deposition Model – Fluid Phase Velocity Profile for a light oil, Run L 13 (μ = 25 mPa.s, W_f = 13.65 cm/s, d = 0.5 cm) . 131

Figure 6.24: Gravity Deposition Model – Solid Phase Velocity Profile for a light oil, Run L 13 (μ = 25 mPa.s, W_f = 13.65 cm/s, d = 0.5 cm) . 132

Figure 6. 25: Light Oil/Effect of oil viscosity – Profile of sand deposit at different times for two light oils, Run L 01 (μ = 25 mPa.s) and Run L 07 (μ = 100 mPa.s), W_f = 6.825 cm/s, ρ_o = 0.90 g/cm^3, d = 0.5 cm . 137

Figure 6. 26: Light Oil/Effect of oil viscosity – Profile of sand deposit at different times for two light oils, Run L 02 (μ = 25 mPa.s) and Run L 08 (μ = 100 mPa.s), W_f = 13.65 cm/s, ρ_o = 0.90 g/cm^3, d = 0.5 cm . 139

Figure 6. 27: Light Oil/Effect of oil viscosity – Profile of sand deposit at different times for two light oils, Run L 03 (μ = 25 mPa.s) and Run L 09 (μ = 100 mPa.s), W_t = 27.30 cm/s, ρ_o = 0.90 g/cm^3, d = 0.5 cm . 141

Figure 6. 28: Light Oil/Effect of oil viscosity – Profile of sand deposit at different times for two light oils, Run L 04 (μ = 25 mPa.s) and Run L 10 (μ = 100 mPa.s), W_t = 6.825 cm/s, ρ_o = 0.90 g/cm^3, d = 0.1 cm . 143

Figure 6. 29: Light Oil/Effect of oil viscosity – Profile of sand deposit at different times for two light oils, Run L 05 (μ = 25 mPa.s) and Run L 11 (μ = 100 mPa.s), W_t = 13.65 cm/s, ρ_o = 0.90 g/cm^3, d = 0.1 cm . 145

Figure 6. 30: Light Oil/Effect of oil viscosity – Profile of sand deposit at different times for two light oils, Run L 06 (μ = 25 mPa.s) and Run L 12 (μ = 100 mPa.s), = 27.30 cm/s, ρ_o = 0.90 g/cm^3, d = 0.1 cm . 146

Figure 6. 31: Light Oil/Effect of flow velocity – Profile of sand deposit at different times for three velocities, Run L 01 (W_t = 6.825 cm/s), Run L 02 (W_t = 13.65 cm/s) and Run L 03 (W_t = 27.3 cm/s), ρ_o = 0.90 g/cm^3, μ = 25 mPa.s, d = 0.5 cm . 148

Figure 6. 32: Light Oil/Effect of flow velocity – Profile of sand deposit at different times for three velocities, Run L 04 (W_t = 6.825 cm/s), Run L 05 (W_t = 13.65 cm/s) and Run L 06 (W_t = 27.3 cm/s), ρ_o = 0.90 g/cm^3, μ = 25 mPa.s, d = 0.1 cm . 150

Figure 6. 33: Light Oil/Effect of flow velocity – Profile of sand deposit at different times for three velocities, Run L 07 (W_t = 6.825 cm/s), Run L 08 (W_t = 13.65 cm/s) and Run L 09 (W_t = 27.3 cm/s), ρ_o = 0.90 g/cm^3, μ = 100 mPa.s, d = 0.5 cm . 152

Figure 6. 34: Light Oil/Effect of flow velocity – Profile of sand deposit at different times for three velocities, Run L 10 (W_t = 6.825 cm/s), Run L 11 (W_t = 13.65 cm/s) and Run L 12 (W_t = 27.3 cm/s), ρ_o = 0.90 g/cm^3, μ = 100 mPa.s, d = 0.1 cm . 155

Figure 6. 35: Light oil/Effect of particle size – Profile of sand deposit at different times for two sand sizes, Run L 01 (d = 0.5 cm) and Run L 04 (d = 0.1 cm), W_t = 6.825 cm/s, ρ_o = 0.90 g/cm^3, μ = 25 mPa.s . 157

Figure 6. 36: Light oil/Effect of particle size – Profile of sand deposit at different times for two sand sizes, Run L 02 (d = 0.5 cm) and Run L 05 (d = 0.1 cm), W_t = 13.65 cm/s, ρ_o = 0.90 g/cm^3, μ = 25 mPa.s . 158

Figure 6. 37: Light oil/Effect of particle size – Profile of sand deposit at different times for two sand sizes, Run L 03 (d = 0.5 cm) and Run L 06 (d = 0.1 cm), W_t = 27.3 cm/s, ρ_o = 0.90 g/cm^3, μ = 25 mPa.s . 160

Figure 6. 38: Light oil/Effect of particle size – Profile of sand deposit at different times for two sand sizes, Run L 07 (d = 0.5 cm) and Run L 10 (d = 0.1 cm), W_t = 6.825 cm/s, ρ_o = 0.90 g/cm^3, μ = 100 mPa.s . 161

Figure 6. 39: Light oil/Effect of particle size – Profile of sand deposit at different times for two sand sizes, Run L 08 (d = 0.5 cm) and Run L 11 (d = 0.1 cm), W_t = 13.65 cm/s, ρ_o = 0.90 g/cm^3, μ = 100 mPa.s . 163

Figure 6. 40: Light oil/Effect of particle size – Profile of sand deposit at different times for two sand sizes, Run L 09 ($d = 0.5$ cm) and Run L 12 ($d = 0.1$ cm), $W_l = 27.3$ cm/s, $\rho_o = 0.90$ g/cm^3, $\mu = 100$ mPa.s . 164

Figure 6. 41: Heavy Oil/Effect of oil viscosity – Profile of sand deposit at different times for two heavy oils, Run H 02 ($\mu = 1\,500$ mPa.s) and Run H 05 ($\mu = 10\,000$ mPa.s), $W_l = 5.0$ cm/s, $\rho_o = 1.00$ g/cm^3, $d = 0.5$ cm . 167

Figure 6. 42: Heavy Oil/Effect of oil viscosity – Profile of sand deposit at different times for two heavy oils, Run H 03 ($\mu = 1\,500$ mPa.s) and Run H 06 ($\mu = 10\,000$ mPa.s), $W_l = 6.825$ cm/s, $\rho_o = 1.00$ g/cm^3, $d = 0.5$ cm . 168

Figure 6. 43: Heavy Oil/Effect of oil viscosity – Profile of sand deposit at different times for two heavy oils, Run H 07 ($\mu = 1\,500$ mPa.s) and Run H 10 ($\mu = 10\,000$ mPa.s), $W_l = 2.5$ cm/s, $\rho_o = 1.00$ g/cm^3, $d = 0.1$ cm . 170

Figure 6. 44: Heavy Oil/Effect of oil viscosity – Profile of sand deposit at different times for two heavy oils, Run H 08 ($\mu = 1\,500$ mPa.s) and Run H 11 ($\mu = 10\,000$ mPa.s), $W_l = 5.0$ cm/s, $\rho_o = 1.00$ g/cm^3, $d = 0.1$ cm . 171

Figure 6. 45: Heavy Oil/Effect of oil viscosity – Profile of sand deposit at different times for two heavy oils, Run H 09 ($\mu = 1\,500$ mPa.s) and Run H 12 ($\mu = 10\,000$ mPa.s), $W_l = 6.825$ cm/s, $\rho_o = 1.00$ g/cm^3, $d = 0.1$ cm . 172

Figure 6. 46: Heavy Oil/Effect of flow velocity – Profile of sand deposit at different times for three velocities, Run H 01 ($W_l = 2.5$ cm/s), Run H 02 ($W_l = 5.0$ cm/s) and Run H 03 ($W_l = 6.825$ cm/s), $\rho_o = 1.00$ g/cm^3, $\mu = 1\,500$ mPa.s, $d = 0.5$ cm . 173

Figure 6. 47: Heavy Oil/Effect of flow velocity – Profile of sand deposit at different times for three velocities, Run H 07 ($W_l = 2.5$ cm/s), Run H 08 ($W_l = 5.0$ cm/s) and Run H 09 ($W_l = 6.825$ cm/s), $\rho_o = 1.00$ g/cm^3, $\mu = 1\,500$ mPa.s, $d = 0.1$ cm . 175

Figure 6. 48: Heavy Oil/Effect of flow velocity – Profile of sand deposit at different times for three velocities, Run H 10 ($W_l = 2.5$ cm/s), Run H 11 ($W_l = 5.0$ cm/s) and Run H 12 ($W_l = 6.825$ cm/s), $\rho_o = 1.00$ g/cm^3, $\mu = 10\,000$ mPa.s, $d = 0.1$ cm . 176

Figure 6. 49: Heavy oil/Effect of particle size – Profile of sand deposit at different times for two sand sizes, Run H 01 ($d = 0.5$ cm) and Run H 07 ($d = 0.1$ cm), $W_l = 2.5$ cm/s, $\rho_o = 1.00$ g/cm^3, $\mu = 1\,500$ mPa.s . 178

Figure 6. 50: Heavy oil/Effect of particle size – Profile of sand deposit at different times for two sand sizes, Run H 02 ($d = 0.5$ cm) and Run H 08 ($d = 0.1$ cm), $W_l = 5.0$ cm/s, $\rho_o = 1.00$ g/cm^3, $\mu = 1\,500$ mPa.s . 179

Figure 6. 51: Heavy oil/Effect of particle size – Profile of sand deposit at different times for two sand sizes, Run H 03 ($d = 0.5$ cm) and Run H 09 ($d = 0.1$ cm), $W_l = 6.825$ cm/s, $\rho_o = 1.00$ g/cm^3, $\mu = 1\,500$ mPa.s . 180

Figure 6. 52: Heavy oil/Effect of particle size – Profile of sand deposit at different times for two sand sizes, Run H 05 ($d = 0.5$ cm) and Run H 11 ($d = 0.1$ cm), $W_l = 5.0$ cm/s, $\rho_o = 1.00$ g/cm^3, $\mu = 10\,000$ mPa.s . 181

Figure 6. 53: Heavy oil/Effect of particle size — Profile of sand deposit at different times for two sand sizes, Run H 06 (d = 0.5 cm) and Run H 12 (d = 0.1 cm), $W_f = 6.825$ cm/s, $\rho_o = 1.00$ g/cm^3, $\mu = 10\,000$ mPa.s . ____ 183

Nomenclature

a – radius of solid particle sphere, L

C – coefficient (as in drag coefficient or lift coefficient), dimensionless

d – diameter of solid particle sphere, L

D – (particulate phase) diffusivity, L^2/t

F – force (as in drag force or lift force, or gravitational force), M. L $/t^2$

g – gravitational acceleration constant, L/t^2

G – mass flow rate of fluid (Eq. 2.5), M/t

h – height, L

L – length, L

p – pressure, $M/L.t^2$

Δp – pressure drop, $M/L.t^2$

q – volumetric rate (of the influx) per unit volume of horizontal well, $L^3/t.L^3$

r – radial distance, L

t – time, t

u – velocity along the radial direction, L/t

(Δu) – slip velocity between fluid phase and solid phase along the radial direction, L/t

v – (generic) velocity, L/t

(Δv) – slip velocity used in determination of Saffman's lift force, L/t

w – fluid phase velocity along the axial direction, L/t

(Δw) – slip velocity between fluid phase and solid phase along the axial direction, L/t

z – axial distance, L

N_{Fr} – Froude Number, dimensionless

N_{Re} – Reynolds Number, dimensionless

N_{M} – Momentum Transfer Number, dimensionless

$N_{Kn,p}$ – Knudsen Number, dimensionless

Greek Symbols

β – interphase interaction coefficient, $M/L^3.t$

γ – specific gravity, dimensionless

ε – fluid phase concentration measured in terms of volume fraction, dimensionless

$\Im$ – inverse of relaxation time, 1/t

ϕ – solid phase concentration measured in terms of volume fraction, dimensionless

$\bar{\rho}$ – material density, M/L^3

ρ – phase density, M/L^3

μ – viscosity, M/L.t

υ – kinematic viscosity, L^2/t^2

Superscript:

$*$ – quantity measured at standard condition

n – present time step/level of numerical discretization

$n+1$ – next time step/level of numerical discretization

Subscript:

D – drag

f – fluid phase

in. – influx flow from reservoir into horizontal well

k – kinematic (as in kinematic pressure)

L – lift

o – single solid sphere (as in terminal settling velocity) (as in Eq. 2.6)

p – penetration distance of a saltating particle into fluid stream (as in Eq. 2.8)

r – along radial direction

s – solid phase (also particulate phase)

z – along axial direction

critical – critical (velocity of suspensions) (as in Eq. 4.41)

m – (superficial velocity) measured at mean pressure (as in Eq. 2.4)

mixture – mixture of solid and fluid phases

MT – minimum transport (velocity) (as in Eq. 2.10)

settl. – settling (velocity of suspensions) (as in Eq. 2.6)

w – wall-sheared (velocity) (as in Eq. 2.10)

Chapter 1. Introduction

Horizontal wells are currently finding ever-increasing applications to recover oil and gas worldwide. The main advantages of horizontal wells over vertical wells include larger wellbore-reservoir contact area, possibility to reduce the effects of water/gas coning, as well as higher probability of intersecting systems of vertical fissures in fractured reservoirs. In thermal recovery applications, horizontal wells – due to their extended contact with the reservoir and current drilling capability to position them at the optimum horizon in the pay zone – offer the means to improve the recovery efficiency of conventional steam injection recovery methods, especially in marginal heavy oil reservoirs like those commonly found in Western Saskatchewan and Southeastern Alberta.

For unconsolidated and poorly consolidated formations, sand production presents a serious production problem. The sand and/or fines produced into the wellbore impairs production either by choking the wellbores, or by reducing production by preventing the proper operation of the downhole pumping equipment. For horizontal wells sand production potentially poses an even more serious problem than for vertical wells. Not only can it reduce well productivity for the above reasons, but the production of sand into a horizontal well could result in the sand settling and accumulating at different positions along the well length, and consequently reducing the cross-sectional area of the wellbore open to flow. The ultimate effect of sand deposition could be the partitioning of the horizontal well into several non-communicating segments, leading to a loss of production and negation of the principal advantage of a horizontal well (large contact area with the reservoir).

This study is an attempt to contribute to an understanding of the multiphase flow of oil and sand in a horizontal well. Specifically, it involves the formulation of several mathematical models describing the transport of oil and accumulation of sand/fines in a horizontal well. Numerical simulators are developed from the mathematical models for a 1-dimensional problem, focusing on transient multiphase transport phenomena in the case of an accumulation and/or constriction in the horizontal well. The simulators are used to generate results for various flow conditions, which encompass different fluid and solid particle properties. Scaling criteria are also derived, in view of future applications in experimental studies of similar problem(s).

Chapter 2. Survey of the Literature

The flow of solid-fluid mixtures has been examined and studied for many years, and today encompasses many different areas of science and engineering — including transport of colloids in rain water, sediment transport in river streams, waste transport in sewers, fluidized beds, flotation to slurry pipeline transportation, drill cuttings removal and transport of fracture proppants etc. In the following a survey of the pertinent literature from various sources is presented. Figure 2.1 provides a view of the overall organization of this chapter. Due to the close intertwining of theoretical concepts and experimental investigations common to multiphase flow topics, there is a great deal of overlapping of material presented in the surveyed literature. As such, it is entirely plausible that each of the surveyed studies can be classified in any of several pertinent sections. An effort is made to organize each reference into the section most appropriately matched with its main idea or area of contribution.

2.1. Motion of a Solid Particle in a Fluid

A prerequisite to the study of any solid-liquid multiphase flow problem is an understanding of the basic interaction between a solid particle and the fluid in which it is immersed. For multiple particle-fluid systems such as suspensions and slurries the interaction among the solid particles, and the effect of this intraphase interaction on the (interphase) interaction between the solid particles and the surrounding fluid needs to be considered.

2.1.1. Fundamentals

A solid particle in motion relative to the surrounding fluid is subject to the action of many forces, the most important of which are the drag force and the lift force. These forces contribute to the transfer of momentum between the solid particle and the surrounding fluid. The shape of the solid particle, and the rheology of the fluid are the main factors influencing the momentum transfer between the particle and the fluid.

2.1.1.1. Drag Force

According to Soo [1], in 1710 Newton determined experimentally the magnitude of the drag force exerted on a spherical particle in the steady motion of a viscous fluid, moving at a relatively high velocity, to be proportional to the square of the particle radius multiplied by the fluid density and the square of the fluid velocity. This relationship was shown to be valid when inertial effects predominate,

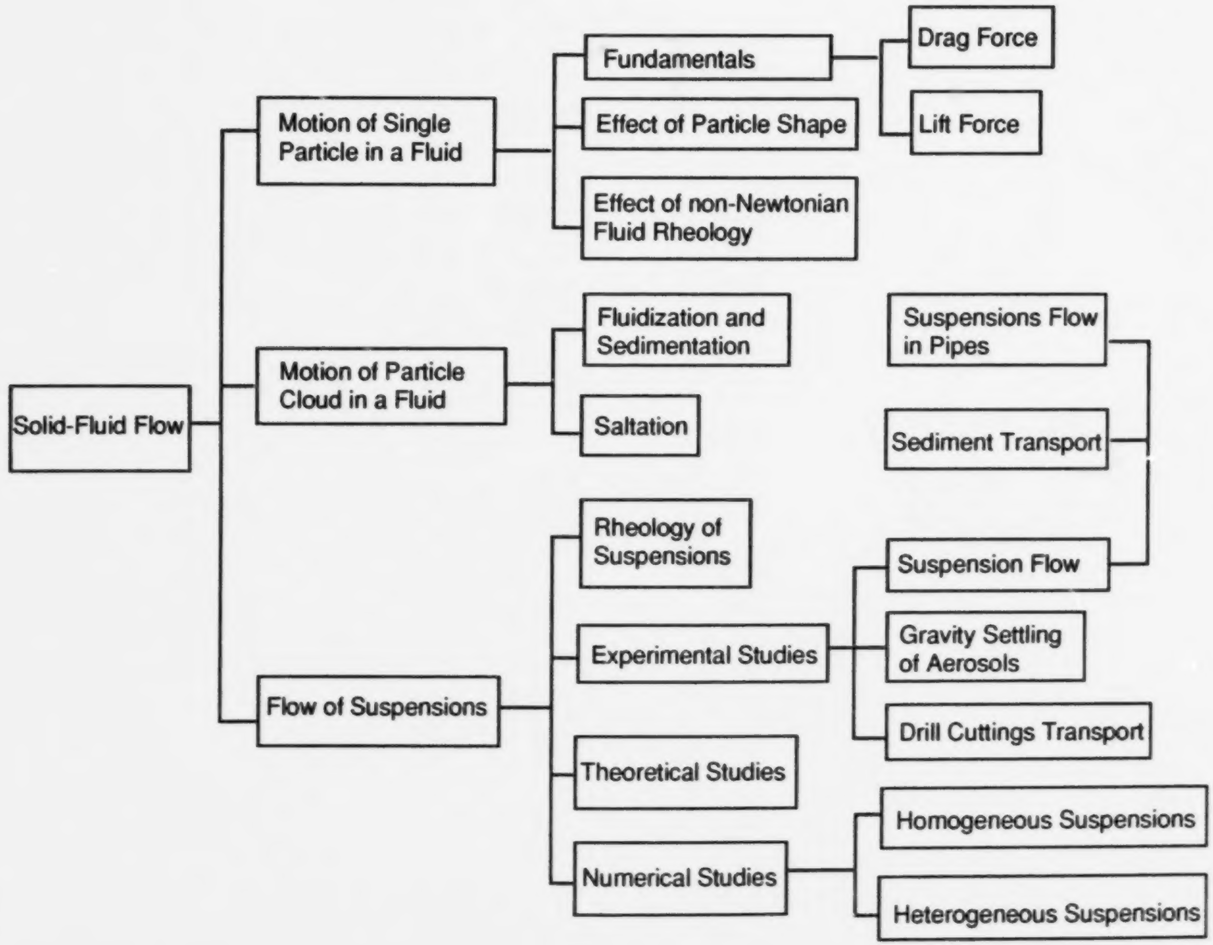
Solid-Fluid Flow
Motion of Single Particle in a Fluid
Fundamentals
Drag Force
Lift Force
Effect of Particle Shape
Effect of non-Newtonian Fluid Rheology
Motion of Particle Cloud in a Fluid
Fluidization and Sedimentation
Saltation
Flow of Suspensions
Rheology of Suspensions
Experimental Studies
Suspension Flow
Suspensions Flow in Pipes
Sediment Transport
Gravity Settling of Aerosols
Drill Cuttings Transport
Theoretical Studies
Numerical Studies
Homogeneous Suspensions
Heterogeneous Suspensions

Figure 2.1: Organization of Chapter 2 – Survey of Multiphase Flow Literature.

$$F_D = 0.22\pi a^2 \overline{\rho_f} (\Delta v)^2 \tag{2.1}$$

When viscous effects predominate (i.e. at low fluid velocities), Stokes in 1850 calculated the drag force exerted on a sphere to be proportional to the product of fluid viscosity, sphere radius and relative velocity – as shown below. One-third of this drag force was determined to be form drag (due to the pressure force), while the remaining two-thirds was friction drag due to the shear force [2],

$$F_D = 6\pi a \mu_f (\Delta v) \tag{2.2}$$

Between these two extremes a standard drag curve (Figure 2.2) applicable to a single solid sphere moving at constant velocity in a still, isothermal, infinite, incompressible fluid was determined experimentally by many investigators over the years [1].

2.1.1.2. Lift Force

Segré and Silberberg [3] described an experimental apparatus to determine the passage of solid particles in suspension undergoing Poiseuille flow through any selected point of a tube cross-section. The main component of the apparatus was an optical system utilizing two mutually perpendicular light beams to focus on two "corridors" along the x and y directions of an x-y plane. A "hit" coincidence was registered and counted electronically every time a solid particle simultaneously blocked out the common region of the two mutually perpendicular light beams. As such, the concentration distribution of particles within various regions in a tube was determined – enabling an analysis of particle trajectory in the flow channel as a function of time.

Segré and Silberberg [4] using the apparatus described in [3] studied the motion of rigid spheres transported in Poiseuille flow through a pipe. The authors assumed a parabolic profile for the velocity distribution in the flow channel, and a particle velocity dependent only on the radial distance from the pipe wall. Analysis of the solution to the equation of motion of the particles revealed the inertia of the moving fluid causing particle radial displacement. More important, the "tubular pinch" effect – whereby the particles achieved an equilibrium position at approximately 0.60 pipe radius from the pipe axis, irrespective of the radial position at which the spheres first entered the pipe – was observed. This was similar to Poiseuille's observation of a corpuscles-free region some distance away from the wall of blood capillaries. The "tubular pinch" effect proved the existence of radially outward forces acting on the particles. This result contravened conventional hypotheses of radially inward acting forces stemming from the criterion of minimum energy dissipation proposed by Jeffery in 1922.

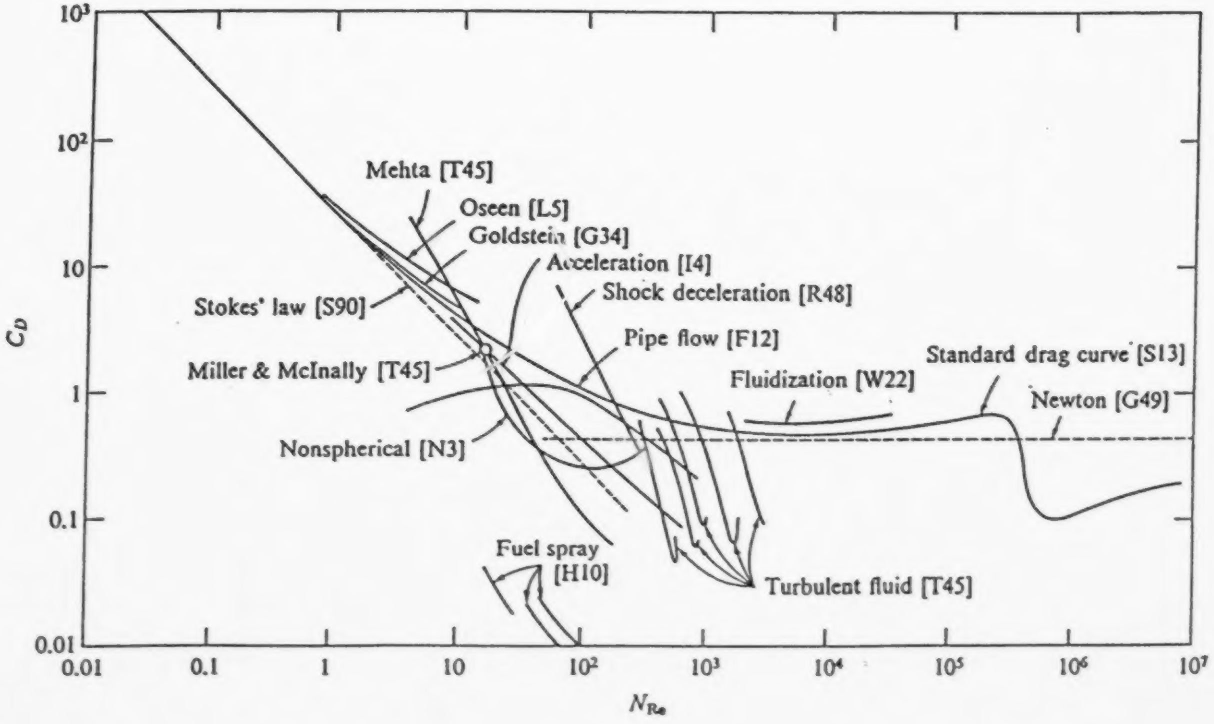

Figure 2.2: Drag coefficient of a single sphere. (After Reference [1].)

Saffman [5] pointed out that the extra drag due to the pipe wall tended to make the particle velocity lag behind that of the fluid. The resultant velocity difference was deemed to depend on the relative size of the particle and the pipe, and distance of the particle from the wall. Matching inner and outer expansions approximating the solution to the equation of motion of the fluid and the particle permitted the determination of the lift force in the z-direction, perpendicular to the flow direction. The magnitude of the lift force was determined to be

$$F_L = 81.2 \frac{v}{\nu^{0.5}} a^2 \left| \frac{dv}{dy} \right|^{0.5} . \qquad (2.3)$$

This lift force was seen to act in a manner so as to deflect the particle towards the streamlines moving in the direction opposite to the velocity difference. In other words, if the particle velocity was less than that of the fluid then the radial lift force tended to push the particle towards the flow axis and vice versa. This result was not compared quantitatively with those by Segré and Silberberg [4] mainly due to the uncertainty of the velocity difference in that study. {In the above equation, as well as in other equations cited in this chapter, the nomenclature used originally by the various authors in their respective studies are changed to conform to the nomenclature used in this dissertation.}

Rouhiainen and Stachiewicz [6] studied the deposition of small particles from turbulent streams. The effects of the shear-flow-induced transverse lift force on the motion of particles in the viscous sublayer were shown, theoretically and experimentally, to be sufficiently significant to result in much smaller particle radial velocities required at the edge of the viscous sublayer for ensuring particle deposition at the wall than was the case if Stokes drag were the only force present. This finding invalidated the Stokes stopping distance assumption invoked for most diffusion-based deposition models. In addition, it was shown that the two fundamental assumptions (equality of particle and fluid diffusivity, and purely inertial coasting of particles within the viscous sublayer) of these diffusion-based deposition models were untenable under most actual flow conditions. It was shown experimentally that there was a definite particle size most affected by the action of the lift force at any given Reynolds number. Light particles also seemed to benefit most from the lift force.

Lee [7], on the basis of results of experiments involving particles of different sizes and densities, stated the primary reason for the experimental finding of a particle-free zone at the pipe wall for large particles was the interaction between the lift force pushing the particles toward the pipe axis, and the drag force opposing this particles movement. In these cases, the velocity gradient was highest near the pipe wall, resulting in large lift forces pushing the particles away from the wall. For small particles, the turbulent diffusion force and the drag force governed the transverse transport of particles. The loss of longitudinal momentum of the particles, due mainly to their interaction with the slow-moving fluid near the wall rather than their collision with the wall itself, led to the formation of a slip-velocity reversal zone near the pipe wall.

2.1.2. Effect of Particle Shape

Moreland [8] measured the terminal velocities of crushed coal particles (diameter ranging from 80 to 2000 microns) in Marcol GX (a mineral oil), as well as the settling velocities of coal particle-Marcol oil slurries. Experimental results for the terminal velocities suggested a direct relationship between particle terminal velocities and their 'diameter'. It was determined that applying a constant shape factor to the 'diameter' term of the experimental correlation was not sufficient to enable a direct comparison with a correlation for spherical particles. Data on settling velocities of slurries having different "porosities" (void volume fractions) were found to obey the Maude and Whitmore [23] correlation between slurry settling velocities and the terminal velocity of a single particle along with the porosity. The exponent of the porosity was found to vary from 6.5 to 7.5.

Blumberg and Mohr [9] studied the settling characteristics of cylindrical particles in a mixture of polyalkenes and their derivatives. The aluminum cylinders were symmetrical and of eight different diameters and lengths. The density of the cylinders was 2.875 g/cc. The relation characterizing the dimensionless terminal settling velocity of the cylinders included a correction factor for the effect of the boundary on the settling motion. Terminal velocities were measured by timing the fall of the particles between two markers. Orientations of the falling cylinders were measured using a two-lens magnifying system, with one lens aligned with the vertical markings on the container and the other lens oriented along the cylinder axis. The dimensionless terminal velocities of the cylinders computed from the measured time intervals and fluid properties agreed reasonably closely (within experimental error) with previously reported experimental data.

O' Brien [10] developed a semi-analytical approach to determine the drag ratios – defined as the ratio of the drag of a deformed body to that of a sphere – as a function of the axial deformation for a variety of spheroids. This approach involved utilizing a computer program to calculate the coefficients of the Stokes stream function at a finite number of points on the spheroid body contour. The resultant flow field description enabled calculation of the drag value. A form factor, based on the calculated drag ratio, was found to correlate closely (1%) with the normalized deformational volume.

Peden and Luo [11] measured the static settling velocity of spherical and non-spherical (disks and rectangular plates) particles in both Newtonian and non-Newtonian (power-law and viscoelastic) fluids. The rheological properties of these fluids were measured at high, as well as low shear rates. From these measurements, various drag coefficient correlations were developed for spherical particles in laminar and transitional flow regimes. For non-spherical particles, equations defining the shape factor for disks and plates were given on the basis of their sphericity. A generalized equation was developed from the settling velocities in stagnant fluids to predict the settling velocities of particles of various shapes in both Newtonian and power-law fluids for all flow regimes.

Clark, Gabrielle, Shuker and Turton [12] utilized polygonal harmonics analysis to characterize the drag coefficient for irregularly shaped particles in Newton's flow regime. A computer-based imaging procedure was employed to generate polygons based on the drawing of fixed-length arcs between intercepts of the arcs and the edges of 2-D projections of the particles. The second harmonic persistence, related to the aspect ratio of the projected 2-D images, was found to have the strongest effect on drag. Accordingly, a correlation between the irregularly shaped particle drag and the sum of the persistences of the second harmonic for all three sides of the particle was proposed.

2.1.3. Effect of non-Newtonian Fluid Rheology

Hedstrom [13] pointed out that dense suspensions and many other two-phase systems follow plastic, non-Newtonian flow behaviour. As such, their behaviour was believed to be influenced by particle size, shape, weight, distribution as well as surface properties of the different phases. Utilizing experimental data available in the literature it was determined that the criterion distinguishing laminar flow from turbulent flow was a function of the yield stress, pipe diameter, plastic viscosity and average velocity. Furthermore, the usual Fanning friction factor curve for Newtonian fluids was found to be a good approximation for plastic fluids – as long as the fluid Reynolds number was defined in terms of the plastic viscosity.

Ansley and Smith [14] experimentally studied the drag coefficient of spherical particles in a Bingham plastic fluid. Dimensional analysis, coupled with an analysis of the stresses (inertial, viscous, yield) acting on the fluid surrounding the particle as well as the stress field associated with the relative motion of the solid sphere led to the development of a "dynamic parameter" to describe the laminar settling regime. This parameter was defined mathematically as the ratio of the inertial stress to the sum of the viscous stress and the yield stress. Experimental data including spherical particles of various diameter sizes, densities and fluids (tomato sauce, clay and kaolin solutions) of different yield stresses and coefficients of rigidity were used to test the validity of the proposed dynamic parameter. The particle drag coefficients, when plotted against the dynamic parameter on a log-log graph, followed a profile similar to that normally seen for the drag coefficient vs. sphere Reynolds number curve for Newtonian fluids.

Shah [15] analyzed the settling velocity of spherical proppants of different sizes and specific densities in six different non-Newtonian, pseudo-plastic fracturing fluids to develop correlations between drag coefficient and particle Reynolds number. The experiments were carried out under both static and dynamic conditions. Incorporating the flow behaviour index and consistency index of power-law fluids into the particle Reynolds number, and raising the power of the drag coefficient to reflect the effect of the flow behaviour index enabled the experimental data to be plotted as a family of curves dependent on the flow behaviour index. Despite the reasonable agreement between static and dynamic experimental data, the dynamic test results were deemed to be less reliable due to potential error attributable to the large number of variables involved in the dynamic tests. The proposed correlation between a modified particle drag coefficient and the generalized particle Reynolds number for pseudoplastic fluids required the evaluation of three curve-fitting parameters specific to each fluid.

Meyer [16] developed a generalized drag coefficient correlation applicable for all flow regimes for non-Newtonian, power-law fluids. It was compared with experimental and other empirical correlations to predict the drag coefficient and terminal settling velocity for fracture proppants of various mesh sizes. This correlation fitted experimental data much closer than Stokes ' law which was found to underestimate the drag coefficient and overestimate the terminal settling velocity of particles at high Reynolds numbers. In addition, the settling velocity was deemed to be independent of power-law fluid rheological properties such as the fluid consistency index and the fluid flow behaviour index at large Reynolds numbers.

Dedegil [17] examined the forces acting on a spherical particle settling at terminal velocity in a homogeneous, incompressible slurry. One of the assumptions invoked in the force balance was the negligible effect of the container wall on the particle settling motion. By defining the particle drag coefficient on the basis of the force equilibrium, which included the shear stress experienced by the particle and the particle Reynolds number in terms of the shear stress, the author obtained drag curves typical of those for conventional Newtonian fluids for both the laminar and transition regions. An equation for the settling velocity of a particle in suspensions based on the force equilibrium was given.

Mena, Manero and Leal [18] experimentally measured the drag coefficients for spheres of different diameters travelling, with constant translational velocity, longitudinally along the central axis of cylindrical containers of various radii. Newtonian, viscoelastic, inelastic and constant viscosity-elastic liquids were used in the experiments. For fluids exhibiting shear-thinning properties, wall effects on the translational motion of a sphere were found to be less pronounced in non-Newtonian fluids than in Newtonian fluids. For viscoelastic fluids, elastic effects were found to influence the drag force at low shear rates – with the drag departure from Stokes' law being a quadratic function of the Weissenberg number, which is a ratio of the characteristic relaxation time for a fluid to its convection time. At moderate and high shear rates elastic effects were determined to be negligible, and shear-thinning properties of the fluid phase dominated the drag reduction on the sphere.

McMechan and Shah [19] also performed tests in a Plexiglas rectangular slot to evaluate the static proppant settling characteristics of non-Newtonian fracturing fluids, which included both uncross-linked and cross-linked systems. Sand loadings from 240 to 1797 kg/m3, corresponding to 8-40% solids volume fraction, were used. Settling velocities higher than the single-particle settling velocity were caused by proppant clustering in linear gels at solids concentrations less than 1198 kg/m3. Above this critical value, hindered-settling effects were observed to be dominant – leading to much slower settling and more uniform distribution of proppants.

2.2. Motion of Particle Clouds in a Fluid

The hydrodynamic behaviour of multiple particle-fluid systems such as suspensions and slurries is, as stated above, controlled mutually by two types of interaction: intraphase and interphase. Interphase interaction occurs between the solid particles and the surrounding fluid, whereas intraphase interaction takes place due to the collision of the solid particles with one another. As expected, these interactions depend on – among many other parameters – the concentration of the solid particles in the solid-liquid mixtures and the rheology of the fluid.

2.2.1. Fluidization and Sedimentation

Steinour [20] studied laminar flow in the composite spaces between particles to determine the effect of particle concentration on the settling velocity of uniform spheres. It was assumed that the fluid friction was equal to the weight of the spherical particle less its buoyancy; as well, it was assumed that the loss in potential energy accompanying the falling sphere was equal to the work done against viscous resistance. Theoretical consideration of the viscous resistance tangential to the sphere surface and the buoyancy acting on the nonflocculated particles, along with application of the hydraulic radius concept, led to the formulation of an equation for the rate of sedimentation – relative to a fixed horizontal plane – as a function of the particle concentration. Experiments using suspensions of tapioca seed in oil, and microscopic glass beads in water were also performed to determine empirically the functions affecting the size and shape of the flow spaces for various void volume fractions.

Ergun and Orning [21] observed experimentally three distinct states when gas flowed through packed columns: fixed bed, expanded bed and fluidized bed. In the fixed bed state the pressure drop across the packed column increased with flow rate, without bed expansion. In the expanded state the fluid velocity was sufficiently large to cause a pressure gradient slightly larger than the buoyant weight of the solid particles – enabling the solid bed to expand. The pressure drop across the column remained mostly constant as the particles started to be dislodged. In the fluidized bed state high fluid velocity resulted in two-phase fluidization: a denser, continuous phase and the discontinuous phase consisted of solid particles in suspension. The relative proportion of these phases was dependent on the fluid flow rate. The Kozeny assumption of granular beds being equivalently represented by bundles of parallel and equal sized channels, along with the pressure drop relationship in Poiseuille flow were used to develop the following pressure drop correlation for the fixed bed state

$$\frac{\Delta p}{L} = \left[1 + 96.0\left(\frac{\alpha}{\kappa}\right)\left(\frac{1.0-\varepsilon}{N_{\mathrm{Re}}}\right)\right]\left(\frac{1.0-\varepsilon}{\varepsilon^3}\right)\frac{\kappa}{8.0}S_v\rho_{f,m}v_m^2 \ , \tag{2.4}$$

where α, κ were dimensionless coefficients, and S_v was the specific surface of a particle having a unit of (1/length). The gas density and superficial velocity were measured at the mean pressure. The two dimensionless coefficients represented the effect of kinetic losses in the capillaries.

Ergun [22] included the effects of fluid flow rate, viscosity and density along with the proximity and orientation of particle packing, and particle size, shape and surface in the development of an equation for the pressure drop in fluid flow across beds of granular solids, showing viscous and kinetic energy losses dependent on fractional void volume, i.e.,

$$\left(\frac{\Delta p}{L}\right)g_c = 150\left(\frac{(1.0-\varepsilon)^2}{\varepsilon^3}\right)\frac{\mu v_m}{D_p^2} + 1.75\left(\frac{1.0-\varepsilon}{\varepsilon^3}\right)\left(\frac{G v_m}{D_p}\right) \tag{2.5}$$

This pressure drop relation was validated with extensive experimental data from various independent studies. Furthermore, a transformation of the above correlation enabled the development of a linear relationship between a modified friction factor with the particle Reynolds number modified for the effect of fractional void volume. The modified friction factor related the magnitude of the pressure drop to that of the viscous energy loss. Values of the coefficients representing the intercept and slope of the straight line relationship were determined from experimental data.

Richardson and Zaki [23] also experimentally studied the effect of uniform-sized particle concentration on their settlement. Dimensional considerations were employed to determine the settling velocity of the suspensions as functions of the Reynolds number (based on the terminal falling velocity of a single particle), void volume fraction and ratio of particle diameter to pipe diameter. Experiments involving both sedimentation and fluidization of liquid-solid systems were carried out in two different apparati. It was determined that the falling velocity of a suspension relative to a horizontal plane was equal to the upward velocity of the fluid required to maintain a suspension at the same concentration. For different flow regimes (i.e. Reynolds numbers), separate correlations were developed from experimental data for the exponent corresponding to the slope of log-log plot straight lines between suspension falling velocities and suspension porosities.

Maude and Whitmore [24] – based on a consideration of the circulatory fluid movement through the volume of spheres added to a suspension, as well as the reduced force acting on spheres within a radius of each other – derived the following equation for the sedimentation rate of a non-flocculated suspension,

$$v_{settl.} = v_0(1 - \phi)^{\beta} \tag{2.6}$$

A log-log plot of this equation for different experimental data was linear, thus enabling the determination of the value for the exponent. For monodisperse, equidense spheres the value for the exponent was approximately equal to 5.

Fan, Lee and Bailie [25] used the gamma-ray attenuation technique to determine the axial bulk density profile for an air-solid fluidized bed. Glass beads of different sizes were used, ranging from 35 microns to 250 microns. Two distinct zones were observed in typical concentration distribution curves: a lower bed whose density was relatively constant, and an upper bed having noticeably large density gradients. The distinction between these two zones became less apparent as the air velocity was increased. Increasing the air velocity led to a decreasing density in the lower zone, as well as smaller density gradients in the upper zone, as expected. Static bed height was deemed to have only a small effect on the density profile. On the other hand, particle size and bed composition were found to have definite effects on the axial particle distribution profiles, leading to the development of various correlations for the density profiles of the lower zone for different particle sizes. A chart was also constructed to provide correlations for the pressure drop.

Round and Kruyer [26] measured the water velocities required to keep a single solid sphere in suspension in inclined tubes (diameters of 0.970, 1.280, 2.489 and 5.133 cm). Spheres of different sizes, densities and materials were employed. Four main flow regimes were experimentally observed. At low angles of inclination ($0\text{-}20^0$), the motion of the particle was predominantly gentle rocking in the transverse direction. At higher angles of inclination ($20\text{-}65^0$), the particle became still. The drag coefficient was independent of the Reynolds number in this region. There was a "bounce-point" regime at the end of the still region, whereas the friction between the sphere and the tube was reduced to zero. In this case, the drag coefficient was dependent only on the diameter ratio (i.e. sphere diameter to tube diameter). At larger angles, the sphere bounced radially until at angles close to 90^0, it rotated slowly and was freely suspended in water. Graphical correlations were developed for the suspension velocity, pressure drop and drag coefficient of these solid particles in the still region.

Batchelor [27] studied the sedimentation of uniform sized, rigid spherical particles homogeneously dispersed (statistically) in a Newtonian fluid. Assumptions utilized in the formulation and solution of the problem included equal probability of centres of various spheres to occupy different positions (thus excluding the overlapping of two spheres) and negligible inertial effects on either the fluid or the solid particles. The resulting equation

$$v = v_0(1.0 - 6.55\phi), \tag{2.7}$$

showed that the mean velocity of a sphere in a dilute dispersion of identical rigid spheres was proportional to the volume concentration of the spheres. Analysis of this equation showed that in a homogeneous dispersion having zero mean volumetric flux at various points in the system the downward volumetric flux of solid spheres was accompanied by a corresponding net upward flux of fluid volume. This primarily caused a reduction in the particle settling speed.

Glendinning and Russell [28] included thermodynamic effects in mutual diffusion in their determination of the sedimentation velocity for monodisperse concentrated suspensions. The final relation included the effect of "backflow" of fluid necessary to compensate for the volumetric flux of the particles as well as the slight hindrance due to nearby-fluid hydrodynamic interactions. This equation was seen to reduce to Batchelor's equation in the limit of a very dilute suspension [27].

Tadros [29] comprehensively reviewed the settling characteristics of both dilute and concentrated (dense) suspensions. A simplified treatment of the force balance permitted the determination of the sedimentation velocity for dilute suspensions of non-interacting particles. Interacting particles in relatively dense suspensions (solids volume fraction ≤ 0.10) led to the hindered settling effect, and this was corrected for in the sedimentation velocity by the use of the fraction void volume and an empirical constant. For the sedimentation of concentrated suspensions mention was made of several studies of sedimentation velocity, including Steinour's [20], Richardson and Zaki's [23], and Glendinning and Russell's [28].

2.2.2. Saltation

Bagnold [30] analyzed the saltation behaviour of particles-water systems whereby the solid particles move by leaping and jumping after striking a hard surface. The concept of threshold shear stress was proposed to explain the differences in the saltatory motion of solid particles in air and water. It was observed that in the case of saltation in air a falling grain hit the bed surface at a sufficiently high velocity to impart momentum to other rising grains, helping them to rise to distances many times their diameters off the bed. On the other hand, the high drag exerted by water on a solid particle reduced its final impact velocity sufficiently so that little or no momentum was imparted to other solid particles in the bed. The following equation was developed to determine the penetration distance of a saltating particle into the fluid stream – based on a consideration of the fluid force and gravity acting on the particle,

$$h_p = \frac{4}{3} \log_e \left(\frac{2\overline{\rho_s}}{C_D \rho_f} d \right) . \qquad (2.8)$$

Shook and Daniel [31] examined cases of suspension flows when there was a stationary and stable bed at the bottom of an open channel, and above the bed a region of decreased solids concentration upward. A force balance analysis, including the dispersive stress supporting the "bed load", along with experimental observations led to an equation for the hydraulic gradient necessary to transport solids where the Bagnold dispersive stress affected particle suspension. The values of the empirical constant of this equation were determined from experiments involving different materials (sand, nickel, lead) having different sizes, shapes, specific gravities and median settling velocities. They agreed reasonably well with the values obtained by Bagnold, with the deviation attributed to inadequate estimations of the shear stress at the upper boundary.

Shook, Daniel, Scott and Holgate [32] employed the same experimental apparatus as used in a previous study [31] to measure the vertical distribution of particles flowing in a horizontal, rectangular channel. The spatial distribution of particles was reflected by the absorption of gamma rays. Sand of different mesh sizes and nickel particles were used. It was determined that the particles were kept in suspension by two mechanisms. When the solid particle (whose diameter was small, < 0.2 mm) concentration was low and the ratio of the particle settling velocity to the flow friction velocity was less than 0.20, the particles were suspended by turbulent eddies. Deviations in particles concentration from the profile associated with the turbulent flow under high solid particle concentration were found to agree qualitatively with Bagnold's dispersive stress analysis. Furthermore, it was determined that the effect of a higher solid particles concentration was not to damp out the turbulent effect, but rather to increase the suspending capacity of the fluid phase.

Noda, Kawashima and Masuyama [33] experimentally studied three-phase (air, solid and water) flow in inclined pipes. The transparent pipe used in the experiments permitted visual observation as well as camera recording of the transition of the three-phase flow from the settling flow regime to the fully developed flow regime. Experimental data of flow, both upward and downward flow along the inclined pipe, were collected. The authors were unable to propose any correlation for the pressure drop from the downward flow experimental results. For upward flow, it was found that the air and solids flowed separately regardless of mean velocity, and that the rate of air flow did not significantly affect the flow of solids. An equation for the hydraulic gradient as a function of the mixture flow rate, air volume, solid specific weight and pipe inclination was proposed.

2.3. Flow of Suspensions

2.3.1. Rheology of Suspensions

Yan, Pal and Masliyah [34] presented experimental data on the rheological behaviour of oil-in-water emulsions with added solids. The oil (refined mineral oil, Bayol-35) concentration in the emulsion, without solids, was varied up to 70% by volume. The solids were either irregular shaped silica sand (mean diameter of 9, 22, 33 and 40 microns) or spherical glass beads (mean diameter of 19, 27 and 44 microns). The solids volume fraction was varied up to 20% of the total mixture volume. Experimental data for the solids-free oil-in-water emulsions were fitted by a power-law model, with the power-law index being equal to 1 (indicating Newtonian behaviour) for oil concentrations less than 40%, and less than 1 (indicating pseudo-plastic behaviour) for greater oil concentrations. The size of the solids affected the viscosity of the emulsion-solids mixtures significantly, with the result of a higher viscosity for smaller solids size. In addition, the oil-in-water emulsions behaved as a continuous phase towards the solid particles when the ratio of particle size to oil droplet size was greater than 3.

Yan, Pal and Masliyah [35] experimentally measured the viscosity of oil-in-water emulsions with added solid particles as functions of the volume fraction of solids and the volume fraction of oil in the emulsion. Three different oils, both refined and crude, and four types of solid particles were used. In all cases the size ratio of the solid particles to that of the oil droplets was bigger than three. As such, the oil-in-water emulsions behaved as a continuous phase to the added solid particles. Using the concept of bimodal mixtures, the viscosities measured for the oil/water/solid particles (a ternary system) were successfully correlated from the viscosity of the binary components (oil/water emulsion and solids/water suspension).

Shah [36] examined the effects of polymer gelling-agent concentration, proppant concentration, temperature, and fracture-flow shear rate on the rheological properties of fracturing slurries. The proppant used in the experiments was 20/40-mesh sand, and the temperature was varied from 26.7 ^{0}C to 43.3 ^{0}C and 60.0 ^{0}C. It was seen that the addition of sand to the base gels resulted in a significant increase in their apparent viscosities, the increase being a strong function of gelling-agent concentration, lower fracture shear rate, proppant concentration, and temperature. Specifically, lower gelling-agent concentration, lower fracture shear rate, higher proppant concentration, and higher temperature led to higher viscosity increases.

2.3.2. Experimental Studies

2.3.2.1. Suspension Flow

2.3.2.1.1. Sediment Transport

Graf and Acaroglu in a two-part study [37,38] presented analytical and experimental investigations of sediment transport in open channels, as well as in closed conduits. In the first study [37], a consideration of forces acting on a particle (including the resistance due to the particle surrounded by moving fluid, and the submerged weight of the particle) enabled the derivation of the following correlation between particle Reynolds number – based on shear velocity – along with particles concentration and a shear intensity parameter,

$$\frac{(\phi \cdot v \cdot R)}{\sqrt{\left[(\gamma_s - 1.0) \cdot d^3\right]}} = 10.39\left[\frac{(\gamma_s - 1.0) \cdot d}{SR}\right]^{-2.52} \tag{2.9}$$

where S, R were slope of the energy grade line and the hydraulic radius of the conduit, respectively. The shear intensity parameter (left-hand side of above equation) represented the ratio of the critical shearing stress, which was defined as the bed shear when the cohesion-less particles in a stationary bed started to move along with the fluid phase, to the shearing stress created by fluid flow. The right-hand side of the above equation was the transport parameter. Experimental data from various sources including total load data obtained in laboratory flumes, closed conduits with different cross-sectional areas and shapes, as well as in natural rivers were evaluated to obtain a relationship between the transport parameter and the shear intensity parameter.

Acaroglu and Graf [38] observed that the particles entrained in fluid flow moved in different modes (suspension, bed load, or a combination of these two modes) depending on the strength of the flow intensity. Bed forms such as ripples and dunes were influenced by particles moving in the vicinity of the bed. Based on open channel and closed conduit experimental data, qualitative functional relationships between the shear intensity parameter and the particle Reynolds number were established. It was determined that at low flow intensities the model of sediment transport was bed load, and the loose bed was shaped predominantly as ripples and/or dunes. At intermediate flow intensities, the ripples and/or dunes were washed out and the appearance of the solids bed became plane-like. The bed load motion still occurred, but a large number of solid particles started to be entrained. At high flow intensities the predominant mode of sediment transport was suspension. In this region antidunes formed in free surface flow, and a sliding bed formed in closed-conduit flow.

2.3.2.1.2. Flow of Suspensions in Pipes

Alves, Boucher and Pigford [39] pointed out that most solutions and suspensions followed Newtonian behaviour at low concentrations, and became non-Newtonian beyond a certain critical concentration. For suspensions, this critical concentration was deemed to depend on particle size and shape, concentration as well as degree of dispersion. The authors stated that Poiseuille's equation for the pressure drop due to friction in laminar pipe flow for Newtonian fluids was equally valid for non-Newtonian fluids provided that the Newtonian fluid viscosity was replaced by an apparent viscosity term. Several methods were presented to convert data obtained from either a rotational or a "pipeline" viscometer to a form readily applicable in the design of plant-scale pipelines.

Durand [40] systematically performed experiments to investigate slurry transportation in pipes. The solids used in the experiments were carefully graded to consist of uniform sizes only, and included coal, sand, and gravel. The average grain diameter varied from 20-30 microns up to 100 mm. Pipe sizes ranged from 40 mm to 700 mm. The behaviour of various slurries was determined to be influenced by the sizes of the solid particles. Grains of 20-30 microns in size were homogeneously distributed, and did not settle unless there was no movement of the carrier phase (water) or the flow was too slow (laminar). In turbulent flow, it was seen that the movement of turbulence eddies was sufficient to maintain the homogeneity of the mixture, and eliminate all stratifying due to gravity. For these homogeneous slurries the head losses were determined by taking into account the specific gravity of the mixture.

Grains of over 50 microns in size were observed to be heterogeneously distributed – irrespective of the existence of turbulence eddies – with the smaller grains (between 50 microns and 0.2 mm) kept in suspension due to turbulence fluctuations, while larger grains (> 2 mm) moved along the pipe by saltation. Properties of homogeneous slurries were described by the Bingham plastic model. An equation was derived for the critical (deposit) velocity based on a critical Reynolds number of 2000. It was stated that for heterogeneous slurries, unlike for homogeneous systems, the specific gravity of the suspension had no direct effect on the value of the head losses. For the flow of suspensions having a wide granulometric range it was observed from preliminary experimental data that the fine solids seemed to be able to reduce the head losses considerably.

Newitt, Richardson and Shook [41] performed numerous experiments involving flow of water suspensions of five different solid materials (Perspex, gravel, coarse sand, fine sand and zircon) in a 1-inch diameter horizontal pipe. It was seen that in the case of coarse solids the slip velocity increased towards the pipe bottom as the solids concentration was increased. This resulted in concentration gradients for the solids in the upper part of the pipe. In the fine solids case, the fine sand was observed to be evenly distributed over the pipe cross-section. In addition, as the coarse solids concentration increased, the water velocity – particularly in the centre of the pipe – was reduced. As such, the point at which the maximum fluid velocity occurred rose as the concentration was increased. Three mechanisms were postulated for the suspension of the particles in the fluid phase: a vertical component of fluid velocity at any point exceeding the settling velocity of the particles, a lifting effect on the particles as a result of their rotation in the fluid (Magnus effect), and dispersive forces as postulated by Bagnold [30] in the case of bed formation. It was suggested that the relationship between the terminal settling velocity and the friction velocity was generally a better criterion than particle size for characterizing the method of suspension.

Thomas [42,43] discussed transport characteristics of non-Newtonian suspensions in laminar and turbulent flow, respectively. Mention was made of Einstein's viscosity-solids volume fraction for dilute suspensions consisting of spherical, non-interacting particles, as well as modified versions of this equation to account for the hydrodynamic interaction between particles for relatively dense suspensions. An equation was proposed, based on experimental data, for the critical particle concentration at which particle bridging and hindered settling of flocculated suspensions occurred. In addition, it was shown that for a suspension following Bingham plastic behaviour the laminar friction loss followed closely the profile for Newtonian fluids, so long as the Reynolds number was defined on the basis of the Bingham plastic effective viscosity. Based on a critical Reynolds number of 2100 for the laminar-turbulent transition, an equation was obtained for the critical velocity for the flow of a Bingham plastic fluid in a large (> 1.0 inch diameter) pipe [42]. For turbulent flow, experimental data showed the transport characteristics of non-Newtonian suspensions to be functions of the intrinsic and extrinsic physical properties of the suspensions (e.g. density and specific heat for the intrinsic properties; and settling rate and viscosity for the extrinsic properties), independent of the composition of the solid particle phase. For low-yield stress suspensions the friction factors tended to approach those for Newtonian fluids as the Reynolds number was increased. On the other hand, the friction factors tended to diverge from the Newtonian values as the Reynolds number was increased for Bingham plastic suspensions with high yield stress. This phenomenon was attributed to the turbulent fluctuations being damped throughout the flow channel by the suspended solid particles [43].

Thomas [44] observed two distinctly different flow regimes, depending on the concentration of the suspensions. When the suspension was flowed at high rates, and the particles were sufficiently concentrated to be in the compaction zone, the settling rate of the flocculated suspension was very small. On the other hand, for dilute suspensions the particles were not in contact with one another and, despite the effect of hindered settling, settled at rates many times those for particles in the compaction zone. The critical concentration for transition from the compaction zone to the hindered settling regime was determined to depend on pipe diameter, and on the degree of particle flocculation. Based on this critical concentration criterion a correlation was suggested for the minimum transport of dilute suspensions,

$$\frac{v_t}{(v_w)_{MT}} = 0.0083\left[\frac{d \cdot \overline{\rho_f}(v_w)_{MT}}{\mu}\right]^{2.61} . \tag{2.10}$$

The minimum transport (subscript *MT* in the above equation) velocity was thus defined as the mean stream velocity required to prevent the accumulation of a layer of either stationary or sliding particles on the bottom of a horizontal conduit.

Thomas [45] carried out experiments employing a wide range of flocculated suspensions having solid volume fractions between 0.02 and 0.23. The particle sizes ranged from 0.35 to 13 microns. The Bingham plastic model was fitted satisfactorily to flow data at high shear rates, showing the yield stress to be directly proportional to the cube of the solid volume fraction and inversely proportional to the first or second power of the particle diameter. In addition, it was determined that the logarithm of the ratio of the coefficient of rigidity of the suspension to the viscosity of the continuous, suspending medium was directly proportional to the solids volume fraction. These experimental results led to the conclusion that the main factors influencing the magnitude of the laminar-flow properties of flocculated suspensions following the Bingham plastic model were particle concentration and particle size.

Thomas [46] determined the turbulent flow friction factors for flocculated suspensions of thoria, kaolin, and titania in pipes of different sizes (1/8, 3/8 and 1.0 inch). The Bingham plastic model was used to fit the non-Newtonian laminar flow data. Solids volume concentration in the experiments was varied from 4.2% to 23%. Experimental results regarding friction factors for the turbulent flow of Bingham-plastic suspensions having low and high yield stresses approaching and diverging, respectively, from those for Newtonian fluids at high Reynolds numbers were consistent with those obtained from a previous study [45]. The convergence toward Newtonian friction factors for suspensions having low yield stresses was postulated to be the result of a "thickened laminar wall layer". For suspensions having high yield stresses, the departure of the turbulent friction factors from the Newtonian values was believed to be due to the damping of the turbulent fluctuations by the flocculated solids, with this effect becoming more pronounced with solids volume fraction, and ratio of the attractive force between particles to the disruptive force due to turbulent fluctuations.

Thomas [47] examined the minimum transport velocity when the solid particles were larger than the thickness of the laminar sublayer and extended into the turbulent core. Experimental data obtained from flow tests of aqueous suspensions of glass beads (diameter ranging from 78 to 310 microns) in a 1.0-inch pipe, coupled with pneumatic- and hydraulic-transport data for air and water suspensions in the literature led to the following correlation

$$\frac{v_t}{v_0^*} = k\left\{\left(d \cdot v_0^* / \nu\right)^a \left(D \cdot v_0^* / \nu\right)^b \left[\left(\overline{\rho_s} - \overline{\rho_f}\right) / \overline{\rho_f}\right]^c\right\}, \tag{2.11}$$

which showed the ratio of particle minimum transport velocity to friction (wall-sheared) velocity at the minimum transport condition $\left(v_0^*\right)$ to be a function of the particle Reynolds number, pipe Reynolds number, and the relative density ratio of the particle to the fluid. The constant and the exponents in the correlation were determined experimentally, and were unique to each particular suspension. In addition, a map was developed on the basis of particles distribution and nature of fluid flow around the particles to classify different flow regimes for the minimum transport correlation.

For a Bingham-plastic suspension, Thomas experimentally found that the ratio of the yield stress of to the cubic power of the solids volume fraction, and the natural logarithm of the coefficient of rigidity–fluid viscosity ratio of a Bingham-plastic suspension to its solids volume fraction were constants and independent of suspension concentration [48]. In addition, they were proportional to the ratio of the fluid volume immobilized by the structure of a floc to the solids volume in the floc structure. As such, the rheological properties of a Bingham-plastic suspension, and hence its hindered settling characteristics, were determined by the degree of flocculation and concentration. Particle size was found to be the primary factor affecting the degree of flocculation for a suspension. A correlation was proposed to determine the diameter of a floc from an apparent particle diameter which accounted for both the particle size distribution, and the non-symmetrical particle shape.

Thomas [49] identified four different flow regimes (transverse waves, longitudinal waves, heterogeneous flow, homogeneous flow) as the velocity was varied during the transport of dilute suspensions through horizontal pipes in turbulent flow. These different regimes were classified based on the distribution of solid particles in the flow channel. A generalized phase diagram for suspension transport was constructed, with the terminal settling velocity, friction velocity, and Reynolds number – defined in terms of particle diameter and friction velocity – being the coordinates. In the first flow regime particle movement was initiated. The beginning of the second regime (or end of the first regime) was independent of pipe diameter. Depending on the magnitude of the particle Reynolds number, defined on the basis of friction velocity, the effect of particle density was accounted for either by the terminal settling velocity or by a relative density. Scarcity of experimental data precluded a clear demarcation between the heterogeneous flow and the homogeneous flow regimes.

Soo, Trezek, Dimick and Hohnstreiter [50] experimentally investigated the distributions of concentration, mass flow and velocity of solid particles in a gas-solid suspension. Experiments involving glass particles (210-250 microns) and magnesia particles (105-125 microns) were carried out in a 5-inch diameter pipe loop. Air velocity was maintained at around 135 ft/sec to ensure fully developed (i.e. steady state) turbulent flow for the test suspensions. Fiber-optic probes along with an electrostatic impact ball probe were used to measure the concentration and velocity of the particles. A higher particle concentration near the pipe wall was attributed to the electrostatic charge induced on the solid particles by impact with the wall, whereas the drift component of the particle velocity was due to electrostatic repulsion and particle diffusion. In addition, it was observed that the fluid velocity followed closely the 1/7 turbulent velocity law, whereas the velocity profile for the particles varied nearly linearly with distance from the wall. An equation for the diffusivity of the solid particles was determined, based on the experimental results.

Soo and Trezek [51] analyzed the results of experiments involving the turbulent flow of magnesia particles (logarithmic mean size of 36 microns) in air. The maximum mass ratios used in these experiments were 3 pounds of solids per pound of air. It was observed that solid particles addition to the system, up to a certain mass ratio of solid to gas, led to a decrease in the pipe flow friction factors. However, beyond this critical mass ratio, the pipe flow friction factors increased as the mass ratio was increased. The density distribution of solid particles was strongly influenced by the ratio of their charge to their mass. The velocity distribution of the particles did not follow the 1/7 turbulent flow velocity profile of the fluid phase, and instead varied nearly linearly with distance from the pipe wall.

Wasp, Aude, Seiter and Thompson [52] studied pressure losses due to friction in the turbulent flow of hetero-homogeneous slurries in pipelines. The solid particles, consisting of different sizes, were divided mainly into a small-size portion homogeneously suspended in the fluid phase, and a large-size portion heterogeneously distributed. The vehicle or continuous phase was assumed to follow Newtonian behaviour. The overall pressure drop was composed of pressure drop due to the homogeneous slurry, and a pressure drop due to the heterogeneous behaviour. The empirical Colebrook correlation between friction factor and Reynolds number, defined in terms of the slurry viscosity, was used to calculate the pressure drop due to the homogeneous portion of the suspension. The pressure drop due to the heterogeneous portion was determined by first applying the Durand equation to each size fraction of the solid particles in the heterogeneous portion, and then summing all of the individual size contributions. This method closely predicted experimental slurry friction pressure drops for many different materials.

Rose and Duckworth [53] combined analysis of dimensionless groups and experimental data to study the transport of mustard seed in air, and lead shot in water in horizontal pipe flow. The dimensionless groups derived included those governing the pressure drop required for the acceleration of solid particles, solid particles velocities, length of conduit required for the particles to attain a steady-state velocity, and the minimum transport velocity. The effect of pipe inclination was also examined. Experimental data were employed to determine the functional relationships between various dimensionless groups. The validity of these functional relationships was proven by the close agreement between their predicted values for the acceleration length, acceleration pressure, and total pressure drop with independent experimental data.

Gay, Nelson and Armstrong [54] related rheological behaviour of high solid-concentration suspensions to the physical properties of both the solid particles and the liquids. A mathematical model, based on the yield stress required to initiate flow and the force necessary to overcome inter-particle contact, was developed. The resulting equation for the viscosity parameter as a function of fluid viscosity, solid and liquid volume fractions was validated with experimental data to determine the value of an empirical constant. For high solids-concentration suspensions it was experimentally discovered that there were three regions of flow on a shear stress versus shear rate diagram. At low and high shear rates the relative viscosity coefficient was dependent on the ratio of the solids volume fraction to the maximum solids fraction of the system. At intermediate shear rates the flow was pseudo-plastic and the viscosity coefficient was a complex function of both the liquid and the solids properties.

Kaskas [55] studied settling velocities of particle swarms in polydisperse suspensions. Theoretically a geometric model describing the particle arrangement with time and a hydraulic model describing the fluid motion due to the settling particles were formulated jointly to determine the swarm velocity of any particle size fraction in a polydisperse suspension. Experimentally it was observed that the dimensionless swarm velocity – defined as the ratio of the swarm velocity of a size fraction to the Stokes settling velocity of a single sphere of the size fraction – of the bigger particles decreased with increasing initial concentration. For the smaller particles, at a critical concentration their dimensionless swarm velocity first approached zero and then became negative – indicating that these smaller particles now moved upward instead of downward. This upward motion reached a maximum and then decreased with increasing concentration. The change in the direction of the smaller particle motion was postulated to have been caused by an upward motion of the fluid, which itself was a consequence of the faster settling of the larger particles.

Hanks and Dadia [56] derived a theoretical model, based on the Bingham plastic rheological model, to calculate the friction factor–Reynolds number curves for non-Newtonian slurries flowing in smooth pipes, with assumed values for the modified mixing length constant and the damping parameter in turbulent momentum flux. A correction involving the Hedstrom number was used to determine the end of the laminar flow regime (and the beginning of the transition to turbulent flow). Excellent agreement was achieved between the friction factor–Reynolds number relationship predicted by this model and independent experimental data for turbulent flow for a wide range of Hedstrom Number values. It was also seen that above the Hedstrom number of $5x10^5$ the friction factor reached a maximum – suggesting an enhancement in the turbulence nature of these systems.

Turian, Yuan and Mauri [57] collected 1511 data points, including 917 data points from the authors' own experiments which covered several different pipe sizes, and solid particles of 12 different sizes (ranging from 31 microns to 4380 microns) and five different densities (2.3, 3.0, 4.4, 7.5 and 11.3 g/cc) to study the flow of heterogeneous suspensions in pipelines. The vehicle in these experiments was water. A functional relationship between the friction factor for heterogeneous suspension flow and the ratio of the inertial to the viscous force (i.e. Reynolds number), drag coefficient of a single free-falling sphere, and the discharge volumetric concentration of solids was derived. The empirical constants for this functional relationship were determined using the experimental data. The final forms of the functional relations for the friction factor for heterogeneous suspensions were generally similar to that obtained by Durand [40].

Hsu, van der Beken, Landweber and Kennedy [58] utilized the diffusion-convection equation, along with the assumption of constant and equal diffusion coefficients in both the radial and tangential directions, to obtain an exponential distribution of suspended sediment concentration along the vertical direction for uniform, steady, turbulent flow of suspensions in circular pipes. Five experiments, utilizing clean and uniform quartz sand (mean diameter=0.16 mm), were performed in a pipeloop (i.d.=2.125 inches) to verify the analytical result of exponential solids distribution along the vertical direction. It was found that for moderately low sediment concentrations used in the experiments the model predicted results close to the experimentally measured values, particularly with respect to the friction factor.

Freshwater and Goodacre [59] considered flow of a heterogeneous suspension in a horizontal pipe, with the solids divided into the "bed load" and the "suspended load". The particle-particle, and particle-fluid momentum transfer were based on Bagnold's shearing stresses, and particle suspension by fluid turbulent eddies. The total shear force on the pipe wall was composed of the shear force accounting for particle-particle interaction and the shear stresses within the interstitial fluid. The liquid (vehicle) phase of the suspension was made up of 85% volume toluene and 15% volume ethanol. Crushed Pyrex glass particles of three size fractions (between 0.4 mm and 1.5 mm) were used for the solid particles. Experimental measurements of particle velocity distribution, fluid velocity distribution and particle concentration distribution showed good agreement with values predicted from the model incorporating a momentum balance between the bed load and the suspended load.

Masuyama, Kawashima and Noda [60] measured the pressure loss for flow of coarse particles (crushed rock and plastic pellets)-bentonite slurry mixtures in a horizontal pipe. The coefficient of pressure loss was obtained both experimentally and from a theoretical model, which was based on the sum of the pressure drop due to the heterogeneously distributed coarse particles and the pressure drop due to the homogeneously pseudo-plastic (bentonite) slurry. These showed good agreement with one another. A linear correlation was also developed between the friction coefficient and a modified Froude number, based on a straight-line trend of the experimental data on a log-log graph. The authors also obtained a critical velocity for the pseudo-plastic carrier fluid from an experimentally determined lower critical Reynolds number.

Thomas [61] conducted laminar and turbulent flow tests of hetero-homogeneous suspensions in a pipeloop system. The coarse particles consisted of different sizes of sand and crushed coals. The vehicle phase was different clay/water suspensions. For turbulent flow it was consistently observed that the turbulent pressure gradients for coarse sand were 10% less than those measured for fine coal. The results for fine and coarse sand particles were less conclusive. As such, the addition of coarse particles to a heavy medium could lead to a lower pressure drop if the same quantity of fine particles were added. The laminar flow data included flow without and with particle deposition. In this case, the experimental data revealed an inverse relationship between the modified Shields number and the modified Reynolds number, both for Bingham plastics. As such, for laminar flow to be maintained at any typical velocity the concentration of the slurry (i.e. the heavy medium portion) was necessarily increased with an increase in pipe size.

Hashimoto, Noda, Masuyama and Kawashima [62] examined the effect of pipe inclination on solids deposition velocity. The experimental apparatus was a pipeloop consisting of hard glass pipes (55.8-mm i.d.) which could be supported at any arbitrary inclination. Crushed rock particles having a specific gravity of 2.83 and three different diameters were used. It was determined that the deposition velocity – below a critical maximum – increased rapidly with solids concentration. Beyond this, a further increase of solids concentration resulted in a reduction in the deposition velocity. This effect was more pronounced for the down-pipe inclination. Furthermore, the limiting deposition velocity increased with pipe inclination for up-pipe inclination – leading to a higher possibility of pipe blockage. These results agreed qualitatively with those obtained from a numerical model of saltating flow with a stationary bed.

Kao, Nosrati and Schaefer [63] also studied the effects of pipe inclination and declination on the transport of heterogeneous suspensions. Experimental results, including the in-situ transport solids concentration and the friction pressure loss, were analyzed and compared with results calculated from various empirical relationships for homogeneous flow. Large discrepancies between experimental and calculated results led to the development of two new equations for the transport of solids (measured in terms of volumetric concentrations): one for negative grade (declination) and the other for positive grade (inclination). The final equation for frictional head loss was similar to the Durand equation [40], and was a function of the frictional head loss for the transport phase along with the solids volumetric concentration and pipe inclination.

Weber [64] extended the applicability of the Durand equation [40] for the pressure loss in the transport of monodisperse heterogeneous Newtonian mixtures to polydisperse materials. This was achieved through the use of a correction which took into account the size distribution of the particles. Experimental data, including pressure gradient and solids concentration profiles, for homogeneous and heterogeneous slurries of different types and sizes of solids (sand, coal, lead, lead-tixoton and iron ore), agreed reasonably closely with the results predicted by this modified Durand equation. For concentrations of fine materials exceeding 20%, the non-Newtonian influences on the pressure gradient were described by a Reynolds number modified for a Bingham plastic fluid.

Hauge and Sharma [65] utilized the maximum deposition velocity of the fluid phase as the primary parameter in their study of particle deposition and bed formation for slurry flow in inclined pipes. Experimentally it was determined that particle transport behaviour varied with the angle of inclination, and that there were three separate regions in this behaviour. In the low inclination region (0 to 40^0), the deposition velocity gradually increased with increasing angle of inclination. In the intermediate inclination region there was negligible change in the deposition velocity with increasing angle of inclination. In the high inclination region the deposition velocity decreased with increasing angle of inclination, thus leading to conditions more favourable for efficient transport of particles. These results agreed generally with a simple force analysis, which considered the particle drag force, the friction force between the particles and the pipe wall, and the weight of the particles in both the radial and axial direction. The maximum deposition velocity was observed at an angle of inclination 35^0 from the vertical.

Ponce-Campos and Motan [66] measured the resistance due to shear stresses at the pipe wall at incipient pipe blockage conditions in a vertical pipeloop. The diameter ratio between the test pipe and particles used for the sand-water slurry was 50:1. It was hypothesized that a disruption of the mean flow resulted in a local buildup of the solids concentration, which in turn led to a decrease in the holdup. Gradually the pipe became blocked as the holdup approached zero. Analyzing the dynamics of the plug movement, it was assumed that the fluid seepage velocity was a good approximation of the fluid velocity after pipe blockage. Experimental results confirmed this assumption. The average friction factors, calculated from experimental data, were found to be significantly greater than those computed using correlations for steady heterogeneous flow. At incipient blockage conditions the friction factor calculated was between 400 to 800 times greater than that for pure fluid flow.

Nasr-El-Din, Shook and Colwell [67] measured the solids concentration distribution in a horizontal plane through the pipe axis for slurries of sand (median diameter of 0.19, 0.45 and 0.90 mm) and solid polystyrene (diameter of 0.30 and 1.40 mm) in water. Different mean velocities were used. A resistivity probe was used to measure local values of the solids concentration. It was determined experimentally that for coarser particles there were significant differences in particle concentration between the bottom and the top of the pipe at the lowest mean concentration.

There was no variation of concentration in the central 80% of the pipe at low solids concentrations, particularly for fine particles. A region of reduced concentration near the pipe wall was observed with higher solids concentrations and/or larger particles. This concentration reversal was believed to be caused by Bagnold dispersive stresses. For sand particles, gravity had a strong effect on the concentration profiles. It was noted that the combined effects of the dispersive stresses and hindered settling became significant at solids concentrations greater than 40%, by volume. At 50%, a concentration reversal occurred as the dispersive stresses became more dominant than gravity settling.

2.3.2.2. Gravity Settling of Aerosols

Thomas and Knuth [68] experimentally investigated the settling patterns of aerosols in streamline flow in a horizontal pipe. Monodisperse polystyrene latex aerosols of 1.305 microns diameter and 1.05 g/cc density were passed, at low flow rates, through a 1.58-cm diameter, 271-cm long horizontal pipe. The parabolic settling patterns for the aerosols at different flow rates agreed closely with the results predicted by an equation derived previously by Thomas [1953].

Pich [69] utilized the fluid laminar velocity profiles along with the effect of the gravitational force to determine the particle velocity vector. Knowledge of particle trajectories, including those of particles deposited in the flow channel and those of particles carried by the fluid through the flow channel, enabled the calculation of the precipitation efficiency of the transport process. Several flow channel geometries were examined: rectangular, circular, and elliptical. The author also determined that the critical length of the circular horizontal pipe required for complete deposition of particles with a given sedimentation velocity to be proportional to the ratio of the mean velocity of fluid flow through the pipe and the stationary sedimentation velocity of the particles.

2.3.2.3. Drill Cuttings Transport

Tomren, Iyoho and Azar [70] experimentally studied drill cuttings transport in directional wells. Actual drill cuttings were used, and the main component of the experimental rig was a 40-ft Lucite pipe section. The annulus angles were varied, in increments of 10^0, from 0^0 (vertical) to 90^0 (horizontal). Parameters studied included pipe rotation and eccentricity, as well as types of drilling muds and flow regimes. It was determined that an increase in hole angle reduced the cuttings transport performance, especially for inclination angles greater than 40^0, when the formation and buildup of a bed of cuttings took place – even at high fluid velocities. In addition, within a particular flow regime better cuttings transport was achieved with more viscous fluids. Pipe rotation was deemed to have a small effect on transport performance. However, cuttings transport was greatly affected by pipe eccentricity – with the best transport performance (indicated by lowest annular cuttings concentration) achieved when the pipe was concentric with the hole.

Okrajni and Azar [71], using the same experimental apparatus [70], identified three separate regions of hole inclination in the transport of cuttings in directional wells. In low-angle wells (0-45^0 from true vertical), the effect of the mud yield value was observed to be significant, particularly in the laminar flow regime, as a higher mud yield value reduced the annular cuttings concentration and improved transport. In high-angle wells (55-90^0), the effect of the mud yield value was insignificant. Improved cuttings transport was achieved with turbulent flow. Highest annular cuttings concentration (indicating poor cuttings transport performance) was observed in the "critical angles" region of 45-55^0 inclination from vertical, especially for low annular mud velocities. Generally, the mud rheological properties did not affect significantly cuttings transport performance in the turbulent flow regime.

Becker, Azar and Okrajni [72] – from the analysis of 180 tests – correlated rheological properties such as mud yield point, plastic viscosity, power-law exponent, consistency index, Fann V-G Meter readings at various speeds, effective viscosity and gel strengths with cuttings transport performance in directional drilling. It was determined that the 6-revolutions/minute Fann V-G dial reading, along with the mud shear stress at the average annular shear rate and the initial gel strength correlated well with cuttings transport performance. The linear-regression correlation coefficients for steady, laminar flow between annular cuttings concentration and these parameters were over 90%, especially for angles of inclination less than 45^0. The authors recommended laminar flow for hole angles between 0 and 45^0 from true vertical. For angles greater than 60^0 from true vertical turbulent flow was recommended.

Summarizing it can be seen that the surveyed literature, though not comprehensive from a multiphase flow view point, does cover a wide range of experimental investigations of solid-liquid systems. They include different properties for the solid particles (e.g. sizes, shapes, densities), fluid phase (e.g. , type of fluid (gas versus liquid), rheology, density), as well as different phase concentrations for the solid-liquid mixtures. They also take into account different operating conditions such as size of the flow conduit, pipe orientation, flow regime (i.e. laminar, transition, turbulent), and type of solid-liquid mixtures (i.e. homogeneous, heterogeneous, and hetero-homogeneous).

Some of the surveyed studies stand out more than others, and serve as benchmarks for their respective areas of investigation and application. The studies performed by Steinour [20], Ergun and Orning [21], Richardson and Zaki [23], Maude and Whtlmore [24] and Batchelor [27] contribute to the establishment of the functional relationship between the settling (or sedimentation) velocity of suspensions with solid concentrations. Bagnold's finding [30] of a threshold dispersive stress for the saltatory transport of particles in a fluid stream improves the understanding of different modes of particle transport. Graf and Acaroglu's finding [37-38] of a flow intensity necessary for the entrainment of sediment in an open channel, as well as in a closed conduit, is important for the understanding of different sediment bed structures. The comprehensive nature of Durand's experimental investigation [40] enables the establishment of different transport correlations appropriate for various types of suspension. The experimental study by Newitt et al. [41] serves to improve the understanding of particle distribution in the flow conduit. Thomas's studies [42-48] provide the groundwork for studies into the transport of flocculated suspensions.

2.3.3. Theoretical Studies

Van Deemter and van der Laan [73] formulated differential equations to describe the mass, momentum and energy conservation for the flow of a homogeneously dispersed solid-liquid suspension. The derivation, which was based on integral volume elements containing sufficiently numerous particles that it was valid to use continuous variables to describe local properties of the system, took into account the effect of differences in the velocity between the fluid and the particles. The stress tensors appearing in the momentum and energy balance equations were not, however, explicitly defined.

Hinze [74] utilized a different approach to derive the same differential equations for the momentum and mechanical energy balance. In this case, the momentum and mechanical energy balance equations for the continuous fluid phase were derived first. The effects of the suspended discrete particles were treated as akin to those of external forces acting on the fluid phase. This approach enabled an explicit definition of the shear stress tensors appearing in both of these equations.

Hershey and Song [75] studied pulsatile flow phenomena such as those existing in engineering pumping systems and circulatory blood flow in the human body. The authors derived a theoretical equation, from the Navier-Stokes equation and a modified Fanning equation, to calculate the friction factor and pressure drop for sinusoidal, laminar flow in tubes. The friction factor was determined to depend on the average Reynolds number (i.e. based on the average fluid velocity) and a function of the frequency of pulsation. Pressure drop values predicted from this friction factor agreed within 5% of experimental results for lower frequencies, and within 11% for frequencies higher than 40 cycles/minute.

Soo [76] examined the fully developed flow of dilute suspensions in pipes with negligible effect, and under the influence of an electric field force. Equations of motion were derived separately for the fluid phase and the particulate phase. The density distribution of the solid particles was described by diffusion under the influence of field forces, including the electric field force and the lift force acting on each particle. The fluid phase velocity for laminar flow was assumed to have the conventional parabolic profile. For turbulent flow, the 1/7 power law was used to describe fluid phase velocity profile. A series expansion was used to obtain an analytical solution for the axial velocity of the particulate phase, which was then used to determine its density distribution. The velocity and density distribution of the particulate phase were found to be dependent on five dimensionless flow parameters representing the effects of fluid shear, diffusion of the particles inside the fluid phase and relaxation of the momentum transfer between the fluid and the particles. Two different examples were examined: laminar flow of a liquid-solid suspension and turbulent flow of a gas-solid charged suspension. For both of these cases, analytical results compared favourably with experimental data.

Soo [77] formulated equations to describe the transport of dense suspensions in pipes. In these cases, it was postulated that the relative motion between particles was small, particle-particle interaction was strong and particle diffusivity was small due to the lack of vacant spaces between particles for randomized movement. As such, the effect of fluid presence was overshadowed by particle-particle collision. Additionally, fluid turbulence eddies were damped out by the dense particle concentration – leading to a form of laminar flow. An example solution was given for the case of stratified flow, with a dilute suspension in the upper part of the horizontal conduit, and a dense suspension below. The velocity distribution of the fluid phase in the dilute phase was assumed to be unaffected by the presence of the particles. The viscosity of particle-particle interaction was assumed to predominate in the lower-layer dense suspension. The transfer of inertia forces between the dilute phase and the dense phase, along with the lag in the phase, affected the motion of the interface – resulting in flow regimes ranging from a wavy interface to intermittent plugs.

Roco [78] included both colloidal and hydrodynamic effects such as Brownian diffusion, electrostatic repulsion, mass attraction, fluid drag, lubrication, inter-particle friction, collisions and inertial effects in the construction of a flow diagram for solid-liquid mixtures. The mass averaging approach was employed to incorporate micromechanical forces (such as those between particles, between the particles and the fluid, and between the particles and the pipe wall) into the macroscopic transport equations. The flow patterns were constructed based on threshold dimensionless numbers, and the criteria chosen for pattern classification included the degree of dispersion of solid particles in the fluid, particle interaction mechanisms and flow stability of the solid-liquid mixture. There were four main zones in the flow diagram: drag zone, lubrication zone, collision zone, and friction zone.

2.3.4. Numerical Studies

Within the last fifteen years many numerical simulation studies of suspension flow have also been performed, quite often in conjunction with experimental investigations.

2.3.4.1. Homogeneous Suspensions

Murthy and Zandi [79], from the equations of continuity and motion, as well as from a general functional relationship for the viscous interaction between solid particles and fluid, derived two equations to describe the velocity profiles and head losses of turbulent flows of non-Newtonian (power-law) suspensions in circular pipes. The velocity, pressure and shear stress parameters were composed of time-smoothed and fluctuating components. Experimental data from several independent sources on the flow of suspension systems, covering a wide range of materials for the disperse and continuous phases, pipe diameter, density and mean flow velocity were used to validate the above equations. In the case of the friction factor (or head losses), the maximum deviation between calculated and experimentally determined values was found to be 9%, with the average deviation commonly less than 5%. Furthermore, the equation derived for the velocity profiles was not constrained by the boundary conditions at the pipe wall and pipe centre.

Soo [80] studied the hydraulic transport of solids in inclined pipes. Equations of motion for the fluid phase and the particulate phase, along with the equation describing the diffusion of the particulate phase under field forces similar to those reported previously [80] were solved numerically. It was determined that the Reynolds and Froude numbers controlled the motion of the fluid phase, whereas the diffusion response number, shear response number, momentum transfer number and particle Knudsen number influenced the motion of the particles. Gravity effect was observed to become significant in suspension systems having high particle concentrations and flowing in large diameter pipes. The numerical results matched closely with experimental data of silica sand transported in air, and zircon sand transported in water.

Soo and Tung [81] formulated equations for the fully developed flow of a dilute suspension in a turbulent fluid with electrically charged particles and/or with a significant gravity effect. Pipe inclination was also a variable of the study. Sedimentation was not allowed for in the formulation of the problem. The motion of the fluid phase and the particulate phase were controlled by the pipe flow Reynolds number, Froude number, electro diffusion number, diffusion response number, momentum transfer number and particle Knudsen number. Four different examples were considered, with various combinations of the effects of the electrostatic and gravity forces. In all cases, for given fluid velocity profiles the distributions of particle velocity and concentration were completely determined from the basic properties of the fluid and the particles. Numerical results compared favourably with independent experimental data for gas-solid and liquid-solid suspensions. It was shown that the gravity effect became significant in the case of large pipe diameters and large particle concentrations.

Soo and Tung [82] extended their previous study [81] to include the effect of sedimentation. However, the axial gradient of the total particle flow was assumed sufficiently small such that the overall flow was treated as quasi-steady. In addition, inertia terms in the equations of motion were neglected. The deposition of particles was assumed to be controlled by the diffusion of these particles in the fluid phase. A sticking factor was introduced, and numerical values between 0 and 1 were assigned to account for the probability of particles sticking to or settling at the pipe wall as against their complete re-entrainment in the fluid phase. The sticking factor was related to the force of adhesion of particles to a surface. A shear-flow-induced lift force was also included in the formulation of forces acting on the particles. Numerical solutions were obtained for different cases – ranging from electrostatic sedimentation only, to gravity sedimentation only, to a combination of both. For the case of gravity sedimentation of a coarse sand-water suspension, close agreement was observed between the numerical results obtained by this study and the experimental data obtained by Newitt et al. [41].

Givler and Mikatarian [83] examined the conditions leading to the initiation of a particulate plug for flow of an initially homogeneous suspension. The suspension was assumed monodisperse, with the liquid phase incompressible and Newtonian. Inter-phase interactions were dominated either by interfacial drag forces or un-equilibrated pressure forces. In addition, the pressure associated with the particulate phase was assumed to be the sum of the fluid phase pressure and the kinematic pressure of the solids. This kinematic pressure of the solids was dependent on the fluid phase density, a function accounting for particles interactions vis-à-vis particles concentration, and the slip (relative) velocity between the fluid phase and the particulate phase. A numerical solution was obtained for one-dimensional, two-phase flow in a duct whose cross-sectional area was variable due to the existence of a constriction which changed with time. It was determined that a reduction in the fluid phase pressure resulted in an increase in the particle concentration in the constriction. In addition, high interfacial drag forces quickly equilibrated phase velocities – despite an initially large disparity in their values.

Lee and Wiesler [84] developed a new model to explain the behaviour of transverse particle transport due to turbulent diffusion in dilute suspension flow. The transverse fluid velocity was divided into two superimposed components representing the transverse turbulent fluid fluctuations and the transverse local fluid drifting velocity, respectively. The local fluid drifting velocity component was due to the effect of the transverse oscillatory component of the fluid motion on the transverse concentration distribution of particles. For the transverse turbulent fluctuations, it was seen that the response of the particles generally lagged the driving fluctuating fluid velocity by a phase angle. The local drifting velocity of the particles was determined to be a function of the turbulence properties of the surrounding fluid and the fractional particle concentration gradient in the transverse direction.

Rasteiro and Rebola [85] developed and numerically solved the steady-state (i.e. fully developed flow), two-dimensional convection-dispersion equation for the particulate phase. This model took into account the dynamic equilibrium between the settling tendency of the particles and their tendency to disperse from regions of high concentration. Isotropic dispersion was assumed. The correlation used to describe the dispersion coefficient and concentration was based on results reported for liquid-liquid diffusion coefficients and measurements of heat transfer in solid-liquid suspensions. To solve the non-linear convection-dispersion equation a modification of the discrete Newton method was used. It was determined from the numerical results that the particle concentrations varied significantly in both the y- and the x-direction, and that the particle concentration profile was strongly dependent on the dispersion coefficient–vertical-direction velocity ratio. For very low values of this ratio the particles tended to concentrate in the bottom half of the pipe cross-section. There was a general agreement between these results with selective experimental data reported in the literature.

2.3.4.2. Heterogeneous Suspensions

Toda, Konno and Saito [86] compared results from a two-dimensional numerical model with experimental data for the deposition velocity of slurry flow in horizontal pipes. The numerical model consisted of two parts: the suspension and the particle bed. Furthermore, it was assumed that the velocity at which the stationary bed began to move coincided with the velocity at which the stationary deposit occurred in a pipeline (i.e. limit-deposition velocity). Among the forces included in the analysis were the frictional force, the normal force caused by collision of particles with the surface of the particle bed, and the drag force of the fluid within the particle bed. Empirical correlations were used for the coefficient of friction and roughness. The equations of motion for the particles in the suspension above the bed were solved by the Runge-Kutta-Gill method. Numerical results for the limit-deposit velocities agreed closely with experimental results. Furthermore, the transport of solid particles at low solid concentrations was controlled mainly by the shear stress of the fluid acting on the surface of the particle bed. For higher solids concentrations, the drag force of the fluid within the particle bed played a significant role in the transport of solid particles.

Roco and Shook [87] incorporated the "supported load" model to account for the interaction through contact among solid particles, or between solid particles and the pipe wall into the partial differential equations of motion for the carrier liquid and solid phase. The distribution of solids concentration was influenced by gravity, turbulent fluctuating motion of the liquid phase, solid-liquid slippage, mixing effects due to solid particle fluctuating velocities caused by reciprocal interaction, dispersive effect in shear suspension flows, and supported load. The system of partial differential equations was solved numerically, with the results compared against experimental data obtained for sands of four different sizes (diameter of 0.165, 0.48, 0.52 and 13 mm) and pipe diameters between 50 and 500 mm. The solids volume fraction was kept below 40%. There was close agreement between the calculated and the measured concentration distribution for the three smallest sands. The differences between the calculated and the measured concentration distribution for the largest-sized sand was attributed to the high particle diameter-pipe diameter ratio, which affected the relative velocity between the phases, and effects of large-scale eddies.

Roco and Shook [88] numerically calculated the solids velocity at the pipe bottom to enable the establishment of a criterion for the critical velocity of slurry transport in pipelines. The numerical model was valid for solids concentration at up to 40% by volume. Increased particle interactions at higher solids concentration was manifested by the supported load (Coulombic contact), dispersive stress (particle collisions) and increased particle diffusivity (mixing effects). Solution of the equations of motion and for the concentration of the particles phase, given the mixture velocity, provided the solid velocity distribution for both laminar and turbulent flow of uniform particles in horizontal pipes. The numerical results thus obtained were compared with experimental results of water-sand slurries flowing in pipes of different sizes, showing close agreement. Inflection points between flow without deposition, with a sheared bed, as well as with a stationary compact bed led to the characterization of the critical flow regime (i.e. when the particles were not transported by water).

In conclusion, it can be seen that corresponding to the two main types of suspensions (homogeneous and heterogeneous) there are two distinct trends of numerical modelling of suspension flow. For the case of homogeneous suspensions the surveyed studies, especially those by Soo et al. [81-82], investigate mainly flow conditions leading to the deposition of particles from the fluid stream. A common assumption used in these studies is fully developed flow for the fluid phase. The known velocity profile of the fluid phase enables the determination of the interphase momentum transfer term, and thus the calculation of the velocity profile and concentration distribution of the solid particles. For dense and heterogeneously distributed suspensions the studies by Roco and Shook [87-88] investigate the interaction of the particles in the solid bed (bed load) and particles entrained in the fluid stream (suspended load), and the impact of this interaction on the solid concentration distribution in the flow conduit. As such, these studies examine different aspects of suspension flow. To simulate the problem of suspension flow fully (i.e. from the initial state of homogeneous distribution of particles, to particle deposition and bed formation due to field forces, to movement of solid bed) requires, if it is possible, an incorporation of both of these models. Additional references on various mathematical models, and numerical studies of the multiphase flow of solids and fluids are given in the next chapter.

Chapter 3. Statement of the Problem

The research undertaken in this study examines the transient transport of oil and sand/fines in a horizontal well. This investigation is motivated by the persistent problem of sand deposition in horizontal wells in Saskatchewan heavy oil reservoirs under primary production. The objectives are to develop a mathematical model describing the transport of particulate material in a liquid stream, with gravity effects included, and to attempt to gain an understanding of the transient transport phenomena of this multiphase transport through an analysis of numerically generated results. The specific objectives of the proposed study are as follows:

1. To formulate mathematical models describing the transport of solid particles in oil in a horizontal well, allowing for the influx of such particles and oil from the reservoir into a horizontal well along its length.

2. To develop numerical simulators from the mathematical models, and use them to solve a problem typical of sand deposition and accumulation inside a horizontal well. This includes evaluating a previously reported mathematical model of fluid-particle transport in a constricted horizontal channel, and developing a model simulating the process of solid particle deposition and accumulation inside a horizontal well due to gravity.

3. To derive scaling criteria for the transport of oil and sand in a horizontal well to permit the design of suitable laboratory experiments in the future.

Chapter 4. Development of Mathematical Models

The derivation of the mathematical models for the hydrodynamic transport of oil and sand in a horizontal well is presented in this chapter. Given the preponderance of empirical studies of various solid-liquid multiphase flow processes, the main objective of this model formulation is to examine the mechanisms involved in the hydrodynamic transport of solids and liquids mechanistically – keeping in view the necessity of invoking simplifying assumptions to keep the formulation tractable. Secondary objectives include recasting the mathematical models in a form suitable for numerical solution by the finite difference method, and also suitable for stochastic analysis through the use of dimensionless scaling groups.

This chapter is divided into three main sections. In the first section a brief introduction is given, along with a review of the main features of various mathematical models commonly encountered in the literature. Mathematical formulations for a general two-dimensional model, as well as two one-dimensional models – including one that is directly applicable to the modelling of oil and sand flow inside a horizontal well in this particular investigation – are given in the second section. A description of the numerical solution – including the finite difference formulation, discretization scheme and solution procedure – of the one-dimensional models is provided in the last section.

4.1. Introduction

The diversity of solid-fluid multiphase flow processes, coupled with the complexities inherent to all multiphase flows have resulted, over the years, in correspondingly diverse mathematical formulations of these flow processes. As shown in the surveyed literature (Chapter 2) the increasingly sophisticated formulation of models has occurred directly as a result of an increase in the knowledge and understanding of the mechanisms involved in multiphase transport processes, in particular those describing the interaction between the two phases, viz. solid and liquid. When there is more than one solid particle flowing in a fluid, the effect of intraphase interaction – in the form of particle-particle collisions, and hydrodynamic interference of the flow fields of adjoining particles – on the interphase momentum transfer between the solid and fluid phase increases still further the complexities of solid-fluid multiphase flow modelling. In the following, a review of the features of several mathematical models for solid-fluid flow is provided.

4.2. Review of Available Mathematical Models for Solid-Fluid Multiphase Flow

In general, mathematical models for solid-fluid multiphase flow can be divided – ranging from the simplest to the most comprehensive – into three groups: pseudo single-phase fluid flow, two-phase flow with a single pressure for both phases, and two-phase flow with two distinct pressures (one for each phase).

4.2.1. Pseudo Single-phase Fluid

The simplest approach used to model two-phase, solid-fluid flow treats the solid-fluid mixture as a pseudo single-phase fluid whose properties are derived from the intrinsic properties of its constituent phases, as stated by Thomas [42-43]. As shown in Chapter 2, the solid-fluid mixture is assumed to be homogeneous in the majority of experimental (and theoretical) studies conducted. The focus of these experimental studies consists in determining the rheological properties of the solid-fluid mixture mainly as functions of solid particle concentration, intrinsic properties of the respective fluid and solid phases, as well as examining the settling behaviour of solid particles for the determined rheological properties. The settling behaviour of a single solid particle was investigated, and the results from the investigation usually formed the basis for correlations predicting the settling behaviour of clouds (or swarms) of solid particles. These correlations invariably link the hindered settling behaviour of clouds of solid particles with solid concentration. Several experimental investigations treated slurries and suspensions as either heterogeneous or homo-heterogeneous mixtures. In these instances the solid phase was usually sub-divided into groups according to size, and properties [40,52,55].

The pseudo single-phase fluid approach to model the flow of solid-fluid mixtures, as described above, enables conservation equations derived for single-phase fluid flow to be used – with appropriate modifications introduced to reflect the rheological properties of the overall mixtures – in the calculation of various parameters. Depending on the application, the most important parameter to be calculated varies from the pressure drop (or pressure gradient) in the pipeline transport of slurries, to the deposition and/or the critical velocity in solid-fluid separation processes such as fluidized beds, pneumatic transport of solids, to the deposition efficiency in aerosol transport.

4.2.2. Two-phase Flow with One Pressure

This approach of modelling solid-fluid multiphase flow involves treating the solid phase and the fluid phase as two distinct, but interacting continua. As such, the behaviour of each phase is governed by its own conservation equations. Interphase interaction terms are usually added to, and subtracted from, the equation of motion for the disperse (usually solid) phase, and the equation of motion for the continuous (usually fluid) phase, respectively, to account for the momentum transfer due to the drag exerted by the fluid phase on the solid particles. van Deemter and van der Laan (in 1961) and Hinze (in 1963) were among the first investigators to provide conservation equations, employing this approach, for dispersed multiphase flows. van Deemter and van der Laan's formulation did not provide any explanation of the stress tensors and drag forces which appeared in the momentum balance and mechanical energy balance equations [73]. Hinze's model, on the other hand, treated the stress tensor on the basis of a composite velocity made up of the dispersed (solid phase) velocity and the fluid phase velocity – thus, accounting for the slippage between the two phases. However, the effect of particle concentration on the shear viscosity of the stress tensor was not considered [74]. In addition, it was pointed out that Hinze's equation of motion for the overall solid-fluid mixture contained a virtual mass term whose presence violated Newton's third law [89]. Standart [90] used the integral transformation theorems to obtain the 'local' form of the differential equations governing the conservation of mass, momentum and mechanical energy for heterogeneous flow systems from their original integral forms. Of special interest is the subsequent derivation of the first law of thermodynamics and Bernouilli's equation from the differential conservation equations to render them independent of the absolute velocity of the phase boundary. The author emphasized that the system of equations, as derived, is as equally applicable to slug, bubble, spray flows as well as stratified flow.

Rudinger and Chang [91] applied the method of characteristics to obtain solutions for two problems of suspension flow. The analysis excluded interphase mass transfer; as well, it assumed that the wall shear force acted on the fluid phase (gas) uniformly over the entire cross-sectional area of the flow channel. The pressure gradient term appeared only in the equation of motion for the gas phase, and it was weighted for concentration effects. The solid particles, on the other hand, were characterized according only to their velocity, concentration, and temperature. The two examples considered were designed to investigate the effects of the formation and strength of a shock wave in the gas phase on the transport and distribution of the solid particles.

Soo and his co-workers, in several studies [76,80-82], presented a model for solid-fluid (gas, mainly) multiphase flow in inclined pipes. The main feature of this model was its assumption of fully developed, steady state flow. In addition, inertia forces were excluded in the formulation of the equation of motion for the solid particulate phase. External forces acting on the solid particles, in addition to the drag force exerted by the fluid phase, included Saffman's lift force [5] , the electric field force, and gravity. An equation describing the distribution of the density (i.e. concentration) of the particulate phase under the influence of field force(s) was derived from the continuity equation of the particulate phase and an equation relating the diffusion of solid particles under the influence of different field forces. Appropriate boundary conditions were prescribed at the top, and at the bottom of the inclined pipe. The equation of motion and the density distribution equation for the particulate phase were solved simultaneously, for a pre-selected velocity distribution for the fluid phase (a consequence of the fully developed flow assumption), to determine the velocity and concentration distribution for the particulate phase.

A more recent modification to the basic model involved the introduction of a sticking factor which was assigned values between 0 and 1 to denote the percentage of solid particles coming to a stop when coming into contact with the top surface of the deposit bed, and the percentage of solid particles bouncing off this surface and subsequently becoming re-entrained in the suspension above [82]. However, no functional relationship was provided explicitly, and the values assigned to the sticking factor were arbitrarily chosen depending on the flow problem at hand. The authors mentioned only that these values should be chosen to reflect the force of adhesion of solid particles to a surface. They claimed to have success matching the numerical results of their model with experimental data for solid-gas flow, as well as for water-Perspex flow. Appendix A provides a step-by-step derivation of the model, along with an explanation of the solution procedure, which has only been mentioned but never provided in the cited references. Appendix B provides the derivation of the scaling groups used by Soo and his co-workers as matching parameters in their numerical simulation runs.

Despite the success claimed for this model, it has many limitations which prevent it from being considered for use in studying the transport of sand and oil in a horizontal well. The principal limitations include its steady state, fully developed flow assumption, as well as its assumption of a dilute suspension (solid particulate phase concentration of less than 8%, meaning there is negligible intraphase interaction). This restriction on particulate phase concentration, coupled with its rather "ad hoc" use of the sticking factor to vary the height of the deposit bed – not according to any explicit functional relationship(s) reflective of the prevalent hydrodynamic conditions – render the model inappropriate and incapable of modelling the transient formation and/or expansion of a solid deposit bed in a horizontal well. In addition, the authors – despite their claims of a successful match of experimental data – failed to provide values for individual parameters used in their simulation runs. Instead, they provided only values for the various dimensionless groups in which different variables and parameters were embedded. Consequently, the influence of individual variables could not be determined.

Another model which was also examined in some depth for its suitability to model the transport of sand and oil in a horizontal well is that by Roco and Shook [87-88]. The main feature of this model is its two-layer geometry, the upper layer being the suspension (having a relatively low solid phase concentration) and the lower layer being the deposit bed (having a high solid phase concentration, and a small fluid phase concentration). The interaction among the solid particles in the upper layer and lower layer was described through the "support load" concept. This two-layer formulation renders this model less restrictive than Soo's model, as described above, with regard to the solid phase concentration. In addition, even though the formulation allowed for a transient flow condition the actual numerical solution for the two studies cited [87-88] invoked steady state flow assumption. A good match between the numerical results and the experimental data was demonstrated. In one of the studies [87] Reynolds stresses were incorporated to model turbulent flow. The principal reason preventing the use of this model to study the transport of oil and sand in a horizontal well is its two-layer formulation, which in effect only examines the transport process *after* the formation of a solid deposit bed, and *after* flow conditions reaching steady state. As such, it excludes the deposition stage of the transport process altogether. Neither does it model the dynamic expansion/contraction of the deposit bed, after its formation, with time.

It can be safely stated that to model the problem of suspension flow fully – i.e. from the initial state of homogeneous distribution of solid particles in the fluid phase, to solid particle deposition and deposit bed formation due to various field forces, to subsequent expansion/contraction and possible movement of the deposit bed – requires some combination of both of the above models.

Harlow and Amsden [92] described a numerical technique (the so-called IMF or Implicit, Multi Field method) for the solution of multiphase flow problems involving fields which interpenetrate and interact with one another. Finite-differenced continuity equation, equation of motion, and energy conservation equation for each of the two phases – together with their interphase transfer terms – were implicitly coupled. Considerable generality was kept in the implicit coupling process to enable a wide range of multiphase flow problems to be modelled. The authors pointed out that a Lagrangian mesh of computational cells, in the usual sense, could not be uniquely defined and used with the IMF method because of the existence of separate and distinct fields of material velocity. The equation of motion for the two phases contained one, and only one, pressure (in the pressure gradient term) which was assumed to be locally in equilibrium between the two fields. Unlike Soo's model, the pressure gradient term was adjusted for the disperse (solid) phase concentration, and the continuous (fluid) concentration in their equation of motion. The actual solution procedure was semi-implicit, as it required iteration of values for various terms in the equation of motion for both phases before using their converged values to determine the solid phase and fluid phase densities (i.e. concentrations) from their respective continuity equations.

Stewart [93] examined the stability of the solution of two-phase models, keeping in view the fact that two of the six characteristic roots of the system of six partial differential equations (consisting of the continuity equation, equation of motion, and energy balance equation for each of the two phases) for one-dimensional, two-phase flow problems are complex, and the remaining four roots are real. The model described the interaction of the various fields under one common pressure field, with the interphase exchange term being non-differential. As in Harlow and Amsden's model [92] the pressure gradient term was adjusted for phase concentration. A mesh size criterion was derived from considering the existence of complex roots, and applying von Neumann stability analysis. The critical mesh size, for momentum exchange models based on bubble or droplet flow, was determined to be a multiple of the bubble or droplet radius. This meant that approximate numerical solutions could be well behaved if and only if the phenomena to be solved for were not smaller than the scale implied in the momentum transfer law. In such an instance, the numerical solution was shown to be well behaved – despite the fact that the mathematical model was ill-posed.

A numerically stable hydrodynamic model describing the fluidization process in a semi-circular bed is reported by Ettehadieh, Gidaspow and Lyczkowski [94]. The model consisted of the continuity equation, the equation of motion in the r- (radial) direction, and the equation of motion in the y- (vertical) direction for both the gas and solid phases. The energy equations for the two phases were not included, given the process modelled was 'cold' fluidization. A correlation relating the modulus of elasticity (defined akin to a particle-particle interaction coefficient) with the particle concentration was developed for the solid-phase stress, by fitting experimental data for glass beads and polypropylene particles. The resulting function was substituted into the equations of motion for the solid phase. The resulting system of governing partial differential equations was finite-differenced, and subsequently solved semi-implicitly by a combination of PSOR (Pointwise Successive OverRelaxation) and interval-halving methods for the radial and axial velocities of the solid phase, along with its concentration, pressure, and the axial velocity of the gas phase. The drag relation between the solid particles and the surrounding gas phase was the only other empirical input used in the simulation runs. The authors claimed a close match between their numerical results and experimental data independently obtained by other investigators, without resorting to the use of any other "fitted" parameters.

Jones [95] compared the spatial discretization schemes employed in three different commercial programs for steam bubbles and water flow in nuclear reactors, and their respective results for several different flow situations to determine the validity and applicability of different discretization methods. Emphasis was placed on the finite differencing of the equation of motion for the two phases. For one program (SIMMER) the momentum conservation equation was discretized normally. In the second program (TRAC) multiples of the mass conservation equation for the two phases were subtracted from their respective momentum conservation equation to give equations describing the evolution of the phase velocities (not momenta). These equations were then discretized and solved. The last approach (ATHENA) took the derivation a step further by, on the one hand adding the two velocity equations to produce a velocity equation for the "mixture momentum", and on the other hand subtracting the same equations to give an equation describing the evolution of the slip (relative) velocity between the two phases. In all three approaches a common pressure was used for both phases, but the pressure gradient was adjusted appropriately for phase concentration. A comparison of their results for two flow scenarios including for the first case the steady, incompressible, single-phase flow in a non-uniform, but smoothly-changing duct, and for the second case transient single-phase flow in a suddenly enlarged/constricted conduit showed that the SIMMER approach yielded results which were – despite their well-behaved nature (i.e. no spurious oscillations) – incompatible with physical reality. Based on these observations the author proposed a new criterion of "engineering consistency" – beside the usual criteria of consistency, accuracy and convergence – to validate the numerical results of a model. This engineering consistency criterion required that the solution must also be qualitatively and intuitively correct. As such, the SIMMER approach failed to satisfy this engineering consistency requirement.

4.2.3. Two-phase Flow with Two Distinct Pressures (One for Each Phase)

The most comprehensive approach to modelling two-phase flow allows for the existence of two pressures for the two phases, i.e. the motion of each phase is governed by its own distinct pressure (and pressure gradient). As such, the continuum basis for multiphase flow (each of the phases, whether disperse or continuous, is assumed to be a continuum) is taken to its fullest sense, mathematically. It must be pointed out here that the models presented in the above subsection – which allow for the two phases to share a common pressure – are but a special case of the two-phase, two-pressure modelling approach. Indeed, as far back as 1965 Murray [89,96] formulated governing equations for fluidization processes with separate stress tensors for the fluid and solid phases. The stress tensors, in this case, were defined to include both the pressure and the usual viscous stress tensors. The solid phase pressure was hypothesized to be a form of collision pressure. Despite being formulated as such, the solid phase pressure was assumed to be, in general, negligible. The main reason for this assumption was based on experimental data showing lack of particle collisions at high enough frequencies to cause appreciable attrition of the solid phase energy.

Stuhmiller [97] examined the consequences of various assumptions about the interfacial pressure distribution in two-phase flow equations. If the interfacial pressure was set constant, and equal to the bulk pressure (i.e. pressure of the continuous phase), then the resulting set of governing equations would include a single pressure. As such, the solution set would possess real characteristics (i.e. roots) if and only if the two phase velocities were equal. In many multiphase flow processes the phases move at different velocities, thus rendering this assumption unrealistic. A more general assumption allows for the interfacial pressure to be constant, but different from the bulk pressure. The author stated that in this case the system of equations possesses real characteristics if and only if the difference between the bulk pressure (larger) and the interfacial pressure (smaller) was proportional to the square of the relative velocity.

Nunziato [98] combined the second law of thermodynamics with three Lagrangian multipliers to account for the entropy inequality common in two-phase flows, and thus established restrictions on the form of the constitutive equations – particularly those at the fluid-particle interface – for the fluid-particle mixtures. The end result of this approach was the introduction of a distinct hydrostatic pressure for each phase, along with an interfacial pressure. It was explained, physically, that the hydrostatic pressures were required to maintain the incompressibility of the two phases, and the interfacial pressure was required to ensure the saturation constraint dynamically valid. As such, the difference between the interfacial pressure and the hydrostatic pressure of a phase, coupled with its concentration gradient, represented the momentum transfer due to its diffusion into the other phase. The author, based on numerical results, pointed out that the common practice of equating the hydrostatic pressures with the interfacial pressure (i.e. pressure equilibrium between the two phases) often results in aphysical phenomena. These, as described previously, are usually manifested in the form of unstable solutions. As well, the "pressure equilibrium" approach eliminates, aphysically, the diffusive momentum transfer processes – be they due to particle collisions at high particle concentrations, or Brownian diffusion in dilute systems – altogether.

Stewart and Wendroff [99] formulated several mathematical models for various two-phase flow (including non-isothermal flow) situations, which include non-interacting and interacting flow fields. Non-interacting flow fields were defined as fields which "communicate" with each other through only the saturation constraint (i.e. the two fields/phases cannot occupy the same volume at the same time) and the pressure term. Interacting fields, on the other hand, allow for mass transfer through evaporation/condensation – with associated changes in the momentum and energy, momentum and energy transfer due to friction and/or other forces such as surface tension, buoyancy, and lift force. All of the models were derived on the basis of one-dimensional stratified flow of two inviscid fields (or fluids), with distinct pressures ascribed for the two fields. Consideration of the nature of the system of governing equations (well-posed versus ill-posed), along with initial and boundary conditions – in particular, those at the interface – led to different choices for the pressures. They ranged from separate pressures, separate velocities for the two phases to "averaged" pressure, "averaged" velocity, to single-pressure and similar velocities. The authors recognized that while their basic model of equal pressure for the two phases was (in their words) "derived in a physically reasonable way, it suffered from a serious mathematical difficulty: the system of partial differential equations is ill-posed in the sense of Hadamard", i.e. the solutions probably do not depend continuously on the initial values. In-depth discussion of the finite difference method, as well as rather cursory discussions on the method of characteristics and the method of weighted residuals, for solutions to the two-phase flow problems were provided.

Prosperetti and Jones [100] used a different approach to formulate the governing equations for disperse two-phase flow. They analyzed the motion of a single bubble or particle of the disperse phase in the continuous fluid phase by dividing the pressure of the fluid phase into a rapidly varying component, and a slowly varying component which was identified to be the volume-averaged pressure. The rapidly varying pressure component – depending on the spatial motion of the particle – accounted for the pressure drag, added mass forces, as well as a pressure which arose when there was a significant difference between the pressure averaged over the entire surface of the particle and the volume-averaged pressure in the continuous fluid phase. Situations when this phenomenon arises include high relative velocity between the disperse and continuous phases, and an expanding or contracting particle (which was assumed to be deformable). In the case of high particle concentrations, collisions among the particles also give rise to growth in the rapidly varying component of the pressure field. Unlike the models surveyed in References [96-100], the rapidly varying pressure component appeared only in the equation of motion for the continuous fluid phase.

McTigue, Givler and Nunziato [101] attempted to characterize the rheological behaviour of dilute suspensions, due to non-uniform particle distributions, by extending Nunziato's model [98] to plane Poiseuille flow. In this case, the effects which arose from particle-fluid interaction (at the particle scale) and Brownian diffusion were represented by a difference in the two phase pressures. In addition, effects of gravitational force and lift forces were included. Analytical solutions of a set of simplified governing equations showed the apparent viscosity of a suspension, whose particle distribution was controlled by diffusion, was less than that of a homogeneous suspension at the same mean concentration. In the case of neutrally buoyant particles, the analytical solutions showed an off-axis region devoid of particle concentration – thus, agreeing with Segré and Silberberg's experimental results [4]. Numerical solutions of the coupled, non-linear system of equations were also obtained for the velocity and concentration distributions for the respective phases. These results, in turn, enabled the computation of an apparent viscosity for the solid-fluid suspensions over wide ranges of Reynolds number, and aspect ratios (defined on the basis of particle size and conduit size). The inhomogeneous particle distributions, being rate-dependent, caused the solid-fluid suspensions to behave as non-Newtonian fluids. This study was unique in that it employed a theoretical basis first to calculate and then to validate the results of numerous experimental studies on the rheological behaviour of suspensions.

Other examples of using this two-phase, two-pressure approach to model various multi-phase flow problems include the work reported by Givler and Mikatarian [83], and Hwang and Shen [102]. Givler and Mikatarian's work involved the numerical modelling of the formation and evolution of a particulate plug due to a constriction in the flow conduit. A preliminary description of this study was previously provided in Chapter 2. Even though no comment about this work is given here, except to point out the fact that this model used two distinct pressures – one for each phase – the study is examined critically at a later stage (in both Chapter 5 and Chapter 6) of this investigation. As alluded to in the opening paragraphs of this chapter, Givler and Mikatarian's work serves as the starting point for the present investigation.

Hwang and Shen [102] modelled Poiseuille flow of a suspension through a vertical, two-dimensional channel. Two different models were used: one having two distinct pressures, one for the solid phase, and one for the fluid phase; and the other model in which there was only one pressure (fluid phase pressure). As such, the interphase interaction was modelled differently. Approximate analytical solutions were obtained for both models. They showed that in the case of the first model settling particles moved ahead of the fluid, and buoyant particles lagged behind. In the second model (single-pressure) case settling particles were seen to lag aphysically behind the fluid, for finite pressure gradients, while buoyant particles aphysically move ahead of the fluid. The authors concluded, on the basis of these findings, that how the interaction term was modelled did have an impact on the behaviour of the solutions for the same system of governing equations.

In conclusion, it can be stated that mathematical modelling of solid-fluid flow is very diverse, and more importantly, very complex. There has yet been a single model formulated which is truly applicable to several (let alone all !) different flow situations. The biggest reason for this diversity, indeed lack of unity, in the models presented is the interphase interaction term. As has been shown above, the most comprehensive and mathematically rigorous approach – in terms of proper description of the interface, and closure of the system of equations constituting a model – is to model the disperse and continuous phases as two distinct, separate yet at the same time interacting continua. These continua, as such, must have their own properties including velocity, concentration, and pressure/stress fields. Models which either ignore the difference between the two phase pressures, or *a priori* assume it to be zero (or negligible) run the risk of making the system of governing equations ill-posed mathematically, and subsequently predicting the existence of aphysical phenomena in their solutions. The two-phase, two-pressure approach is selected, because of the reasons cited above, to model the transport – including the deposition of solid particles due to gravity – of solid particles and oil in a horizontal well for this study.

4.3. Development of Mathematical Models

In the following formulation the flow of sand and oil in a horizontal well is treated as the isothermal flow of a monodisperse, dilute suspension. As such, the solid phase is assumed to be composed of spherical sand particles which are uniform in size, and uniformly and homogeneously dispersed in the continuous fluid phase. In addition, the overall sand-oil suspension is assumed to behave as a continuum. Consequently, the constituent solid phase and fluid phase are themselves treated as continua. The assumption of a dilute suspension stipulates that the volume fraction occupied by the solid sand particles, ϕ , is equal to or less than some critical particle concentration. Soo [76-77,80-82] defined this critical concentration to be 8%, whereas other investigators [83,94,98,101] defined a critical concentration of 20% volume fraction of the overall suspension. Under this condition of dilute suspension solid particles of usual size ranges for sand, silt, and clay particles are at least 2 diameters apart. As such, the mean-free-path of particle-particle interaction (collision) is much larger than the particle-fluid interaction length. Consequently, particle-particle intraphase interaction is considered small, or negligible when compared to the interaction between the solid particles and the surrounding fluid phase. It is further assumed that the solid particles do not move due to their own rotation. Rather, their movement arises due to the movement of the surrounding fluid phase, influence of the gravitational field force, and Saffman's lift force which act only along the radial direction. The fluid phase, oil in this study, could also be oil-in-water or water-in-oil emulsion so long as it behaves as a Newtonian fluid (i.e. low concentration of the dispersed phase of the emulsion).

4.3.1. Formulation of a Two-dimensional Model

Referring to Figure 4.1, the control volume element representing an arbitrary space inside the horizontal well is seen to be positioned along the horizontal plane – perpendicular to the true direction of gravity. The positive z-coordinate extends from left to right, and the positive r-coordinate extends upward from the bottom of the horizontal well. The flow inside the horizontal well also goes from left ("toe" of the horizontal well) to right ("heel" of the horizontal well). The flow along the azimuth direction is assumed to be negligible, thus reducing the flow geometry from

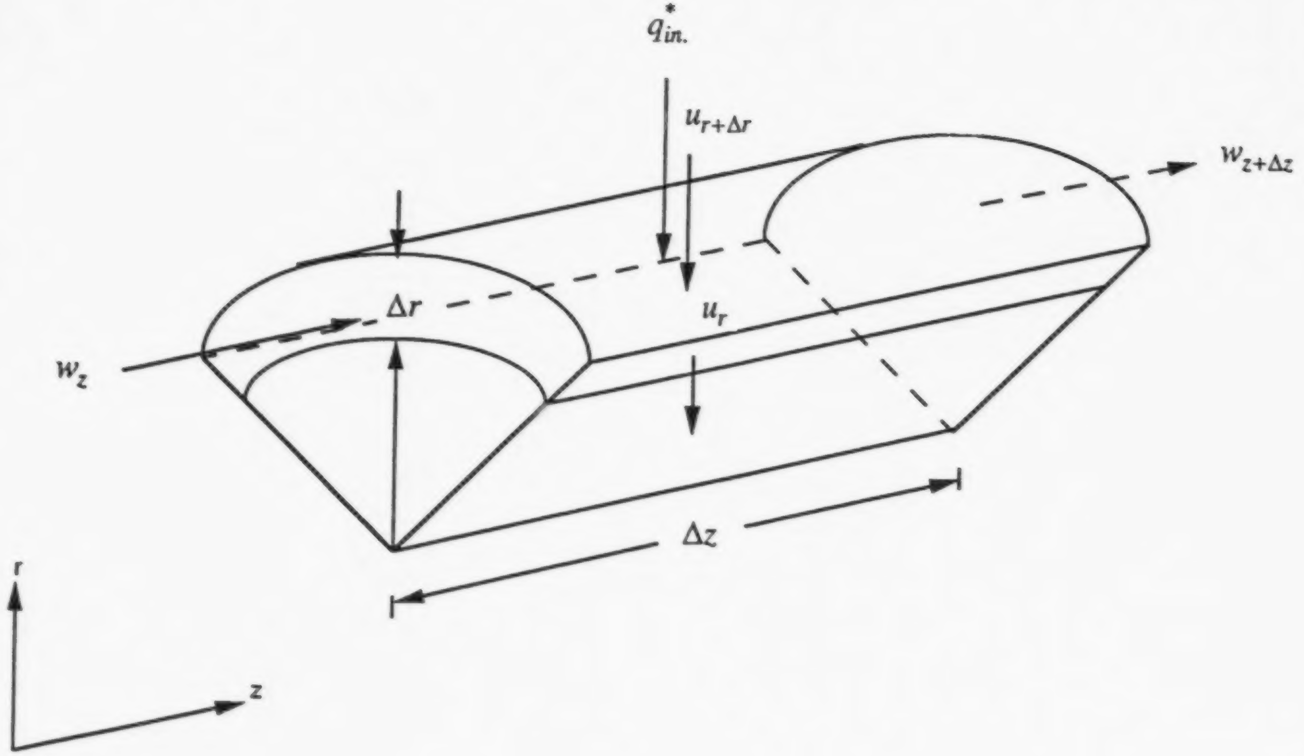
$q^*_{in.}$
$u_{r+\Delta r}$
$w_{z+\Delta z}$
Δr
u_r
w_z
Δz
r
z

Figure 4.1: Control volume element for flow inside a horizontal well.

three-dimensional to two-dimensional. The horizontal well is uniform in size (i.e. its diameter is constant).

Beside the fluxes coming into, and out of, the control volume element along the r- and z-axes, there is also a flux coming into the control volume element through its "top" surface (i.e. along the same direction as gravity), as shown in Figure 4.1. This flux, $\overset{*}{q}_{in.}$, which is measured in terms of a standard volumetric rate per unit volume of the control volume element, represents the influx of fluid and solid particles volumes from the reservoir into the horizontal well. In the case of a horizontal well completed with a slotted liner the control volume element, as drawn, is taken to represent the (very small) volume straddling two adjacent slots. For a horizontal well completed with a perforated casing the control volume element represents the volume between perforations (which could be potentially very large, depending on the perforation density). In the latter case the flow in the annulus between the casing and the horizontal well is not included in the formulation. In addition, the model does not consider the pressure drop across the perforation. Rather, the influx is simply treated as a source/sink term in the control volume element. As such, this source/sink influx term is a constant, invariant within each time step of the numerical solution procedure.

To simplify the model further, the solid and fluid compositions of the influx term, $(\phi)^{*}_{in.}$ and $(\varepsilon)^{*}_{in.}$, are assumed to be known. In reality neither the volume or rate of the influx nor its (solid phase and fluid phase) composition is known with any degree of precision. The influx from the reservoir into a horizontal well depends on many factors, including the drawdown, well drainage area, skin factor due to partial completion (i.e. the horizontal well does not completely penetrate the whole extent of the drainage area), skin factor due to convergence of flow streams toward the horizontal well. This influx volumetric rate could be estimated from various horizontal well productivity formulae [103-110]. Several of these studies obtained horizontal well productivity index by treating the horizontal well as an infinite-conductivity line sink. The assumption underlying this approach is that the pressure drop across the horizontal well is negligible [103-107]. Other studies incorporated the flow inside the horizontal well, including the influence of frictional resistance to flow, with the flow between the reservoir and the horizontal well to determine its productivity [108-110]. Dikken [108] simply coupled the reservoir flow with the conventional pipe flow model, and used correlations for the frictional pressure drop due to the flow regime and pipe roughness to estimate the total pressure loss across the horizontal well. The major conclusion of this study was that total well productivity will start to level off when the horizontal well exceeds a critical length. Asheim, Kolnes, and Oudeman [109] considered the momentum required to accelerate the influx mass to the same speed as that of the (main) axial flow. This approach, by including the effect of the influx in the formulation of the governing differential equations, is physically much more rigorous than the approach of simply adapting conventional pipe flow model(s) to describe flow inside a horizontal well. Plaxton – based on experimental results of immiscible, stratified oil-water flow in a horizontal well, with influx coming in through a perforation – showed the influx capable of significantly increasing the pressure drop across the horizontal well over that predicted by conventional pipe flow models [111].

Currently, the causes of sand production into a wellbore are not well understood. However, they are thought to include low wellbore pressure compared to very high reservoir pressure in the vicinity of wellbore (leading to the collapse of the sand arch around the wellbore), extremely high fluid rates, high water cuts, and cyclic loading of the region around the wellbore [112-113]. As a result, when there is sand production the actual composition of the influx coming into a wellbore, in terms of its solid phase and fluid phase composition, cannot be realistically determined easily. To calculate the amount of sand produced into a wellbore requires a comprehensive study, including most definitely numerical simulation, of the stress distributions around a wellbore. This is outside the scope of this study which is focused on the transport of sand particles inside a horizontal well, after their production into the wellbore.

These assumptions lead to the following governing partial differential equations, which describe the conservation of mass and momentum for both the fluid phase (oil) and the solid phase (sand particles). Appendix C contains the derivation of these governing equations from first principles. It is important to point out that in the derivation of the equations of motion for both the fluid phase and the solid phase the influx mass is assumed to be instantaneously accelerated, at the point of passage through the slot or perforation into the horizontal well, to the radial and axial velocities of the flow inside the well. In reality this is not often the case. Rose and Duckworth on the basis of their experimental study of the pneumatic transport of mustard seed obtained a correlation for the pressure drop required to accelerate the mustard seed to the mean stream velocity [53]. Functions akin to these authors' correlation could be obtained analytically and/or experimentally to describe the pressure drop or distance required to accelerate the influx mass to the mean stream velocities, along both the radial and the axial directions, and then incorporated into the set of governing equations in the future. This is one of the many follow-up studies which could and should be conducted to bring the mathematical models more into line with the actual physics of this multiphase transport process in a horizontal well. The symbols appearing in the equations below are defined in the Nomenclature.

- Continuity equation

* Mass conservation for the fluid phase

$$\frac{\partial \rho_f}{\partial t} - \frac{1}{r}\frac{\partial}{\partial r}\left(r\rho_f u_f\right) + \frac{\partial}{\partial z}\left(\rho_f w_f\right) - \left(\rho_f q\right)^{\bullet}_{in.} = 0 \tag{4.1}$$

* Mass conservation for the solid phase

$$\frac{\partial \rho_s}{\partial t} - \frac{1}{r}\frac{\partial}{\partial r}\left(r\rho_s u_s\right) + \frac{\partial}{\partial z}\left(\rho_s w_s\right) - \left(\rho_s q\right)^{\bullet}_{in.} = 0 \tag{4.2}$$

- Equation of motion

* Conservation of momentum for the fluid phase

Along the radial (r-) direction

$$\begin{aligned}\frac{\partial}{\partial t}\left(\rho_f u_f\right) - \frac{\partial}{\partial r}\left(\rho_f u_f u_f\right) + \frac{\partial}{\partial z}\left(\rho_f w_f u_f\right) = -\varepsilon\frac{\partial p_f}{\partial r} + \mu_f\left[\frac{\partial}{\partial r}\left(\frac{1}{r}\frac{\partial}{\partial r}\left(-ru_f\right)\right) + \frac{\partial^2 u_f}{\partial z^2}\right] - \left(\rho_f q\right)^{\bullet}_{in.} u_f \\ -\rho_f g - \frac{3}{8}C_L\rho_s\frac{\underline{\overline{\rho_f}}}{\rho_s}\frac{\left(u_s - u_f + \Delta u\right)^2}{a} + \beta_r\left(u_f - u_s\right)\end{aligned} \tag{4.3}$$

Along the axial (z-) direction

$$\begin{aligned}\frac{\partial}{\partial t}\left(\rho_f w_f\right) - \frac{\partial}{\partial r}\left(\rho_f u_f w_f\right) + \frac{\partial}{\partial z}\left(\rho_f w_f w_f\right) = -\varepsilon\frac{\partial p_f}{\partial z} + \mu_f\left[\frac{1}{r}\frac{\partial}{\partial r}\left(r\frac{\partial w_f}{\partial r}\right) + \frac{\partial^2 w_f}{\partial z^2}\right] \\ -\left(\rho_f q\right)^{\bullet}_{in.} w_f + \beta_z\left(w_f - w_s\right)\end{aligned} \tag{4.4}$$

• Conservation of momentum for the solid phase

Along the radial (r-) direction

$$\frac{\partial}{\partial t}(\rho_s u_s) - \frac{\partial}{\partial r}(\rho_s u_s u_s) + \frac{\partial}{\partial z}(\rho_s w_s u_s) = -\phi \frac{\partial p_s}{\partial r} + \left[\frac{1}{r}\frac{\partial}{\partial r}\left(-r\mu_s \frac{\partial u_s}{\partial r}\right) + \frac{\partial}{\partial z}\left(\mu_s \frac{\partial u_s}{\partial z}\right)\right] - p_{k,r}\frac{\partial \phi}{\partial r} - \rho_s g$$
$$-(\rho_s q)^{*}_{in.} u_s + \frac{3}{8} C_L \rho_s \frac{\overline{\rho_f}}{\overline{\rho_s}} \frac{(u_s - u_f + \Delta u)^2}{a} - \beta_r (u_f - u_s)$$

(4.5)

Along the axial (z-) direction

$$\frac{\partial}{\partial t}(\rho_s w_s) - \frac{\partial}{\partial r}(\rho_s u_s w_s) + \frac{\partial}{\partial z}(\rho_s w_s w_s) = -\phi \frac{\partial p_s}{\partial z} + \left[\frac{1}{r}\frac{\partial}{\partial r}\left(-r\mu_s \frac{\partial w_s}{\partial r}\right) + \frac{\partial}{\partial z}\left(\mu_s \frac{\partial w_s}{\partial z}\right)\right]$$
$$-p_{k,z}\frac{\partial \phi}{\partial z} - (\rho_s q)^{*}_{in.} w_s - \beta_z (w_f - w_s)$$

(4.6)

If the fluid phase density and solid phase density in the above equations are defined according to the respective concentrations – measured in terms of the volume fractions – and their material densities (i.e. densities of the materials constituting the fluid phase and the solid phase, in this case oil and quartz sand), i.e.

$$\rho_f = \varepsilon * \overline{\rho_f} \qquad (4.7)$$

$$\rho_s = \phi * \overline{\rho_s} \qquad (4.8)$$

In Equations 4.7-4.8 the solid phase density is determined on the basis of the volume occupied by the solid particles compared to the total volume of the suspension. The fluid phase density is based on the density of the fluid material and the volume occupied by the fluid phase. As such, it excludes the mass of the fluid volume displaced by the solid particles. Given that the material densities for the fluid phase and solid phase are constant, and only the phase concentrations vary with time and space, the conservation equations above can be rewritten as follows,

- Continuity equation

* Mass conservation for the fluid phase

$$\frac{\partial \varepsilon}{\partial t} - \frac{1}{r}\frac{\partial}{\partial r}\left(r\varepsilon u_f\right) + \frac{\partial}{\partial z}\left(\varepsilon w_f\right) - (\varepsilon q)^{*}_{in.} = 0 \tag{4.9}$$

* Mass conservation for the solid phase

$$\frac{\partial \phi}{\partial t} - \frac{1}{r}\frac{\partial}{\partial r}\left(r\phi u_s\right) + \frac{\partial}{\partial z}\left(\phi w_s\right) - (\phi q)^{*}_{in.} = 0 \tag{4.10}$$

- Equation of motion

* Conservation of momentum for the fluid phase

Along the radial (r-) direction

$$\begin{aligned}\frac{\partial}{\partial t}\left(\varepsilon u_f\right) - \frac{\partial}{\partial r}\left(\varepsilon u_f u_f\right) + \frac{\partial}{\partial z}\left(\varepsilon w_f u_f\right) = &-\frac{\varepsilon}{\rho_f}\frac{\partial p_f}{\partial r} + \frac{\mu_f}{\rho_f}\left[\frac{\partial}{\partial r}\left(\frac{1}{r}\frac{\partial}{\partial r}\left(-r u_f\right)\right) + \frac{\partial^2 u_f}{\partial z^2}\right] - (\varepsilon q)^{*}_{in.} u_f \\ &-\varepsilon g - \frac{3}{8} C_L \phi \frac{\left(u_s - u_f + \Delta u\right)^2}{a} + \frac{\beta_r}{\rho_f}\left(u_f - u_s\right)\end{aligned} \tag{4.11}$$

Along the axial (z-) direction

$$\begin{aligned}\frac{\partial}{\partial t}\left(\varepsilon w_f\right) - \frac{\partial}{\partial r}\left(\varepsilon u_f w_f\right) + \frac{\partial}{\partial z}\left(\varepsilon w_f u_f\right) = &-\frac{\varepsilon}{\rho_f}\frac{\partial p_f}{\partial z} + \frac{\mu_f}{\rho_f}\left[\frac{1}{r}\frac{\partial}{\partial r}\left(r\frac{\partial w_f}{\partial r}\right) + \frac{\partial^2 w_f}{\partial z^2}\right] \\ &-(\varepsilon q)^{*}_{in.} w_f + \frac{\beta_z}{\rho_f}\left(w_f - w_s\right)\end{aligned} \tag{4.12}$$

- Conservation of momentum for the solid phase

Along the radial (r-) direction

$$\frac{\partial}{\partial t}(\phi u_s) - \frac{\partial}{\partial r}(\phi u_s u_s) + \frac{\partial}{\partial z}(\phi w_s u_s) = -\frac{\phi}{\overline{\overline{\rho_s}}}\frac{\partial p_s}{\partial r} + \left[\frac{1}{r}\frac{\partial}{\partial r}\left(-r\mu_s\frac{\partial u_s}{\partial r}\right) + \frac{\partial}{\partial z}\left(\mu_s\frac{\partial u_s}{\partial z}\right)\right] - \frac{p_{k,r}}{\overline{\overline{\rho_s}}}\frac{\partial \phi}{\partial r}$$

$$-\phi g - (\phi q)^{\bullet}_{in.} u_s + \frac{3}{8} C_L \phi \frac{\left(u_s - u_f + \Delta u\right)^2}{a} - \frac{\beta_r}{\overline{\overline{\rho_s}}}\left(u_f - u_s\right)$$

(4.13)

Along the axial (z-) direction

$$\frac{\partial}{\partial t}(\phi w_s) - \frac{\partial}{\partial r}(\phi u_s w_s) + \frac{\partial}{\partial z}(\phi w_s w_s) = -\frac{\phi}{\overline{\overline{\rho_s}}}\frac{\partial p_s}{\partial z} + \frac{1}{\overline{\overline{\rho_s}}}\left[\frac{1}{r}\frac{\partial}{\partial r}\left(-r\mu_s\frac{\partial w_s}{\partial r}\right) + \frac{\partial}{\partial z}\left(\mu_s\frac{\partial w_s}{\partial z}\right)\right]$$

$$-\frac{p_{k,z}}{\overline{\overline{\rho_s}}}\frac{\partial \phi}{\partial z} - (\phi q)^{*}_{in.} w_s - \frac{\beta_z}{\overline{\overline{\rho_s}}}\left(w_f - w_s\right)$$

(4.14)

In the above equations the lift coefficient, C_L , is defined as follows

$$C_L = C_1\left(\frac{\nu_f}{2au_f}\right)^m \left|\frac{2a}{u_f}\frac{du_f}{dr}\right|^n \left(\frac{a}{R}\right)^p \quad , \qquad (4.15)$$

with the values for the constant, C_1 , and exponents m, n, and p as determined by various investigators provided in Table 4.1,

Table 4.1: Values of constant and exponents for lift coefficient (after Ref. 81)

Source	C_1	m	n	p	Note
Saffman (theoretical)	19.92/π	0.5	0.5	0	very small particles, small slip
Eichorn (empirical)	70 000	2	2	2	large particles, Poiseuille flow
Graf & Acaroglu	50	1	0.5	0	Turbulent boundary layer

The solid phase viscosity, μ_s , is given by [83]

$$\mu_s = \frac{\mu_{mix.}}{\phi} - \frac{\varepsilon}{\phi}\mu_f \tag{4.16}$$

This equation assumes that the viscosity of the fluid-solid mixture is proportionally made up of the fluid phase viscosity and solid phase viscosity.

The viscosity of a fluid-solid particles suspension is determined empirically to be [83],

$$\mu_{mix.} = 4\phi * \mu_f\left[\frac{1.0}{h(\phi) - 1.0} + 0.80 + 0.767(h(\phi) - 1.0)\right] \tag{4.17}$$

The function $h(\phi)$ accounts for the increased interaction (i.e. collisions) among solid particles as the solid particle concentration increases, giving rise to higher solid phase viscosity. This function also appears in the definition for the kinematic pressure; in this case, the increase in the frequency of particle-particle collision contributes to a rise in the kinematic pressure – according to its definition below [83],

$$p_k = \frac{1}{2}\overline{\rho_f} * h(\phi) * \left|v_f - v_s\right| * \left|v_f - v_s\right| \tag{4.18}$$

As defined above, the function $h(\phi)$ is dependent on solid particle concentration. When the solid particle concentration is less than or equal to 20% volume fraction [83],

$$h(\phi) = 1.0 + 4(\phi) + 10(\phi)^2 + 18.36(\phi)^3 + 29.94(\phi)^4 \tag{4.19}$$

On the other hand, when the solid particle concentration is more than 20% volume fraction Kirkwood, Maun and Adler [114] obtained the following results from the radial distribution function describing the frequency of particle collisions in dense gases,

Table 4.2: The function $h(\phi)$ versus ϕ (after Ref. 114)

ϕ	$h(\phi)$
0.00	1.00
0.0884	1.44
0.1563	1.91
0.2128	2.39
0.2618	2.89
0.3060	3.40
0.3443	3.91
0.3818	4.43
0.4160	4.93
0.4513	5.44
0.4835	5.95
0.5145	6.46
0.5400	6.99
0.5695	7.50
0.5968	7.93
0.7405	∞

The interphase interaction coefficient β in the above equations is given as [83],

$$\beta = 150\frac{(\phi)^2\mu_f}{\varepsilon(2aS)^2} + 1.75\frac{(\phi)\overline{\rho_f}}{(2aS)}\left|v_f - v_s\right| , \quad \text{for } \phi > 0.20 \text{ (dense suspensions)} \qquad (4.20a)$$

and

$$\beta = 0.75C_D\frac{\phi(\varepsilon)}{(2aS)}\overline{\rho_f}\left|v_f - v_s\right| * \frac{1}{(\phi)^{2.65}} , \quad \text{for } \phi \le 0.20 \text{ (dilute suspensions)} \qquad (4.20b)$$

The drag coefficient, and the particle Reynolds number are defined as follows [83],

$$\mathrm{Re}_p = \varepsilon\frac{\overline{\rho_f} * \left|v_f - v_s\right| * 2a}{\mu_f} \qquad (4.21)$$

$$C_D = \frac{24}{\mathrm{Re}_p}\left(1 + 0.15\,\mathrm{Re}_p^{0.687}\right) , \quad \text{for } \mathrm{Re}_p < 1\,000 \text{ (laminar flow)} \qquad (4.22a)$$

$$C_D = 0.44 , \quad \text{for } \mathrm{Re}_p \ge 1\,000 \text{ (turbulent flow)} \qquad (4.22b)$$

Equations (4.18, 4.20–4.22) apply for flow along both the radial (r-) and axial (z-) directions, by introducing subscripts r and z to correspond appropriately with the velocity components u and w.

As can be seen, the system of partial differential equations, along with their auxiliary equations, describe the conservation of mass and momentum for the fluid and solid phases, as well the effects of interphase and intraphase interaction on momentum transfer between the two phases. The large number of equations, along with the coupled nature of the non-linear equations of motion for the fluid and solid phase, precludes any analytical solution from being readily developed. To determine the solution to the problem of sand and oil transport inside a horizontal well, in terms of calculating the distribution in the pressure, velocity, and concentration for both phases numerical methods have to be employed. The finite difference methods have been proven to be especially readily adaptable to the computation of fluid flow problems. One particularly successful finite difference technique which has been applied widely and successfully for a variety of transient fluid flow problems, both incompressible and compressible, has been the Marker-And-Cell (MAC) method [115-125]. This method, unlike the vorticity-and-stream-function method, obtains the solution to the flow problem on the basis of primitive variables like pressure and velocity. As such, it requires the formulation of another equation – on top of the equations governing the conservation of mass and momentum – to describe the pressure distribution in the system. For this study into the transport of oil and sand inside a horizontal well the pressure equation for the solid phase, in finite difference form, is given below. Appendix D contains a complete derivation of the same equation from the conservation equations for the solid phase.

$$\begin{aligned}
&\frac{1}{r_{i,k}}\left[\frac{(rA)_{i-1/2,k}\,p^{n+1}_{si-1,k}-\left[(rA)_{i-1/2,k}+(rA)_{i+1/2,k}\right]p^{n+1}_{si,k}+(rA)_{i+1/2,k}\,p^{n+1}_{si+1,k}}{(\Delta r)^2}\right]\\
&+\left[\frac{B_{i,k-1/2}\,p^{n+1}_{si,k-1}-\left[B_{i,k-1/2}+B_{i,k+1/2}\right]p^{n+1}_{si,k}+B_{i,k+1/2}\,p^{n+1}_{si,k+1}}{(\Delta z)^2}\right]\\
&=\frac{1}{\Delta t}\Bigg[\left(\frac{r_{i-1/2,k}}{r_{i,k}}\frac{F_{si-1/2,k}}{\Delta r}\right)-\left(\frac{r_{i+1/2,k}}{r_{i,k}}\frac{F_{si+1/2,k}}{\Delta r}\right)+\frac{1}{\Delta z}\left(G_{si,k-1/2}-G_{si,k+1/2}\right)\\
&-\left\{(\phi q)^{*}_{in.}\right\}^{n+1}_{i,k}\Bigg]+\frac{1}{(\Delta t)^2}\left(\phi^{n+1}_{i,k}-\phi^{n}_{i,k}\right)
\end{aligned} \tag{4.24}$$

where,

$$
\begin{aligned}
F_{si+1/2,k} = \Delta t \Bigg\{ & \left[\frac{(\phi u_s u_s)_{i+1,k} - (\phi u_s u_s)_{i,k}}{\Delta r}\right]^{n+1} + \left[\frac{(\phi w_s u_s)_{i+1/2,k+1/2} - (\phi w_s u_s)_{i+1/2,k-1/2}}{\Delta z}\right]^{n+1} \\
& + \Bigg[\bigg(\Big(p_{kr}^{n} + \frac{\partial p_{kr}}{\partial \phi}\Big)^{n} (\phi^{n+1} - \phi^{n})\bigg)_{i+1/2,k} * \bigg(\frac{\phi_{i+1,k}^{n+1} - \phi_{i,k}^{n+1}}{\Delta r}\bigg)\Bigg] - \big[g(\phi)_{i+1/2,k}^{n+1}\big] \\
& + \frac{1}{\bar{\bar{\rho}}_s} \frac{1}{r_{i+1/2,k}} \frac{1}{\Delta r} \Bigg[\Bigg\{ r_{i+1,k} \bigg(\mu_s^{n} + \frac{d\mu_s}{d\phi}\bigg|^{n} (\phi^{n+1} - \phi^{n})\bigg)_{i+1,k} * \bigg(\frac{u_{si+3/2,k}^{n+1} - u_{si+1/2,k}^{n+1}}{\Delta r}\bigg)\Bigg\} \\
& - \Bigg\{ r_{i,k} \bigg(\mu_s^{n} + \frac{d\mu_s}{d\phi}\bigg|^{n} (\phi^{n+1} - \phi^{n})\bigg)_{i,k} * \bigg(\frac{u_{si+1/2,k}^{n+1} - u_{si-1/2,k}^{n+1}}{\Delta r}\bigg)\Bigg\}\Bigg] + \big[(\phi q)_{in.}^{*} u_s\big]_{i+1/2,k}^{n+1} \\
& + \frac{1}{\bar{\bar{\rho}}_s} \frac{1}{\Delta z} \Bigg[\Bigg\{ \bigg(\mu_s^{n} + \frac{d\mu_s}{d\phi}\bigg|^{n} (\phi^{n+1} - \phi^{n})\bigg)_{i+1/2,k+1/2} * \bigg(\frac{u_{si+1/2,k+1}^{n+1} - u_{si+1/2,k}^{n+1}}{\Delta z}\bigg)\Bigg\} \\
& - \Bigg\{ \bigg(\mu_s^{n} + \frac{d\mu_s}{d\phi}\bigg|^{n} (\phi^{n+1} - \phi^{n})\bigg)_{i+1/2,k-1/2} * \bigg(\frac{u_{si+1/2,k}^{n+1} - u_{si+1/2,k-1}^{n+1}}{\Delta z}\bigg)\Bigg\}\Bigg] \\
& - \frac{1}{\bar{\bar{\rho}}_s} \Bigg[\bigg(\beta_r^{n} + \frac{\partial \beta_r}{\partial \phi}\bigg|^{n} (\phi^{n+1} - \phi^{n})\bigg)_{i+1/2,k} \big(u_{fi+1/2,k}^{n+1} - u_{si+1/2,k}^{n+1}\big)\Bigg]\Bigg\} + (\phi u_s)_{i+1/2,k}^{n}
\end{aligned}
$$

(4.25a)

$$
\begin{aligned}
F_{si-1/2,k} = \Delta t \Bigg\{ & \left[\frac{(\phi u_s u_s)_{i,k} - (\phi u_s u_s)_{i-1,k}}{\Delta r}\right]^{n+1} + \left[\frac{(\phi w_s u_s)_{i-1/2,k+1/2} - (\phi w_s u_s)_{i-1/2,k-1/2}}{\Delta z}\right]^{n+1} \\
& + \Bigg[\bigg(\Big(p_{kr}^{n} + \frac{\partial p_{kr}}{\partial \phi}\Big)^{n} (\phi^{n+1} - \phi^{n})\bigg)_{i-1/2,k} * \bigg(\frac{\phi_{i,k}^{n+1} - \phi_{i-1,k}^{n+1}}{\Delta r}\bigg)\Bigg] - \big[g(\phi)_{i-1/2,k}^{n+1}\big] \\
& + \frac{1}{\bar{\bar{\rho}}_s} \frac{1}{r_{i-1/2,k}} \frac{1}{\Delta r} \Bigg[\Bigg\{ r_{i,k} \bigg(\mu_s^{n} + \frac{d\mu_s}{d\phi}\bigg|^{n} (\phi^{n+1} - \phi^{n})\bigg)_{i,k} * \bigg(\frac{u_{si+1/2,k}^{n+1} - u_{si-1/2,k}^{n+1}}{\Delta r}\bigg)\Bigg\} \\
& - \Bigg\{ r_{i-1,k} \bigg(\mu_s^{n} + \frac{d\mu_s}{d\phi}\bigg|^{n} (\phi^{n+1} - \phi^{n})\bigg)_{i-1,k} * \bigg(\frac{u_{si-1/2,k}^{n+1} - u_{si-3/2,k}^{n+1}}{\Delta r}\bigg)\Bigg\}\Bigg] + \big[(\phi q)_{in.}^{*} u_s\big]_{i-1/2,k}^{n+1} \\
& + \frac{1}{\bar{\bar{\rho}}_s} \frac{1}{\Delta z} \Bigg[\Bigg\{ \bigg(\mu_s^{n} + \frac{d\mu_s}{d\phi}\bigg|^{n} (\phi^{n+1} - \phi^{n})\bigg)_{i-1/2,k+1/2} * \bigg(\frac{u_{si-1/2,k+1}^{n+1} - u_{si-1/2,k}^{n+1}}{\Delta z}\bigg)\Bigg\} \\
& - \Bigg\{ \bigg(\mu_s^{n} + \frac{d\mu_s}{d\phi}\bigg|^{n} (\phi^{n+1} - \phi^{n})\bigg)_{i-1/2,k-1/2} * \bigg(\frac{u_{si-1/2,k}^{n+1} - u_{si-1/2,k-1}^{n+1}}{\Delta z}\bigg)\Bigg\}\Bigg] \\
& - \frac{1}{\bar{\bar{\rho}}_s} \Bigg[\bigg(\beta_r^{n} + \frac{\partial \beta_r}{\partial \phi}\bigg|^{n} (\phi^{n+1} - \phi^{n})\bigg)_{i-1/2,k} \big(u_{fi-1/2,k}^{n+1} - u_{si-1/2,k}^{n+1}\big)\Bigg]\Bigg\} + (\phi u_s)_{i-1/2,k}^{n}
\end{aligned}
$$

(4.25b)

$$
\begin{aligned}
G_{si,k+1/2} = \Delta t \Bigg\{ & \left[\frac{\langle \phi u_s w_s \rangle_{i+1/2,k+1/2} - \langle \phi u_s w_s \rangle_{i-1/2,k+1/2}}{\Delta r}\right]^{n+1} + \left[\frac{\langle \phi w_s w_s \rangle_{i,k+1} - \langle \phi w_s w_s \rangle_{i,k}}{\Delta z}\right]^{n+1} \\
& + \Bigg[\bigg(\bigg(p_{kz}^{n} + \frac{\partial p_{kz}}{\partial \phi}\bigg)\bigg|^{n} (\phi^{n+1} - \phi^{n})\bigg)_{i,k+1/2} * \left(\frac{\phi_{i,k+1}^{n+1} - \phi_{i,k}^{n+1}}{\Delta z}\right)\Bigg] + \frac{1}{\overline{\overline{\rho}}_s}\frac{1}{\Delta r}\frac{1}{r_{i,k+1/2}} * \\
& \Bigg[\Bigg\{ r_{i+1/2,k+1/2}\bigg(\mu_s^{n} + \frac{d\mu_s}{d\phi}\bigg|^{n} (\phi^{n+1} - \phi^{n})\bigg)_{i+1/2,k+1/2} * \left(\frac{w_{si+1,k+1/2}^{n+1} - w_{si,k+1/2}^{n+1}}{\Delta r}\right)\Bigg\} \\
& - \Bigg\{ r_{i-1/2,k+1/2}\bigg(\mu_s^{n} + \frac{d\mu_s}{d\phi}\bigg|^{n} (\phi^{n+1} - \phi^{n})\bigg)_{i-1/2,k+1/2} * \left(\frac{w_{si,k+1/2}^{n+1} - w_{si-1,k+1/2}^{n+1}}{\Delta r}\right)\Bigg\}\Bigg] \\
& + \frac{1}{\overline{\overline{\rho}}_s}\frac{1}{\Delta z}\Bigg[\Bigg\{\bigg(\mu_s^{n} + \frac{d\mu_s}{d\phi}\bigg|^{n} (\phi^{n+1} - \phi^{n})\bigg)_{i,k+1} * \left(\frac{w_{si,k+3/2}^{n+1} - w_{si,k+1/2}^{n+1}}{\Delta z}\right)\Bigg\} \\
& - \Bigg\{\bigg(\mu_s^{n} + \frac{d\mu_s}{d\phi}\bigg|^{n} (\phi^{n+1} - \phi^{n})\bigg)_{i,k} * \left(\frac{w_{si,k+1/2}^{n+1} - w_{si,k-1/2}^{n+1}}{\Delta z}\right)\Bigg\}\Bigg] + \left[\langle \phi q \rangle_{in.}^{*} w_s\right]_{i,k+1/2}^{n+1} \\
& - \frac{1}{\overline{\overline{\rho}}_s}\Bigg[\bigg(\beta_z^{n} + \frac{\partial \beta_z}{\partial \phi}\bigg|^{n} (\phi^{n+1} - \phi^{n})\bigg)_{i,k+1/2} \left(w_{fi,k+1/2}^{n+1} - w_{si,k+1/2}^{n+1}\right)\Bigg]\Bigg\} + \langle \phi w_s \rangle_{i,k+1/2}^{n}
\end{aligned}
\tag{4.26a}
$$

$$
\begin{aligned}
G_{si,k-1/2} = \Delta t \Bigg\{ & \left[\frac{\langle \phi u_s w_s \rangle_{i+1/2,k-1/2} - \langle \phi u_s w_s \rangle_{i-1/2,k-1/2}}{\Delta r}\right]^{n+1} + \left[\frac{\langle \phi w_s w_s \rangle_{i,k} - \langle \phi w_s w_s \rangle_{i,k-1}}{\Delta z}\right]^{n+1} \\
& + \Bigg[\bigg(\bigg(p_{kz}^{n} + \frac{\partial p_{kz}}{\partial \phi}\bigg)\bigg|^{n} (\phi^{n+1} - \phi^{n})\bigg)_{i,k-1/2} * \left(\frac{\phi_{i,k}^{n+1} - \phi_{i,k-1}^{n+1}}{\Delta z}\right)\Bigg] + \frac{1}{\overline{\overline{\rho}}_s}\frac{1}{\Delta r}\frac{1}{r_{i,k-1/2}} * \\
& \Bigg[\Bigg\{ r_{i+1/2,k-1/2}\bigg(\mu_s^{n} + \frac{d\mu_s}{d\phi}\bigg|^{n} (\phi^{n+1} - \phi^{n})\bigg)_{i+1/2,k-1/2} * \left(\frac{w_{si+1,k-1/2}^{n+1} - w_{si,k-1/2}^{n+1}}{\Delta r}\right)\Bigg\} \\
& - \Bigg\{ r_{i-1/2,k-1/2}\bigg(\mu_s^{n} + \frac{d\mu_s}{d\phi}\bigg|^{n} (\phi^{n+1} - \phi^{n})\bigg)_{i-1/2,k-1/2} * \left(\frac{w_{si,k-1/2}^{n+1} - w_{si-1,k-1/2}^{n+1}}{\Delta r}\right)\Bigg\}\Bigg] \\
& + \frac{1}{\overline{\overline{\rho}}_s}\frac{1}{\Delta z}\Bigg[\Bigg\{\bigg(\mu_s^{n} + \frac{d\mu_s}{d\phi}\bigg|^{n} (\phi^{n+1} - \phi^{n})\bigg)_{i,k} * \left(\frac{w_{si,k+1/2}^{n+1} - w_{si,k-1/2}^{n+1}}{\Delta z}\right)\Bigg\} \\
& - \Bigg\{\bigg(\mu_s^{n} + \frac{d\mu_s}{d\phi}\bigg|^{n} (\phi^{n+1} - \phi^{n})\bigg)_{i,k-1} * \left(\frac{w_{si,k-1/2}^{n+1} - w_{si,k-3/2}^{n+1}}{\Delta z}\right)\Bigg\}\Bigg] + \left[\langle \phi q \rangle_{in.}^{*} w_s\right]_{i,k-1/2}^{n+1} \\
& - \frac{1}{\overline{\overline{\rho}}_s}\Bigg[\bigg(\beta_z^{n} + \frac{\partial \beta_z}{\partial \phi}\bigg|^{n} (\phi^{n+1} - \phi^{n})\bigg)_{i,k-1/2} \left(w_{fi,k-1/2}^{n+1} - w_{si,k-1/2}^{n+1}\right)\Bigg]\Bigg\} + \langle \phi w_s \rangle_{i,k-1/2}^{n}
\end{aligned}
\tag{4.26b}
$$

$$A_{i+1/2,k} = \left(\phi^n + \left.\frac{\partial\phi}{\partial p_s}\right|^n (p_s^{n+1} - p_s^n)\right)_{i+1/2,k} \tag{4.27a}$$

$$A_{i-1/2,k} = \left(\phi^n + \left.\frac{\partial\phi}{\partial p_s}\right|^n (p_s^{n+1} - p_s^n)\right)_{i-1/2,k} \tag{4.27b}$$

$$B_{i,k+1/2} = \left(\phi^n + \left.\frac{\partial\phi}{\partial p_s}\right|^n (p_s^{n+1} - p_s^n)\right)_{i,k+1/2} \tag{4.28a}$$

$$B_{i,k-1/2} = \left(\phi^n + \left.\frac{\partial\phi}{\partial p_s}\right|^n (p_s^{n+1} - p_s^n)\right)_{i,k-1/2} \tag{4.28b}$$

A complete solution of the problem of two-dimensional transport of oil and sand in a horizontal well entails determining the distributions – both as functions of space and time – of the solid phase concentration, fluid phase concentration, radial and axial velocities of the fluid phase, radial and axial velocities of the solid phase, fluid phase pressure, solid phase pressure, and kinematic pressure, i.e.

$$\phi = \phi(r, z, t) \tag{4.29a}$$

$$\varepsilon = \varepsilon(r, z, t) \tag{4.29b}$$

$$u_f = u_f(r, z, t) \tag{4.29c}$$

$$u_s = u_s(r, z, t) \tag{4.29d}$$

$$w_f = w_f(r, z, t) \tag{4.29e}$$

$$w_s = w_s(r, z, t) \tag{4.29f}$$

$$p_f = p_f(r, z, t) \tag{4.29g}$$

$$p_s = p_s(r, z, t) \tag{4.29h}$$

$$p_k = p_k(r, z, t) \tag{4.29i}$$

Altogether there are nine variables. Going back to the derivation above it is seen that the following equations are available:

1. Continuity equation for the fluid phase (Equation 4.1 or Equation 4.9)
2. Continuity equation for the solid phase (Equation 4.2 or Equation 4.10)
3. Equation of motion along the r-direction for the fluid phase (Equation 4.3 or Equation 4.11)
4. Equation of motion along the z-direction for the fluid phase (Equation 4.4 or Equation 4.12)
5. Equation of motion along the r-direction for the solid phase (Equation 4.5 or Equation 4.13)
6. Equation of motion along the z-direction for the solid phase (Equation 4.6 or Equation 4.14)
7. Pressure equation for the solid phase (Equation 4.24)
8. Definition of the kinematic pressure (Equation 4.18)

To obtain a deterministic solution to the problem, there have to be nine equations for the nine variables. The last equation needed is the "saturation constraint" equation, as follows

$$\phi + \varepsilon = 1.0 \tag{4.30}$$

Equation 4.30 states that at any time the sum of the solid phase and fluid phase concentrations at any point in space has to be equal to unity. The mathematical model is now complete – with equal number of equations and variables to be solved for; as such, a deterministic solution set is now feasible for any prescribed initial and boundary conditions for the above variables.

4.3.2. Formulation of One-dimensional Models

A mathematical model describing the two-dimensional transport process of oil and sand in a horizontal well is given above. Appendix D provides the finite difference analogs of the equations constituting this mathematical model. As such, a numerical programme can be written to obtain the solution for this set of finite-differenced, algebraic equations. It is felt, however, that despite this complete formulation for the two-dimensional problem, focus for this study should be on the formulation and solution of one-dimensional models of the same transport process. The reasons for this strategy are based on many different considerations, as discussed below [126].

First and foremost it can be seen from above that despite invoking many simplifying assumptions the resulting mathematical model is still formidable to attempt any solution, analytical as well as numerical. This is due to the presence of a large number of variables involved in the transport process. The coupled nature of many of these variables, as expressed through the particle Reynolds number, drag coefficient, and interphase interaction coefficient often obscures the effects of individual variables, as well as the effects of their interactions on the overall transport process because these have to be largely estimated. A very important factor entering into consideration is the lack of results (analytical, experimental and/or numerical) in the literature against which numerical results from the above two-dimensional model can be compared. Numerous experimental studies of solid-fluid flow are available in the literature, as shown in Chapter 2, but not one of these studies dealt with the transient two-dimensional transport of oil and sand in a horizontal well (or pipe). In fact, many of these studies relied heavily on assumptions even more restrictive (for example, a steady state flow profile, no deposition of solid particles) than those employed in the formulation of the two-dimensional model above. There are, however, some numerical results for the one-dimensional transport of fluid and solid particles in a constricted channel [83]. These results, theoretically, can be used to compare with the results of comparable one-dimensional models, as developed in this study. Another consideration is the fact that numerical algorithms for two-dimensional flow problems are much more complex to develop and solve for than numerical algorithms for one-dimensional flow problems. This is especially true in the case of multiphase flow where the equations for individual phases are not only coupled, but also highly non-linear themselves (as seen in the equations of motion for the fluid phase and solid phase above).

Consequently, two other one-dimensional models are also developed in this study. The first one-dimensional model is, with some modifications, similar to Givler and Mikatarian's model [83]. The intent of formulating this model is first and foremost to reproduce these authors' results, and second (as a result of the first task) to modify and/or adapt it to study sand deposition inside a horizontal well. It is important to point out that Givler and Mikatarian's model does not have any feature describing the gravitational deposition of solid particles. Rather, its results apply only for the transient flow of solid particles and a Newtonian fluid inside a constricted channel – with the geometry and expansion rate of the constriction *a priori* fixed.

The second one-dimensional model is also developed from Givler and Mikatarian's Constriction model. However, there are major differences between them. The most important feature of the second model is its formulation to allow for deposition (or lack of) of solid particles (sand) as a result of the prevalent hydrodynamic conditions, including the effect of gravity, inside the horizontal well. Physically, this Gravity Deposition model simulates a flow process going from an initial condition of homogeneous distribution of solid particles in the fluid phase to some final condition as these solid particles settle, due to gravity, at the bottom of the horizontal well. As such, there is no constriction *a priori* prescribed to the solution of the flow process. In the following a detailed description of both of these one-dimensional models is provided.

4.3.2.1. Givler & Mikatarian's Constriction Model

Givler and Mikatarian set out to investigate the strategy of plugging fracture networks which are intersected by geothermal wells – by initiating the formation of particulate plugs in the fractures – thus, preventing excessive mud loss during the drilling of these wells [83]. The fractures are assumed to be of an intermediate size which is much smaller than the wellbore diameter, but on the other hand also much larger than the size of the solid particles used for the plugging operation. The fluid phase carrying the suspended solid particles is assumed to be Newtonian, and the overall suspension is treated as a continuum. The solid phase is composed of rigid, spherical solid particles of uniform, macroscopic size so as to exclude Brownian motion. Both the solid phase and the fluid phase are treated as a continuum. Empirical correlations for the drag coefficient, the particle-particle collision function $h(\phi)$, and the mixture viscosity used by these two authors in the formulation of their model are similar to those shown above, in the formulation of the two-dimensional model for this study (Section 4.3.1.). In fact, the formulation of the two-dimensional model in this work utilizes many elements provided by Givler and Mikatarian in their work [83].

Figure 4.2 provides a sketch of the problem studied by Givler and Mikatarian. It represents a one-dimensional channel, of constant height. A portion of this channel is assumed to be occupied by a constriction whose profile, and expansion rate are prescribed (as given by Equation 4.36 below). The constriction expands with time, and in so doing reduces the cross-sectional area of the channel open to flow. This gives rise to the formation of a particle plug which in turn affects the transport process. For this problem the following equations are given for the conservation of mass, and momentum for the two phases. Despite the one-dimensional geometry of the problem gravitational effects are included in the equations of motion for the two phases, as the authors intuitively assume that gravity opposed the transport process.

* Mass conservation for the fluid phase

$$\frac{\partial \varepsilon}{\partial t} + \frac{\partial}{\partial z}\left(\varepsilon w_f\right) = 0 \qquad (4.31)$$

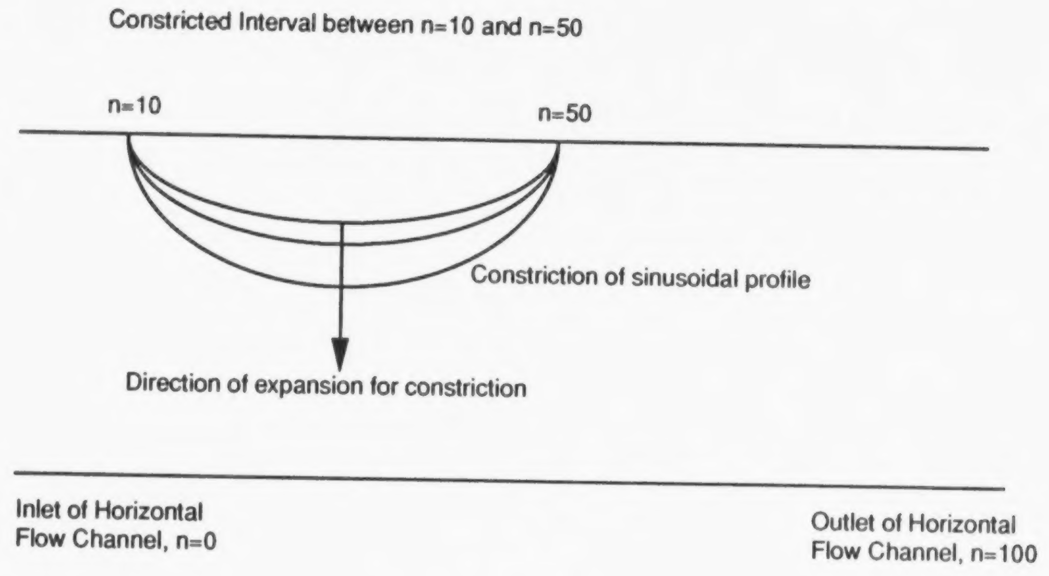
Constricted Interval between n=10 and n=50
n=10
n=50
Constriction of sinusoidal profile
Direction of expansion for constriction
Inlet of Horizontal Flow Channel, n=0
Outlet of Horizontal Flow Channel, n=100

Figure 4.2: Schematic drawing of flow geometry for Constriction Model [after Reference [83].)

- Mass conservation for the solid phase

$$\frac{\partial \phi}{\partial t} + \frac{\partial}{\partial z}(\phi w_s) = 0$$

(4.32)

- Conservation of momentum for the fluid phase

$$\frac{\partial}{\partial t}(\varepsilon w_f) + \frac{\partial}{\partial z}(\varepsilon w_f w_f) = -\frac{\varepsilon}{\overline{\rho_f}}\frac{\partial p_f}{\partial z} - (\varepsilon g) + \frac{\beta}{\overline{\rho_f}}(w_f - w_s)$$

(4.33

- Conservation of momentum for the solid phase

$$\frac{\partial}{\partial t}(\phi w_s) + \frac{\partial}{\partial z}(\phi w_s w_s) = -\frac{\phi}{\overline{\rho_s}}\frac{\partial p_s}{\partial z} - \frac{p_{k,z}}{\overline{\rho_s}}\frac{\partial \phi}{\partial z} - (\phi g) - \frac{\beta}{\overline{\rho_s}}(w_f - w_s)$$

(4.34)

It is important to note that the equations of motion do not include viscous stresses for both the fluid phase and the solid phase. The pressure equation for the solid phase is derived from the above mass and momentum conservation equations, and is given below. Appendix E provides the actual derivation of this solid phase pressure equation.

$$\frac{\partial^2 p_s}{\partial z^2} + \left(\frac{\left(\overline{\rho_s} - \overline{\rho_f}\right)}{\phi\left(\overline{\rho_s} - \overline{\rho_f}\right) - \overline{\rho_s}} \cdot \frac{\partial \phi}{\partial z}\right)\frac{\partial p_s}{\partial z} = \left[\frac{\overline{\rho_f} \cdot \overline{\rho_s}}{\phi\left(\overline{\rho_s} - \overline{\rho_f}\right) - \overline{\rho_s}}\right]\frac{\partial}{\partial z}\left\{-\frac{\varepsilon}{\overline{\rho_f}}\frac{\partial p_k}{\partial z} + \frac{p_k}{\overline{\rho_s}}\frac{\partial \phi}{\partial z}\right.$$
$$\left. - \frac{\left(\overline{\rho_s} - \overline{\rho_f}\right)}{\overline{\rho_f} \cdot \overline{\rho_s}}\beta\left(w_f - w_s\right) + \frac{\partial}{\partial z}\left[\phi w_s w_s + \varepsilon w_f w_f\right]\right\}$$

(4.35)

The profile of the constriction is given as follows,

$$h(z,t) = \begin{cases} h_o & \mathrm{n} < 10 \\ h_o\left[1.0 - t \cdot \sin\left(\dfrac{\pi z^*}{l}\right)\right] & 10 \le \mathrm{n} \le 50 \\ h_o & \mathrm{n} > 50 \end{cases}$$

(4.36)

where n is the computational cell number, i.e. the length of the channel is divided into 100 equal intervals. The profile of the constriction is fixed to be sinusoidal initially, and maintained as such with time.

The resulting system of five equations (Equations 4.31 – 4.35) can be solved to determine the distribution of solid phase pressure, velocity, and concentration, as well as fluid phase velocity and concentration.

4.3.2.2. Gravity Deposition Model

Givler and Mikatarian's Constriction model examines the solid-fluid transport process due to the presence of an *a priori* prescribed constriction [83]. However, it is incapable of describing and examining the deposition of solid particles, due to gravity, from initial homogeneous flow conditions. It is important to remember that without gravity settling of the solid particles in the first place there would be no constriction in the flow channel to influence the transport process thereafter. In addition, Givler and Mikatarian's model – by artificially fixing the profile and expansion rate of the constriction – is rather removed from actual physical processes where neither the profile of the deposit bed nor its expansion/contraction rate is known precisely. In the following a different model is developed to include gravity deposition of solid particles, and its subsequent influence on the transport process. It does not prescribe the profile or the expansion/contraction rate of the deposit bed. Instead, it allows them to be determined by the hydrodynamic conditions prevalent inside the horizontal well.

The oil-sand mixture is again treated as a continuum, and hence, automatically extending the continuum assumption to the solid phase and fluid phase. Other assumptions are similar to those invoked for Givler and Mikatarian's Constriction model. In addition, symmetry across a plane vertically cutting the horizontal well, at its centre, into two halves is assumed (Figure 4.3). To incorporate gravity deposition of solid particles into the model an additional term, treated as a source/sink term, is added to the mass conservation equation for the solid phase. This term (third term in Equation 4.38 below) physically states that the change in the solid phase concentration with respect to time (i.e. accumulation) arises due not only to the spatial flux of solid phase momentum, but also due to deposition of solid particles whose velocities are less than (or equal to) the critical velocity. When this imbalance of velocities occurs these solid particles are no longer carried along in the suspension, and instead are deposited by gravity at the bottom of the horizontal well. Similarly, an additional term is incorporated into the equation of motion for the solid phase (last term of Equation 4.40 below) to denote the momentum transfer due to this source/sink term. Again, the influx is assumed to be instantaneously accelerated to the mean stream velocity. What

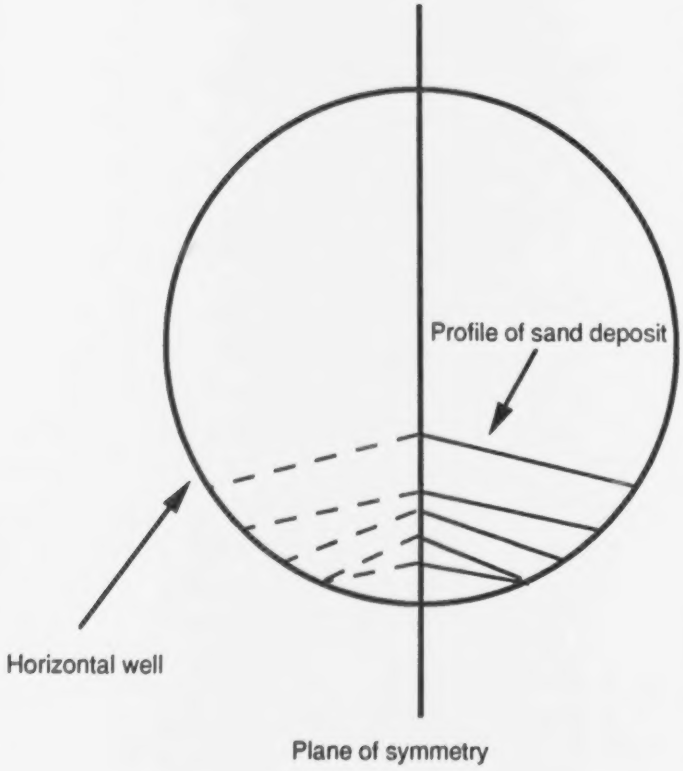
Profile of sand deposit
Horizontal well
Plane of symmetry

Figure 4.3: Plane of symmetry assumed for Gravity Deposition Model.

this means is that the fluid phase component of the influx stream takes on the mean stream fluid phase velocity, and the solid particles in the influx stream are accelerated to the same velocity of the solid phase.

* Mass conservation for the fluid phase

$$\frac{\partial}{\partial t}(\varepsilon h)+\frac{\partial}{\partial z}\left(\varepsilon h w_f\right)=0 \tag{4.37}$$

* Mass conservation for the solid phase

$$\frac{\partial}{\partial t}(\phi h)+\frac{\partial}{\partial z}\left(\phi h w_s\right)+\left(\phi v_{critical}\right)=0 \tag{4.38}$$

* Conservation of momentum for the fluid phase

$$\frac{\partial}{\partial t}\left(h\varepsilon w_f\right)+\frac{\partial}{\partial z}\left(\varepsilon h w_f w_f\right)=-\frac{\varepsilon}{\overline{\rho_f}}\frac{\partial}{\partial z}\left(hp_f\right)-(\varepsilon hg)+\frac{\beta h}{\overline{\rho_f}}\left(w_f-w_s\right) \tag{4.39}$$

* Conservation of momentum for the solid phase

$$\begin{aligned}\frac{\partial}{\partial t}(\phi h w_s)+\frac{\partial}{\partial z}(\phi h w_s w_s)&=-\frac{\phi}{\overline{\rho_s}}\frac{\partial}{\partial z}\left(hp_s\right)-\frac{p_{k,z}}{\overline{\rho_s}}\frac{\partial}{\partial z}(\phi h)-(\phi hg)\\&\quad-\frac{\beta h}{\overline{\rho_s}}\left(w_f-w_s\right)-\left(\phi v_{critical}\right)w_s\end{aligned} \tag{4.40}$$

In these equations the critical velocity, $v_{critical}$, is defined to be the mean stream velocity required to prevent the accumulation of a layer of either stationary or sliding particles on the bottom of a horizontal conduit [44]. As shown in Chapter 2, there is a multitude of empirical correlations expressing the critical velocity (or minimum transport velocity) as a function of, among many variables, particle concentration [20-28]. They, however, often contained coefficients valid only for the specific conditions used in the respective studies, and they are, therefore, quite restrictive. Instead, the following equation for the critical velocity is derived, by applying Stokes' law to the overall solid-fluid suspension, and used in the numerical simulation of this study.

$$v_{critical} = \frac{gd^2(\rho_s - \rho_{mixture})}{18\mu_{mixture}} \qquad (4.41)$$

The main reason for using this equation is its theoretical basis, and the fact that the mixture viscosity, $\mu_{mixture}$, can be calculated readily from Equation 4.17.

In this model, the pressure equation is derived for the fluid phase instead of for the solid phase. It is believed that, despite the continuum treatment for both the fluid phase and the solid phase, it is physically more appropriate to obtain the pressure distribution for the continuous fluid phase first, and then calculate the pressure distribution for the disperse solid phase from the kinematic pressure equation (Equation 4.18). This is in keeping with the logic of various investigators who – for the two-phase, two-pressure modelling approach – enunciated the fluid phase pressure to be the bulk-volume-averaged pressure [97-102]. Equation 4.42 govening the pressure distribution for the fluid phase is derived in the same manner as that shown in Appendix E for the solid phase pressure equation of Givler & Mikatarian's Constriction Model. It is given below.

$$\begin{aligned}\frac{\partial^2}{\partial z^2}(hp_f) = {} & \left(\frac{\overline{\rho_f}}{\phi(\overline{\overline{\rho_s}} - \overline{\overline{\rho_f}}) - \overline{\overline{\rho_s}}}\right)\frac{\partial}{\partial z}\cdot\frac{\partial}{\partial z}(\phi h p_k) + \left[\frac{(\overline{\rho_s} - \overline{\rho_f})}{\phi(\overline{\overline{\rho_s}} - \overline{\overline{\rho_f}}) - \overline{\overline{\rho_s}}}\right]\frac{\partial}{\partial z}\{\beta h(w_f - w_s)\} \\ & + \left[\left[\frac{\overline{\rho_f}\cdot\overline{\rho_s}}{\phi(\overline{\overline{\rho_s}} - \overline{\overline{\rho_f}}) - \overline{\overline{\rho_s}}}\right]\right]\frac{\partial}{\partial z}\left\{hg + \frac{\partial}{\partial z}[(\phi w_s)hw_s + (\varepsilon w_f)hw_f]\right\}\end{aligned}$$

$$(4.42)$$

Comparing the mass and momentum conservation equations of this model with their counterparts in Givler and Mikatarian's model [83] two major differences stand out. The first difference is, as stated in the above paragraphs, the incorporation of the gravity deposition terms into the mass and momentum conservation equations for the solid phase in this model. The second difference is that the height of the flow channel is no longer *a priori* and arbitrarily fixed in this model. Rather, it is allowed to vary with space and time – naturally, and as a result of the dynamics of the transport process. The variation in the flow channel height, at each spatial position, with time is given below by Equation 4.43,

$$\frac{dh}{dt} = -\frac{\phi}{\phi_{critical}}v_{critical} \qquad (4.43)$$

This equation is derived by considering the vertical expansion of the deposit bed on a layer-by-layer basis. What this means physically is that the solid particles which settle down due to gravity (because their velocities are less than the critical velocity) at the bottom of the horizontal well instantaneously and automatically rearrange themselves to fill the unoccupied spaces of the current layer. As such the height of the deposit bed only changes when there are no more unoccupied slots in the current layer, and the depositing solid particles, by default, are forced to stay on top of the current layer and thus form a new layer. Given the previous assumption of uniform-size spherical particles constituting the solid phase, and a porosity of 0.476 for cubic packing of uniform-size spheres, the value for the critical particle concentration, $\phi_{critical}$, is assigned a value of 0.524. The motion of the settling particles is toward the bottom of the horizontal well, against the normal positive direction for height. As such, the velocity of the deposition process which is (less than or) equal to the critical velocity $v_{critical}$ automatically assumes a negative sense.

The derivation, as such, does not allow for any saltatory movement of the depositing solid particles, i.e. they are not allowed to bounce back after coming into contact with the uppermost layer of the deposit bed, and become re-entrained in the fluid stream and subsequently deposited downstream – as examined by Bagnold [30]. Nor does the model consider the possibility of the solid particles become re-entrained in the fluid stream due to the contraction and/or disintegration of the deposit bed. The matter of structural shape and structural strength (for example, cohesion) of the deposit bed, and their influences on the transport process is highly complex and deserves, on its own, a separate investigation. This is, however, beyond the scope of this study. In summary, there are two choices facing a solid particle in the solid phase. At any point in space and time if the solid particle velocity is greater than the critical velocity then it is kept in suspension in the fluid phase. On the other hand, it will settle out of the suspension and "sink" to the bottom of the horizontal well if its velocity is less than the critical velocity.

It is interesting to note the following result is obtained by adding the two mass conservation equations together,

$$\frac{\partial}{\partial z}\left(\phi h w_s + \varepsilon h w_f\right) = -\phi v_{critical} \tag{4.44}$$

As such, it is seen that the source/sink term depicting the gravity deposition of solid particles applies to the overall suspension, and not just to the solid phase.

This mathematical model is consistent, as the six variables (fluid phase pressure, velocity, and concentration distributions, along with solid phase velocity and concentration distributions, along with the height of the deposit bed) are calculated using the system of six governing equations (Equations 4.37 – 4.40, Equation 4.42, and Equation 4.44).

A careful examination of the equations presented above, and elsewhere in this work, shows them all to be dimensionally consistent.

4.4. Initial Conditions and Boundary Conditions

Some comments about initial conditions and boundary conditions are in order. To obtain the solution for the various mathematical models developed above both initial conditions and boundary conditions have to be provided, given the fact that the governing equations are partial differential equations expressing the changes of different variables with space and time.

4.4.1. Initial and Boundary Conditions for Multiphase Flow Modelling

It is interesting to note that all three mathematical models (two-dimensional as well as one-dimensional) have, as their core, the mass and momentum conservation equations for the two phases. {They are all that are needed, physically, to model the isothermal transport of oil and sand in a horizontal well (or any other isothermal transport process, for that matter).} In each of the two equations of motion the pressure gradient term is a first-order derivative. To obtain the solid phase and fluid phase velocity distributions from their respective equation of motion it is usual to fix their pressures at the inlet, and at the outlet of a flow channel of finite length. However, it is just as valid to prescribe a value (i.e. a constant) for the pressure gradient term, mathematically, as to specify two pressure values, one at each end of the finite-length flow channel. On the other hand, by deriving the pressure equation for one of the two phases, from their mass and momentum conservation equations and a constitutive relation between the phase pressures, this choice disappears completely. The pressure equation, as seen above, is second-order. As such, it is now necessary to provide – explicitly – two boundary conditions for one of the phase pressures. This requirement of explicitly prescribing two boundary conditions for a phase pressure is a direct consequence of solving the system of governing equations for the primitive variables of velocity and pressure.

Another interesting fact about the pressure equation is its implicit dependence on time. As seen in Equation 4.35 or Equation 4.42, there is no explicit expression linking the pressure distribution with time. Rather, the pressure equation – in its differential form – describes only the spatial distribution of the pressure (for a specific phase) as a function of other variables which include velocity, concentration, density, interaction coefficient, velocity slippage. The pressure distribution varies with time only because it is dependent on the other variables, as listed above, which all change with time. This fact is more readily observable in the solid phase pressure equation for the two-dimensional model (Equation 4.24), which is expressed in finite-difference form. The presence of time level(s) assigned for the pressure arises strictly from applying discretization to terms in the mass and momentum conservation equations for the two phases. This observation is akin to that seen for the IMPES (Implicit Pressure, Explicit Saturation) method in reservoir simulation. The implicit dependence of time for the pressure does not preclude the initial condition from being prescribed for the pressure equation, however. In fact, it is easily seen that by setting initial conditions for the velocity and concentration of the two phases, along with an initial condition for the pressure of one phase (for example, the fluid phase), the initial conditions for the other phase pressure (for example, solid phase) and kinematic pressure are also fixed, by default because of the constitutive relation between the two phase pressures (see Equation 4.18). This argument also applies to the boundary conditions.

Boundary conditions of either the Dirichlet type (constant value) or the Neumann type (constant flux) can be assigned for the variables, including one phase pressure, at the edges of the domain of the problem. Given the coupled nature of the different variables it is important to remember that boundary conditions, and also the initial condition, for the pressure equation must be specified to be physically compatible with those prescribed for the mass and momentum conservation equations.

For the numerical solution of the two one-dimensional models performed in this study the following initial and boundary conditions are used.

4.4.2. Initial & Boundary Conditions for Givler & Mikatarian's Constriction Model

Givler and Mikatarian, based on the assumption of a homogeneous initial condition, fixed the initial solid phase concentration, solid phase pressure, solid phase velocity, and fluid phase velocity constant (at 0.10, 1.0, 0.9, and 1.0, respectively). These initial condition values are also assigned to be the same as the boundary conditions for the same variables, both at the inlet and outlet of the flow channel. The authors did not provide any explicit units for these values, except to say that they were defined to be consistent with the cgs systems of units [83]. This matter of values and units for the different variables and parameters used in the Constriction model is examined more critically in Chapter 6. The solution procedure is considerably simpler by this choice of Dirichlet-type boundary conditions for all of the relevant variables. A natural outcome of fixing the concentration and velocity constant at the inlet and outlet of the flow channel is that the momentum for both the fluid phase and solid phase are also, by default, fixed at constant values.

4.4.3. Initial and Boundary Conditions for Gravity Deposition Model

Unlike the boundary conditions used by Givler and Mikatarian in their model, the boundary conditions for the Gravity Deposition model are predominantly of the Neumann type. In performing the simulation runs, the fluid phase pressure is fixed at the inlet and outlet of the horizontal well. However, the total momentum flux and the solid phase momentum flux are fixed – both at the inlet and outlet. The total momentum flux is defined to be the sum of the fluid phase momentum flux and the solid phase momentum flux. In addition, the Neumann constant-flux boundary conditions are also specified for the solid phase concentration. This combination of constant flux boundary conditions for the solid phase permits the fluid phase to adjust automatically and naturally its momentum flux, velocity, and concentration. As well, the solid phase velocity is allowed to adjust itself to conform to the above boundary conditions. It is believed that these boundary conditions are, physically, much more realistic and appropriate in modelling the transport of oil and sand in a horizontal well.

4.5. Numerical Solution Procedures

As stated above, despite invoking many simplifying assumptions the resulting mathematical models – even in the case of the one-dimensional models – are still formidable to solve. An analytical solution is not possible to obtain for such a system of five coupled and non-linear equations. It is, however, possible to solve this system of equations numerically. In the following a brief description is provided for the numerical techniques and procedures, in particular those used to obtain the solution for the one-dimensional models.

4.5.1. Discretization

In the two-dimensional model case forward difference is employed for spatial discretization, and the temporal derivatives are discretized using the forward (Euler) difference. The mass and momentum conservation equations for both phases are discretized implicitly, as shown in Appendix E. For the one-dimensional models, on the other hand, the conservation equations are explicitly discretized. This is out of the need to compare results generated by this investigation (where it is appropriate to do so) with those presented by Givler and Mikatarian who employed the explicit discretization method. For spatial discretization forward difference is used at the inlet of the horizontal well, backward difference at the outlet of the horizontal well, and central difference elsewhere.

Recalling the MAC formulation approach employed in this study, the mass and momentum conservation equations are discretized on a grid system different from that used to discretized the pressure equation. In short, a staggered mesh system is used whereas the pressure nodes occupy the central position of each mesh square, and the velocity nodes are at the edges of the same square. The staggered mesh system used in the two-dimensional model is shown in Figure 4.4. It is seen that the radial velocity nodes are directly above and below the pressure node (the so-called North and South nodes), and the axial velocity nodes are to the left and right of the same pressure node (East and West nodes). The staggered mesh system for the one-dimensional models is shown in Figure 4.5. In both of these cases the velocity nodes are to the left and right of the pressure node.

4.5.2. Solution Procedure

The solution procedure for a numerical model, particularly in the case of multiphase flow, is dictated by how the equations are discretized, explicitly or implicitly, as well as the geometry of the flow problem being solved (one-dimensional or multi-dimensional). Given the non-linear characteristics of the governing equations, in particular the equations of motion, and the coupling between different variables and equations (through the interface interaction term(s)) in multiphase flow it is often necessary to employ semi-iterative or iterative methods [127–130]. Issa [131-132] proposed a non-iterative procedure which required the splitting of the solution process into a series of steps whereby the pressure equation was decoupled from velocity. What this meant is that the pressure distribution was calculated from the most recent velocity distribution, which was then in turn updated by the new pressure values, within each step. This approach was akin to the predictor-corrector method, and the author found two stages of prediction and correction to be sufficient to achieve an accurate solution within each time step for incompressible flow problems. For compressible flow three stages of prediction and correction were found to be adequate in getting a reasonably accurate solution. For multi-dimensional flow problems, quite often the ADI (Alternating Direction Implicit) method is used [133].

For the Constriction model, Givler and Mikatarian formulated and solved their system of equations explicitly. The mass and momentum conservation equations for the solid phase were solved simultaneously to obtain the solid phase velocity and concentration values, which were then used to obtain the solid phase pressure distribution from the solid phase pressure equation. The concentration and velocity distributions for the fluid phase were determined last. A flux-corrected transport algorithm was used to handle the convective terms in the equations of motion. The time step for this explicit solution procedure was very small, with 0.24 second of the transport process being represented by300 time steps [83].

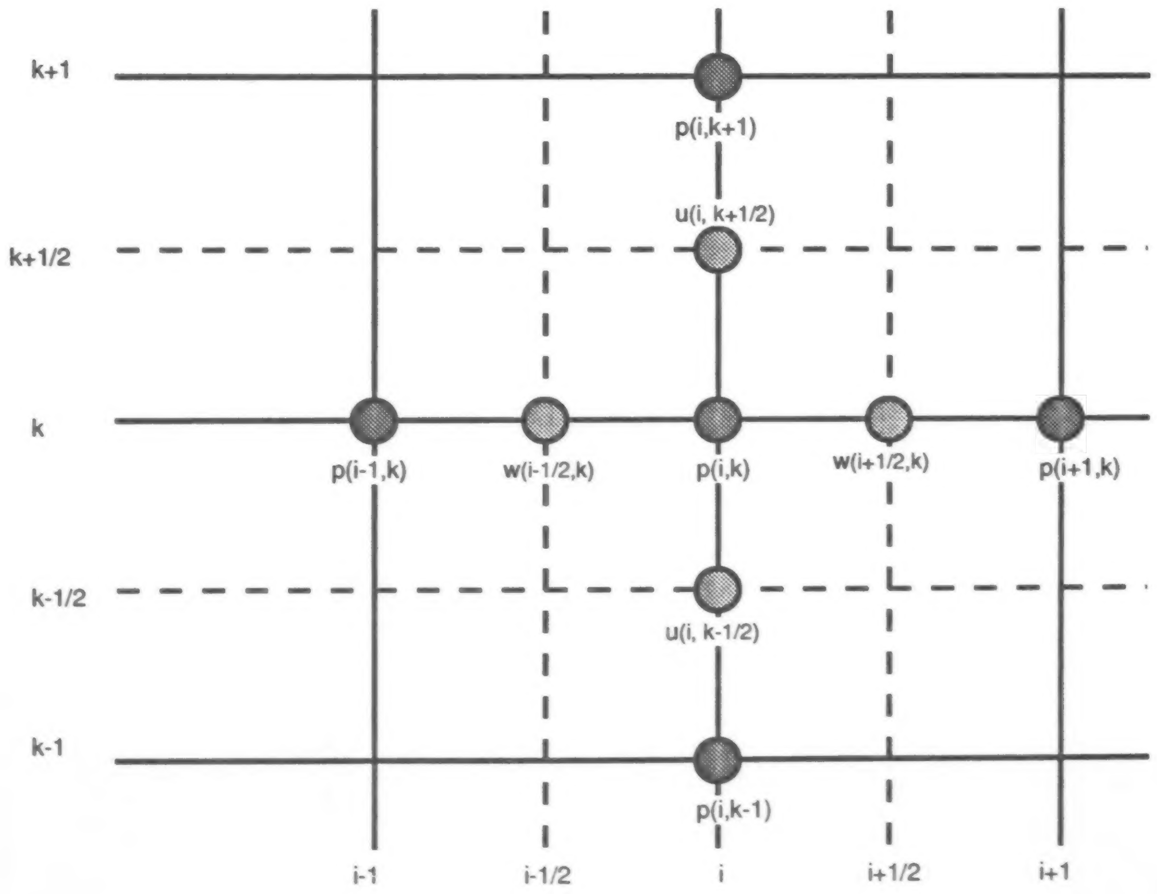
k+1
k+1/2
k
k-1/2
k-1
p(i,k+1)
u(i, k+1/2)
p(i-1,k)
w(i-1/2,k)
p(i,k)
w(i+1/2,k)
p(i+1,k)
u(i, k-1/2)
p(i,k-1)
i-1
i-1/2
i
i+1/2
i+1

Figure 4.4: Schematic drawing of staggered mesh for 2-D model.

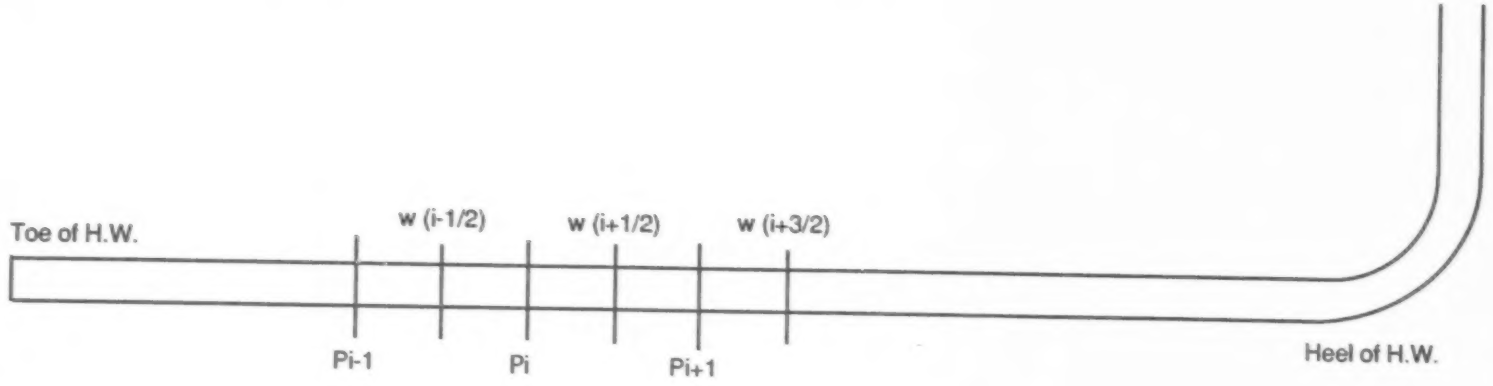
Toe of H.W.
w (i-1/2)
w (i+1/2)
w (i+3/2)
Pi-1
Pi
Pi+1
Heel of H.W.

Figure 4.5: Schematic drawing of staggered mesh for 1-D Gravity Deposition Model.

For the Gravity Deposition model the equations were also discretized explicitly. However, in this case the solution sequence followed that of the MAC method: the pressure distribution (for the fluid phase) was determined first. The solid phase momentum flux was next calculated together with the solid phase concentration flux. From these the solid phase velocity distribution was obtained. The fluid phase velocity and concentration were obtained next, and a convergence test was performed before the solution was advanced to the next time step.

4.5.3. Stability Considerations

The nonlinearities in the equations of motion for both phases prevented a stability analysis to be carried out. Issa provided a discussion on performing a stability analysis for a linearized, single-phase flow equation [131-132]. This approach could not be used for this study due to the coupled nature of the equations (of motion for the two phases), and the unknown magnitude for the interphase momentum transfer term(s).

Givler and Mikatarian analyzed the characteristics of their system of governing equations, and came to the conclusion that a value of 0.1 for the Courant Number (defined to be the ratio of the distance traversed in a time period to the dimension of the mesh cell of the discretized domain), based upon their characteristic velocity and cell size, was needed to maintain stability for their numerical solution, as well as to ensure that all of the solutions obtained were real [83].

For the Gravity Deposition model, the approach used was trial-and-error – several values were assigned to the Courant Number, for a particular flow condition, and the numerical results were observed for spurious oscillations. This was repeated until the solution showed no oscillations and no aphysical behaviour with regard to the different distributions for the variables. The Courant Number was then assigned this value (of no oscillations in the results), and the simulation run was extended. As the cell size, fluid viscosity and velocity, and particle size changed for the different runs, it was often necessary to try out several values for the Courant Number. It is important to point out that once an optimum value for the Courant Number was determined, it was then fixed for the run (or series of runs of similar conditions). The time step was automatically adjusted, depending on velocity fluctuations, to satisfy the Courant Number condition.

Chapter 5. Development of Scaling Criteria

5.1. Introduction

An in-depth experimental investigation of the transport problem of oil and sand in a horizontal well requires costly equipment, such as a Laser-Doppler Anemometer (LDA) system needed to measure the in-situ concentration of the solid phase (and by default, the fluid phase concentration). Although experimental work in this direction is not part of the present research, scaling criteria for the transport process are derived in this chapter to lay the groundwork for future experimental studies. Also, in the case of multiphase flow the interactions between the different variables and parameters involved in the transport process are not often apparent, as in the case of single-phase flow. As such, it is important to be able to examine how these variables and parameters are interconnected. This plays a useful role not only in terms of permitting an order-of-magnitude analysis to be performed for future experiments, but also for future numerical simulation studies. Given the complexities inherent in the multiphase transport of oil and sand, as well as the still evolving knowledge of the flow inside a horizontal well, it is fully understood that any investigation of this transport process has to be multi-staged, systematic and multi-faceted. The aim has always been to combine all the tools available to study this transport process, including both numerical and physical modelling – with a view to using one tool to calibrate the other.

This chapter is organized into three parts. In the first part the scaling criteria for the two-dimensional model are derived. The scaling criteria for one-dimensional models are presented in the second part. The last part contains concluding remarks. In the following work both Inspectional Analysis and Dimensional Analysis are used to obtain, independently, the dimensionless similarity groups required for the design of scaled physical model(s) and operating conditions for the scaled model experiments. A general overview of scaling principles and techniques is provided in the following.

Scaling theory as it is applied to the design and operation of physical models is based upon the Principle of Similarity. What this means is that the models are characterized by the same ratios of dimensions, forces, velocities, temperature differences, and concentration differences as those occurring in the prototypes. The performance of these models is governed by the values of a number of dimensionless similarity groups. As stated above, the dimensionless similarity groups are derived independently by Inspectional Analysis and Dimensional Analysis.

Dimensional Analysis is based on the Buckingham π-Theorem. This method is used when the differential equations describing the flow process being studied are not known. It only requires that all of the relevant variables for the process are known. The variables are combined and arranged in a set of dimensionless (π-) groups. The set is complete if all the groups in the set are independent of each other, and if every dimensionless group containing the same variables, and not belonging in the set, can be formed by combining groups belonging to the set. A general rule for Dimensional Analysis is that if there are n separate variables, and m primary dimensions (for example, mass, length, time, force, temperature) then the set is complete when there are $(n - m)$ dimensionless groups. In petroleum engineering Dimensional Analysis has been successfully applied to obtain the scaling criteria for waterflood [134 – 136], miscible (solvent) flood [137,138], hot water injection [138] and steam injection [139].

Inspectional Analysis, on the other hand, is more systematic in its approach for obtaining the dimensionless similarity groups provided the process being examined can be described satisfactorily by means of differential equations. For this technique, the differential equations relating the independent and dependent variables, as well as the constraints of the flow process serve as the basis from which the set of dimensionless groups is obtained. This is done first by making the equations dimensionally homogeneous. The dependent variables are next rendered dimensionless by dividing each equation by one of its coefficients. Geertsma, Croes and Schwarz pointed out that, in general, the set of dimensionless similarity groups from Dimensional Analysis is larger than that from Inspectional Analysis [138]. However, the physical meaning of the similarity groups derived by Dimensional Analysis is less apparent, generally, than that of the groups derived by Inspectional Analysis [138]. Inspectional Analysis has been used to design scaled model experiments for CO_2-immiscible displacement process [140], steam injection methods [141 – 143].

Given the findings by various investigators [138,140,142-143], both the Inspectional Analysis and Dimensional Analysis are used together to ensure that a complete set of scaling criteria is obtained.

5.2. Two-dimensional Model

5.2.1. Inspectional Analysis

The set of differential equations describing the conservation of mass and momentum for the fluid phase and the solid phase serves as the basis for the analysis. The pressure equation for the solid phase is not included in the analysis primarily because it is an auxiliary equation, derived from a consideration of the mass and momentum conservation equations mostly to facilitate the numerical solution to the equations.

* Mass conservation for the fluid phase

$$\frac{\partial \varepsilon}{\partial t} - \frac{1}{r}\frac{\partial}{\partial r}\left(r\varepsilon u_f\right) + \frac{\partial}{\partial z}\left(\varepsilon w_f\right) - (\varepsilon q)^{\bullet}_{in.} = 0 \tag{5.1}$$

* Mass conservation for the solid phase

$$\frac{\partial \phi}{\partial t} - \frac{1}{r}\frac{\partial}{\partial r}\left(r\phi u_s\right) + \frac{\partial}{\partial z}\left(\phi w_s\right) - (\phi q)^{\bullet}_{in.} = 0 \tag{5.2}$$

* Conservation of momentum for the fluid phase

Along the radial (r-) direction

$$\begin{aligned}\frac{\partial}{\partial t}\left(\varepsilon u_f\right) - \frac{\partial}{\partial r}\left(\varepsilon u_f u_f\right) + \frac{\partial}{\partial z}\left(\varepsilon w_f u_f\right) = -\frac{\varepsilon}{\bar{\rho}_f}\frac{\partial p_f}{\partial r} + \frac{\mu_f}{\bar{\rho}_f}\left[\frac{\partial}{\partial r}\left(\frac{1}{r}\frac{\partial}{\partial r}\left(-r u_f\right)\right) + \frac{\partial^2 u_f}{\partial z^2}\right] - (\varepsilon q)^{\bullet}_{in.} u_f \\ -\varepsilon g - \frac{3}{8} C_L \phi \frac{\left(u_s - u_f + \Delta v\right)^2}{a} + \frac{\beta_r}{\bar{\rho}_f}\left(u_f - u_s\right)\end{aligned} \tag{5.3}$$

Along the axial (z-) direction

$$\begin{aligned}\frac{\partial}{\partial t}\left(\varepsilon w_f\right) - \frac{\partial}{\partial r}\left(\varepsilon u_f w_f\right) + \frac{\partial}{\partial z}\left(\varepsilon w_f u_f\right) = -\frac{\varepsilon}{\bar{\rho}_f}\frac{\partial p_f}{\partial z} + \frac{\mu_f}{\bar{\rho}_f}\left[\frac{1}{r}\frac{\partial}{\partial r}\left(r\frac{\partial w_f}{\partial r}\right) + \frac{\partial^2 w_f}{\partial z^2}\right] \\ -(\varepsilon q)^{\bullet}_{in.} w_f + \frac{\beta_z}{\bar{\rho}_f}\left(w_f - w_s\right)\end{aligned} \tag{5.4}$$

* Conservation of momentum for the solid phase

Along the radial (r-) direction

$$\frac{\partial}{\partial t}(\phi u_s) - \frac{\partial}{\partial r}(\phi u_s u_s) + \frac{\partial}{\partial z}(\phi w_s u_s) = -\frac{\phi}{\rho_s}\frac{\partial p_s}{\partial r} + \left[\frac{1}{r}\frac{\partial}{\partial r}\left(-r\mu_s \frac{\partial u_s}{\partial r}\right) + \frac{\partial}{\partial z}\left(\mu_s \frac{\partial u_s}{\partial z}\right)\right] - \frac{p_{k,r}}{\rho_s}\frac{\partial \phi}{\partial r}$$

$$-\phi g - (\phi q)^{\bullet}_{in.} u_s + \frac{3}{8} C_L \phi \frac{\left(u_s - u_f + \Delta v\right)^2}{a} - \frac{\beta_r}{\rho_s}\left(u_f - u_s\right)$$

(5.5)

Along the axial (z-) direction

$$\frac{\partial}{\partial t}(\phi w_s) - \frac{\partial}{\partial r}(\phi u_s w_s) + \frac{\partial}{\partial z}(\phi w_s w_s) = -\frac{\phi}{\rho_s}\frac{\partial p_s}{\partial z} + \frac{1}{\rho_s}\left[\frac{1}{r}\frac{\partial}{\partial r}\left(-r\mu_s \frac{\partial w_s}{\partial r}\right) + \frac{\partial}{\partial z}\left(\mu_s \frac{\partial w_s}{\partial z}\right)\right]$$

$$-\frac{p_{k,z}}{\rho_s}\frac{\partial \phi}{\partial z} - (\phi q)^{\bullet}_{in.} w_s - \frac{\beta_z}{\rho_s}\left(w_f - w_s\right)$$

(5.6)

In the equations of motion for the fluid phase and solid phase along the radial direction (Equations (5.3) and (5.4)) the velocity difference used in the determination of the lift force is defined to be

$\langle \Delta v \rangle \approx |dv / dr| a$.

For every variable (or parameter) M included in the equations, it is rewritten in dimensionless form as follows, $M_D = M / M_R$ where M_D is the variable expressed in dimensionless form, and M_R represents some reference value for the same variable. This recasting of variables and parameters into dimensionless form results in the following,

* Mass conservation for fluid phase

$$-\left[\frac{\varepsilon_R u_{fR}}{r_R}\right]\frac{1}{r_D}\frac{\partial}{\partial r_D}(r_D \varepsilon_D u_{fD}) + \left[\frac{\varepsilon_R w_{fR}}{z_R}\right]\frac{\partial}{\partial z_D}(\varepsilon_D w_{fD}) - \left[(\varepsilon_R q_R)^{\bullet}_{in.}\right](\varepsilon_D q_D)^{\bullet}_{in.} = \left[\frac{\varepsilon_R}{t_R}\right]\frac{\partial \varepsilon_D}{\partial t_D}$$

(5.7)

* Mass conservation for the solid phase

$$-\left[\frac{\phi_R u_{sR}}{r_R}\right]\frac{1}{r_D}\frac{\partial}{\partial r_D}\left(r_D\phi_D u_{sD}\right)+\left[\frac{\phi_R w_{sR}}{z_R}\right]\frac{\partial}{\partial z_D}\left(\phi_D w_{sD}\right)-\left[(\phi_R q_R)^{\bullet}_{in.}\right](\phi_D q_D)^{\bullet}_{in.}=\left[\frac{\phi_R}{t_R}\right]\frac{\partial \phi_D}{\partial t_D}$$

(5.8)

* Conservation of momentum for the fluid phase

Along the radial (r-) direction

$$\begin{aligned}&\left[\frac{\varepsilon_R u_{fR}}{t_R}\right]\frac{\partial}{\partial t_D}(\varepsilon_D u_{fD})-\left[\frac{\varepsilon_R u_{fR}u_{fR}}{r_R}\right]\frac{\partial}{\partial r_D}(\varepsilon_D u_{fD}u_{fD})+\left[\frac{\varepsilon_R w_{fR}u_{fR}}{z_R}\right]\frac{\partial}{\partial z_D}(\varepsilon_D w_{fD}u_{fD})=\\&-\left[\frac{\varepsilon_R p_{fR}}{\overline{\overline{\rho}}_{fR}r_R}\right]\left\{\frac{\varepsilon_D}{\overline{\overline{\rho}}_{fD}}\right\}\frac{\partial p_{fD}}{\partial r_D}+\left[\frac{\mu_{fR}u_{fR}}{r_R^2\overline{\overline{\rho}}_{fR}}\right]\left(\frac{\mu_{fD}}{\overline{\overline{\rho}}_{fD}}\right)\frac{\partial}{\partial r_D}\left(\frac{1}{r_D}\frac{\partial}{\partial r_D}(-r_D u_{fD})\right)+\left[\frac{\mu_{fR}u_{fR}}{z_R^2\overline{\overline{\rho}}_{fR}}\right]\frac{\partial^2 u_{fD}}{\partial z_D^2}-[\varepsilon_R g_R]\varepsilon_D g_D\\&-\left[(\varepsilon_R q_R)^{\bullet}_{in.}u_{fR}\right](\varepsilon_D q_D)^{\bullet}_{in.}u_{fD}-\left[\frac{3}{8}C_{LR}\phi_R\frac{[(-\Delta u)_R+\Delta v_R]^2}{a_R}\right]C_{LD}\phi_D\frac{[(-\Delta u)_D+\Delta v_D]^2}{a_D}\\&+\left[\frac{\beta_{rR}}{\overline{\overline{\rho}}_{fR}}[\Delta u]_R\right]\left(\frac{\beta_{rD}}{\overline{\overline{\rho}}_{fD}}[\Delta u]_D\right)\end{aligned}$$

(5.9)

Along the axial (z-) direction

$$\begin{aligned}&\left[\frac{\varepsilon_R w_{fR}}{t_R}\right]\frac{\partial}{\partial t_D}(\varepsilon_D w_{fD})-\left[\frac{\varepsilon_R u_{fR}w_{fR}}{r_R}\right]\frac{\partial}{\partial r_D}(\varepsilon_D u_{fD}w_{fD})+\left[\frac{\varepsilon_R w_{fR}u_{fR}}{z_R}\right]\frac{\partial}{\partial z_D}(\varepsilon_D w_{fD}u_{fD})=\\&-\left[\frac{\varepsilon_R p_{fR}}{z_R\overline{\overline{\rho}}_{fR}}\right]\left(\frac{\varepsilon_D}{\overline{\overline{\rho}}_{fD}}\right)\frac{\partial p_{fD}}{\partial z_D}+\left[\frac{\mu_{fR}w_{fR}}{r_R^2\overline{\overline{\rho}}_{fR}}\right]\left(\frac{\mu_{fD}}{\overline{\overline{\rho}}_{fD}}\right)\frac{1}{r_D}\frac{\partial}{\partial r_D}\left(r_D\frac{\partial w_{fD}}{\partial r_D}\right)+\left[\frac{\mu_{fR}w_{fR}}{z_R^2\overline{\overline{\rho}}_{fR}}\right]\frac{\mu_{fD}}{\overline{\overline{\rho}}_{fD}}\frac{\partial^2 w_{fD}}{\partial z_D^2}\\&-\left[(\varepsilon_R q_R)^{\bullet}_{in.}w_{fR}\right](\varepsilon_D q_D)^{\bullet}_{in.}w_{fD}+\left[\frac{\beta_{zR}}{\overline{\overline{\rho}}_{fR}}(\Delta w)_R\right]\left(\frac{\beta_{zD}}{\overline{\overline{\rho}}_{fD}}(\Delta w)_D\right)\end{aligned}$$

(5.10)

* Conservation of momentum for the solid phase

Along the radial (r-) direction

$$\begin{aligned}
&\left[\frac{\phi_R u_{sR}}{t_R}\right]\frac{\partial}{\partial t_D}(\phi_D u_{sD}) - \left[\frac{\phi_R u_{sR} u_{sR}}{r_R}\right]\frac{\partial}{\partial r_D}(\phi_D u_{sD} u_{sD}) + \left[\frac{\phi_R w_{sR} u_{sR}}{z_R}\right]\frac{\partial}{\partial z_D}(\phi_D w_{sD} u_{sD}) = \\
&-\left[\frac{\phi_R \underline{\underline{p_{sR}}}}{r_R \rho_{sR}}\right]\left(\frac{\underline{\underline{\phi_D}}}{\rho_{sD}}\right)\frac{\partial p_{sD}}{\partial r_D} - \left[\frac{\phi_R \underline{\underline{p_{k,rR}}}}{r_R \rho_{sR}}\right]\left(\frac{\underline{\underline{p_{k,rD}}}}{\rho_{sD}}\right)\frac{\partial \phi_D}{\partial r_D} + \left[\frac{\mu_{sR} u_{sR}}{r_R^2}\right]\frac{1}{r_D}\frac{\partial}{\partial r_D}\left(-r_D \mu_{sD}\frac{\partial u_{sD}}{\partial r_D}\right) \\
&+\left[\frac{\mu_{sR} u_{sR}}{z_R^2}\right]\frac{\partial}{\partial z_D}\left(\mu_{sD}\frac{\partial u_{sD}}{\partial z_D}\right) - [\phi_R g_R](\phi_D g_D) - \left[(\phi_R q_R)^{\bullet}_{in.} u_{sR}\right](\phi_D q_D)^{\bullet}_{in.} u_{sD} \\
&+\left[\frac{3}{8} C_{LR}\phi_R \frac{[(-\Delta u)_R + (\Delta v)_R]^2}{a_R}\right]\left(C_{LD}\phi_D \frac{[(-\Delta u)_D + (\Delta v)_D]^2}{a_D}\right) - \left[\frac{\underline{\underline{\beta_{rR}}}}{\rho_{sR}}(\Delta u)_R\right]\left(\frac{\underline{\underline{\beta_{rD}}}}{\rho_{sD}}\right)(\Delta u)_D
\end{aligned}$$

(5.11)

Along the axial (z-) direction

$$\begin{aligned}
&\left[\frac{\phi_R w_{sR}}{t_R}\right]\frac{\partial}{\partial t_D}(\phi_D w_{sD}) - \left[\frac{\phi_R u_{sR} w_{sR}}{r_R}\right]\frac{\partial}{\partial r_D}(\phi_D u_{sD} w_{sD}) + \left[\frac{\phi_R w_{sR} w_{sR}}{z_R}\right]\frac{\partial}{\partial z_D}(\phi_D w_{sD} w_{sD}) = \\
&-\left[\frac{\phi_R \underline{\underline{p_{sR}}}}{z_R \rho_{sR}}\right]\left(\frac{\underline{\underline{\phi_D}}}{\rho_{sD}}\right)\frac{\partial p_{sD}}{\partial z_D} - \left[\frac{\phi_R \underline{\underline{p_{k,zR}}}}{z_R \rho_{sR}}\right]\left(\frac{\underline{\underline{p_{k,zD}}}}{\rho_{sD}}\right)\frac{\partial \phi_D}{\partial z_D} + \left[\frac{\mu_{sR} \underline{\underline{w_{sR}}}}{r_R^2 \rho_{sR}}\right]\left(\frac{\underline{\underline{1}}}{\rho_{sD}}\right)\frac{1}{r_D}\frac{\partial}{\partial r_D}\left(-r_D \mu_{sD}\frac{\partial w_{sD}}{\partial r_D}\right) \\
&+\left[\frac{\mu_{sR} \underline{\underline{w_{sR}}}}{r_R^2 \rho_{sR}}\right]\left(\frac{\underline{\underline{1}}}{\rho_{sD}}\right)\frac{\partial}{\partial z_D}\left(\mu_{sD}\frac{\partial w_{sD}}{\partial z_D}\right) - \left[(\phi_R q_R)^{\bullet}_{in.} w_{sR}\right](\phi_D q_D)^{\bullet}_{in.} w_{sD} - \left[\frac{\underline{\underline{\beta_{zR}}}}{\rho_{sR}}(\Delta w)_R\right]\frac{\underline{\underline{\beta_{zD}}}}{\rho_{sD}}(\Delta w)_D
\end{aligned}$$

(5.12)

The reference quantities in the square brackets represent the coefficients of the terms in the equations. Dividing each of the above equations by the coefficient of its first term leads to the following equations,

* Mass conservation for fluid phase

$$-\frac{1}{r_D}\frac{\partial}{\partial r_D}(r_D \varepsilon_D u_{fD}) + \left[\frac{r_R w_{fR}}{z_R u_{fR}}\right]\frac{\partial}{\partial z_D}(\varepsilon_D w_{fD}) - \left[\frac{r_R(\varepsilon_R q_R)^{\bullet}_{in.}}{\varepsilon_R u_{fR}}\right](\varepsilon_D q_D)^{\bullet}_{in.} = \left[\frac{r_R}{t_R u_{fR}}\right]\frac{\partial \varepsilon_D}{\partial t_D}$$

(5.13)

* Mass conservation for the solid phase

$$-\frac{1}{r_D}\frac{\partial}{\partial r_D}\left(r_D\phi_D u_{sD}\right)+\left[\frac{r_R w_{sR}}{z_R u_{sR}}\right]\frac{\partial}{\partial z_D}\left(\phi_D w_{sD}\right)-\left[\frac{r_R\left(\phi_R q_R\right)^{\bullet}_{in.}}{\phi_R u_{sR}}\right]\left(\phi_D q_D\right)^{\bullet}_{in.}=\left[\frac{r_R}{u_{sR}t_R}\right]\frac{\partial\phi_D}{\partial t_D} \tag{5.14}$$

* Conservation of momentum for the fluid phase

Along the radial (r-) direction

$$\begin{aligned}&\frac{\partial}{\partial t_D}(\varepsilon_D u_{fD})-\left[\frac{t_R u_{fR}}{r_R}\right]\frac{\partial}{\partial r_D}(\varepsilon_D u_{fD}u_{fD})+\left[\frac{t_R w_{fR}}{z_R}\right]\frac{\partial}{\partial z_D}(\varepsilon_D w_{fD}u_{fD})=-\left[\frac{t_R p_{fR}}{\overline{\overline{\rho}}_{fR}r_R u_{fR}}\right]\left\{\frac{\varepsilon_D}{\overline{\overline{\rho}}_{fD}}\right\}\frac{\partial p_{fD}}{\partial r_D}\\&+\left[\frac{\mu_{fR}t_R}{\varepsilon_R r_R^2\overline{\overline{\rho}}_{fR}}\right]\left(\frac{\mu_{fD}}{\overline{\overline{\rho}}_{fD}}\right)\frac{\partial}{\partial r_D}\left(\frac{1}{r_D}\frac{\partial}{\partial r_D}(-r_D u_{fD})\right)+\left[\frac{\mu_{fR}t_R}{\varepsilon_R z_R^2\overline{\overline{\rho}}_{fR}}\right]\frac{\partial^2 u_{fD}}{\partial z_D^2}-\left[\frac{(\varepsilon_R q_R)^{\bullet}_{in.}t_R}{\varepsilon_R}\right](\varepsilon_D q_D)^{\bullet}_{in.}u_{fD}\\&-\left[\frac{t_R g_R}{u_{fR}}\right]\varepsilon_D g_D-\left[\frac{3}{8}C_{LR}\frac{\phi_R}{\varepsilon_R}\frac{t_R[(-\Delta u)_R+\Delta v_R]^2}{u_{fR}a_R}\right]\left(C_{LD}\phi_D\frac{[(-\Delta u)_D+\Delta v_D]^2}{a_D}\right)\\&+\left[\frac{t_R\beta_{rR}}{\varepsilon_R\overline{\overline{\rho}}_{fR}}\cdot\frac{(\Delta u)_R}{u_{fR}}\right]\left(\frac{\beta_{rD}}{\overline{\overline{\rho}}_{fD}}[\Delta u]_D\right)\end{aligned} \tag{5.15}$$

Along the axial (z-) direction

$$\begin{aligned}&\frac{\partial}{\partial t_D}(\varepsilon_D w_{fD})-\left[\frac{t_R u_{fR}}{r_R}\right]\frac{\partial}{\partial r_D}(\varepsilon_D u_{fD}w_{fD})+\left[\frac{t_R w_{fR}}{z_R}\right]\frac{\partial}{\partial z_D}(\varepsilon_D w_{fD}w_{fD})=-\left[\frac{t_R p_{fR}}{w_{fR}z_R\overline{\overline{\rho}}_{fR}}\right]\left(\frac{\varepsilon_D}{\overline{\overline{\rho}}_{fD}}\right)\frac{\partial p_{fD}}{\partial z_D}\\&+\left[\frac{\mu_{fR}t_R}{\varepsilon_R r_R^2\overline{\overline{\rho}}_{fR}}\right]\left(\frac{\mu_{fD}}{\overline{\overline{\rho}}_{fD}}\right)\frac{1}{r_D}\frac{\partial}{\partial r_D}\left(r_D\frac{\partial w_{fD}}{\partial r_D}\right)+\left[\frac{\mu_{fR}t_R}{\varepsilon_R z_R^2\overline{\overline{\rho}}_{fR}}\right]\frac{\mu_{fD}}{\overline{\overline{\rho}}_{fD}}\frac{\partial^2 w_{fD}}{\partial z_D^2}-\left[\frac{(\varepsilon_R q_R)^{\bullet}_{in.}t_R}{\varepsilon_R}\right](\varepsilon_D q_D)^{\bullet}_{in.}w_{fD}\\&+\left[\frac{t_R\beta_{zR}}{\varepsilon_R\overline{\overline{\rho}}_{fR}}\frac{(\Delta w)_R}{w_{fR}}\right]\left(\frac{\beta_{zD}}{\overline{\overline{\rho}}_{fD}}(\Delta w)_D\right)\end{aligned} \tag{5.16}$$

* Conservation of momentum for the solid phase

Along the radial (r-) direction

$$\frac{\partial}{\partial t_D}(\phi_D u_{sD}) - \left[\frac{t_R u_{sR}}{r_R}\right]\frac{\partial}{\partial r_D}(\phi_D u_{sD} u_{sD}) + \left[\frac{t_R w_{sR}}{z_R}\right]\frac{\partial}{\partial z_D}(\phi_D w_{sD} u_{sD}) = -\left[\frac{t_R p_{sR}}{u_{sR} r_R \bar{\bar{\rho}}_{sR}}\right]\left(\frac{\phi_D}{\bar{\bar{\rho}}_{sD}}\right)\frac{\partial p_{sD}}{\partial r_D}$$
$$-\left[\frac{t_R p_{k,rR}}{u_{sR} r_R \bar{\bar{\rho}}_{sR}}\right]\left(\frac{p_{k,rD}}{\bar{\bar{\rho}}_{sD}}\right)\frac{\partial \phi_D}{\partial r_D} - \left[\frac{\mu_{sR} t_R}{\bar{\bar{\rho}}_{sR} r_R^2 \phi_R}\right]\frac{1}{r_D \bar{\bar{\rho}}_{sD}}\frac{\partial}{\partial r_D}\left(r_D \mu_{sD}\frac{\partial u_{sD}}{\partial r_D}\right) - \left[\frac{\mu_{sR} t_R}{\bar{\bar{\rho}}_{sR} z_R^2 \phi_R}\right]\frac{\partial}{\partial z_D}\left(\mu_{sD}\frac{\partial u_{sD}}{\partial z_D}\right)$$
$$-\left[\frac{(\phi_R q_R)^{*}_{in.} t_R}{\phi_R}\right](\phi_D q_D)^{*}_{in.} u_{sD} + \left[\frac{3}{8} C_{LR} t_R \frac{[(-\Delta u)_R + (\Delta v)_R]^2}{u_{sR} a_R}\right]\left(C_{LD}\phi_D \frac{[(-\Delta u)_D + (\Delta v)_D]^2}{a_D}\right)$$
$$-\left[\frac{t_R g_R}{u_{sR}}\right](\phi_D g_D) - \left[\frac{\beta_{rR}}{\bar{\bar{\rho}}_{sR}}(\Delta u)_R\right]\left(\frac{\beta_{rD}}{\bar{\bar{\rho}}_{sD}}\right)(\Delta u)_D$$

(5.17)

Along the axial (z-) direction

$$\frac{\partial}{\partial t_D}(\phi_D w_{sD}) - \left[\frac{t_R u_{sR}}{r_R}\right]\frac{\partial}{\partial r_D}(\phi_D u_{sD} w_{sD}) + \left[\frac{t_R w_{sR}}{z_R}\right]\frac{\partial}{\partial z_D}(\phi_D w_{sD} w_{sD}) = -\left[\frac{t_R p_{sR}}{z_R \bar{\bar{\rho}}_{sR} w_{sR}}\right]\left(\frac{\phi_D}{\bar{\bar{\rho}}_{sD}}\right)\frac{\partial p_{sD}}{\partial z_D}$$
$$-\left[\frac{p_{k,zR} t_R}{z_R \bar{\bar{\rho}}_{sR} w_{sR}}\right]\left(\frac{p_{k,zD}}{\bar{\bar{\rho}}_{sD}}\right)\frac{\partial \phi_D}{\partial z_D} + \left[\frac{\mu_{sR} t_R}{r_R^2 \bar{\bar{\rho}}_{sR} \phi_R}\right]\left(\frac{1}{\bar{\bar{\rho}}_{sD}}\right)\frac{1}{r_D}\frac{\partial}{\partial r_D}\left(-r_D \mu_{sD}\frac{\partial w_{sD}}{\partial r_D}\right)$$
$$+\left[\frac{\mu_{sR} t_R}{z_R^2 \bar{\bar{\rho}}_{sR} \phi_R}\right]\left(\frac{1}{\bar{\bar{\rho}}_{sD}}\right)\frac{\partial}{\partial z_D}\left(\mu_{sD}\frac{\partial w_{sD}}{\partial z_D}\right) - \left[\frac{(\phi_R q_R)^{*}_{in.} t_R}{\phi_R}\right](\phi_D q_D)^{*}_{in.} w_{sD} - \left[\frac{t_R \beta_{zR}}{\phi_R \bar{\bar{\rho}}_{sR}}\frac{(\Delta w)_R}{w_{sR}}\right]\frac{\beta_{zD}}{\bar{\bar{\rho}}_{sD}}(\Delta w)_D$$

(5.18)

There are altogether 41 dimensionless similarity groups (square-bracket coefficients in the mass and momentum conservation equations), one of which is the reciprocal of another (group # 3 of the mass conservation equation for the fluid phase and group # 1 of the momentum conservation equation along the radial direction for the fluid phase). In addition, there are twelve groups that are repeated twice. As a result, there are 28 independent dimensionless similarity groups, as shown in Table 5.1 below.

Table 5.1: Dimensionless Similarity Groups from Inspectional Analysis
for the Two-dimensional Model

$$\left[\frac{r_R w_{fR}}{z_R u_{fR}}\right], \left[\frac{r_R(\varepsilon_R q_R)^{*}_{in.}}{\varepsilon_R u_{fR}}\right], \left[\frac{r_R}{t_R u_{fR}}\right], \left[\frac{r_R w_{sR}}{z_R u_{sR}}\right], \left[\frac{r_R(\phi_R q_R)^{*}_{in.}}{\phi_R u_{sR}}\right], \left[\frac{r_R}{u_{sR} t_R}\right], \left[\frac{t_R w_{fR}}{z_R}\right], \left[\frac{t_R p_{fR}}{\overline{\rho_{fR}} r_R u_{fR}}\right],$$

$$\left[\frac{\mu_{fR} t_R}{\varepsilon_R z_R^2 \overline{\rho_{fR}}}\right], \left[\frac{(\varepsilon_R q_R)^{*}_{in.} t_R}{\varepsilon_R}\right], \left[\frac{t_R g_R}{u_{fR}}\right], \left[\frac{3}{8} C_{LR} \frac{\phi_R}{\varepsilon_R} \frac{t_R[(-\Delta u)_R + \Delta v_R]^2}{u_{fR} a_R}\right], \left[\frac{t_R \beta_{rR}}{\varepsilon_R \overline{\rho_{fR}}} \cdot \frac{(\Delta u)_R}{u_{fR}}\right],$$

$$\left[\frac{t_R \beta_{zR}}{\varepsilon_R \overline{\rho_{fR}}} \frac{(\Delta w)_R}{w_{fR}}\right], \left[\frac{t_R w_{sR}}{z_R}\right], \left[\frac{t_R p_{sR}}{u_{sR} r_R \overline{\rho_{sR}}}\right], \left[\frac{t_R p_{k,rR}}{u_{sR} r_R \overline{\rho_{sR}}}\right], \left[\frac{t_R p_{k,zR}}{w_{sR} z_R \overline{\rho_{sR}}}\right], \left[\frac{\mu_{sR} t_R}{\overline{\rho_{sR}} r_R^2 \phi_R}\right], \left[\frac{\mu_{sR} t_R}{\overline{\rho_{sR}} z_R^2 \phi_R}\right],$$

$$\left[\frac{(\phi_R q_R)^{*}_{in.} t_R}{\phi_R}\right], \left[\frac{3}{8} C_{LR} t_R \frac{[(-\Delta u)_R + (\Delta v)_R]^2}{u_{sR} a_R}\right], \left[\frac{t_R g_R}{u_{sR}}\right], \left[\frac{\beta_{rR}}{\overline{\rho_{sR}}} (\Delta u)_R\right], \left[\frac{t_R p_{sR}}{z_R \overline{\rho_{sR}} w_{sR}}\right],$$

$$\left[\frac{\mu_{fR} t_R}{\varepsilon_R r_R^2 \overline{\rho_{fR}}}\right], \left[\frac{t_R p_{fR}}{w_{fR} z_R \overline{\rho_{fR}}}\right], \left[\frac{t_R \beta_{zR}}{\phi_R \overline{\rho_{sR}}} \frac{(\Delta w)_R}{w_{sR}}\right]$$

In brief, 28 dimensionless similarity groups are obtained from applying Inspectional Analysis to the system of governing equations for the two-dimensional transport of oil and sand in a horizontal well.

5.2.2. Dimensional Analysis

A careful examination of the governing differential equations used above in Inspectional Analysis reveals that there are altogether 28 variables involved in the flow of oil and sand in a horizontal well. This is expressed, mathematically, as follows

$$f = f\Big(r, z, t, \phi, \varepsilon, u_f, u_s, w_f, w_s, \overset{*}{\phi}_{in.}, \overset{*}{\varepsilon}_{in.}, \overset{*}{q}_{in.}, \overline{\rho_f}, \overline{\rho_s}, \mu_f, \mu_s, g, a, \beta_r, \beta_z, C_L,$$
$$\Delta v, \Delta u, \Delta w, p_f, p_s, p_{k,r} p_{k,z}\Big) \qquad (5.19)$$

The meaning of these variables are given in the Nomenclature. Three of these variables are selected for the three fundamental dimensions of mass, length, and time such that no two of these variables have the same dimensions, and the fundamental dimensions occur in the combination of the three variables. They are: solid phase velocity along the radial direction u_s , radial distance

r, and solid phase material density $\overline{\rho_s}$. Applying the Buckingham π-theorem the following equations are obtained,

$$\pi_1 : u_s^{aa} r^{ab} \overline{\rho_s}^{ac} z = M^0 L^0 t^0 \Rightarrow L^{aa} t^{-aa} L^{ab} M^{ac} L^{-3ac} L^1 = M^0 L^0 t^0 \tag{5.20a}$$

$$\pi_2 : u_s^{ba} r^{bb} \overline{\rho_s}^{bc} t = M^0 L^0 t^0 \Rightarrow L^{ba} t^{-ba} L^{bb} M^{bc} L^{-3bc} t^1 = M^0 L^0 t^0 \tag{5.20b}$$

$$\pi_3 : u_s^{ca} r^{cb} \overline{\rho_s}^{cc} \phi = M^0 L^0 t^0 \Rightarrow L^{ca} t^{-ca} L^{cb} M^{cc} L^{-3cc} = M^0 L^0 t^0 \tag{5.20c}$$

$$\pi_4 : u_s^{da} r^{db} \overline{\rho_s}^{dc} \varepsilon = M^0 L^0 t^0 \Rightarrow L^{da} t^{-da} L^{db} M^{dc} L^{-3dc} = M^0 L^0 t^0 \tag{5.20d}$$

$$\pi_5 : u_s^{ea} r^{eb} \overline{\rho_s}^{ec} u_f = M^0 L^0 t^0 \Rightarrow L^{ea} t^{-ea} L^{eb} M^{ec} L^{-3ec} L^1 t^{-1} = M^0 L^0 t^0 \tag{5.20e}$$

$$\pi_6 : u_s^{ga} r^{gb} \overline{\rho_s}^{gc} w_f = M^0 L^0 t^0 \Rightarrow L^{ga} t^{-ga} L^{gb} M^{gc} L^{-3gc} L^1 t^{-1} = M^0 L^0 t^0 \tag{5.20f}$$

$$\pi_7 : u_s^{ha} r^{hb} \overline{\rho_s}^{hc} w_s = M^0 L^0 t^0 \Rightarrow L^{ha} t^{-ha} L^{hb} M^{hc} L^{-3hc} L^1 t^{-1} = M^0 L^0 t^0 \tag{5.20g}$$

$$\pi_8 : u_s^{ia} r^{ib} \overline{\rho_s}^{ic} \dot{\phi}_{in.} = M^0 L^0 t^0 \Rightarrow L^{ia} t^{-ia} L^{ib} M^{ic} L^{-3ic} = M^0 L^0 t^0 \tag{5.20h}$$

$$\pi_9 : u_s^{ja} r^{jb} \overline{\rho_s}^{jc} \dot{\varepsilon}_{in.} = M^0 L^0 t^0 \Rightarrow L^{ja} t^{-ja} L^{jb} M^{jc} L^{-3jc} = M^0 L^0 t^0 \tag{5.20i}$$

$$\pi_{10} : u_s^{ka} r^{kb} \overline{\rho_s}^{kc} \dot{q}_{in.} = M^0 L^0 t^0 \Rightarrow L^{ka} t^{-ka} L^{kb} M^{kc} L^{-3kc} t^{-1} = M^0 L^0 t^0 \tag{5.20j}$$

$$\pi_{11} : u_s^{ma} r^{mb} \overline{\rho_s}^{mc} \overline{\rho_f} = M^0 L^0 t^0 \Rightarrow L^{ma} t^{-ma} L^{mb} M^{mc} L^{-3mc} M^1 L^{-3} = M^0 L^0 t^0 \tag{5.20k}$$

$$\pi_{12} : u_s^{na} r^{nb} \overline{\rho_s}^{nc} \mu_f = M^0 L^0 t^0 \Rightarrow L^{na} t^{-na} L^{nb} M^{nc} L^{-3nc} M^1 L^{-1} t^{-1} = M^0 L^0 t^0 \tag{5.20l}$$

$$\pi_{13} : u_s^{oa} r^{ob} \overline{\rho_s}^{oc} \mu_s = M^0 L^0 t^0 \Rightarrow L^{oa} t^{-oa} L^{ob} M^{oc} L^{-3oc} M^1 L^{-1} t^{-1} = M^0 L^0 t^0 \tag{5.20m}$$

$$\pi_{14} : u_s^{pa} r^{pb} \overline{\rho_s}^{pc} g = M^0 L^0 t^0 \Rightarrow L^{pa} t^{-pa} L^{pb} M^{pc} L^{-3pc} L^1 t^{-2} = M^0 L^0 t^0 \tag{5.20n}$$

$$\pi_{15} : u_s^{qa} r^{qb} \overline{\rho_s}^{qc} a = M^0 L^0 t^0 \Rightarrow L^{qa} t^{-qa} L^{qb} M^{qc} L^{-3qc} L^1 = M^0 L^0 t^0 \tag{5.20o}$$

$$\pi_{16} : u_s^{ra} r^{rb} \overline{\rho_s}^{rc} \beta_r = M^0 L^0 t^0 \Rightarrow L^{ra} t^{-ra} L^{rb} M^{rc} L^{-3rc} M^1 L^{-3} t^{-1} = M^0 L^0 t^0 \tag{5.20p}$$

$$\pi_{17} : u_s^{sa} r^{sb} \overline{\rho_s}^{sc} \beta_z = M^0 L^0 t^0 \Rightarrow L^{sa} t^{-sa} L^{sb} M^{sc} L^{-3sc} M^1 L^{-3} t^{-1} = M^0 L^0 t^0 \tag{5.20q}$$

$$\pi_{18} : u_s^{ta} r^{tb} \overline{\rho_s}^{tc} C_L = M^0 L^0 t^0 \Rightarrow L^{ta} t^{-ta} L^{tb} M^{tc} L^{-3tc} = M^0 L^0 t^0 \tag{5.20r}$$

$$\pi_{19} : u_s^{ua} r^{ub} \overline{\rho_s}^{uc} (\Delta v) = M^0 L^0 t^0 \Rightarrow L^{ua} t^{-ua} L^{ub} M^{uc} L^{-3uc} L^1 t^{-1} = M^0 L^0 t^0 \tag{5.20s}$$

$$\pi_{20} : u_s^{va} r^{vb} \overline{\rho_s}^{vc} (\Delta u) = M^0 L^0 t^0 \Rightarrow L^{va} t^{-va} L^{vb} M^{vc} L^{-3vc} L^1 t^{-1} = M^0 L^0 t^0 \tag{5.20t}$$

$$\pi_{21} : u_s^{wa} r^{wb} \overline{\rho_s}^{wc} (\Delta w) = M^0 L^0 t^0 \Rightarrow L^{wa} t^{-wa} L^{wb} M^{wc} L^{-3wc} L^1 t^{-1} = M^0 L^0 t^0 \tag{5.20u}$$

$$\pi_{22} : u_s^{xa} r^{xb} \overline{\rho_s}^{xc} p_f = M^0 L^0 t^0 \Rightarrow L^{xa} t^{-xa} L^{xb} M^{xc} L^{-3xc} M^1 L^{-1} t^{-2} = M^0 L^0 t^0 \tag{5.20v}$$

$$\pi_{23} : u_s^{ya} r^{yb} \overline{\rho_s}^{yc} p_s = M^0 L^0 t^0 \Rightarrow L^{ya} t^{-ya} L^{yb} M^{yc} L^{-3yc} M^1 L^{-1} t^{-2} = M^0 L^0 t^0 \tag{5.20w}$$

$$\pi_{24} : u_s^{za} r^{zb} \overline{\rho_s}^{zc} p_{k,r} = M^0 L^0 t^0 \Rightarrow L^{za} t^{-za} L^{zb} M^{zc} L^{-3zc} M^1 L^{-1} t^{-2} = M^0 L^0 t^0 \tag{5.20x}$$

$$\pi_{25} : u_s^{za} r^{zb} \overline{\rho_s}^{zc} p_{k,z} = M^0 L^0 t^0 \Rightarrow L^{za} t^{-za} L^{zb} M^{zc} L^{-3zc} M^1 L^{-1} t^{-2} = M^0 L^0 t^0 \tag{5.20y}$$

The π-groups are determined by solving for values of the various exponents appearing in the equations for each of the three fundamental dimensions. A example is given below for the fluid phase pressure π-group, i.e. π_{22}:

$$L : xa + xb - 3xc - 1 = 0 \Rightarrow (3) : xb = 0$$
$$M : xc + 1 = 0 \Rightarrow (1) : xc = -1$$
$$t : -xa - 2 = 0 \Rightarrow (2) : xa = -2$$

Hence,

$$\pi_{22} : u_s^{xa} r^{xb} \overline{\rho_s}^{xc} p_f^{xd} = u_s^{-2} r^0 \overline{\rho_s}^{-1} p_f^1 \therefore \pi_{22} = \frac{p_f}{u_s^2 \overline{\rho_s}}$$

The other π-groups are similarly determined, and they are given in Table 5.2 below.

Table 5.2: Dimensionless Similarity Groups from Dimensional Analysis
for the Two-dimensional Model

$$\frac{z}{r}, \frac{u_s t}{r}, \phi, \varepsilon, \frac{u_f}{u_s}, \frac{w_f}{u_s}, \dot{\phi}_{in.}, \dot{\varepsilon}_{in.}, \frac{\dot{q}_{in.} r}{u_s}, \frac{w_s}{u_s}, \frac{\overline{\rho_s}}{\overline{\rho_f}}, \frac{p_f}{u_s^2 \overline{\rho_s}}, \frac{r \overline{\rho_s} u_s}{\mu_f},$$

$$\frac{u_s r \overline{\rho_s}}{\mu_s}, \frac{rg}{u_s^2}, \frac{\beta_r r}{\overline{\rho_s} u_s}, C_L, \frac{\Delta u}{u_s}, \frac{\Delta v}{u_s}, \frac{\Delta w}{u_s}, \frac{a}{r}, \frac{\beta_z r}{\overline{\rho_s} u_s}, \frac{p_s}{u_s^2 \overline{\rho_s}}, \frac{p_{k,r}}{u_s^2 \overline{\rho_s}}, \frac{p_{k,z}}{u_s^2 \overline{\rho_s}},$$

In this case Inspectional Analysis is seen to yield more dimensionless similarity groups than Dimensional Analysis. Comparing the two sets of dimensionless (similarity) groups it is seen that first, the physical meaning for the dimensionless groups obtained by Inspectional Analysis is more clear; second, there are groups which appear in one set but not the other set, and vice versa. With regard to the first observation, the origin of the dimensionless groups obtained by Inspectional Analysis is from the conservation equations. As a result, the physical meaning of the different ratios represented by the dimensionless similarity groups is readily determined. On the other hand, the dimensionless similarity groups obtained by Dimensional Analysis are the result of a series of manipulations of the dimensions of the different variables involved in the transport process. As such, their origin is uncertain. With regard to the second observation, the π-groups obtained from Dimensional Analysis can be easily and readily rearranged to produce groups identical to those appearing in the set of dimensionless similarity groups obtained from Inspectional Analysis, as shown below. The dimensionless similarity groups are further combined and rearranged to produce a final set of 32 scaling criteria for the transport of oil and sand in a horizontal well. Table 5.3 presents these 33 scaling criteria, and also explains their physical meaning.

Table 5.3: Physical Meaning of Scaling Criteria for Two-dimensional Model

z/r	ratio of geometrical dimensions (axial length to radial length)
a/r	ratio of particle dimension (sphere radius) to horizontal well dimension
$\left[\left((\phi q)^{*}_{in.} r\right)/(\phi u_s)\right]$	relating solid phase concentration at a radial distance with solid phase concentration due to flux along the radial direction
$\left[(u_f t)/r\right]$	Courant Number for fluid phase relating radial distance traversed per time with radial dimension of system
$\left[(p_f t)/(r u_f \overline{\rho_f})\right]$	ratio of motivational (pressure) force to fluid phase inertia force along the radial direction

Table 5.3: Physical Meanings of Scaling Criteria for Two-dimensional Model (continued)

$\left[(p_f)/(u_f^2\overline{\rho_f})\right]$	ratio of motivational (pressure) force to fluid phase kinetic energy along the radial direction {similar to Euler Number, or Pressure Coefficient}
$\left[(ru_f\varepsilon\overline{\rho_f})/(\mu_f)\right]$	ratio of fluid phase inertia force to viscous force along the radial direction {similar to Reynolds Number}
$\left[(r^2\beta_r(\Delta u))/(\mu_f u_f)\right]$	ratio of interphase momentum transfer to fluid phase viscous force along the radial direction {analogous to Momentum Transfer Number in Refs. 77-82}
$\left[(C_L\phi t(\Delta u+\Delta v)^2)/(\varepsilon a u_f)\right]$	ratio of lift force acting on solid particles due to fluid shear to solid phase inertia force
$\left[(gt)/(u_f)\right]$	ratio of velocity due to gravitational acceleration to fluid phase velocity
$\left[(C_L\phi(\Delta u+\Delta v)^2)/(\varepsilon a g)\right]$	ratio of lift force acting on solid particles due to fluid shear to gravitational force acting on solid particles
$\left[(p_f t)/(zw_f\overline{\rho_f})\right]$	ratio of motivational (pressure) force to fluid phase inertia force along the axial direction
$\left[(p_f)/(u_f^2\overline{\rho_f})\right]$	ratio of motivational (pressure) force to fluid phase kinetic energy along the axial direction {similar to Euler Number, or Pressure Coefficient}
$\left[(zw_f\varepsilon\overline{\rho_f})/(\mu_f)\right]$	ratio of fluid phase inertia force to viscous force along the axial direction {similar to Reynolds Number}

Table 5.3: Physical Meanings of Scaling Criteria for Two-dimensional Model (continued)

$\left[\left(z^2\beta_z(\Delta w)\right)/\left(\mu_f w_f\right)\right]$	ratio of interphase momentum transfer to fluid phase viscous force along axial direction {analogous to Momentum Transfer Number in Refs. 77-82}
$\left[\left(z^2\beta_z(\Delta w)u_f\right)/\left(r^2\beta_r(\Delta u)w_f\right)\right]$	ratio of interphase momentum transfer along the axial direction to interphase momentum transfer along the radial direction
$\left[\left(u_s t\right)/r\right]$	Courant Number for solid phase relating radial distance traversed per time with radial dimension of system
$\left[\left(p_s t\right)/\left(r u_s \overline{\rho_s}\right)\right]$	ratio of motivational (pressure) force to solid phase inertia force along the radial direction
$\left[\left(p_s u_f \overline{\rho_f}\right)/\left(p_f u_s \overline{\rho_s}\right)\right]$	ratio of motivational (pressure) force to inertia force for solid phase to that for fluid phase along the radial direction
$\left[\left(p_{k,r} t\right)/\left(r u_s \overline{\rho_s}\right)\right]$	ratio of kinematic pressure to solid phase inertial force along the radial direction
$p_{k,r} / p_s$	ratio of kinematic pressure to solid phase pressure along the radial direction
$\left[\left(z w_s \phi \overline{\rho_s}\right)/\left(\mu_s\right)\right]$	ratio of solid phase inertia force to solid phase viscous force along the axial direction {similar to Reynolds Number}
$\left[\left(r u_s \phi \overline{\rho_s}\right)/\left(\mu_s\right)\right]$	ratio of solid phase inertia force to solid phase viscous force along the radial direction {similar to Reynolds Number}

Table 5.3: Physical Meanings of Scaling Criteria for Two-dimensional Model (continued)

$\left[\left(\varepsilon\overline{\rho_f}\mu_s\right)/\left(\mu_f\phi\overline{\rho_s}\right)\right]$	ratio of solid phase viscosity to fluid phase viscosity
$\left[\left(p_{k,r}r\phi\right)/\left(\mu_s u_s\right)\right]$	ratio of kinematic pressure to solid phase viscous force
$\left[(gt)/(u_s)\right]$	ratio of velocity due to gravitational acceleration to solid phase velocity
$\left[\left(C_L t(\Delta u+\Delta v)^2\right)/(au_s)\right]$	ratio of lift force acting on solid particles due to fluid shear to solid phase inertia
$\left[\left(C_L(\Delta u+\Delta v)^2\right)/(ag)\right]$	ratio of lift force acting on solid particles due to fluid shear to gravitational force acting on solid phase
$\left[\left(C_L r(\Delta u+\Delta v)^2\right)/\left(au_s^2\right)\right]$	ratio of lift force acting on solid particles due to fluid shear to solid phase kinetic energy
$\left[\left(p_s t\right)/\left(zw_s\overline{\rho_s}\right)\right]$	ratio of motivational (pressure) force to solid phase inertia force along the axial direction
$\left[\left(p_{k,z}\phi z\right)/\left(\mu_s w_s\right)\right]$	ratio of kinematic pressure force to solid phase viscous force
$\left[\left(p_s\phi\right)/\left(z\beta_z(\Delta w)\right)\right]$	ratio of motivational (pressure) force to the interphase momentum transfer along the axial direction

As stated above, the π-groups obtained from Dimensional Analysis can be easily and readily rearranged and combined to produce the scaling criteria given in Table 5.3 (or the dimensionless similarity groups obtained by Inspectional Analysis whence the scaling criteria are derived). For example, the last scaling criterion in Table 5.3 which relates the motivational force to the interphase momentum transfer along the axial direction, $\left[\phi p_s/\left\{z\beta_z\left(w_f-w_s\right)\right\}\right]$, is obtained by combining the following dimensionless π-groups: $\pi_1, \pi_3, \pi_{19}, \pi_{21}, \pi_{22}$, as illustrated below

$$\frac{\phi p_s}{z\beta_z(w_f - w_s)} \Leftarrow \frac{p_s}{\overline{\rho_s} u_s^2} \cdot \phi \cdot \frac{\overline{\rho_s} u_s}{\beta_z r} \cdot \frac{r}{z} \cdot \frac{u_s}{(w_f - w_s)}$$

$$\frac{\phi p_s}{z\beta_z(w_f - w_s)} = \pi_{22} \cdot \pi_3 \cdot \frac{1}{\pi_{21}} \cdot \frac{1}{\pi_1} \cdot \frac{1}{\pi_{19}}$$

5.3. One-dimensional Models

Applying the same techniques to the two one-dimensional models modelling the transport of oil and sand in a horizontal well leads to the following results,

5.3.1. Givler & Mikatarian's Constriction Model

* Inspectional Analysis

In this case the system of governing equations consists of the mass conservation equations for the fluid and solid phases (Equations 4.31-4.32) and the momentum conservation equations (Equations 4.33-4.34). There are 11 dimensionless similarity groups, two of which appear twice. As a result, there are nine unique dimensionless groups; and, they are given in Table 5.4.

Table 5.4: Dimensionless Similarity Groups from Inspectional Analysis for the One-dimensional Constriction Model

$$\frac{w_{fR} t_R}{z_R}, \frac{w_{sR} t_R}{z_R}, \frac{p_{fR} t_R}{z_R \overline{\rho_{fR}} w_{fR}}, \frac{g_R t_R}{w_{fR}}, \frac{\beta_R t_R (w_{fR} - w_{sR})}{\varepsilon_R \overline{\rho_{fR}} w_{fR}}, \frac{p_{sR} t_R}{z_R \overline{\rho_{sR}} w_{sR}}, \frac{p_{kR} t_R}{z_R \overline{\rho_{sR}} w_{sR}},$$

$$\frac{g_R t_R}{w_{sR}}, \frac{\beta_R t_R (w_{fR} - w_{sR})}{\phi_R \overline{\rho_{fR}} w_{sR}}$$

* Dimensional Analysis

For the constriction model, the transport process is expressed as follows,

$$f = f(\phi, \varepsilon, z, t, w_f, w_s, \overline{\rho_f}, \overline{\rho_s}, g, \beta . p_f, p_s, p_k) \qquad (5.21)$$

Selecting the axial distance z, fluid phase velocity w_f, and solid phase material density $\overline{\rho_s}$ for the three primary dimensions of mass, length, and time, the remaining ten π-groups are derived. They are presented in Table 5.5.

Table 5.5: Dimensionless Similarity Groups from Dimensional Analysis for the One-dimensional Constriction Model

$$\varepsilon, \phi, \frac{w_f t}{z}, \frac{w_s}{w_f}, \frac{\overline{\rho_s}}{\overline{\overline{\rho_f}}}, \frac{p_f}{w_f^2 \overline{\overline{\rho_s}}}, \frac{p_s}{w_f^2 \overline{\overline{\rho_s}}}, \frac{p_k}{w_f^2 \overline{\overline{\rho_s}}}, \frac{z\beta}{w_f \overline{\overline{\rho_s}}}, \frac{gz}{w_f^2}$$

5.3.2. Gravity Deposition Model

* Inspectional Analysis

For the gravity deposition model the system of governing equations consists of the mass and momentum conservation equations for the fluid and solid phases (Equations 4.37 – 4.40) and the equation describing the change in height of the deposit bed with time (Equation 4.43). There are 14 dimensionless similarity groups, three of which appear twice. As a result, there are 11 unique dimensionless groups; and, they are given in Table 5.6.

Table 5.6: Dimensionless Similarity Groups from Inspectional Analysis for the One-dimensional Gravity Deposition Model

$$\frac{w_{fR} t_R}{z_R}, \frac{w_{sR} t_R}{z_R}, \frac{v_{crit.R} t_R}{h_R}, \frac{p_{fR} t_R}{z_R \overline{\rho_{fR}} w_{fR}}, \frac{g_R t_R}{w_{fR}}, \frac{\beta_R t_R \left(w_{fR} - w_{sR}\right)}{\varepsilon_R \overline{\rho_{fR}} w_{fR}}, \frac{p_{sR} t_R}{z_R \overline{\rho_{sR}} w_{sR}},$$

$$\frac{p_{kR} t_R}{z_R \overline{\rho_{sR}} w_{sR}}, \frac{g_R t_R}{w_{sR}}, \frac{\beta_R t_R \left(w_{fR} - w_{sR}\right)}{\phi_R \overline{\rho_{fR}} w_{sR}}, \frac{\phi_R v_{crit.R} t_R}{\phi_{crit.R} h_R}$$

* Dimensional Analysis

For the gravity deposition model, the transport process is expressed as follows,

$$f = f\left(\phi, \varepsilon, \phi_{crit.}, z, t, h, w_f, w_s, v_{crit.}, \overline{\rho_f}, \overline{\rho_s}, g, \beta, p_f, p_s, p_k\right) \tag{5.22}$$

The axial distance, fluid phase velocity, and solid phase material density are again selected for the three primary dimensions of mass, length, and time. The remaining 13 π-groups are illustrated in Table 5.7.

Table 5.7: Dimensionless Similarity Groups from Dimensional Analysis for the One-dimensional Gravity Deposition Model

$$\varepsilon, \phi, \phi_{crit.}, \frac{w_f t}{z}, \frac{w_s}{w_f}, \frac{v_{crit.}}{w_f}, \frac{h}{z}, \frac{\overline{\rho_s}}{\overline{\rho_f}}, \frac{p_f}{w_f^2 \overline{\rho_s}}, \frac{p_s}{w_f^2 \overline{\rho_s}}, \frac{p_k}{w_f^2 \overline{\rho_s}}, \frac{z\beta}{w_f \overline{\rho_s}}, \frac{gz}{w_f^2}$$

5.4. Concluding Remarks

Inspectional Analysis and Dimensional Analysis are used to obtain the dimensionless similarity groups characterizing the transport of oil and sand in a horizontal well. Three separate cases, corresponding to the three mathematical models developed in Chapter 4, are considered: two-dimensional transport, one-dimensional transport with a constriction of fixed profile and expansion rate, and one-dimensional transport with the sand deposition process occurring naturally (i.e. no *a priori* fixed constriction profile or expansion rate). The two-dimensional model is examined in depth, with the procedure and technique for both Inspectional Analysis and Dimensional Analysis being shown in detail. The physical meanings of the scaling criteria are also provided. For the one-dimensional models, the dimensionless similarity groups obtained from either of the two approaches are presented. The one-dimensional models are, except for some minor differences, sub-sets of the two-dimensional model. As such, their dimensionless similarity groups are similar to many of those obtained for the two-dimensional model. The scaling criteria developed for the two-dimensional model are, consequently, also valid for the one-dimensional models. In performing physical experiments of the transport process, scaling criteria containing the parameters governing the viscous force, inertial force, gravity force, and momentum transfer between the solid phase and the fluid phase are important. As such, those scaling criteria containing these parameters could be combined further into dimensionless numbers and used as correlation parameters/groups.

There are two important observations concerning the above development of scaling criteria to characterize the flow of oil and sand in a horizontal well. First, many variables are involved in the transport process – as reflected in the large number of scaling criteria obtained. Second, it is difficult to apply many of the scaling criteria directly. This difficulty arises primarily because many of these criteria contain variables whose values are very difficult to determine precisely, and hence to scale properly. A case in point is the interphase interaction coefficient, β, which is itself a function of many other variables including fluid phase and solid phase concentrations and their velocities, particle Reynolds Number, particle drag coefficient. Furthermore, these functions are often empirical correlations, and thus prove restrictive in terms of their application. More important is the fact that many of these empirical correlations are derived on a macroscopic basis of "averaged" flow conditions (for example, average mean stream velocity, and average pressure drop). To apply these macroscopic-scale correlations directly to describing the microscopic-scale process of momentum transfer between solid particles and the surrounding fluid is improper, to say the least. In other words, caution must be exercised in applying these scaling criteria to the design of multiphase flow experimental apparatus, and more important to the analysis of experimental results. It is believed that using the same fluids and solid particles in the model(s) and prototype(s) will eliminate these scale-inconsistency problems.

Chapter 6. Discussion of Results

Sand deposition inside a horizontal well presents a serious problem to its productivity. The deposition expands vertically and laterally with time, effectively reducing the cross-sectional area of the horizontal well open to flow, making it more and more difficult for fluids to be produced through. This study investigates the transport of oil and sand inside a horizontal well, with an emphasis on finding hydrodynamic conditions conducive to sand deposition and accumulation. Mathematical models – both one-dimensional and two-dimensional – of the transport process are presented in Chapter 4. The interaction of different variables involved in the transport process expressed in the form of dimensionless similarity groups are given in Chapter 5. Results of two one-dimensional numerical models simulating the transport of sand and oil inside a horizontal well are presented in this chapter.

6.1. Introduction

The chapter is divided into three sections. The first section examines in depth the Constriction model, including its results and applicability to study realistic flow problems. The second section provides a description of the results of the Gravity Deposition model, along with an examination of the effects of several variables on the formation and expansion of a deposit bed in the horizontal well. The last section examines the implications of various simulation results for field situations, as well as concluding remarks. Figure 6.1 shows the structure of this chapter.

6.2. Givler and Mikatarian's Constriction Model

As described in Section 4.3.2.1 this particular one-dimensional flow model examines the transport of solid particles and a Newtonian fluid in a horizontal channel which has a constriction along its length. The profile and expansion rate of the constriction are *a priori* prescribed. Two different cases are considered. In the first case, the results of a flow process dominated by pressure forces are obtained. In the second case, the interfacial drag force dominates the flow process. Table 6.1 provides data used in the simulation runs for these two cases. It is important to point out that there are no units accompanying the different variables in this table. The data are identical to those used by Givler et al. who, without actually providing any unit for these data, only mentioned that they are defined consistently with the cgs system of units [83]. Consequently, cgs units are attached to these numerical values to facilitate discussion in the following. This matter of units for the data used in the simulation runs is revisited later.

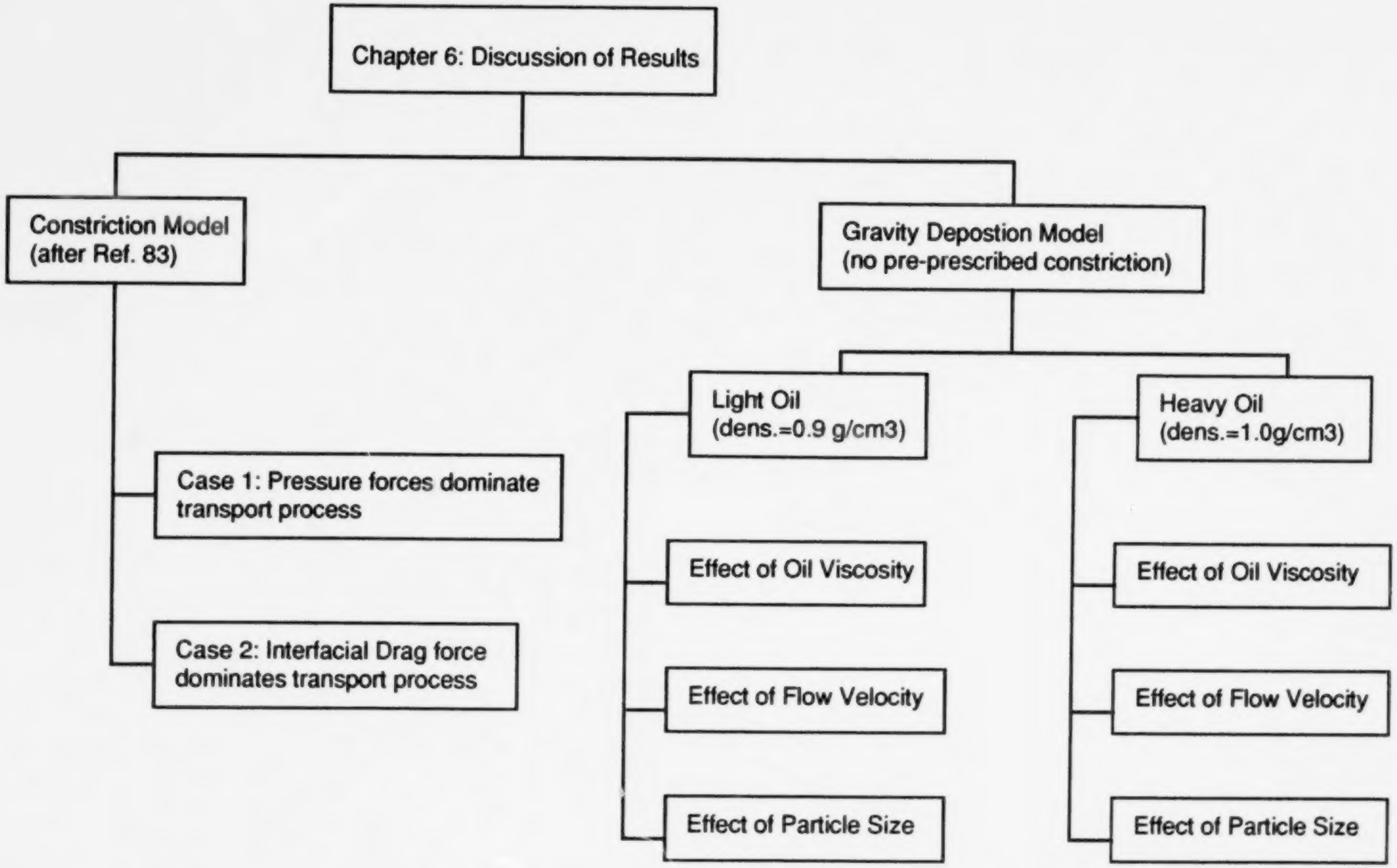
Chapter 6: Discussion of Results
Constriction Model
(after Ref. 83)
Gravity Depostion Model
(no pre-prescribed constriction)
Case 1: Pressure forces dominate transport process
Case 2: Interfacial Drag force dominates transport process
Light Oil
(dens.=0.9 g/cm3)
Heavy Oil
(dens.=1.0g/cm3)
Effect of Oil Viscosity
Effect of Flow Velocity
Effect of Particle Size
Effect of Oil Viscosity
Effect of Flow Velocity
Effect of Particle Size

Figure 6.1: Organization of Chapter 6.

Table 6.1: Data used in simulation runs for Constriction Model

Variable	Case 1	Case 2
Fluid phase velocity, w_f	1.0	1.0
Solid phase velocity, w_s	0.9	0.9
Solid phase concentration, ϕ	0.10	0.10
Solid phase pressure, p_s	1.0	1.0
Fluid phase viscosity, μ_f	0.00001	0.001
Solid particle diameter, d	0.05	0.01
Fluid phase material density, ρ_f	1.0	1.0
Solid phase material density, ρ_s	1.5	1.5

In this table, the values given for the fluid phase velocity, solid phase velocity, solid phase concentration, and solid phase pressure are for the initial conditions, as well as boundary conditions at the inlet and outlet of the flow channel.

As stated previously, an element of symmetry is considered with respect to the vertical plane splicing the horizontal flow channel into two halves. As such, the three-dimensional figures presented in this work (for example, Figures 6.2 – 6.7) display the profiles, against this plane of symmetry, of different variables as they change with time.

Figures 6.2 – 6.7 give the solid phase pressure (Figure 6.2), fluid phase pressure (Figure 6.3), kinematic pressure (Figure 6.4), solid phase concentration (Figure 6.5), solid phase velocity (Figure 6.6) and fluid phase velocity (Figure 6.7) for Case 1, when pressure forces dominate the flow process. Figures 6.8 – 6.13 illustrate the results for the same variables for Case 2, when the transport process is dominated by interfacial drag force. The results of these two cases are cross-compared in Figure 6.14 – 6.19 to examine the influence the pressure forces and the interfacial drag force have on the transport process, in particular the initiation of a particle plug.

6.2.1. Constriction Model – Flow Dominated by Pressure Forces

As stated above, Figures 6.2 – 6.7 illustrate the distribution of pressure and velocity for the solid phase and fluid phase, along with the solid phase concentration distribution and the profile for the kinematic pressure – all of which vary with time. As in Givler et al's study [83], the simulation run

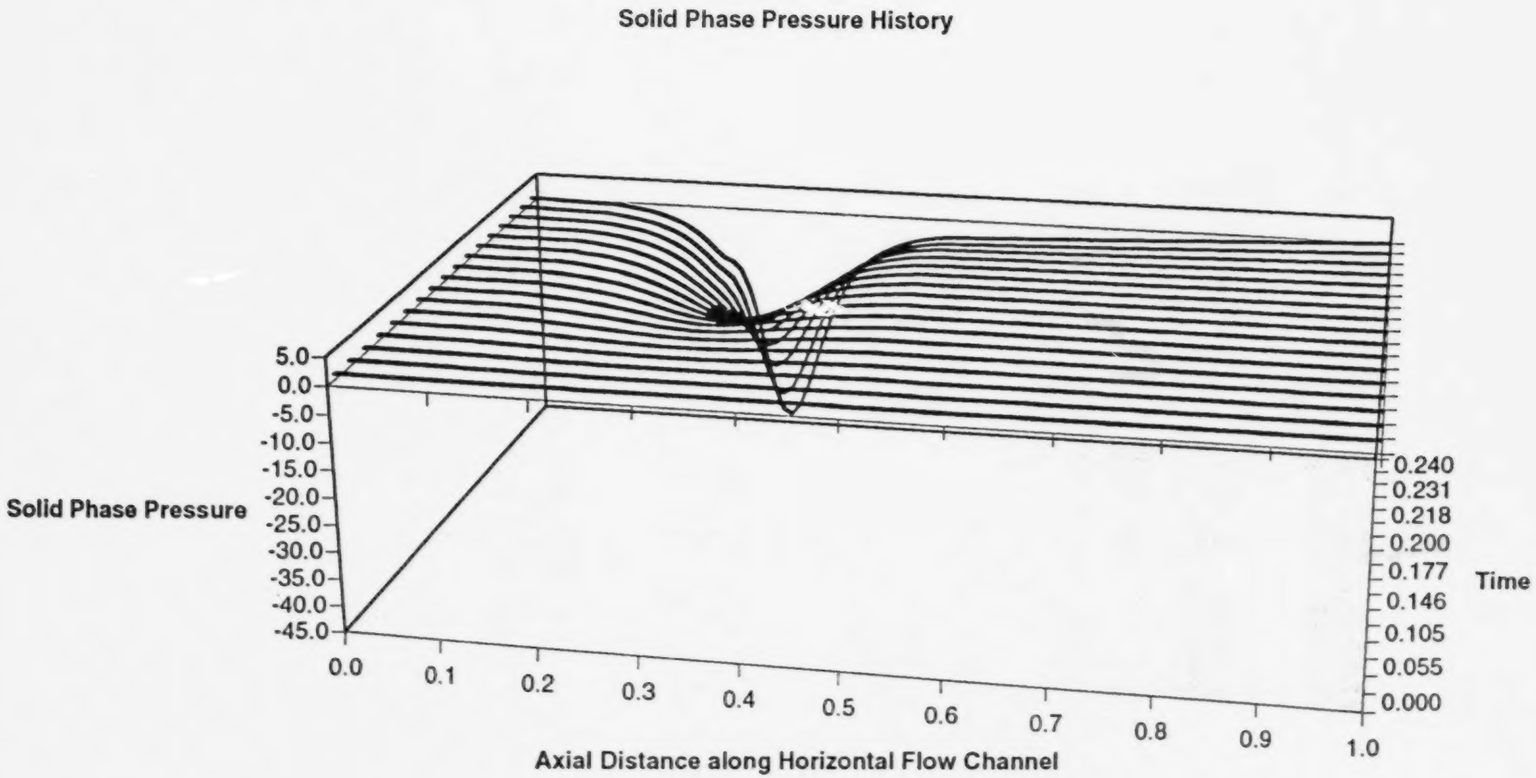

Figure 6.2: Constriction Model – Solid Phase Pressure Profile at different times for Case 1 (transport process dominated by Pressure Forces).

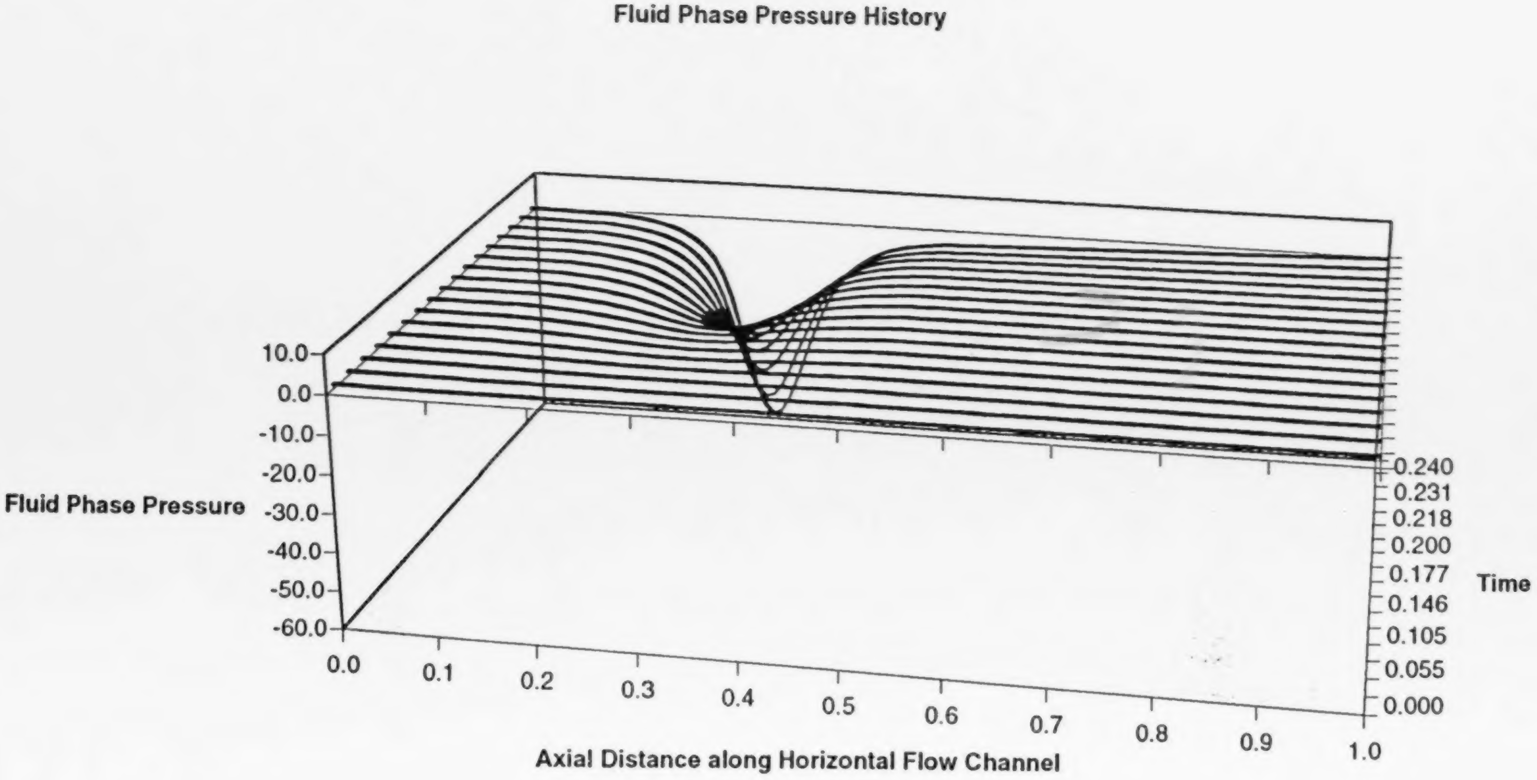

Figure 6.3: Constriction Model – Fluid Phase Pressure Profile at different times for Case 1 (transport process dominated by Pressure Forces).

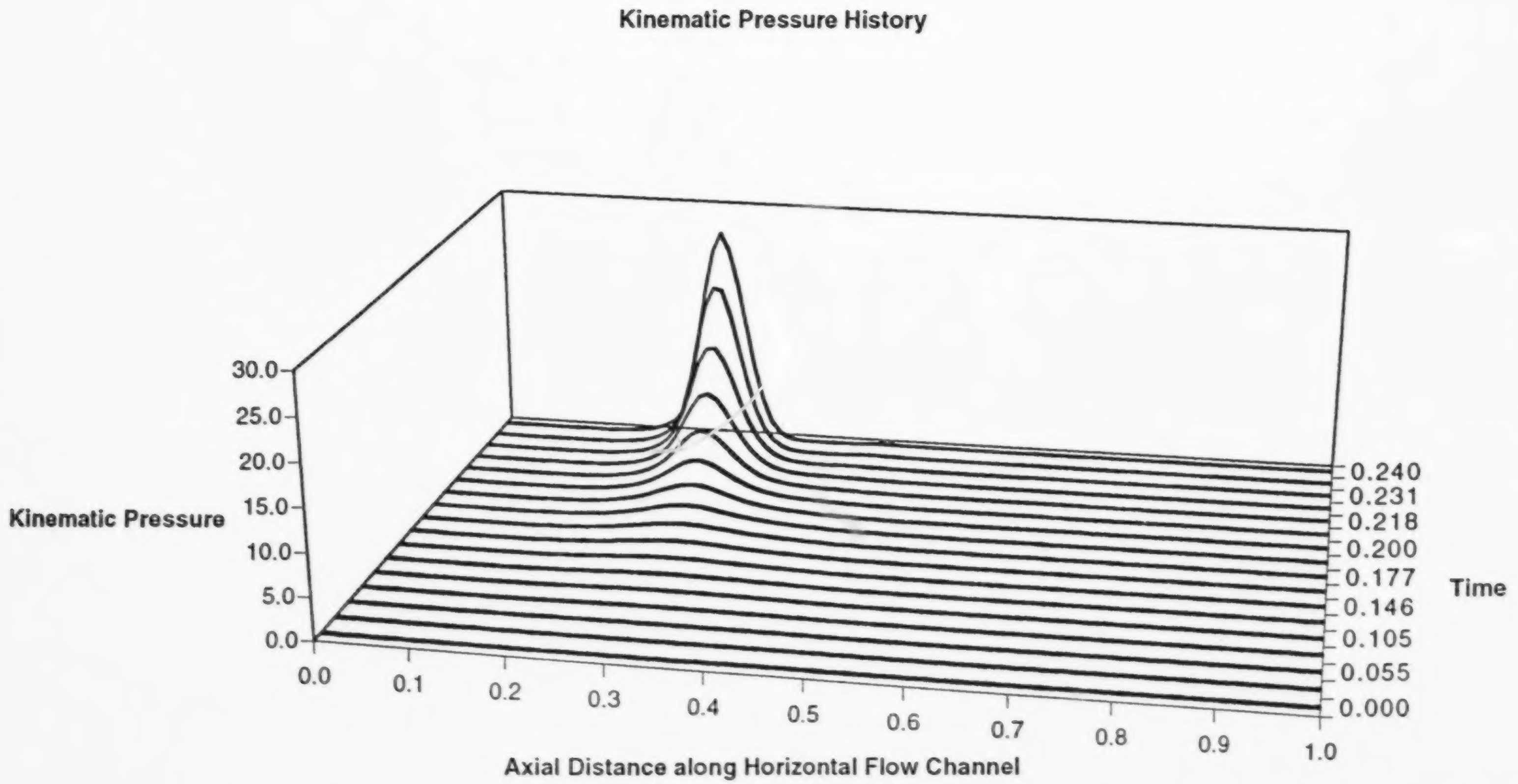

Figure 6.4: Constriction Model – Kinematic Pressure Profile at different times for Case 1 (transport process dominated by Pressure Forces).

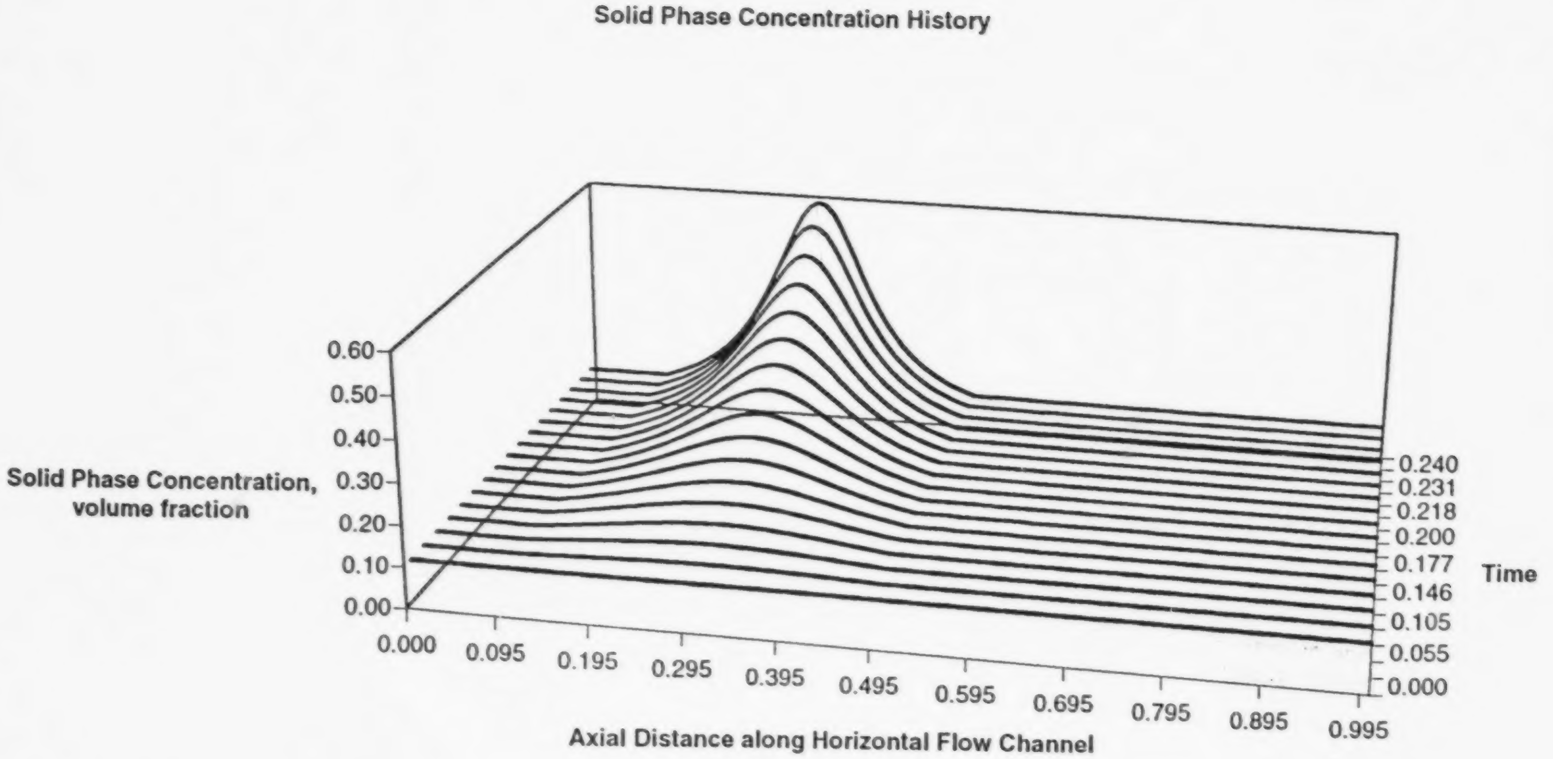

Figure 6.5: Constriction Model –Solid Phase Concentration Profile at different times for Case 1 (transport process dominated by Pressure Forces).

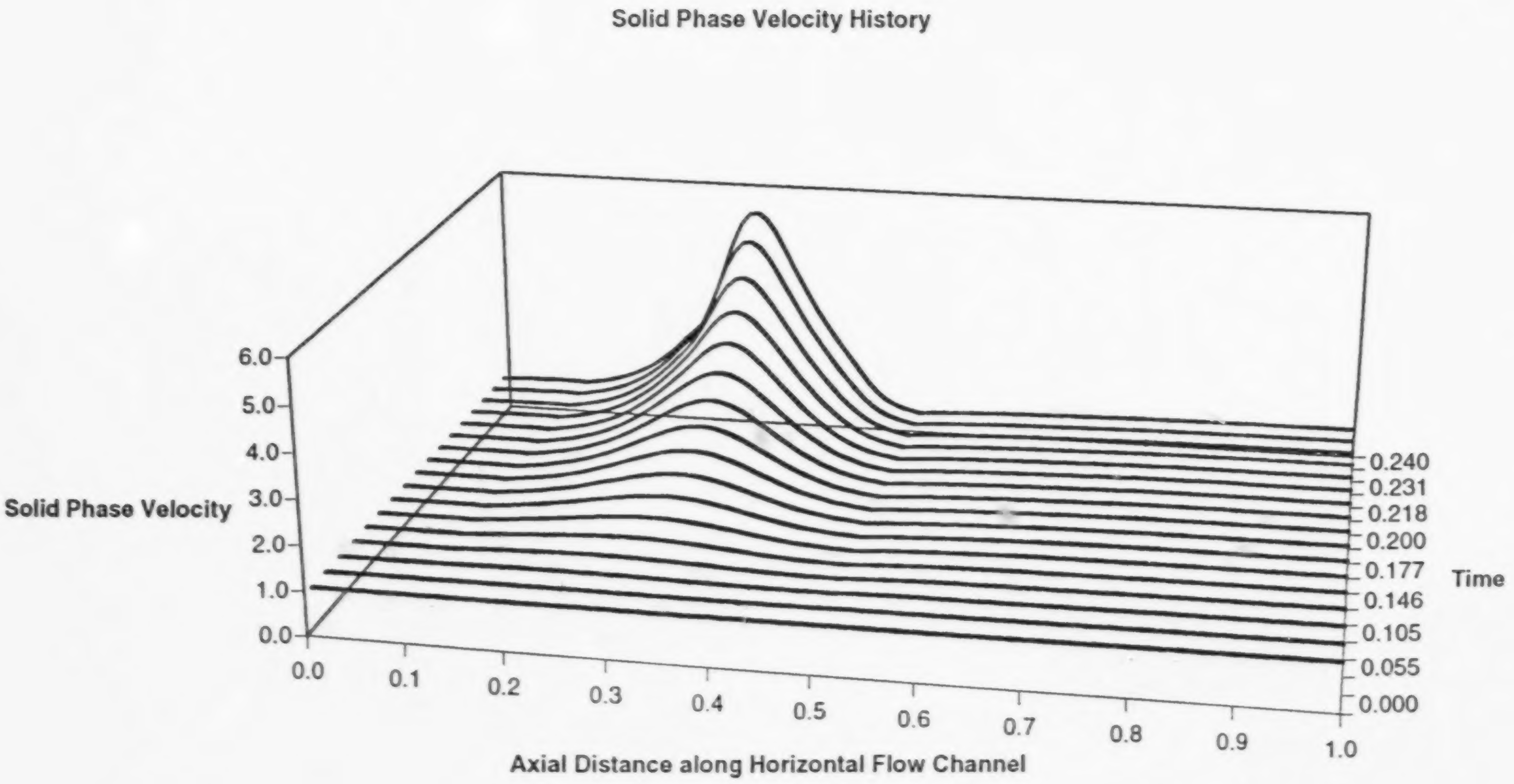

Figure 6.6: Constriction Model – Solid Phase Velocity Profile at different times for Case 1 (transport process dominated by Pressure Forces).

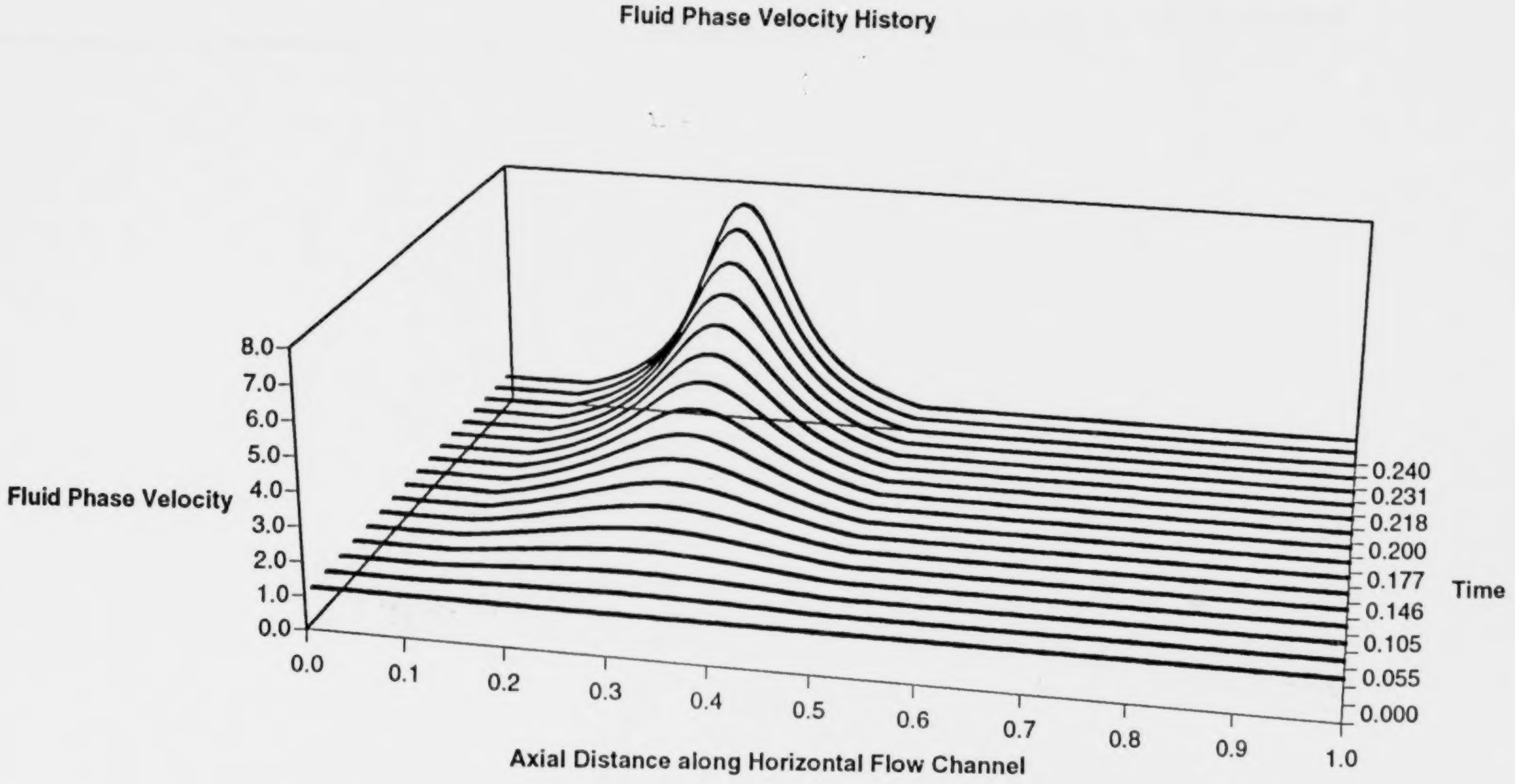

Figure 6.7: Constriction Model – Fluid Phase Velocity Profile at different times for Case 1 (transport process dominated by Pressure Forces).

lasted 0.24 second. The peak of the solid phase concentration "pulse" in the constriction (at n=30) reaches 0.60 (Figure 6.5) at the end of this time. Recalling Table 4.2, it is seen that the value of the function $h(\phi)$ starts to grow exponentially – when the solid phase concentration, ϕ, exceeds 0.60; this, in turn, leads to a corresponding exponential increase in the kinematic pressure. These exponential increases result in the "blowing up" of the numerical solution, given the fact that there is no upper bound in the value calculated for the kinematic pressure. This phenomenon – whose origin is, as stated above, in the empirical function examining the effect of solid particle concentration on particle-particle collisions – repeats itself in Case 2. There are no indications of instability, in the form of spurious oscillations, in any of the solutions.

Comparing these figures with those published in [83] it is seen that they all closely follow the same trends. In the case of the solid phase and the fluid phase velocities the curves produced in this investigation not only follow the same trends, but also match values closely with those given by Givler et al. [83]. For the other variables there are slight differences (approximately 10% or less) between the two sets of results. A possible explanation for these differences is the different numerical solution procedures and techniques used in this study, and [83]. Uncertainties about the physical meanings of the input data could also have easily contributed to these differences. Further elaboration on the second possibility is given below.

The solid phase pressure and fluid phase pressure both show little change for the first 0.10 second. Thereafter they both start to decline quickly – going from 0.0 to -50.0 g/cm.s^2 approximately, in the space of 0.14 second (Figures 6.2 and 6.3). The other four variables – kinematic pressure, solid phase concentration, solid phase velocity, and fluid phase velocity – all follow an opposite trend. Again, there is little change in these variables during the first 0.10 second, as in the case of the solid phase pressure and fluid phase pressure. Just as these two pressures start to decline, however, the above four variables start to increase. The most dramatic increase is in the kinematic pressure which goes from 0.0 initially to 25.0 g/cm.s^2 in 0.24 second. The fluid phase velocity increases from 1.0 to 7.5 cm/s, while the solid phase velocity goes from 0.9 to 6.0 cm/s. As such, the slip velocity (defined to be the difference between the fluid phase velocity and solid phase velocity) increases substantially with time – from 0.1 cm/s at the initial condition to 1.5 cm/s at the most constricted point. It is possible that as the solid particles come into frequent collisions with one another they lose their momentum (or more precisely, their velocity) – resulting, thus, in this increase in the slip velocity. For all six variables the changes, both increases and decreases, occur symmetrically with respect to the peak of their "pulses".

Givler et al. state that the increase in solid particle concentration is caused by a reduction in the fluid phase pressure through the constriction. Also, the solid phase concentration gradient becomes large at elevated solid phase concentrations, and tends to diffuse the concentration peak. This, in turn, results in a reduction in the peak solid phase velocity in the latter stage of the simulation run [83].

The decreasing trend seen in the solid phase and fluid phase pressures is analogous to the behaviour seen in the pressure distribution in a converging nozzle. Given the fact that in this case the constriction sharply reduces the cross-sectional area open to flow, this decreasing trend is therefore in a way anticipated. On the other hand, it is difficult, physically, to explain the negative values for both the solid phase and fluid phase pressures. It is recognized that the negative values for the solid phase and fluid phase pressures might have come about because the initial data were in some way normalized. As such, the negative pressures might not have been meant to be "absolutely negative" pressures, and might instead have described the "relative" reduction in the pressures with time compared to the normalized initial values. This question is investigated by examining different dimensionless similarity groups (or numbers) derived specifically for this purpose. No satisfactory explanations are obtained from this approach for the negative pressures.

Another possibility for this unconventional behaviour lies in the solid phase pressure equation derived for this model. It is important to remember that the pressure equation (in this case, for the solid phase), even though a part of the solution process, is not part of the (original) core of the mathematical model which consists only of mass and momentum conservation equations. During the derivation of this pressure equation errors might have been introduced – not in the calculus/algebraic sense, but in terms of "artificial mechanisms" alien to the actual transport process. It is also important to recall the solution procedure used for this model, which simultaneously solves the mass and momentum conservation equations for the solid phase prior to solving the pressure equation. Given the logical behaviour of the other four variables – including velocities – as elaborated below, it is felt that the problem probably arises from the numerical solution side (in terms of the solution sequence), and not from the introduction of additional artificial mechanisms into the transport process. The solid phase pressure equation, as derived above, appears similar (at least in general form) to many of the pressure equations derived by other investigators who applied the MAC method successfully for a variety of flow situations [115-125].

As for the other four variables, the large increase in the kinematic pressure is more easily explainable, and even anticipated to some degree. As stated above, the increase in the solid phase concentration inside the constricted region leads to more particle-particle collisions; and this increase in the kinetic (collision) energy is reflected in the exponential increase in the function $h(\phi)$ and correspondingly, in an increase in the kinematic pressure. The increase in the slip velocity between the two phases also contributes to this increase in the kinematic pressure. The increase in both the fluid phase and solid phase velocities is a direct consequence of the constricted area open to flow. The constriction forces the velocity streams for both phases to converge (resulting in more friction and a higher pressure loss) and then accelerate.

6.2.2. Constriction Model – Flow Dominated by Interfacial Drag Force

The primary differences between this case and the previous case are that the fluid phase is considerably less viscous (0.001 g/cm.s vs. 0.00001 g/cm.s), and the solid particles are smaller (0.01 cm vs. 0.5 cm) than the values used in Case 1. A lower fluid viscosity leads to, other parameters being the same, a higher particle Reynolds Number, a lower drag coefficient, and a lower interface interaction coefficient. A smaller particle diameter has the opposite effect, i.e. it leads to a lower Reynolds Number, and higher drag coefficient and interface interaction coefficient. As such, the effects of these two variables tend to compete against one another. When the solid concentration is larger than 20% volume fraction, the effects due to the smaller particle diameter become more significant compared to those due to the lower fluid viscosity, as shown by Equation 4.20a.

Givler et al. presented, for Case 2, the results for the solid phase concentration, solid phase and fluid phase velocities [83]. Comparing these with the profiles generated in this study, it is seen that they are to a very large degree identical to one another. Results for the solid phase and fluid phase pressures, and kinematic pressure cannot be similarly checked as they are not presented by Givler et al. [83].

Examining Figures 6.8 – 6.13 it is seen that the profiles for the six variables for this case are quite similar to those observed for Case 1, from the decreasing trend for the fluid phase and solid phase pressures to the increasing trend for the four remaining variables. The magnitudes of increase and decrease are, as expected, different for this case as compared to those for the previous case, for similar elapsed times. In addition, there is a sort of ripple forming at the (right) foot of the kinematic pressure pulse near the end of the simulation run (Figure 6.10). It is postulated that toward the later stage of the simulation run high solid phase concentration gradients at the most constricted position (n=30) lead to solid particles being diffused sideways, in the direction of (fluid) flow. When this happens, the solid phase concentration immediately downstream of the constriction starts to build up, the effect of which is the formation of a kinematic pressure wavelet. Had it been possible for the simulation run to continue longer, it would have been interesting to see if the second, smaller wavelet continues to grow and eventually merge with the first wave to form a larger wave. If this is the case, how would the growth of the second, smaller wavelet be affected by its proximity to the first wave ?

Snapshots of the numerical results for the two cases are taken at five different times, and cross-compared to determine the influence of the pressure forces and the interfacial drag force

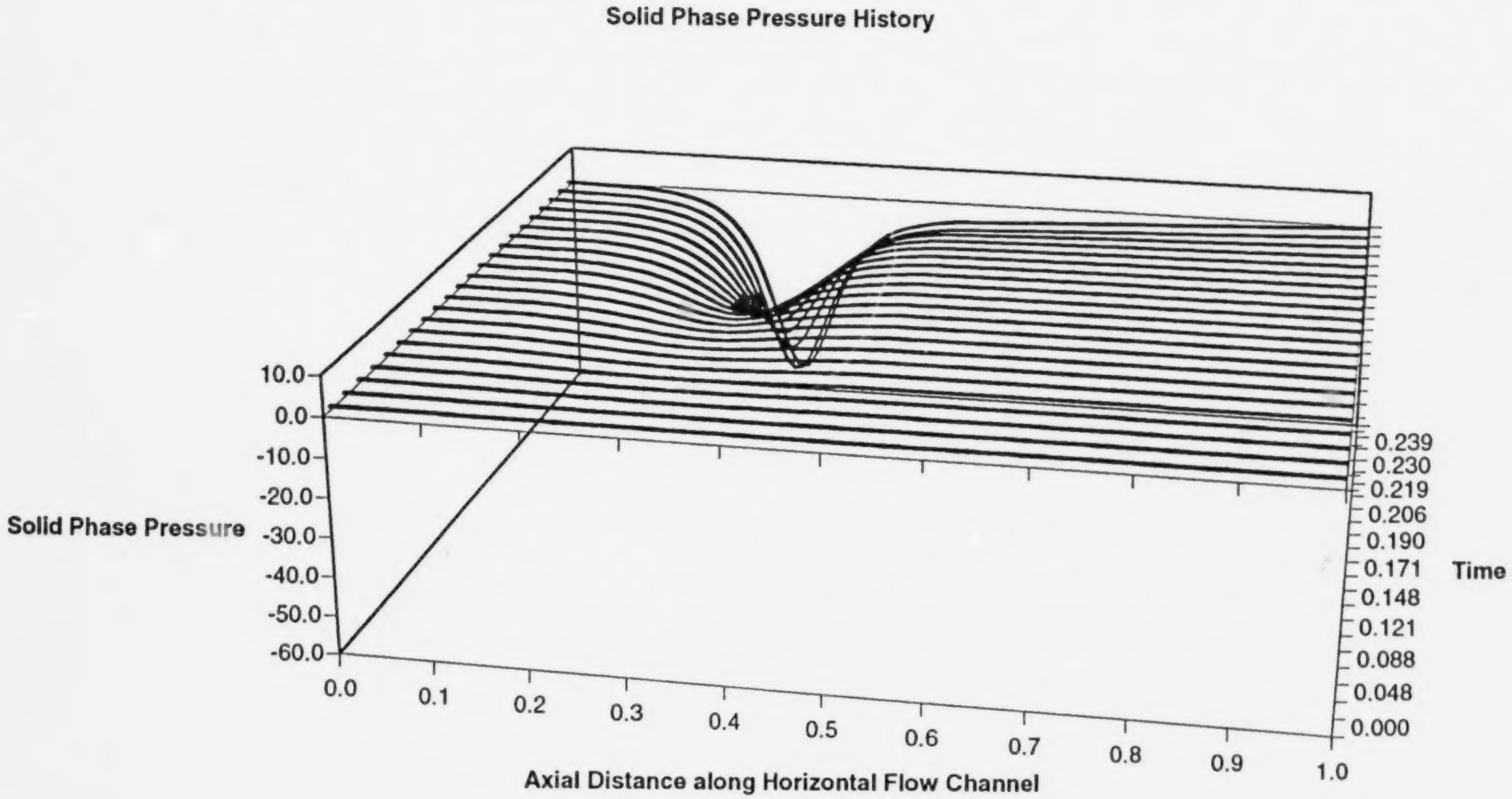

Figure 6.8: Constriction Model – Solid Phase Pressure Profile at different times for Case 2 (transport process dominated by Drag Force).

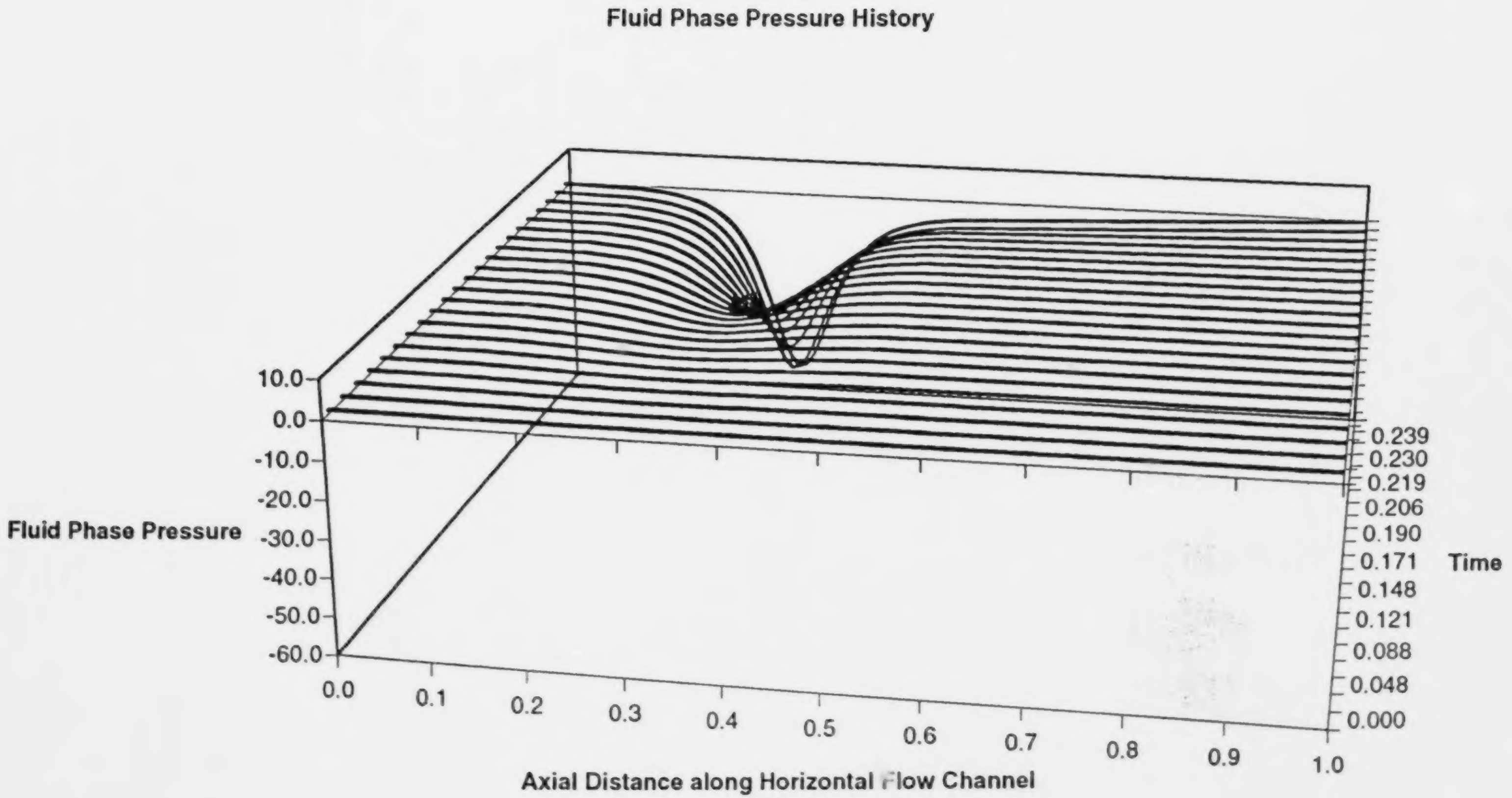

Figure 6.9: Constriction Model – Fluid Phase Pressure Profile at different times for Case 2 (transport process dominated by Drag Force).

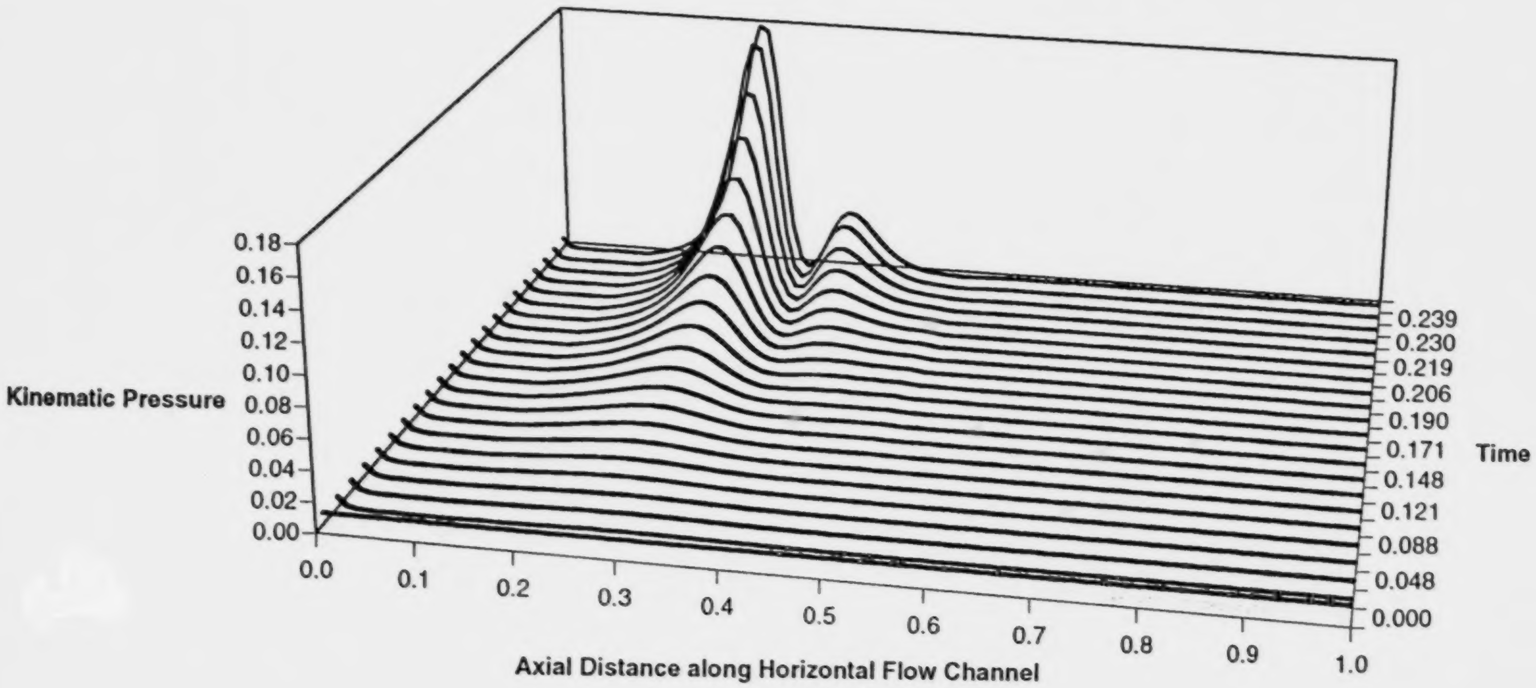
Kinematic Pressure History

Figure 6.10: Constriction Model – Kinematic Pressure Profile at different times for Case 2 (transport process dominated by Drag Force).

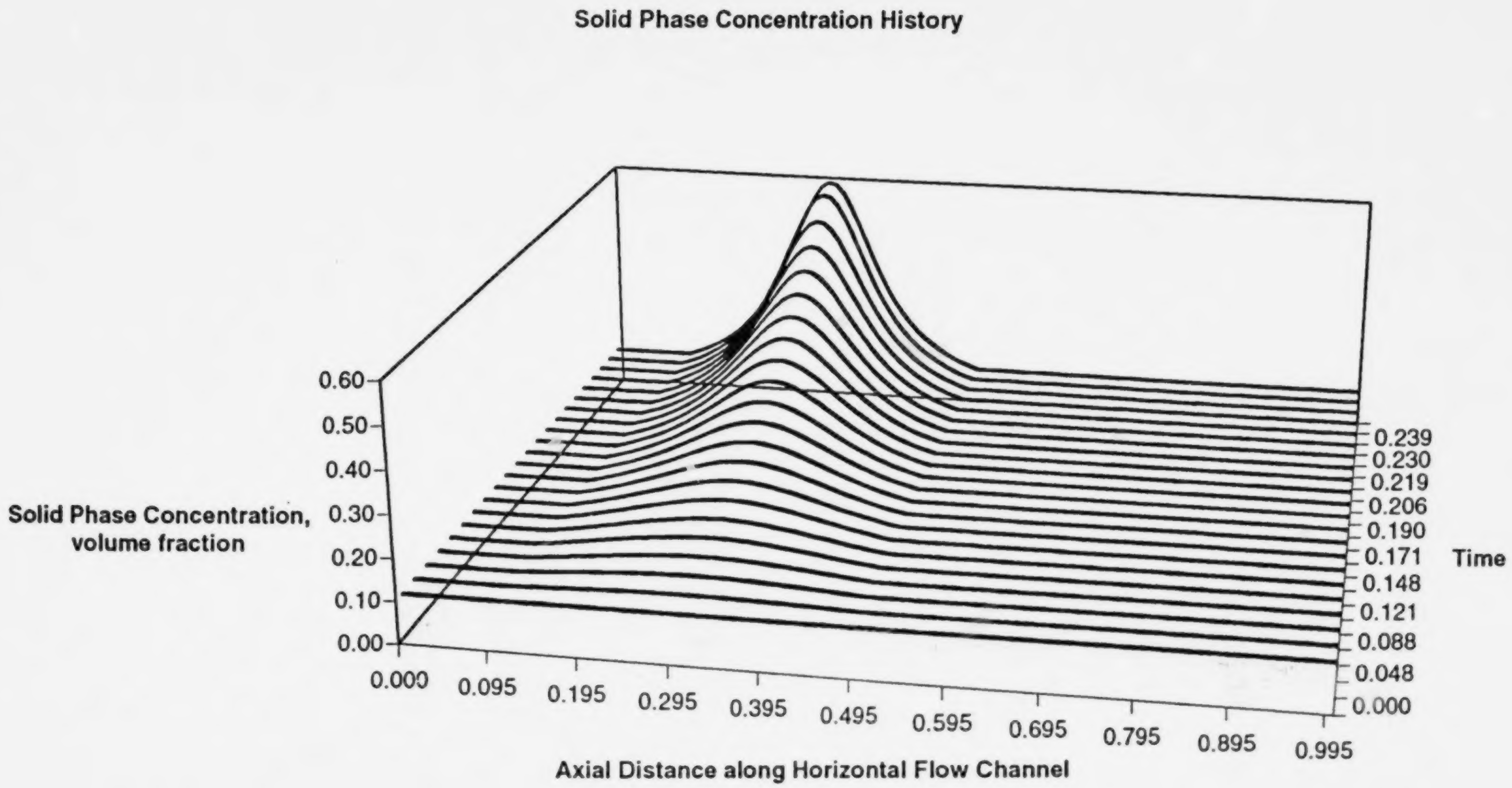

Figure 6.11: Constriction Model – Solid Phase Concentration Profile at different times for Case 2 (transport process dominated by Drag Force).

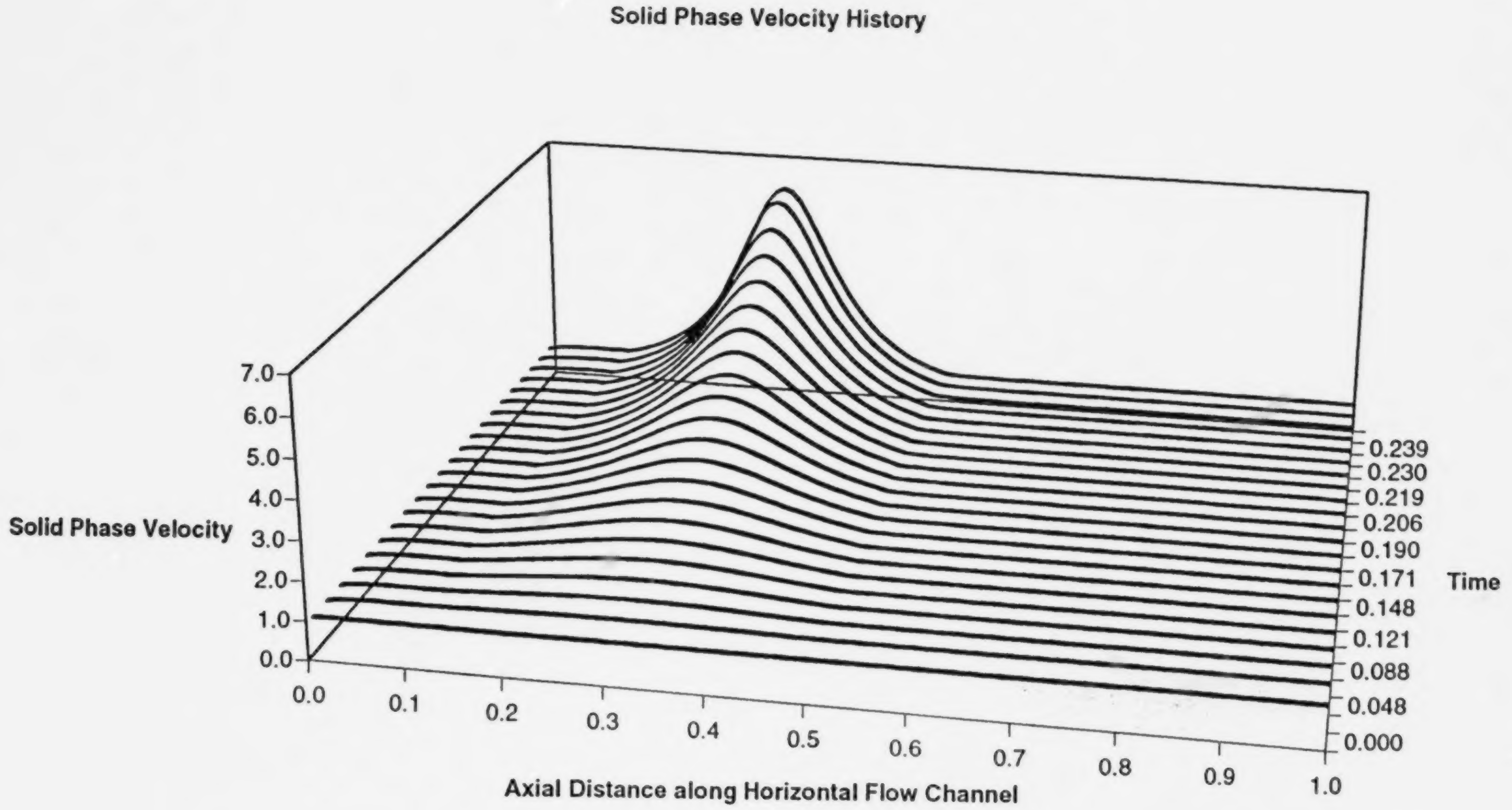

Figure 6.12: Constriction Model – Solid Phase Velocity Profile at different times for Case 2 (transport process dominated by Drag Force).

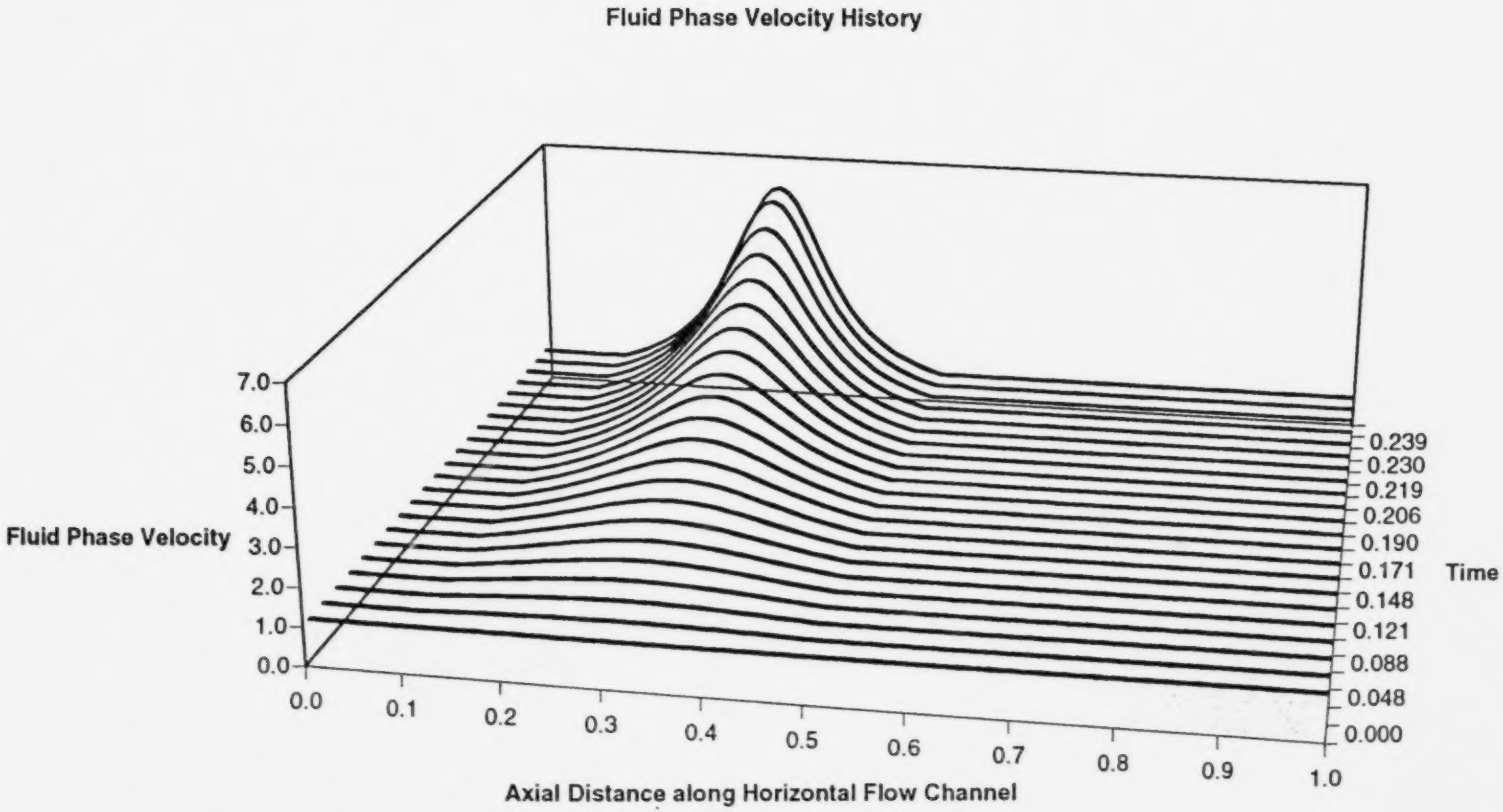

Figure 6.13: Constriction Model – Fluid Phase Velocity Profile at different times for Case 2 (transport process dominated by Drag Force).

on the initiation of a particle plug in the flow channel. These snapshots – taken at 0.0 second, 0.105 second, 0.150 second, 0.220 second, and 0.240 second – are given in Figures 6.14 – 6.19. It is observed in Figure 6.14 that the decline in the solid phase is consistently larger for Case 2 than for Case 1. For the fluid phase pressure the magnitude of the decline is the same for the two cases up to 0.105 second. Thereafter, Case 1 suffers a larger pressure decline (Figure 6.15) than Case 2. At the end of 0.24 second, the solid phase and fluid phase pressures are, respectively, -43.0 $g/cm.s^2$ and -52.0 $g/cm.s^2$ for Case 1, and -52.0 $g/cm.s^2$ and -57.0 $g/cm.s^2$ (approximately) for Case 2.

A major difference in the results of the two cases is seen in Figure 6.16. In contrast to the increase in the kinematic pressure for Case 1, as described above, the kinematic pressure for Case 2 is practically zero for the whole time. This is startling, given that the solid phase concentration profiles for the two cases are (almost) identical, as shown in Figure 6.17. Recalling the previous discussion on the influence of solid particle concentration on the magnitude of the kinematic pressure, the kinematic pressure profiles for the two cases would have been reasonably expected to follow one another. It is interesting to note also that the magnitude of the kinematic pressure for Case 1, approximately equaling 25 $g/cm.s^2$ at the end of 0.24 second, is at variance with the difference in the solid phase and fluid phase pressures (-43.0 $g/cm.s^2$ and -52.0 $g/cm.s^2$, respectively). This observation applies with equal validity to the results presented by Givler et al. [83].

Fluid phase velocity profiles for both cases are given in Figure 6.18. They are similar to one another, except that the velocity for Case 1 is higher than that for Case 2 throughout the duration of the simulation runs. For both cases the fluid velocity opposite the constricted region increases markedly, from 1.0 cm/s (initial, as well as boundary condition values) to 6.2 cm/s for Case 2, and 7.5 cm/s for Case 1. These large changes take place in 0.24 second. A similar comparison for the solid phase velocity profiles is illustrated in Figure 6.19. Case 2 shows smooth, symmetrical velocity profile at all times. The profile for Case 1 is asymmetrical, showing some topsy-turvy behaviour at the right edge of the constriction. The solid phase velocity is higher in Case 2 at all times than in Case 1, even though they initially were the same.

Table 6.2 contains part of the answer for the puzzle of different kinematic pressure profiles in the two cases, as discussed above. It contains the solid phase and fluid phase velocities, calculated at the peak of the constriction (n=30), for these two cases. The slip velocity between the two phases at different times is determined easily from these values.

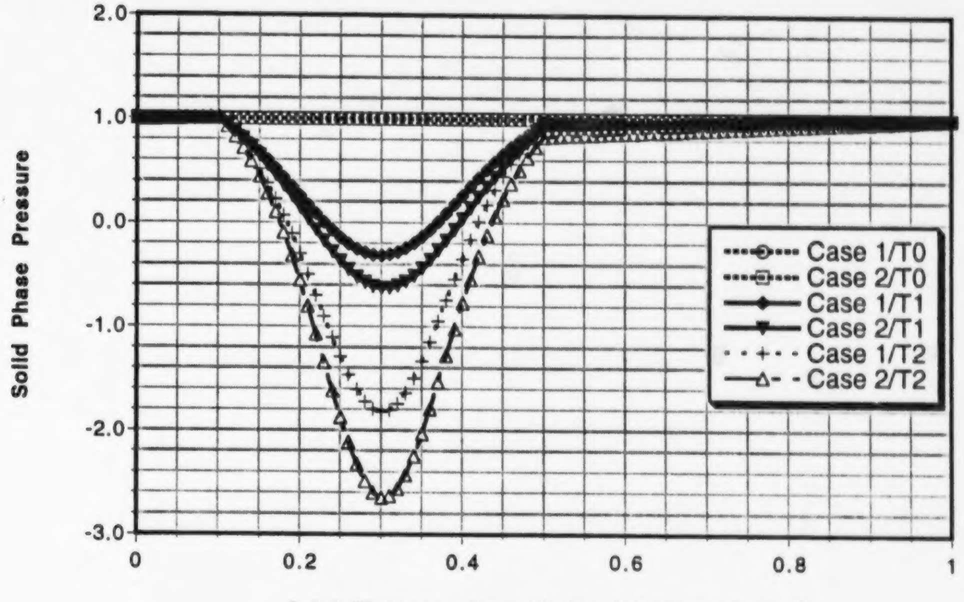

a) Profiles at time T0 (t=0.0 s), T1 (t=0.105 s), and T2 (t=0.150 s)

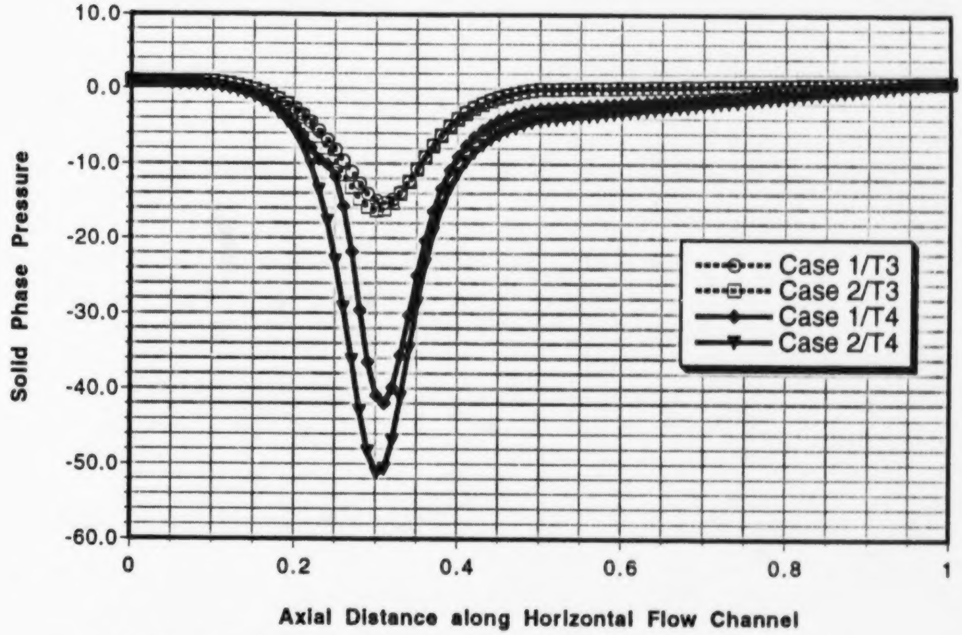

b) Profiles at time T3 (t=0.220 s) and T4 (t=0.240 s)

Figure 6. 14: Constriction Model – Profile of Solid Phase Pressure at different times for Case 1 (Pressure Forces Dominating Process) vs. Case 2 (Interfacial Drag Force Dominating Process).

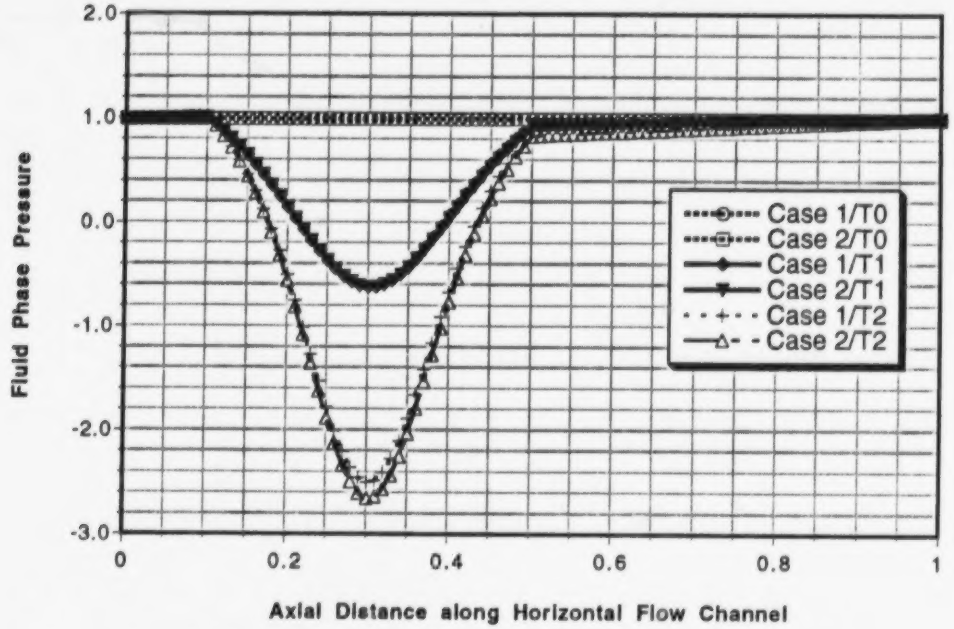

a) Profiles at time T0 (t=0.0 s), T1 (t=0.105 s), and T2 (t=0.150 s)

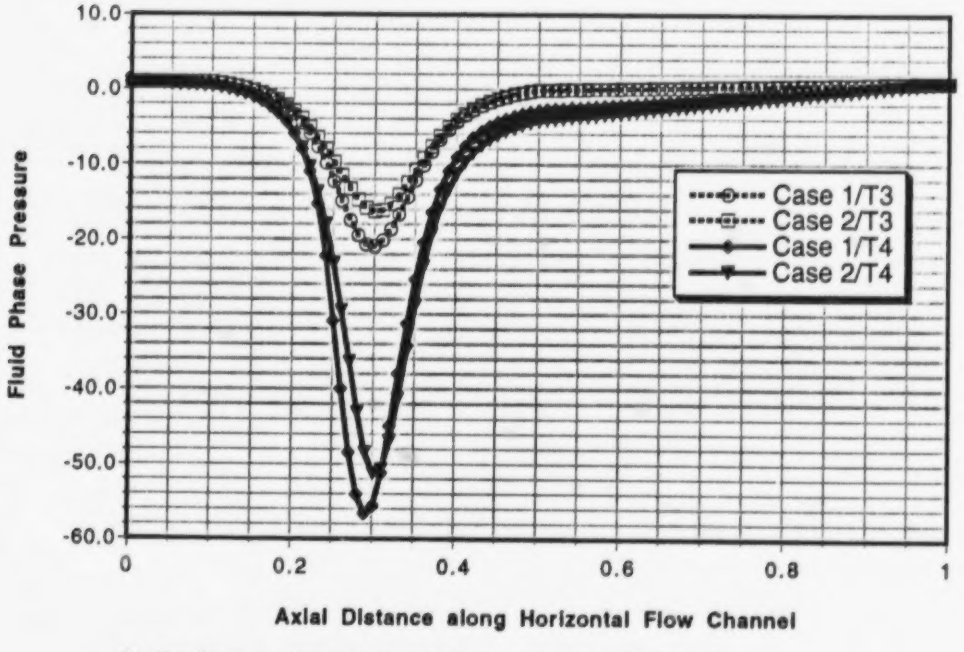

b) Profiles at time T3 (t=0.220 s) and T4 (t=0.240 s)

Figure 6. 15: Constriction Model – Profile of Fluid Phase Pressure at different times for Case 1 (Pressure Forces Dominating Process) vs. Case 2 (Interfacial Drag Force Dominating Process).

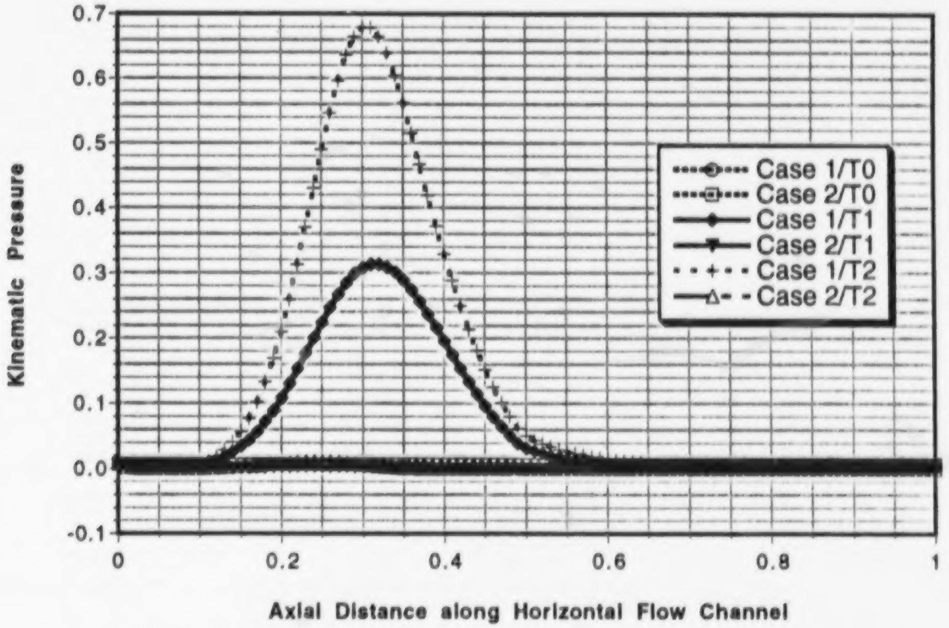

a) Profiles at time T0 (t=0.0 s), T1 (t=0.105 s), and T2 (t=0.150 s)

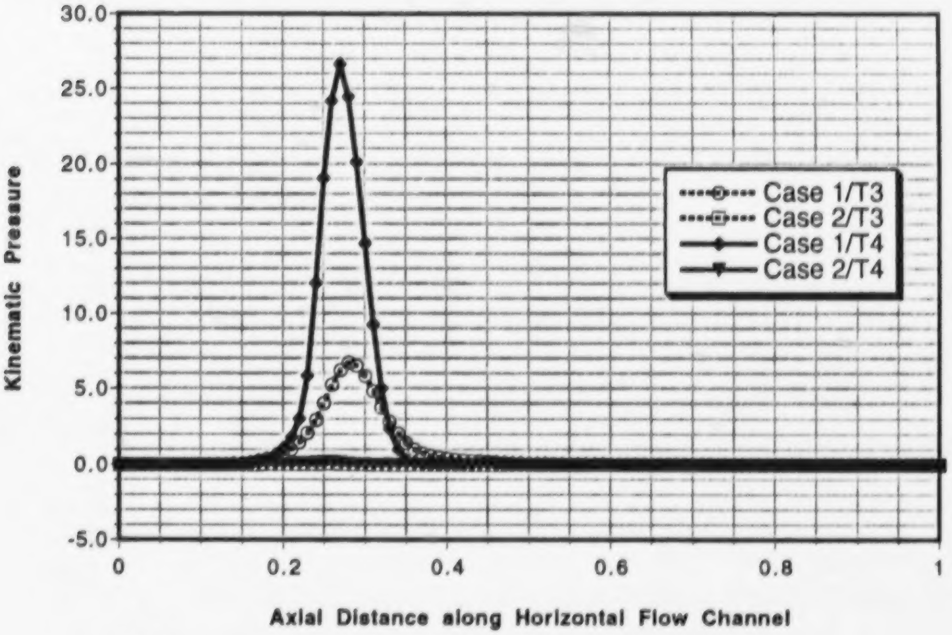

b) Profiles at time T3 (t=0.220 s) and T4 (t=0.240 s)

Figure 6. 16: Constriction Model – Profile of Kinematic Pressure at different times for Case 1 (Pressure Forces Dominating Process) vs. Case 2 (Interfacial Drag Force Dominating Process).

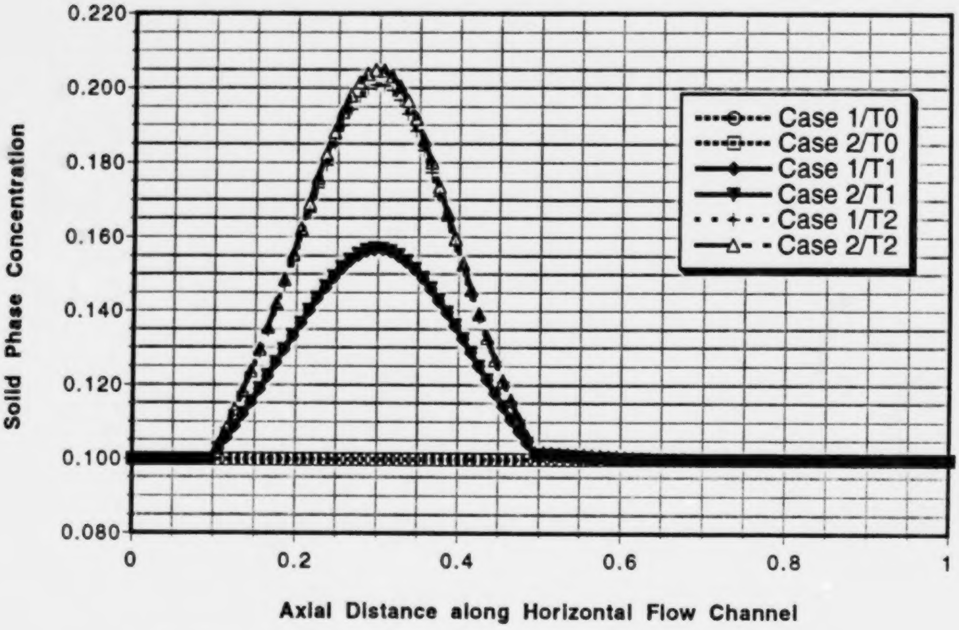

a) Profiles at time T0 (t=0.0 s), T1 (t=0.105 s), and T2 (0.150 s)

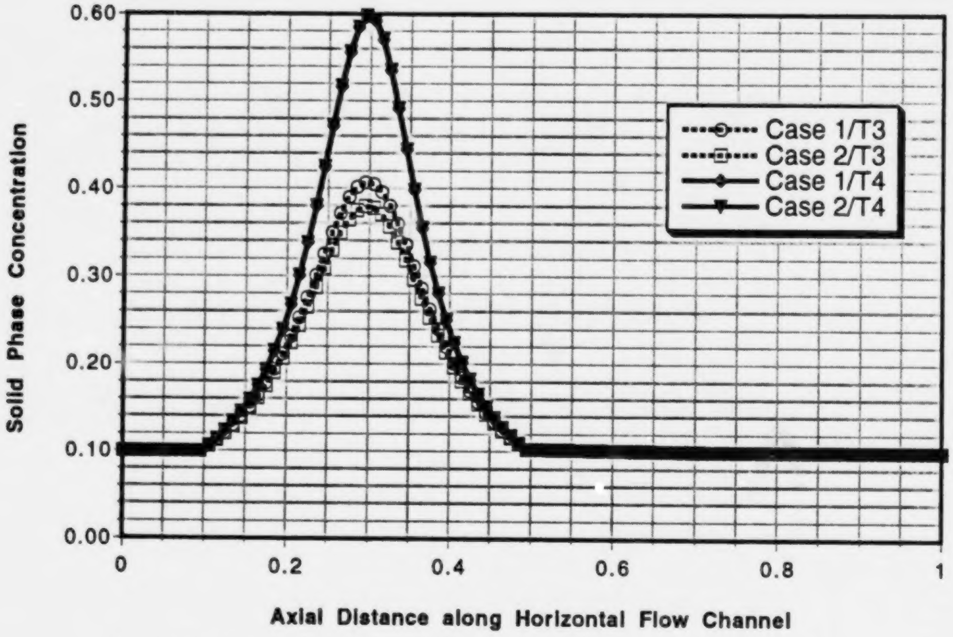

b) Profiles at time T3 (t=0.220 s) and T4 (t=0.240 s)

Figure 6. 17: Constriction Model – Profile of Solid Phase Concentration at different times for Case 1 (Pressure Forces Dominating Process) vs. Case 2 (Interfacial Drag Force Dominating Process).

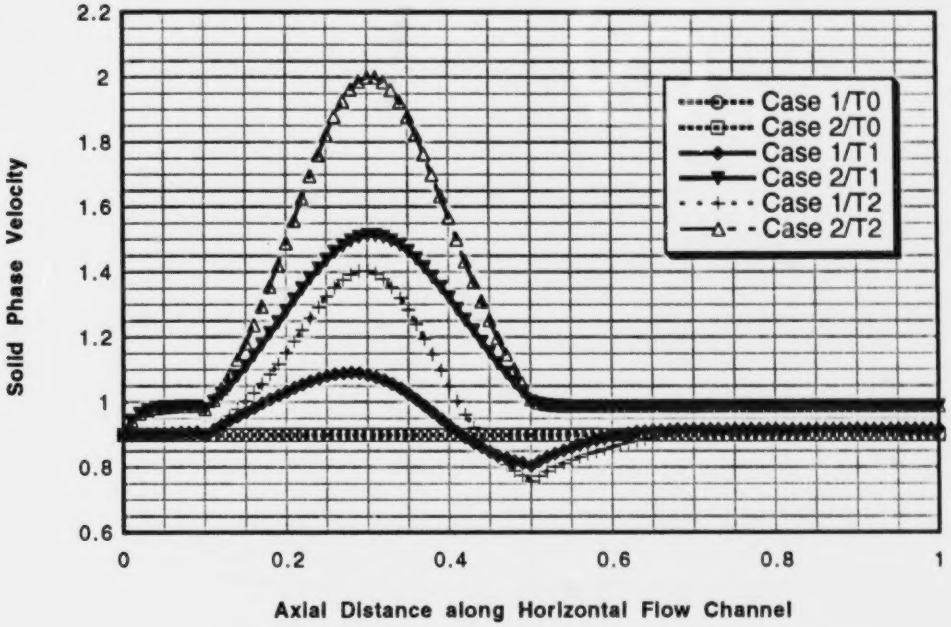

a) Profiles at time T0 (t=0.0 s), T1 (t=0.105 s), and T2 (t=0.150 s)

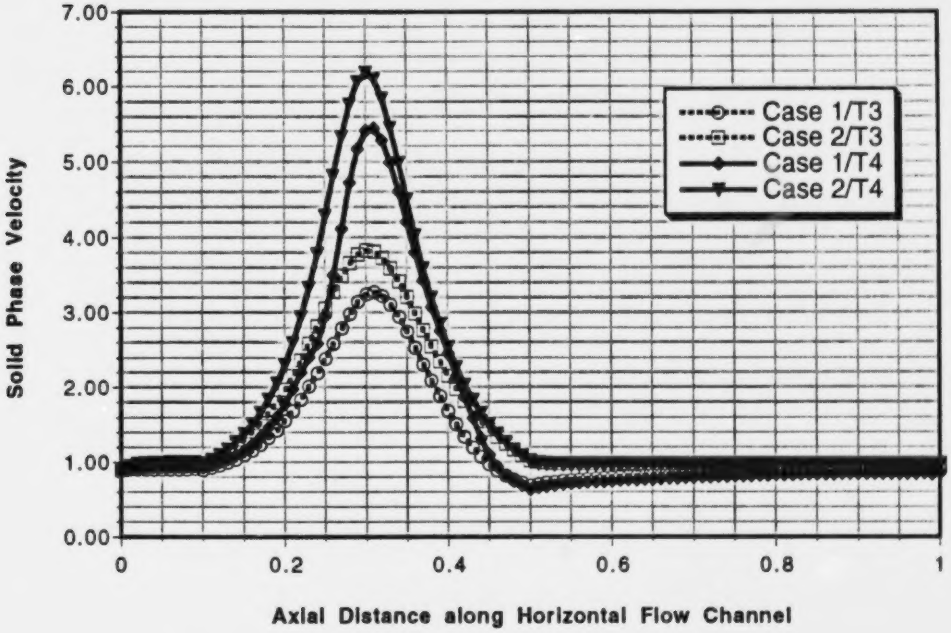

b) Profiles at time T3 (t=0.220 s) and T4 (t=0.240 s)

Figure 6. 18: Constriction Model – Profile of Solid Phase Velocity at different times for Case 1 (Pressure Forces Dominating Process) vs. Case 2 (Interfacial Drag Force Dominating Process).

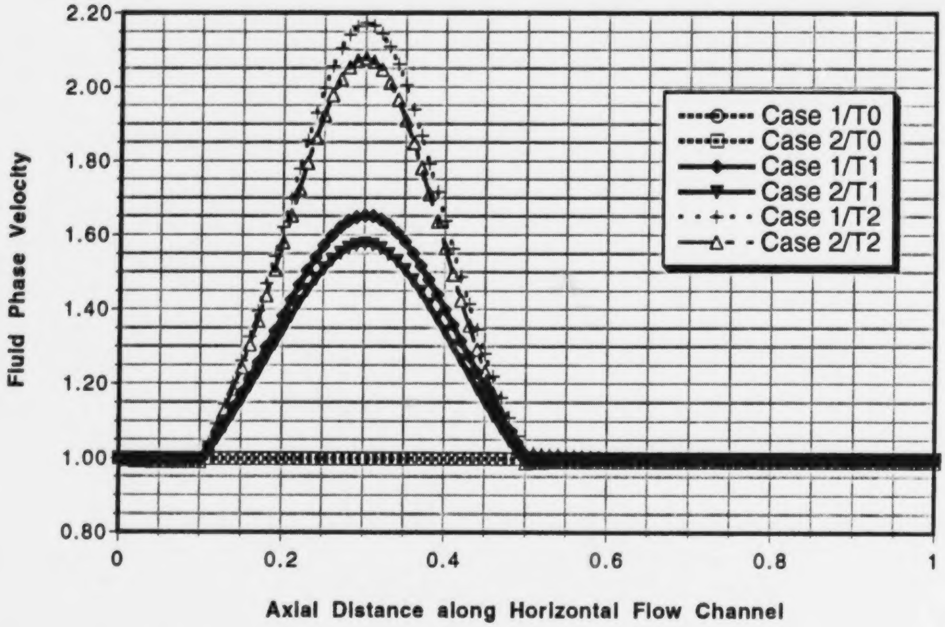

a) Profiles at time T0 (t=0.0 s), T1 (t=0.105 s), and T2 (t=0.150 s)

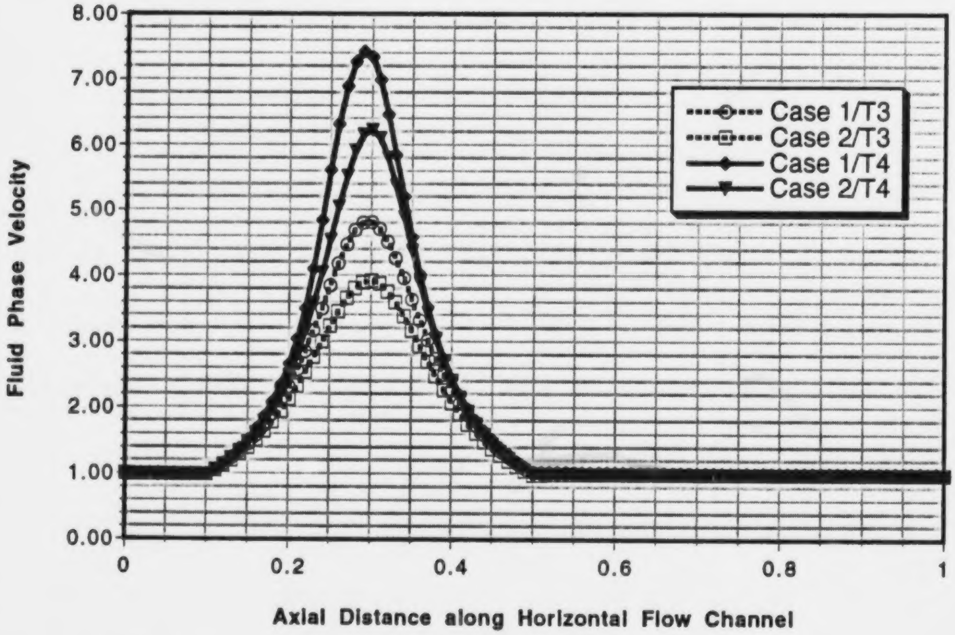

b) Profiles at time T3 (t=0.220 s) and T4 (t=0.240 s)

Figure 6. 19: Constriction Model – Profile of Fluid Phase Velocity at different times for Case 1 (Pressure Forces Dominating Process) vs. Case 2 (Interfacial Drag Force Dominating Process).

Table 6.2: Slip velocity for Case 1 and Case 2 at different times, Constriction Model

Time	Case 1			Case 2		
	w_f	w_s	Δw	w_f	w_s	Δw
T1 (0.105 s)	1.65	1.10	0.55	1.60	1.50	0.10
T2 (0.150 s)	2.17	1.40	0.77	2.07	2.00	0.07
T3 (0.220 s)	4.80	3.30	1.50	3.90	3.80	0.10
T4 (0.240 s)	7.50	5.00	2.50	6.30	6.20	0.10

Substituting appropriate values for the different variables and parameters making up the definition for the kinematic pressure (Equation 4.18) at the end of 0.24 second, a value comparable to that seen in Figure 6.16 is obtained. This does not, however, resolve the question of the value for the kinematic pressure being at some variance with the difference in the values, observed individually, for the solid phase and fluid phase pressures.

It is interesting to observe that for Case 2 the slip velocity is small, and stays largely invariant with time. The explanation for this is the small particle size results in a small particle Reynolds Number, and a high drag (Equations 4.21 and 4.22), which allows the solid particles to be transported at velocities very similar to the velocities of the surrounding fluid phase. The small slip velocity contributes to the small magnitude for the kinematic pressure. As such, in this case (Case 2) the slip velocity plays a more dominant role than the kinetic energy resulting from particle-particle collisions in determining the magnitude of the kinematic pressure.

An overall conclusion can be drawn from this cross-comparison exercise to determine the role played by either the pressure forces or the interfacial drag force on the formation of a particle plug. When the interfacial drag force dominates the transport process, there is little slippage between the two phases. As a consequence, the start of the formation of a particle plug is considerably delayed. On the other hand, when pressure forces are allowed to dominate the transport process a large slippage between the two phases occurs. This, coupled with increased particle-particle collisions, results in the solid particles quickly forming a particle plug.

A secondary conclusion can also be drawn about Givler et al's Constriction model, as it is developed in this study. To a very large degree, the results generated by this study's Constriction model match those presented by Givler et al. [83]. In all the cases that are examined, not only in terms of the overall Case 1 and Case 2, but also in terms of results for individual variables the two sets of results come within 10% of one another, and quite often much less. Taking into account the differences which might have arisen between this study and Givler et al.'s [83], in terms of numerical techniques and procedures, the close match between the results is quite remarkable. This fact might not say much about the validity of the model and its results, but it does enable the numerical solution for the Gravity Deposition model to be developed with some confidence.

6.2.3. Applicability of the Constriction Model

The following discussion is in order before the issue of using the Constriction model to study sand deposition inside a horizontal well can be examined. An important question for the results obtained above, and by extension for the results obtained by Givler et al. [83] – in view of the unconventional behaviour of the solid phase and fluid phase pressures – concerns the physical meanings of the input data for the simulation runs, in particular the fluid phase viscosity. Once an understanding is obtained for the meanings of the input data, and their effects on the results, then a more meaningful analysis of the results can be performed. In view of this, it is seen that the numerical values assigned for the density, velocity and pressure variables appear perfectly acceptable (Table 6.1) under the cgs system of units. However, the same cannot be said about the numerical values assigned for the fluid phase viscosity. Values for the solid phase and fluid phase density, and velocity seem probably valid at 1.5 g/cc, 1.0 g/cc, 0.9 cm/s, and 1.0 cm/s, respectively. Similarly, the particle diameter at 0.05 cm (or 500 microns) is not extraordinary, and comparable to the size of beach sand. The solid phase pressure, being 1.0 g/cm.s^2 (or 0.10 Pa), is rather small but it could be argued that this value is normalized and/or the flow occurs under (very) low pressure conditions. Additionally, the prescribed boundary conditions of similar pressures at either end of the flow channel (i.e. no pressure drop) is acceptable if the channel length is considered small enough. The fluid phase viscosity, fixed at 0.00001 g/cm.s for Case 1 and 0.001 g/cm.s for Case 2, corresponds to 0.001 mPa.s (0.001 cp) and 0.1 mPa.s (0.1 cp), respectively. These magnitudes are one-tenth and ten times the viscosity of natural gases at atmospheric conditions, and as such, are not typical of the viscosity of fluids pumped and used to seal fracture networks in geothermal reservoirs. Of the variables involved in the transport process the fluid phase viscosity, as seen in the results, is one of the most influential. It is used in the calculation of the drag force and the interface interaction coefficient, and as such plays an important role in the transfer of momentum from one phase to another. An attempt to contact and obtain explanations – in particular those about the values assigned for the fluid phase viscosity – from the principal author (Dr. R.C. Givler) of the investigation [83] was not fruitful.

Summarizing these observations it is seen that, for the most part, the results appear to be logically explainable. First and foremost, the constriction increases the resistance to flow, with this effect consequently leading to corresponding increases in the fluid phase and solid phase velocities, as well as more collisions between solid particles. In Case 1 this latter phenomenon, coupled with increases in the slip velocity between the two phases, produces a higher kinematic pressure (which, after all, is defined to reflect the difference between the fluid phase pressure and the solid phase pressure, due to a higher solid phase concentration, and more particle-particle collisions). In Case 2, the effect of increasing the particle-particle collisions is negated by the small slippage between the two phases – thus, resulting in negligible kinematic pressure. Collectively, it can be stated that there is some merit in this model – in so far as it shows the logically proper response of many transport variables due to the constriction in part of the flow channel.

Given the above assessment an attempt was made to test the Constriction model for studying an actual sand deposition problem, in spite (and in view) of the uncertainties about the physical meanings of the input data used to generate the above results. This endeavour involved running the model using field-type data, and using the assumed constriction profile and expansion rate as adjusting parameters to obtain a match with field data. The data used in this endeavour – including pressures, velocities (or rather rate-derived velocities), densities, fluid viscosity, and particle size – were selected to be representative of an unconsolidated heavy oil reservoir being recovered by a horizontal well in Saskatchewan. They were of the same order of magnitude as the data used in the simulation runs for the Gravity Deposition model (Table 6.3), allowing for some flexibility in values assigned to the oil viscosity and pressure. This effort was unsuccessful. The model simply could not handle field-type numbers (magnitudes), even when the data were converted into equivalent cgs values. An attempt to derive values for individual parameters through the normalization (scaling) process also failed. Numerical results were obtained for many of these field-type runs, but they showed spurious oscillations and could not be logically analyzed. As such, no meaningful conclusion could be drawn from them. Consequently, they are not presented here. It is seen from these results that the system of governing equations became "stiff" when field-type data were used; and its numerical solution became very sensitive to the magnitude of many of the input data, in particular pressure (which, if expressed in MPa, became 10 000 000 $g/cm.s^2$) and fluid viscosity (which was expressed as 1.0 g/cm.s for 1 000-cp fluid). Extremely small time steps were used to keep the solution numerically stable, to no avail. In addition, several dimensionless groups were derived to scale Givler and Mikatarian's data [83] to field-scale values which were then used as input values for the numerical model. This was also fruitless. From this exercise it is concluded that the Constriction model was incapable of being used to study field-scale sand deposition in a horizontal well.

6.3. Gravity Deposition Model

The Gravity Deposition model is developed to study gravity deposition of sand particles in a horizontal well. It is different from the Constriction model in that it simulates the deposition process naturally, by ascribing no constriction profile and expansion rate *a priori*. As such, deposition of solid particles and expansion of the resulting deposit bed, if they occur, occur only as a result of the actual hydrodynamic conditions prevailing inside the horizontal well.

6.3.1. Gravity Deposition Model – Input Data

Table 6.3 is a summary of the input data used in the simulation runs for the Gravity Deposition model. The numerical values are expressed in cgs units. Their SI equivalents are also given.

Table 6.3: Some data used in runs for Gravity Deposition Model

Variable	cgs value	SI-based value
Fluid phase material density, ρ_f	0.9, 1.0 g/cc	900, 1 000 kg/m^3
Solid phase material density, ρ_s	2.65 g/cc	2650 kg/m^3
Horizontal well radius, r_w	9.0 cm	0.09 m (7.0" well)

Two different oils are considered: Light Oil (density= 0.9 g/cc or 26 ^{0}API) and Heavy Oil (density=1.0 g/cc or 10 ^{0}API). The solid density is equivalent to the density for quartz sand. The small difference in the densities for the Light Oil and Heavy Oil (0.1 g/cc) likely means that the influence of the density contrast between the solid phase and fluid phase on the gravity deposition process is small compared to those for the other three variables used in this study. For each of the two types of oil two different oil viscosities are specified, to study the effects of oil viscosity on solid transport capacity. For the light oil case the viscosities are 25 mPa.s (25 cp) and 100 mPa.s. The two heavy oil viscosities are 1 500 mPa.s and 10 000 mPa.s. Two different particle sizes are also used: 1 000 microns, and 5 000 microns. They represent larger sands (in view of the "average" sand size being 150 to 500 microns). These sizes are chosen mainly due to the limitation of computer memory storage available. Table 6.4 provides a summary of the 25 simulation runs carried out for the Gravity Deposition model. Each of these runs simulates, for the majority of the runs, only about 3.0 seconds or less of the deposition process. A few runs do simulate the deposition process to a longer duration (6.0-10.0 seconds). Yet, each of these same runs takes, on the average, 8-12 hours (real time) to carry out; when completed, each requires about 6-8 megabytes of memory to store the results and graphs. The 25 simulation runs performed for the Gravity Deposition model, together with the runs performed for the Constriction model, used up all the storage memory available (200 MBs).

It is important to point out that the large amount of memory required for storage of results and graphs for each run, and the long running time taken by each simulation run in Table 6.4 were for runs already purposely designed to facilitate and "expedite" the gravity deposition process. What this statement means is that the particle size was chosen to be larger than the average size

Table 6.4: Summary of simulation runs with the Gravity Deposition Model.

Run	Viscosity, mPa.s	Particle Size, cm	Fluid Vel., cm/s	Solid Vel., cm/s	Press. Inlet, g/cm.s2	Press. Outlet, g/cm.s2	Simul. Time, s
Light Oil (Density = 0.9 g/cm3)							
Run L 01	25	0.5	6.825	6.143	3 000	2 000	1.84987
Run L 02	25	0.5	13.650	12.285	3 000	2 000	1.20042
Run L 03	25	0.5	27.300	24.570	3 000	2 000	1.14293
Run L 04	25	0.1	6.825	6.143	3 000	2 000	3.79386
Run L 05	25	0.1	13.650	12.285	3 000	2 000	1.88640
Run L 06	25	0.1	27.300	24.570	3 000	2 000	1.85789
Run L 07	100	0.5	6.825	6.143	3 000	2 000	1.96711
Run L 08	100	0.5	13.650	12.285	3 000	2 000	1.25903
Run L 09	100	0.5	27.300	24.570	3 000	2 000	1.01186
Run L 10	100	0.1	6.825	6.143	3 000	2 000	10.00128
Run L 11	100	0.1	13.650	12.285	3 000	2 000	6.11996
Run L 12	100	0.1	27.300	24.570	3 000	2 000	3.30715
Run L 13	25	0.05	13.650	12.285	3 000	2 000	17.62678
Heavy Oil (Density = 1.0 g/cm3)							
Run H 01	1 500	0.5	2.500	2.000	3 000	2 000	7.20449
Run H 02	1 500	0.5	5.000	4.000	3 000	2 000	4.11830
Run H 03	1 500	0.5	6.825	5.460	3 000	2 000	3.11719
Run H 04	10 000	0.5	2.500	2.000	3 000	2 000	0.65330
Run H 05	10 000	0.5	5.000	4.000	3 000	2 000	4.25604
Run H 06	10 000	0.5	6.825	5.460	3 000	2 000	3.11838
Run H 07	1 500	0.1	2.500	2.000	2 100	2 000	3.22566
Run H 08	1 500	0.1	5.000	4.000	2 100	2 000	1.62380
Run H 09	1 500	0.1	6.825	5.460	2 100	2 000	1.19298
Run H 10	10 000	0.1	2.500	2.000	2 100	2 000	1.49337
Run H 11	10 000	0.1	5.000	4.000	2 100	2 000	0.74777
Run H 12	10 000	0.1	6.825	5.460	2 100	2 000	0.55051

to allow faster deposition (than normal) to take place. This explanation is more apparent in view of the results in Figure 6.48 showing the lack of gravity deposition by solid particles when they were small (0.1 cm), and the fluid viscosity was high (10 000 mPa.s). Indeed, one simulation run was carried out with "actual" (or average) sand size of 500 microns, and a fluid viscosity of 25 mPa.s (Run L 13 in Table 6.4). These conditions were chosen to allow sand deposition to occur at a "more realistic" rate. This run took 16 hours to complete, and required 11 megabytes of storage memory. Based on these considerations, and a finite memory capacity, a choice had to be made between performing fewer runs of this type (i.e. "average" particle size) and performing more runs of the other type in Table 6.4 (larger particle sizes). It was decided to go with the second choice, mostly out of the desire to be able to examine the influence of as many different variables as possible on the transport process. With additional memory capacity, the numerical model can be run, without any modification, with any type of data.

6.3.2. Gravity Deposition Model – Results of "Representative" Case

Physically the simulation runs were designed and carried out to examine the gravity deposition of sand out of an initially homogeneous oil-sand suspension, and the subsequent formation and expansion of a deposit bed at the bottom of a horizontal well. Keeping in view the above discussion about input data for the numerical model, the results for Run L 13 are presented below. The results show the profiles of different variables between the inlet and outlet of a segment of the horizontal well. The length of this segment is 1 000 cm (or 10 metres). The inlet of this segment represents the inlet of the horizontal well, or any other position, where oil and sand are coming into the horizontal well at known velocities. The solid phase concentration at this point is 20% volume fraction. The initial conditions include a solid phase concentration of 1% and a pressure of 1.0 $g/cm.s^2$. As such, initially the suspension is very dilute (1% volume is occupied by sand, 99% volume is filled up with oil), and stationary. There is (basically) little pressure inside the horizontal well initially. At time zero a suspension (20% solid and 80% oil, on a volume basis) starts coming into the (toe of) the horizontal well at an overall velocity of 13.65 cm/s (equivalent rate is 300 standard m^3/day). The solid particles in the suspension move slower at the well inlet, at 90% of the fluid velocity. There is a pressure difference of 1 000 $g/cm.s^2$ (100 Pa) across the 10-metre segment.

The most prominent features seen in Figures 6.20 – 6.24 are the ripples. They are seen to form at the inlet of the horizontal well, and propagate some distance downstream. In addition, there are more ripples as time goes on. Bagnold [144] provided an excellent discussion about the formation of sand ripples in a shallow water environment. He experimentally observed how initially randomly distributed rolling sand grains came to rest in parallel, transverse zones after some time. These transverse zones expanded as more sand grains congregated, and the zones became little wavy ridges a few grains high. As these ridges expanded they came to shelter a

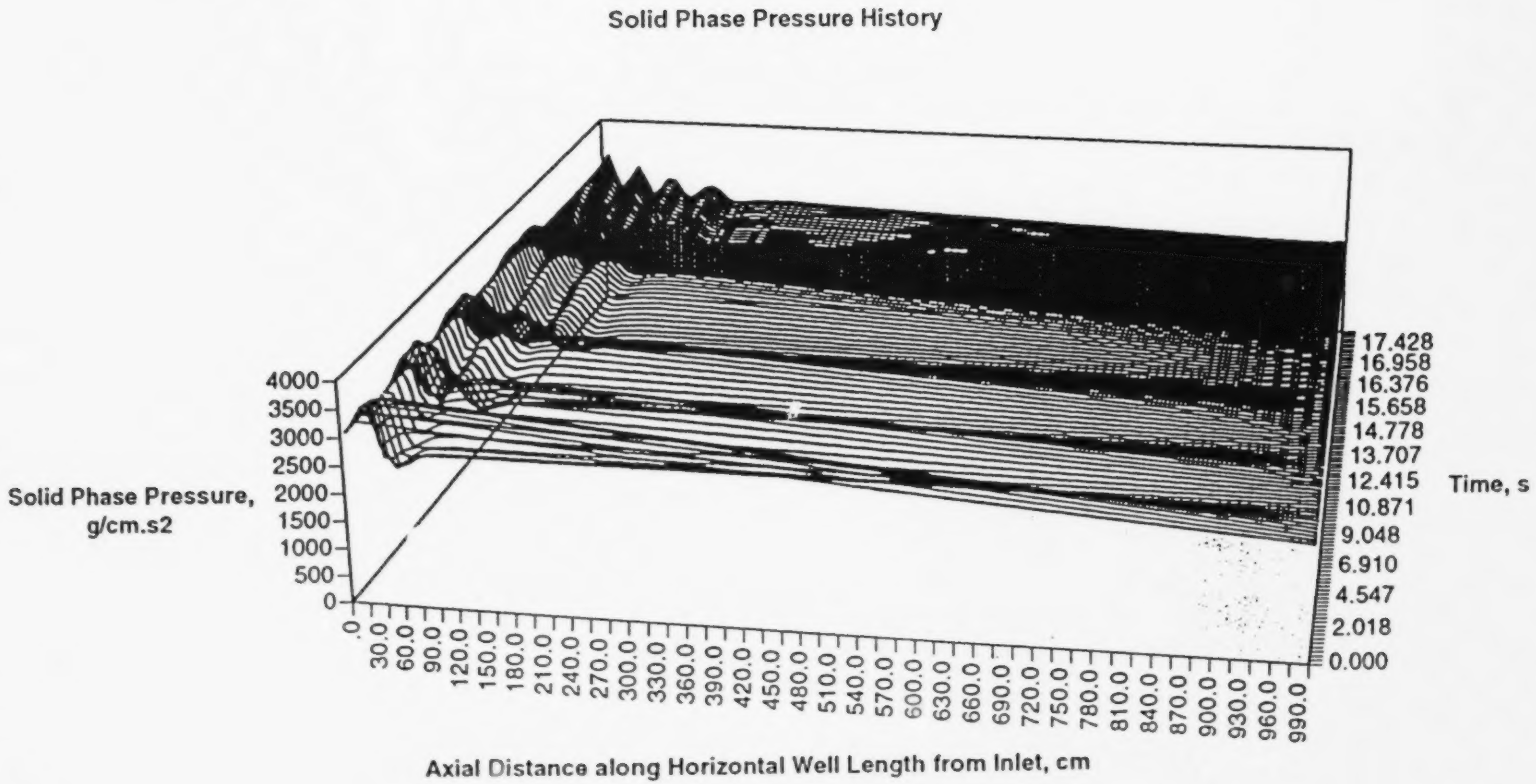

Figure 6.20: Gravity Deposition Model – Solid Phase Pressure Profile for a light oil, Run GD/L/13 (μ = 25 mPa.s, W_t = 13.65 cm/s, d = 0.5 cm) .

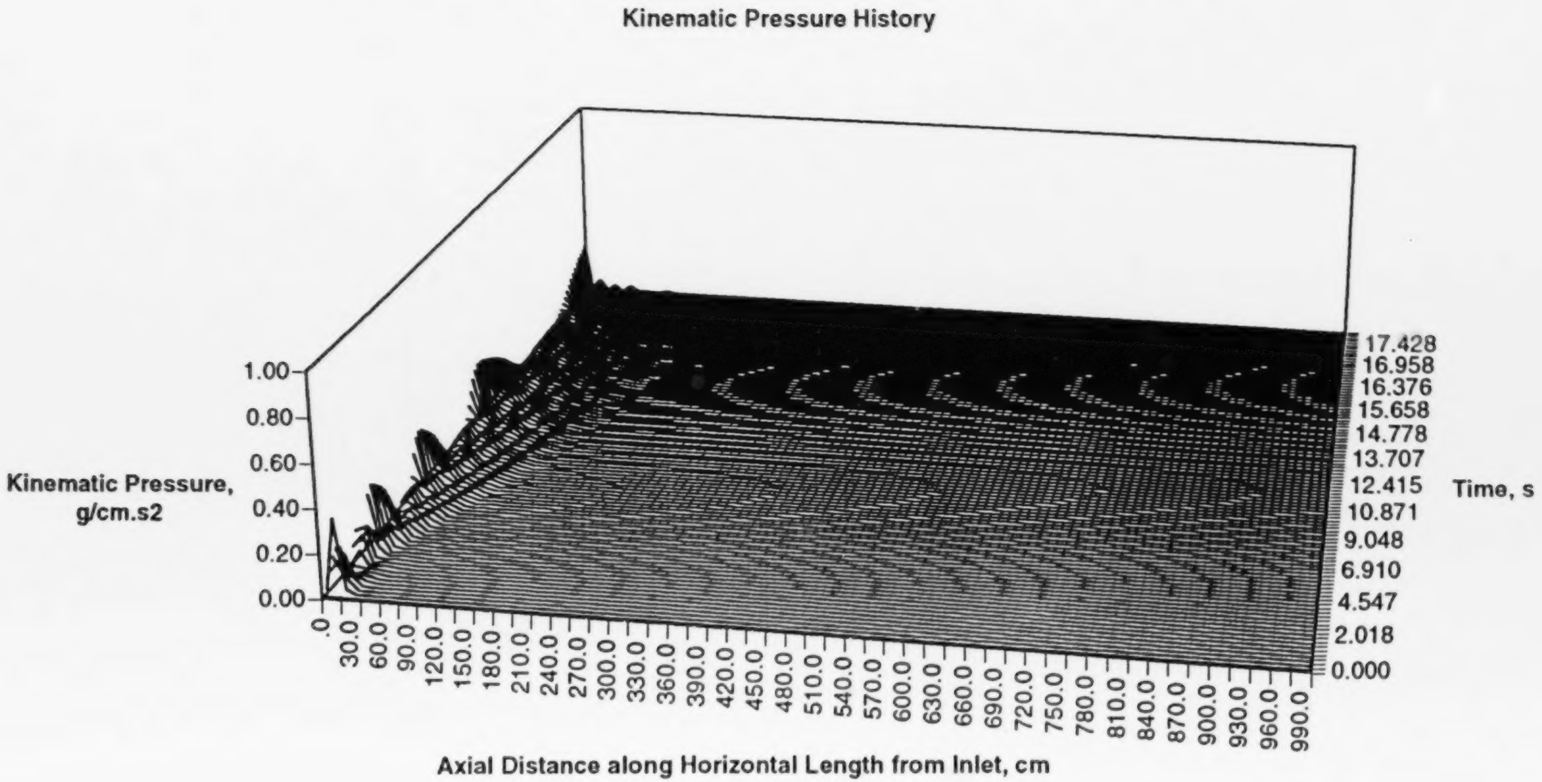

Figure 6.21: Gravity Deposition Model – Kinematic Pressure Profile for a light oil, Run GD/L/13 (μ = 25 mPa.s,W_f = 13.65 cm/s, d = 0.5 cm) .

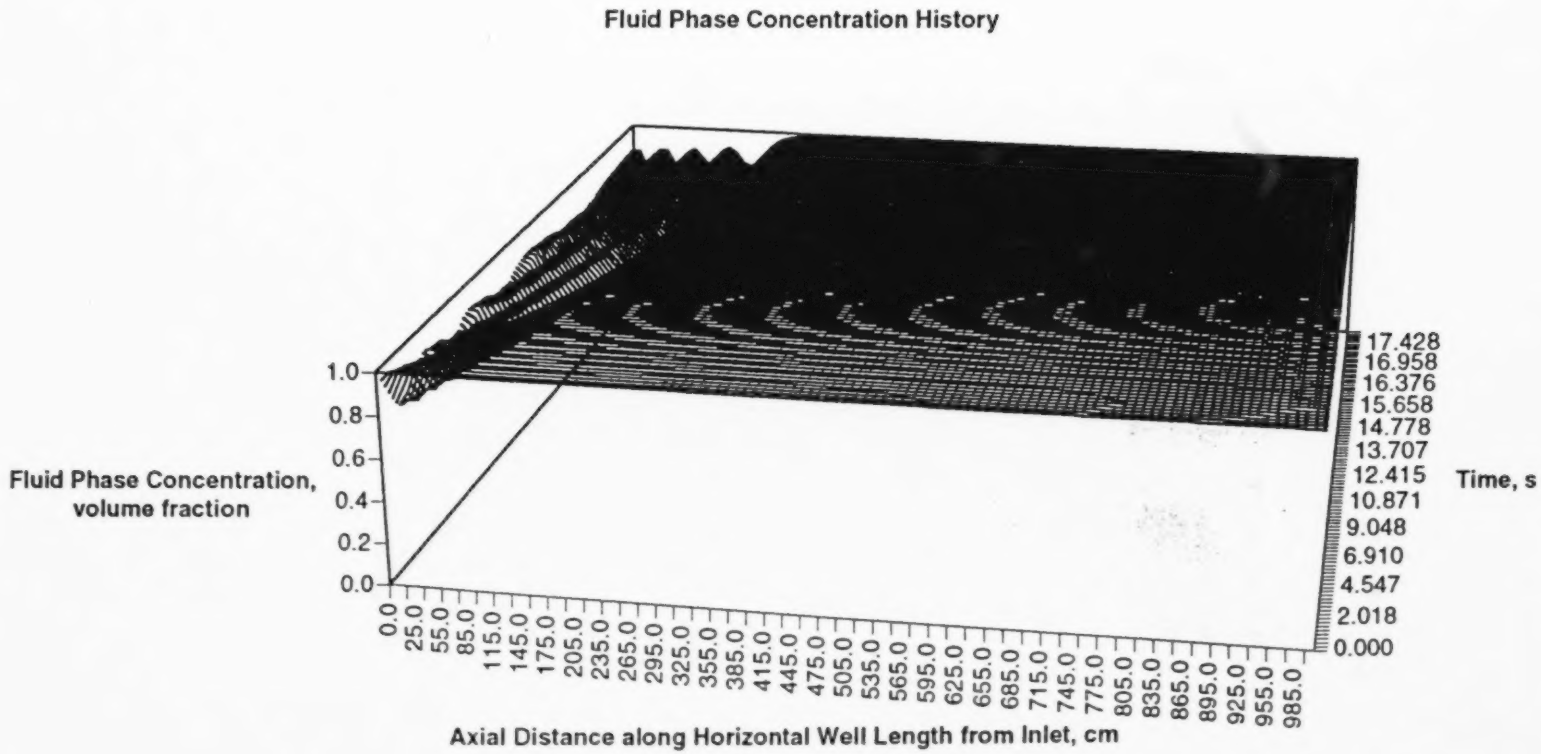

Figure 6.22: Gravity Deposition Model – Fluid Phase Concentration Profile for a light oil, Run GD/L/13 (μ = 25 mPa.s,W_l = 13.65 cm/s, d = 0.5 cm) .

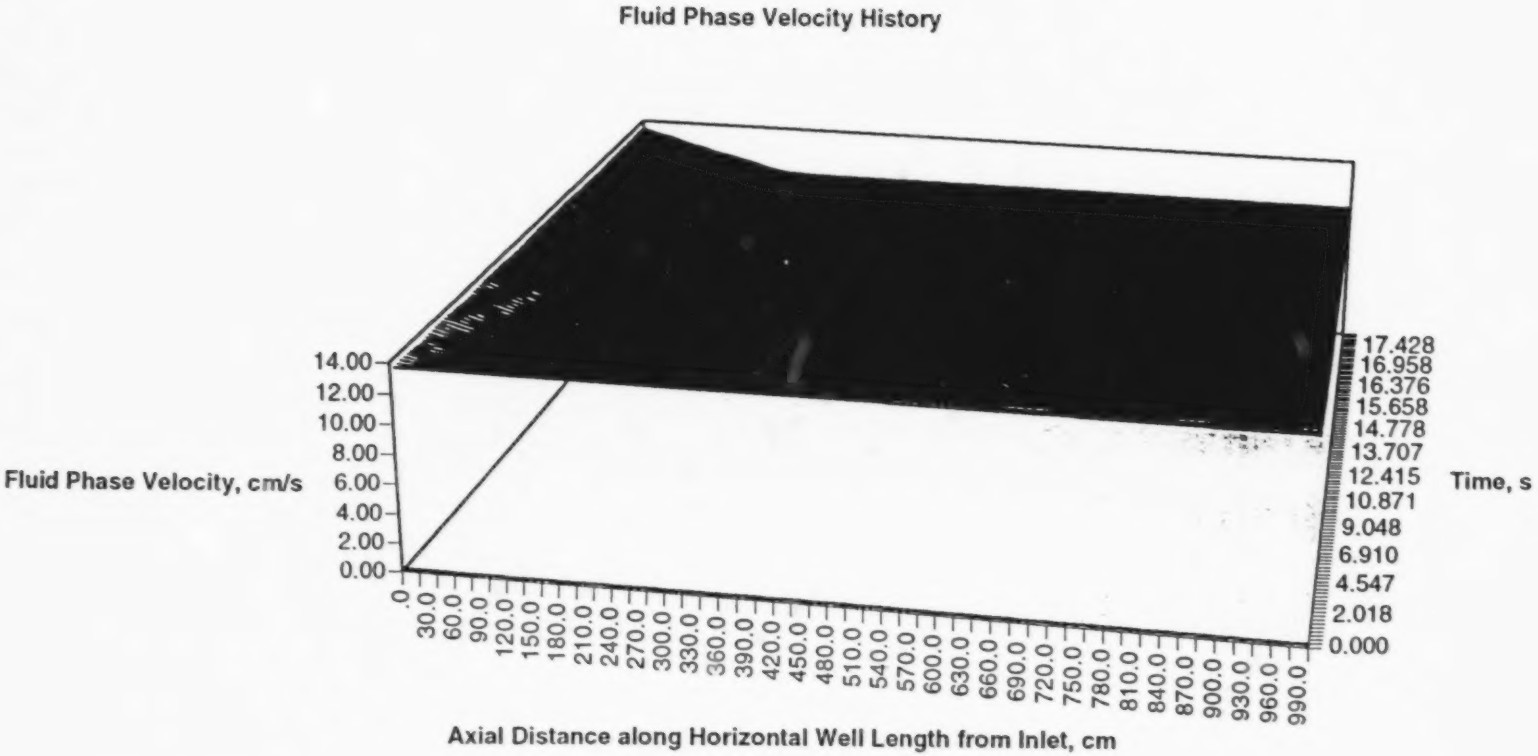

Figure 6.23: Gravity Deposition Model – Fluid Phase Velocity Profile for a light oil, Run GD/L/13 (μ = 25 mPa.s,W_t = 13.65 cm/s, d = 0.5 cm) .

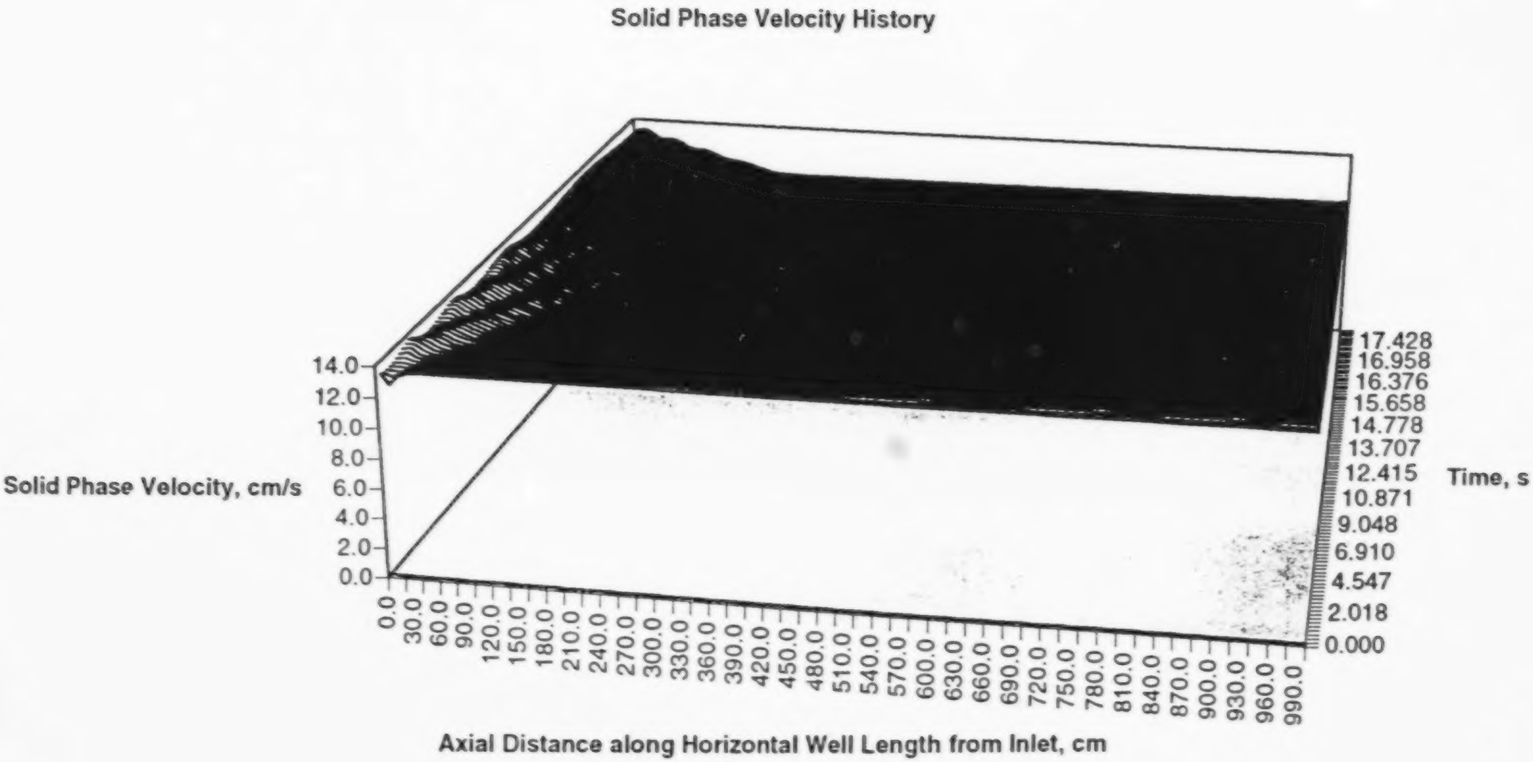

Figure 6.24: Gravity Deposition Model – Solid Phase Velocity Profile for a light oil, Run GD/L/13 (μ = 25 mPa.s,W_t = 13.65 cm/s, d = 0.5 cm) .

wider and wider area of flat surface on their lee-sides. This ridge expansion process, however, was observed to cease (after some time) when the sheltered area between two ridges extended to the next ridge downstream, thus preventing any further movement of the sand grains. It is believed that this mechanism of ripple formation and expansion, as observed and described above by Bagnold, is also at play in the formation of the waves observed in the results here.

Figure 6.20 illustrates the solid phase pressure profile with time. The run simulates the transport process for 17.4 seconds, before the memory allocated for it is used up. The pressure is fixed at 3 000 g/cm.s^2 at the well inlet, and 2 000 g/cm.s^2 at the well outlet. Beyond a certain distance the pressure distribution downstream seems not to be disturbed, and still maintains the initially fixed linear pressure-gradient profile. The pressure moves up and down, not only laterally downstream in the direction of flow (wave-like propagation), but also with time, i.e. it cyclically decreases for some time and then increases thereafter until the next cycle. In addition, these cyclical decreases and increases appear to attenuate with time. For the first wave the decrease is not more than 1 000 g/cm.s^2, and the increase is of the order of 500 g/cm.s^2, approximately. They become smaller thereafter.

The fluid phase pressure profile is very similar to that of the fluid phase pressure. As such, it is not presented here. There seems to be no difference in the magnitudes of these two phase pressures, and this is confirmed in Figure 6.21. Recalling the definition of the kinematic pressure (Equation 4.18), the very small magnitude of the kinematic pressure (less than 1.0 g/cm.s^2) indicates either negligible particle-particle collisions and/or small slippage between the fluid phase and solid phase velocities. This is shown to be the case in the profiles of fluid phase concentration (Figure 6.22), fluid phase velocity (Figure 6.23) and solid phase velocity (Figure 6.24). The solid phase concentration peak is approximately 25% volume fraction. This figure shows a net gain of 5% volume fraction in the solid phase concentration (after approximately 18 seconds), due to gravity deposition in the region near the bottom of the horizontal well. This small gain in the solid phase concentration also indicates little or few collisions among the solid particles. It is interesting to note how the fan-like behaviour seen in the kinematic pressure profile right at the well inlet (Figure 6.21) matches that seen in the fluid phase concentration profile (Figure 6.22).

As seen in Figure 6.23, the fluid phase velocity profile is largely devoid of the ripples prominently seen in the other figures. Its behaviour also contrasts with the solid phase velocity profile, seen in Figure 6.24. It is postulated that the fluid phase, being the continuous phase in the two-phase system, readily maintains its "volume-averaged" velocity distribution. As such, it is less affected by the presence of the small ripples. The (faint) presence of two ripple-like streaks in the fluid phase velocity at the well inlet at the earlier time is proof that the fluid phase velocity is also affected by the deposition process – albeit for only a short duration and lesser degree, before it adjusts to the new flow geometry. The solid phase, on the other hand, is – despite its continuum assumption – still the disperse phase in the model. As such, its velocity distribution is directly affected by the deposition process, including the formation of the ripples at the bottom of the horizontal well.

In addition, it is important to recall the basis for Equation 4.43 which governs the profile of the deposit bed. As stated, the height of the deposit bed varies with time strictly on the basis of how high the solid particles velocity (i.e. solid phase velocity) is in relation to the critical velocity. In the event that the solid phase velocity is less than the critical velocity, the solid particles "sink" and are deposited by gravity. There is no deposition when the reverse situation is true, i.e. the solid phase velocity is larger than the critical velocity. The fluid phase and solid phase velocities away from the deposition area show little change from their prescribed boundary values. This is due to the fact that there is no sand deposition at positions downstream, away from the well inlet for what is still only the initial stage of the deposition process (only 18 seconds, approximately). Additionally, by overlaying the fluid phase concentration profile and the solid phase velocity profile it is seen that the waves in the solid phase velocity profile are out of phase with those seen in the fluid phase concentration profile. As such, even though the magnitude of change is extremely small it is still seen that as the ripples form the solid phase velocity increases over the crest of the ripples, and reduces over their troughs.

In summary, the pressures for both the fluid phase and the solid phase change noticeably at the well inlet, directly as a result of sand deposition there. The fluid phase velocity adjusts very quickly to the formation of ripples at the well inlet, and seems to be largely unaffected. The solid phase velocity profile is pronouncedly influenced by the formation and expansion of the ripples at the bottom of the horizontal well. However, there is very little slip between the two velocities. There is also, for the time interval simulated, very little buildup in the solid phase concentration and consequently negligible particle-particle collisions. These two factors combine to produce a negligible kinematic pressure. As a consequence, there is, basically, no difference between the fluid phase pressure and solid phase pressure. It is seen that the results presented here for the Gravity Deposition model follow more closely the results for Case 2 of the Constriction model, when the interfacial drag force dominates the transport process. This comparison is arrived at in full recognition of the different features in the two models, as discussed above.

Thus, it is seen that the Gravity Deposition model, which is developed on the basis of two distinct pressures for two phases, produces results proving (or at least showing) the two phase pressures being almost identical to one another for the hydrodynamic conditions prescribed. Based on this observation, it can be argued quite convincingly that the simpler one-pressure, two-phase modelling approach would have sufficed. Such argument, however, neglects to consider two important considerations. To counter this argument it is important to recall the many assumptions invoked in the development of both the Constriction model and the Gravity Deposition model. And yet as seen in the results presented above, and the results presented in the next section, there are still many other mechanisms which influence the transport process. More importantly, these mechanisms have in some cases complementary influences, and in other cases competing influences. The two-phase, two-pressure formulation enables insights to be gained into the role and influence the various mechanisms have on the transport process. This is especially important in the case of multiphase flow, when the variables involved are quite often coupled, and interphase interactions are more than likely poorly understood. As such, one-pressure, two-phase models would not, and could not provide easily the window through which these sometimes complementary, sometimes competing influences can be gauged and determined. Second, while some of the results presented by Givler et al. [83] are puzzling, most of them are logical. It may even be argued that these results (especially, results for Case 1) are obtained from exaggerated conditions (for example, very low fluid phase viscosity). On the other hand, the possibility (and even probability) of conditions arising which results in intense intraphase interactions (as in particle-particle collisions) and large slip between the two phases cannot be completely discounted. When this possibility is realized, the one-pressure, two-phase modelling approach will prove inadequate.

6.4. Gravity Deposition Model – Effect of Hydrodynamic Variables

In the following sections, results are presented to examine the effect of different variables on the formation and expansion of a sand deposit bed at the bottom of a horizontal well. It is worthwhile to point out that in the simulation runs the effect of individual variables is determined. This approach is used, instead of evaluating the effect of the interconnection of the variables – as expressed in the form of dimensionless similarity groups – even though it is within the present capability. This is also in view of the readily available dimensionless groups which are derived in Chapter 5. The primary reason for this decision is a desire to learn first, and explicitly, the influence of a specific variable on the gravity deposition process. It is believed that only after a thorough understanding of the influence of each and every variable is obtained can the effects of their combinations be analyzed judiciously.

Two cases are considered: Light Oil and Heavy Oil. For each of these two cases three variables are examined separately: oil viscosity, solid phase velocity, and solid particle diameter. The strategy is to isolate one variable at a time and study its influence on the gravity deposition process – as reflected in the deposition profile against the plane of symmetry (Figure 4.3), while keeping constant all the other variables. Two oil viscosities, three velocities, and two particle sizes are used for each of the two cases. The values are chosen, as stated in the previous section, with consideration of the storage memory limitation of the personal computer (MacIntosh Quadra 800), and the need and desire to investigate the effects of as many variables as possible on the transport process. Altogether, 25 simulation runs were carried out – 13 for the Light Oil case, and 12 for the Heavy Oil case. It is important to point out that in the following discussions the term "well inlet" does not necessarily depict the toe of the horizontal well. Rather, as indicated in the figures, it denotes also the point where oil and sand are introduced into the horizontal well (perforation). The term "well inlet" is used mainly because it is more compact.

6.4.1. Light Oil

For the Light Oil case, the two oil viscosities are 25 mPa.s and 100 mPa.s; the solid phase velocities are 6.1425 cm/s, 12.285 cm/s, and 24.57 cm/s; and the two particle sizes are 0.1 cm and 0.5 cm. The solid phase velocities are chosen, in all three cases, to be nine-tenths of the fluid phase velocities. The corresponding fluid phase velocities are 6.825 cm/s, 13.65 cm/s, and 27.3 cm/s. These fluid velocities are equivalent to an average flow rate of 150.0 m^3/day, 300.0 m^3/day, and 600 m^3/day. These values are judged to be reasonable horizontal well production rates for Light Oils. In all cases, snapshots of the profiles of the deposit bed for different cases are taken. They are then cross-compared to evaluate the influence of the isolated variable. There is a pressure differential of 1 000 g/cm.s^2 (100 Pa) across the 100-cm segment of the horizontal well. For the periods of the deposition process simulated it is seen that changes occur only within the first quarter length of the segment. Beyond this interval there is negligible change in the inside profile of the horizontal well. Consequently, results are only presented for this length interval.

6.4.1.1. Effect of Oil Viscosity

Six different graphs are presented to examine the effect of oil viscosity in the Light Oil case. They are given in Figures 6.25 – 6.30. These figures are studied, individually, below.

a) Well production rate = 150.0 m^3/day, particle diameter = 0.5 cm

It is seen in Figure 6.25 that there is more sand deposition for the less viscous oil (Run L 01, viscosity=25 mPa.s) at the end of 0.20 second, and 0.52 second. The peak of the deposit bed (at the inlet) goes from 0.025 to 0.120 fraction of the horizontal well radius for the more viscous oil (Run L 07, viscosity=100 mPa.s), and from 0.075 to 0.220 fraction of well radius for the less viscous oil. The rate of change in the height, measured on the basis of the peak, of the deposit bed between these time periods is 0.095 and 0.145 of the wellbore radius for the more viscous oil and less viscous oil, respectively. The profile in the vicinity of the well inlet is more abrupt for the less viscous oil, and more gradual (i.e. lower peak, and wider base) for the more viscous oil. Downstream from the inlet the deposition profile is more even, and uniform for both.

There is a clear change in the deposition pattern between the end of the second and fourth time periods (t=0.52 second, and t=1.85 seconds, respectively). The deposit profile for

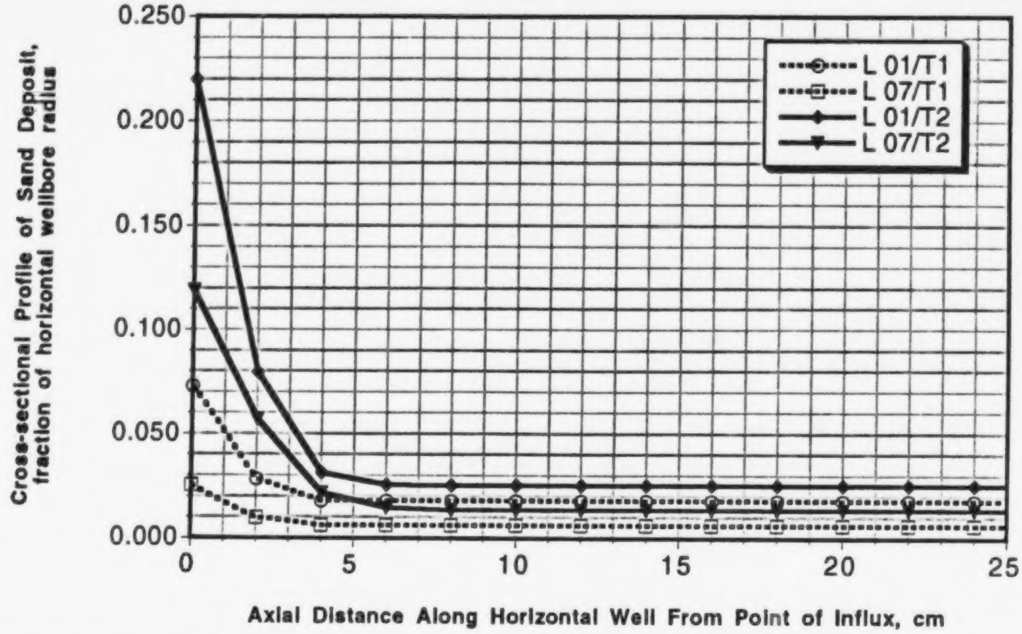

a) Profiles at time T 1 (t = 0.20 s), and at time T 2 (t = 0.52 s)

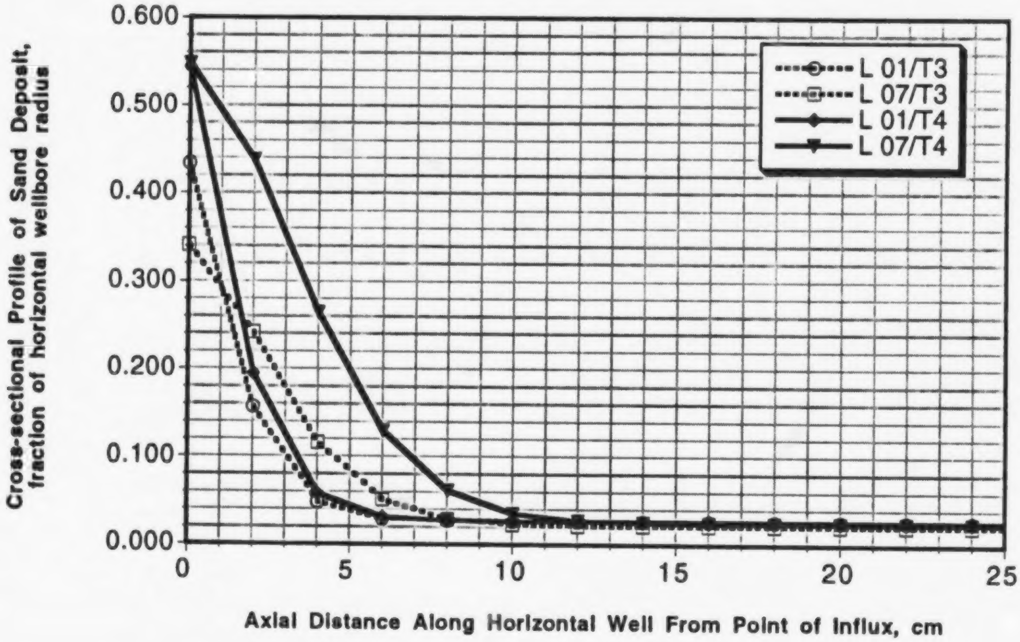

b) Profiles at time T 3 (t = 1.19 s), and at time T 4 (t = 1.85 s)

Figure 6. 25: Light Oil/Effect of oil viscosity – Profile of sand deposit at different times for two light oils, Run L 01 ($\mu = 25$ mPa.s) and Run L 07 ($\mu = 100$ mPa.s), $W_f = 6.825$ cm/s, $\rho_o = 0.90$ g/cm^3, d = 0.5 cm .

the more viscous oil (Run L 07) not only reaches about the same height (peak-wise) as, but expands sideways much more than, the profile for the less viscous oil (Run L 01). This means that there is more sand deposition for the more viscous oil at the end of 1.85 seconds, as indicated by the areas underneath the two curves at the end of this time. This reversal of trend already begins to occur at the end of 1.19 second, when the peak of the more-viscous- oil profile starts to reach (more or less) the same height as that for the less viscous oil. More importantly, its base is already about 1-2 cm wider than that for the less viscous oil.

The deposition rate for both cases is rather fast, especially for the more viscous oil: in about 2.0 seconds there is not only sand deposition, but also the deposit bed is growing quickly both in height and width (i.e. lateral extension). Vertically, more than half of the well radius (or one-quarter of the full height of the horizontal well) – measured from the well bottom – is filled up with sand. This growth is not confined to the vertical direction only. It also proceeds horizontally, in the direction of flow; and it does not occur exclusively at the well inlet, but also takes place 5-7 cm downstream.

b) Well production rate = 300.0 m^3/day, particle diameter = 0.5 cm

The results for this particular case are given in Figure 6.26. At the end of 0.10 second there is more deposition for the less viscous oil (Run L 02, viscosity=25 mPa.s), whose deposit profile is more abrupt. At the end of 0.82 second there is a slight change in the deposition pattern. Again, the profile for the less viscous oil is more abrupt, with the profile peak at the well inlet reaching approximately 0.60 fraction of the well radius, and its base extending 10 cm (beyond this distance the deposit bed height is considered negligible) downstream. The more-viscous-oil (Run L 08, viscosity=100 mPa.s) profile is more gradual, having a lower peak (only 0.26 fraction of well radius) and a more spread out distribution. This difference is the deposition pattern is believed to be due to the solid-carrying characteristics, reflected by the different viscosities of the oils. The total amount (or volume) of sand deposition is approximately the same for the two viscosities. This is observed in the two areas enclosed by the intersection of the two profiles: the first area extending from the well inlet to 3 cm downstream, and the second area extending from 3 cm to 10 cm downstream. They are very comparable to one another.

The small time gap between the last two time periods (end of 1.04 seconds, and 1.20 seconds, respectively) expectedly shows little change in the deposit bed profile, especially for the less viscous oil. The change is more noticeable for the more viscous oil. In going from T2 (t=0.82 second) to T3 (t=1.04 seconds) it is also seen that there is little change, in both the vertical and lateral direction, in the profile for the less viscous oil. This behaviour suggests the deposition and expansion process for the less viscous oil reaches steady/pseudo-steady state.

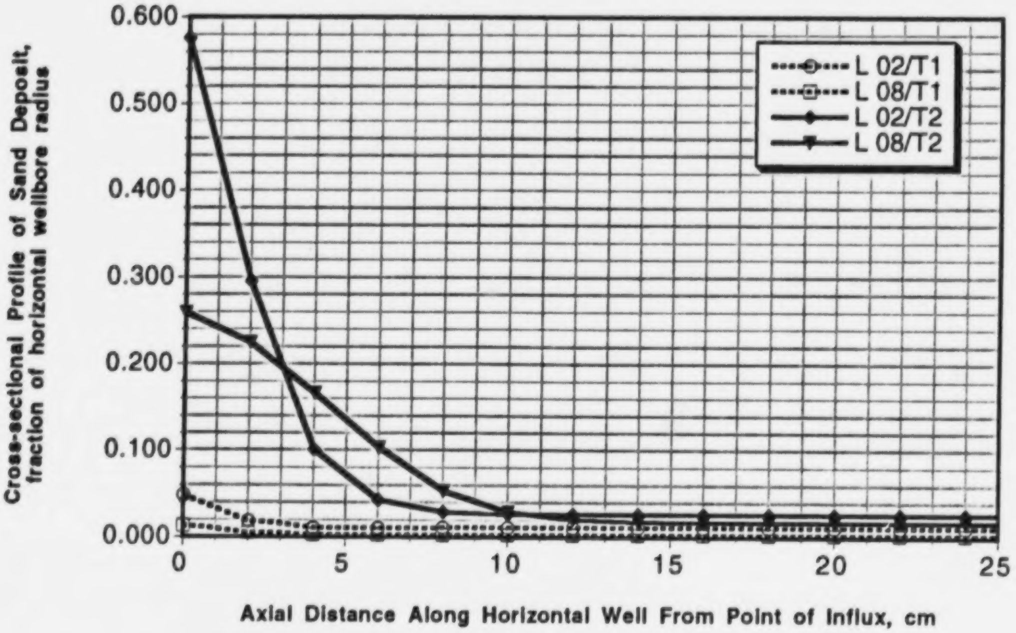

a) Profiles at time T 1 (t = 0.10 s), and at time T 2 (t = 0.82 s)

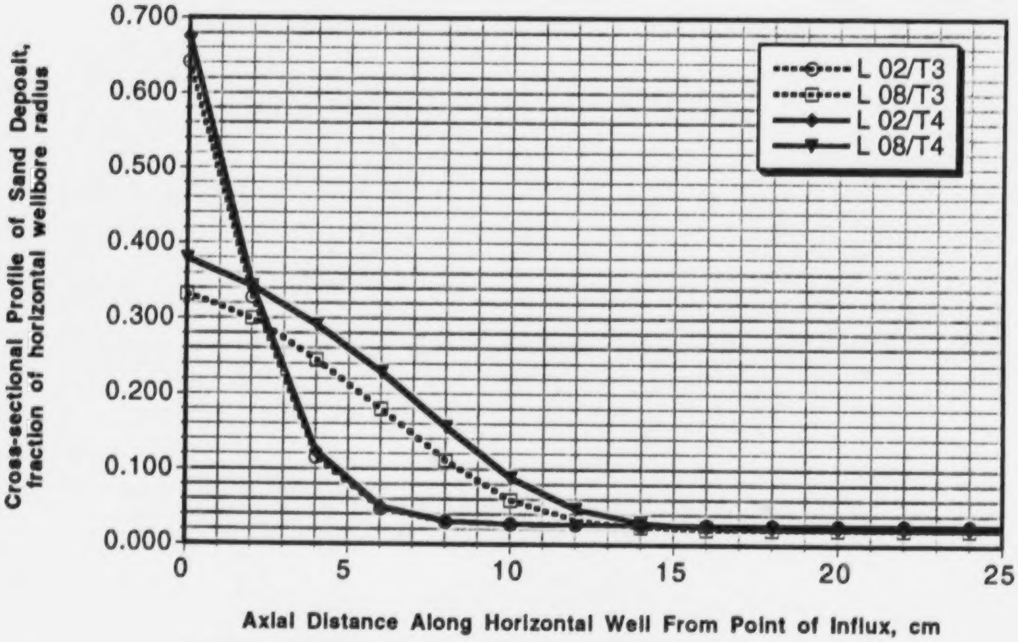

b) Profiles at time T 3 (t = 1.04 s), and at time T 4 (t = 1.20 s)

Figure 6. 26: Light Oil/Effect of oil viscosity – Profile of sand deposit at different times for two light oils, Run L 02 (μ = 25 mPa.s) and Run L 08 (μ = 100 mPa.s), W_f = 13.65 cm/s, ρ_o = 0.90 g/cm^3, d = 0.5 cm .

The more-viscous-oil (Run L 08) profile continues to expand between T2 and T3, as well as between T3 and T4. For the first of these two intervals, the peak of the profile increases from 0.260 to 0.330 fraction of the well radius at the well inlet, and from 0.140 to 0.220 fraction at 5 cm downstream. During the period of 0.16 second between T3 and T4, this profile continues to expand – rather uniformly, as the rate of increase for the profile is approximately 0.05 and 0.04 fraction of well radius at the well inlet and 5 cm downstream, respectively. This observation suggests that the deposition and expansion process for the more viscous oil is about to reach some steady/pseudo-steady state.

Comparing the areas below the two profiles at the end of T4 (t=1.20 seconds) it is seen that the volume of sand deposition is more for the more viscous oil. This is opposite to the results seen at the end of T2 (t=0.82 second). But, it is consistent with the results seen in sub-case a) above.

c) Well production rate = 600.0 m^3/day, particle diameter = 0.5 cm

Figure 6.27 provides results for a sub-case, which except for higher flow velocity, is similar to the above two sub-cases. At the end of T1 (t=0.09 second) there is more deposition for the less viscous oil (Run L 03, viscosity=25 mPa.s). At the end of T2 (t=0.32 second) this trend is still there, except that the gap between the two profiles is bigger – not just at the well inlet, but also 5 cm downstream. It is clear that at the end of this time interval there is much more sand deposition for the less viscous oil, indicated by the fact that the area below the less-viscous-oil profile is larger everywhere than its counterpart below the more-viscous-oil profile. The deposition rate, considered in terms of the peak of the deposit bed being 0.38 fraction of the well radius, is fast for the less viscous oil – despite the high axial fluid (by extension, solid phase) velocity which tends to carry the solid particles further downstream before they settle down.

Between T2 and T3 (t=0.61 second) the high deposition rate for the less viscous oil continues, with the peak of the deposit bed going from 0.38 to 0.75 fraction of the well radius at the well inlet. This expansion is not confined to the immediate vicinity of the well inlet, however. It also occurs, albeit at a lower rate, some distance (8 cm) downstream of the inlet. From this observation, it is seen that the high velocity (equivalent to 600 m^3/day) in this sub-case has only a limited effect in delaying the deposition of sand particles. The growth rate for the more-viscous-oil (Run L 09, viscosity=100 mPa.s) deposition profile is also substantial, with the profile peak increasing from 0.09 to 0.20 fraction of well radius, at the well inlet, in the 0.31- second between T2 and T3. The profile at the end of T3 is quite similar to that at the end of T2, suggesting uniform expansion throughout the deposit bed profile.

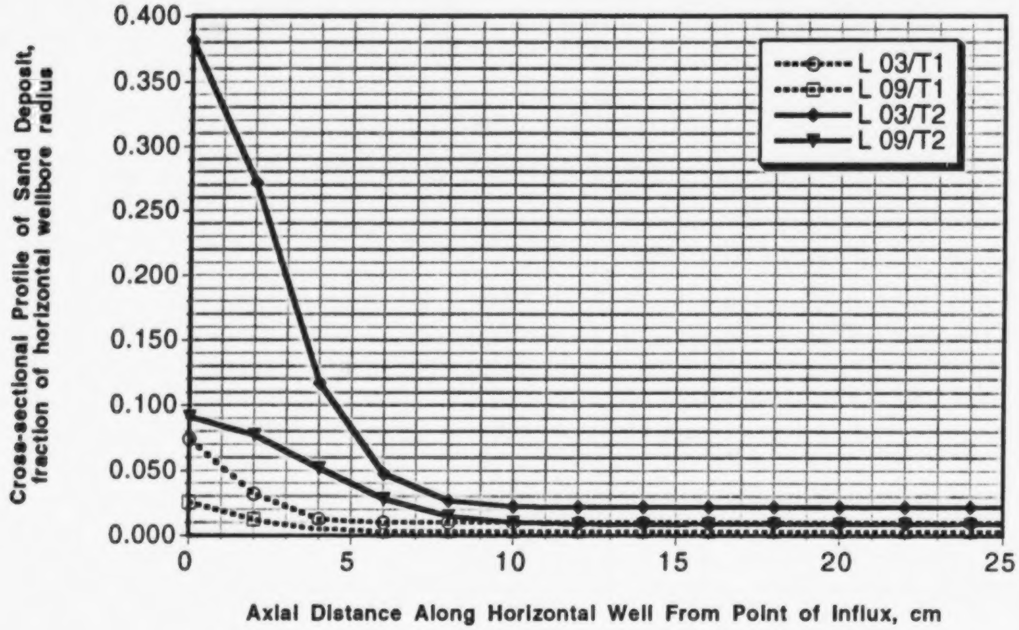

a) Profiles at time T 1 (t = 0.09 s), and at time T 2 (t = 0.32 s)

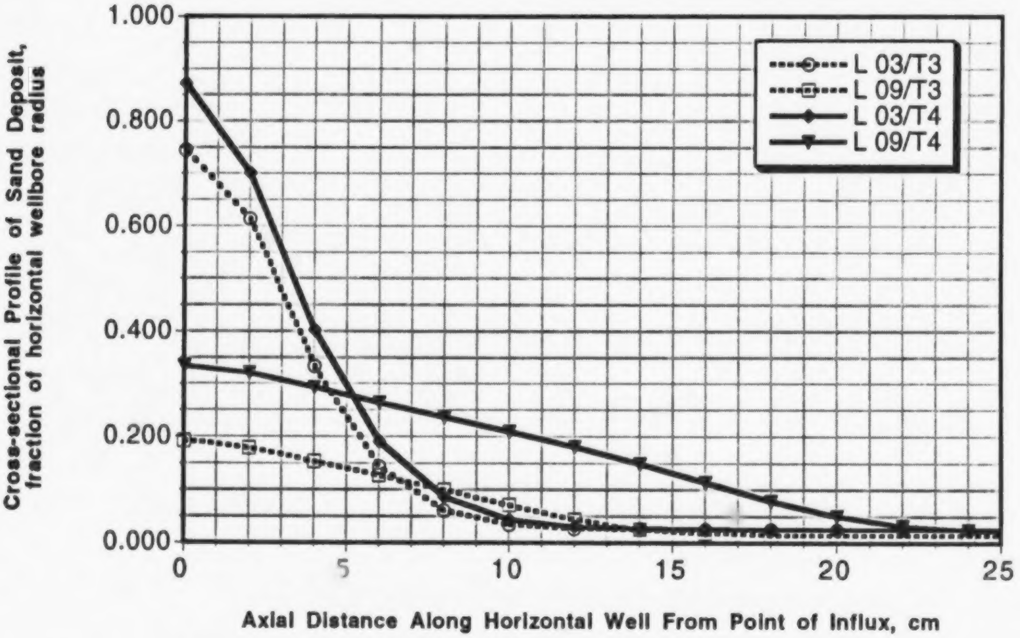

b) Profiles at time T 3 (t = 0.61 s), and at time T 4 (t = 1.01 s)

Figure 6. 27: Light Oil/Effect of oil viscosity – Profile of sand deposit at different times for two light oils, Run L 03 (μ = 25 mPa.s) and Run L 09 (μ = 100 mPa.s), W_t = 27.30 cm/s, ρ_o = 0.90 g/cm^3, d = 0.5 cm .

Between T3 and T4 (t=1.01 seconds) the profiles for both the less viscous and more viscous oil continue to expand, with the expansion rate much reduced for the less-viscous-oil profile. For the less viscous oil, the small gap between the deposition profiles at the end of T3 and T4 – even for the relatively small time interval of 0.40 second – indicates that perhaps the transport process is about to reach steady/pseudo-steady state. It is rather remarkable, keeping in view the previous discussion of input data selected to speed up the deposition process, that the less viscous oil results in such quick deposition. Close to half of the full vertical height of the horizontal well is occupied by a sand deposit bed after only 1.0 second, despite the high axial flow velocity. For the more viscous oil, the deposit bed profile continues to expand at a relatively high rate. In addition, the expansion is very uniform along most of the length of the deposit bed. This uniform expansion results in a gradual, spread-out deposit bed. Keeping in view the fact that although the mathematical model does not include any description of the structural integrity of a deposit, it is still possible to state that the more-viscous-oil deposit bed is more stable than its less-viscous-oil counterpart.

d) Well production rate = 150.0 m^3/day, particle diameter = 0.1 cm

The deposition profiles for the two viscosities are given in Figure 6.28. There is more deposition for the less viscous oil (Run L 04, viscosity=25 mPa.s) at the end of T1 (t=0.75 second). Most of the deposition, as usual, takes place near the well inlet, and there is little deposition downstream at this early time; this observation is true for both oils. The large time interval of 1.0 second between T1 and T2 (t=1.75 second) enables large changes in the deposition profile for both oils, in particular the less viscous oil. The profile peak increases from 0.035 to 0.088 fraction of well radius, at the well inlet, during this interval. As observed, the rate of expansion is highest at the well inlet, and becomes progressively smaller downstream. The expansion rate for the more viscous oil (Run L 10, viscosity=100 mPa.s) is less spectacular, but nevertheless still very noticeable. It is clear that at the end of 1.75 second there is more sand deposition for the less viscous oil. This result is consistent with those observed for sub-cases a), b), and c) previously.

Between T2 and T3 (t=2.50 seconds) the deposit bed profile continues to expand, with the less-viscous-oil profile having a larger vertical expansion rate (particularly, at the well inlet) than the more-viscous-oil profile. The gradual deposit bed profile, i.e. relatively low peak and spread out base, is maintained for both oils. The same trends continue in the interval between T3 and T4 (t=3.77 seconds). The relatively low expansion rate, as indicated by the wide gaps between the profiles, suggests that the deposition process will continue – slowly, but steadily – and will not reach a steady/pseudo-steady state soon. At the end of 3.77 seconds the volume of sand deposition is more for the less viscous oil than for the more viscous oil. This observation contradicts those of the previous sub-cases. This observed difference is probably due to the smaller particle size in this case. It is also possible that in the end (which in this case, t >>> 3.77 seconds) a result

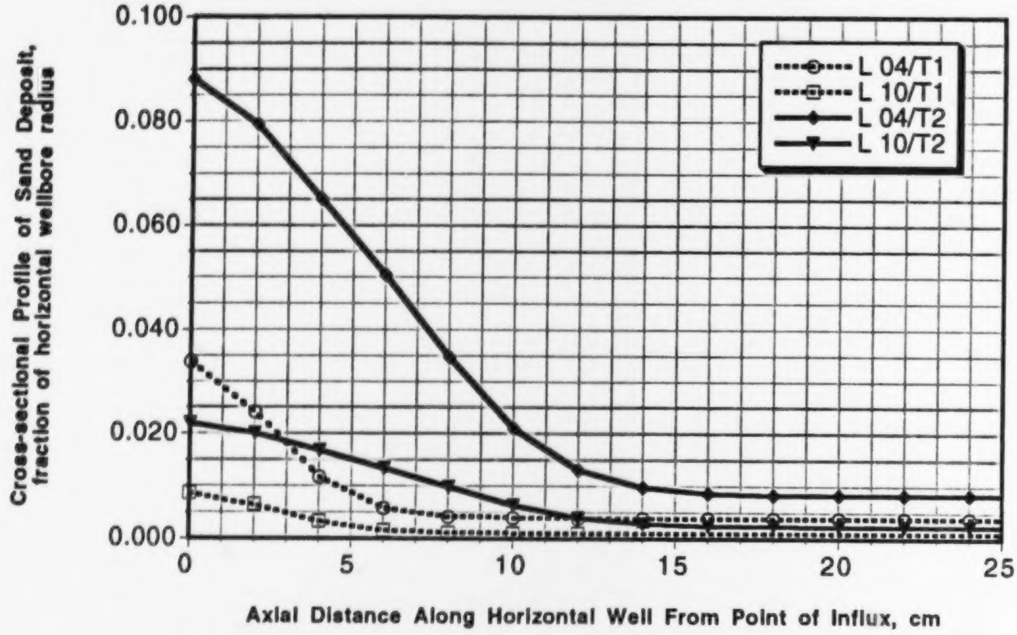

a) Profiles at time T 1 (t = 0.75 s), and at time T 2 (t = 1.75 s)

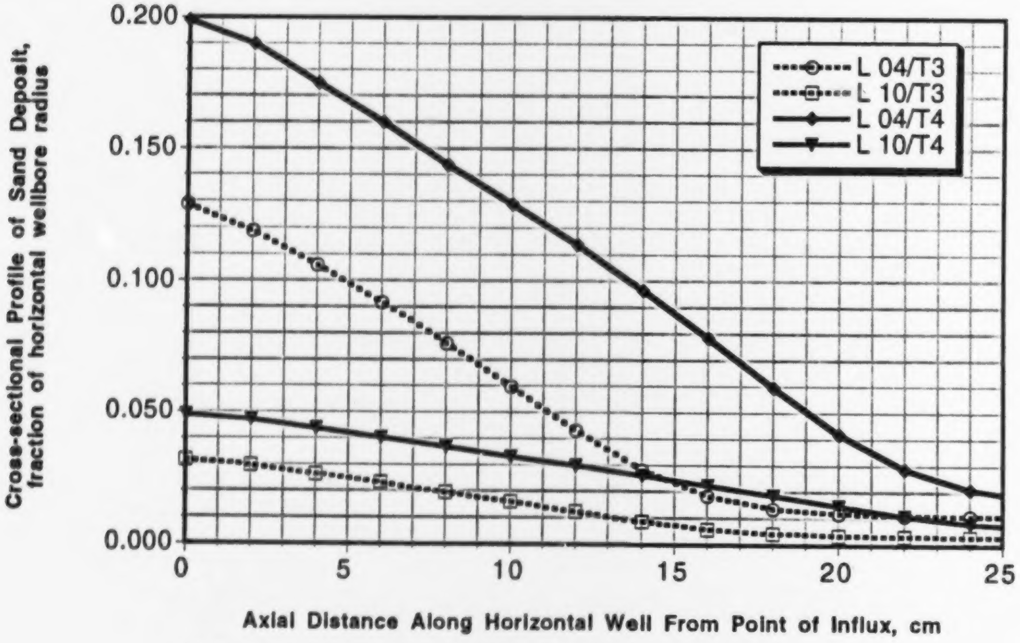

b) Profiles at time T 3 (t = 2.50 s), and at time T 4 (t = 3.77 s)

Figure 6. 28: Light Oil/Effect of oil viscosity – Profile of sand deposit at different times for two light oils, Run L 04 (μ = 25 mPa.s) and Run L 10 (μ = 100 mPa.s), W_f = 6.825 cm/s, ρ_o = 0.90 g/cm^3, d = 0.1 cm .

similar to those from the previous sub-cases is obtained. The smaller particle size, as discussed above, tends to keep them in suspension for a longer time before gravity settling; thus, it stretches the deposition process out, longer.

e) Well production rate = 300.0 m^3/day, particle diameter = 0.1 cm

In this sub-case, the trends are similar to those observed in sub-case d) above, at all times – from T1 (t=0.21 second) to T2 (t=0.75 second), T3 (t=1.25 seconds), and T4 (t=1.89 seconds), as seen in Figure 6.29. Comparing the deposition profiles for the two oils at the end of 1.89 seconds of the present sub-case with those at the end of 1.75 seconds of sub-case d), it is seen that there are also differences in the actual profiles. Given the difference in these two times (1.75 seconds, as opposed to 1.89 seconds), the less-viscous-oil (Run L 05, viscoisty=25 mPa.s) deposition profile for this sub-case is (slightly) higher at the inlet – 0.100 fraction of well radius compared to 0.090 approximately, and at some distance (for example, 12 cm) downstream – 0.060 fraction of well radius compared to 0.015, than the profile for sub-case d). As such, there is more sand deposition with higher axial flow velocity for the less viscous oil (25 mPa.s). The results are, however, opposite for the more-viscous-oil profiles, i.e. there is less sand deposition in the present sub-case than in sub-case d).

f) Well production rate = 600.0 m^3/day, particle diameter = 0.1 cm

First, it is noted that the various time intervals (T1, T2, T3, and T4) selected for the present sub-case approximate those selected for sub-case e). As such, an opportunity exists for, beside a comparison of the results to determine the effect of oil viscosity for this sub-case, a comparison of the results for the two sub-cases to determine – indirectly – the effect of axial flow velocity which at 27.3 cm/s is twice that in sub-case e). For this sub-case, it is seen in Figure 6.30 that the deposition profiles at the end of all time intervals (t=0.25 second, 0.74 second, 1.20 seconds, and 1.81 seconds for T1, T2, T3, and T4, respectively). The observation of more sand deposition for the less viscous oil deviates little from that observed for sub-cases d) and e). The difference is that the profiles in this sub-case are more spread out.

In comparing the results for this sub-case with those for sub-case e) to evaluate the influence of axial flow velocity on the formation and expansion of a deposit bed, it is important to point out that this comparison is rather indirect. In the series of results presented in the next section, the effect of flow velocity is isolated. Hence, its influence on the gravity deposition of sand inside a horizontal well is determined directly. It is seen that the deposition profile for both oils for the present sub-case is more spread out, and changes more gradually than those seen for sub-cases d) and e). The flow velocities in these two sub-cases are, at 6.825 cm/s and 13.65 cm/s, one-quarter and one-half the flow velocity in the present sub-case. Logically, the higher flow velocity

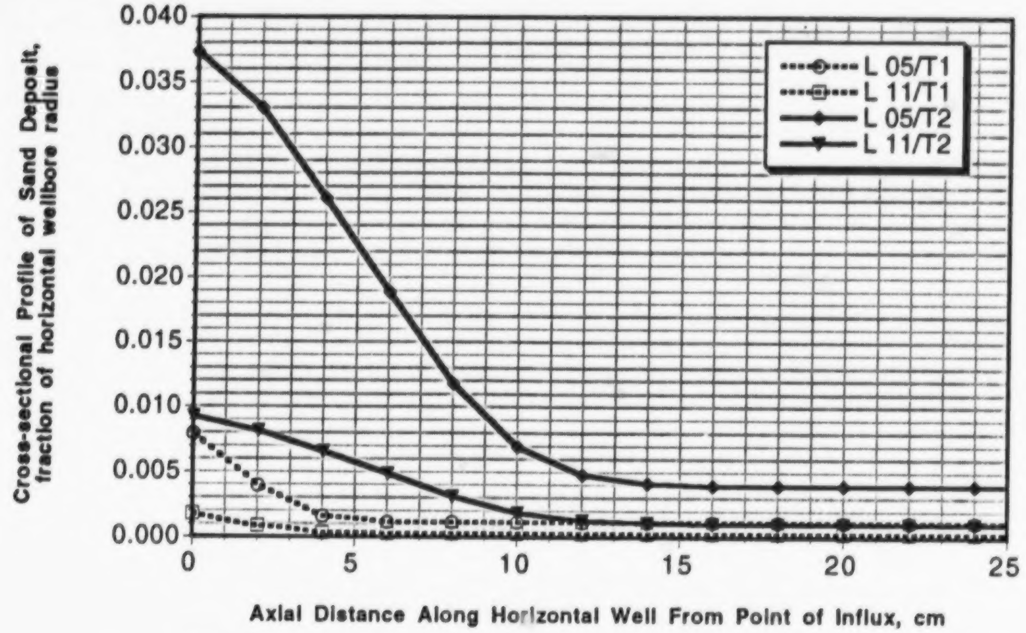

a) Profiles at time T 1 (t = 0.21 s), and at time T 2 (t = 0.75 s)

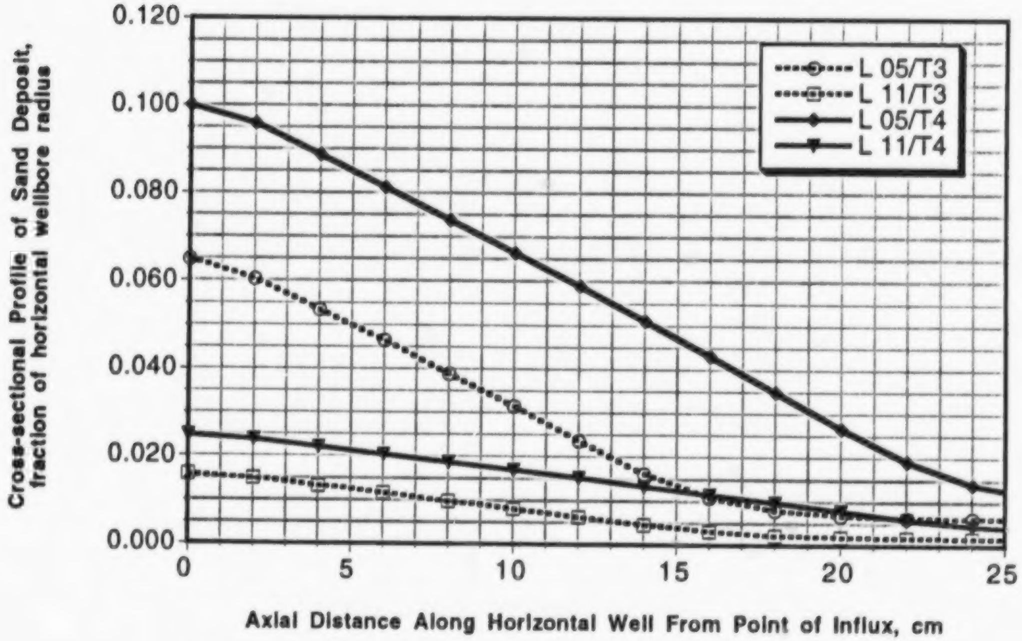

b) Profiles at time T 3 (t = 1.25 s), and at time T 4 (t = 1.89 s)

Figure 6. 29: Light Oil/Effect of oil viscosity – Profile of sand deposit at different times for two light oils, Run L 05 (μ = 25 mPa.s) and Run L 11 (μ = 100 mPa.s), W_f = 13.65 cm/s, ρ_o = 0.90 g/cm^3, d = 0.1 cm .

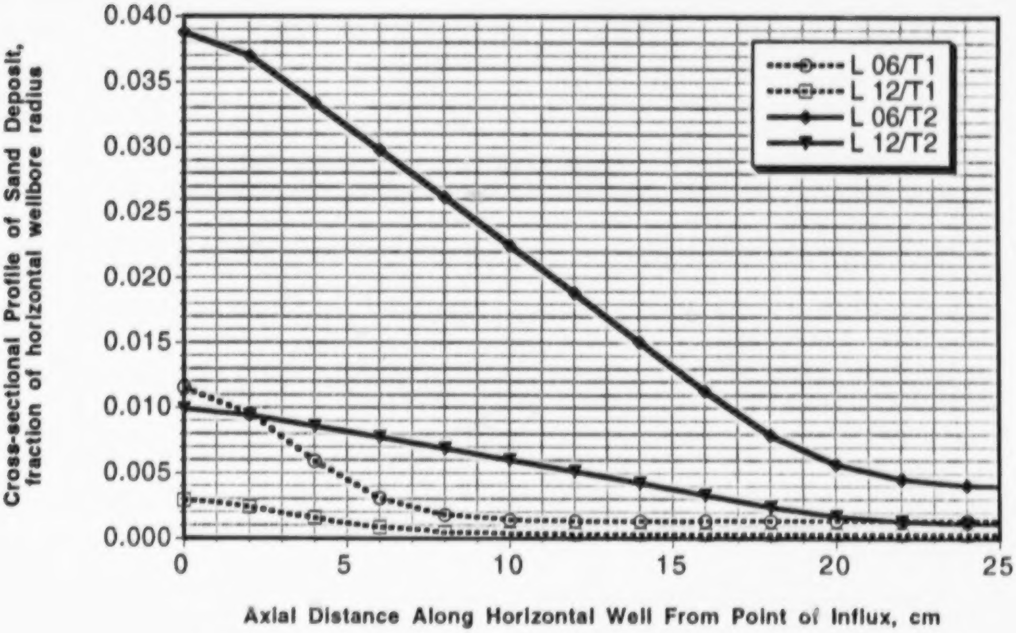

a) Profiles at time T 1 ($t = 0.25$ s), and at time T 2 ($t = 0.74$ s)

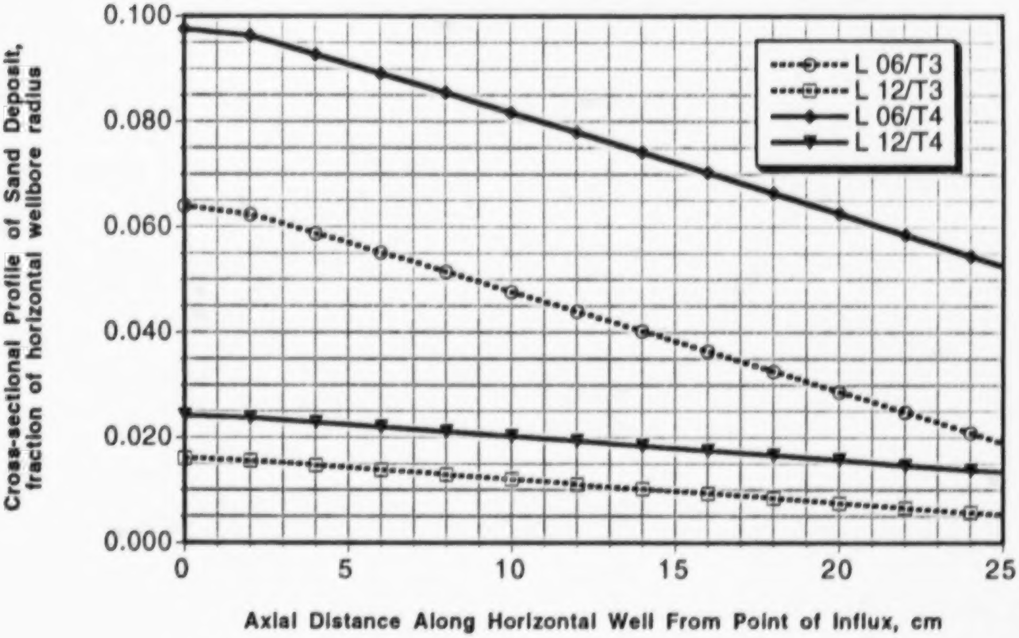

b) Profiles at time T 3 ($t = 1.20$ s), and at time T 4 ($t = 1.81$ s)

Figure 6. 30: Light Oil/Effect of oil viscosity – Profile of sand deposit at different times for two light oils, Run L 06 ($\mu = 25$ mPa.s) and Run L 12 ($\mu = 100$ mPa.s), $W_f = 27.30$ cm/s, $\rho_o = 0.90$ g/cm^3, $d = 0.1$ cm .

tends to carry the solid particles further along the flow channel before they "sink" under the influence of gravity. This logic supports the results observed here. However, it is also noted that the deposition profile for this sub-case – even though it is, as logically expected, more spread out – is more gradual primarily because the base of the deposit bed is larger, and not because the peak of the deposit bed is lower. This result suggests more sand deposition for higher flow velocity. As such, it seems at first to contradict the commonly-shared intuition stating a higher flow velocity results in less, not more, solid deposition. It is important to point out that in this study the solid phase concentration in the oil-sand suspension coming into the horizontal well is constant. As a result, a higher flow velocity corresponds to a higher throughput volume of sand. As such, it is not surprising that there is more sand deposition at higher flow velocity, not just in the sub-cases examined here, but also in the Heavy Oil sub-cases.

6.4.1.2. Effect of Velocity

In this series of results, the flow velocity is isolated to determine its influence on the transport process. Four different graphs are presented to examine the effect of velocity in the Light Oil case. They are given in Figures 6.31 – 6.34. Each of these figures is analyzed individually below. As stated above, three values are assigned for the flow velocity: 6.825 cm/s (Run L 01), 13.65 cm/s (Run L 02), and 27.30 cm/s (Run L 03).

a) Oil viscosity = 25 mPa.s, particle diameter = 0.5 cm

As seen in Figure 6.31 the deposition profiles for all three flow velocities are given at the end of T1 (t=0.09 second), T2 (t=0.38 second), T3 (t=0.80 second), and T4 (t=1.15 second).

Collectively, it is seen that the deposition process occurs at a high rate – as evidenced by the fact that the peak of the deposit bed reaches up to 0.22, 0.33, and 0.45 of the full height of the horizontal well, at the well inlet, after only 1.15 second. A higher flow velocity results in greater deposition, and this observation holds true at the end of every time interval. A higher flow velocity also results in more spread-out deposition pattern, as expected.

Table 6.5 is provided to examine the expansion rate of the deposit bed for the three velocities. It contains values of the peak of the deposit bed for the three velocities at the well inlet, and at 5 cm downstream. The expansion rate is the difference between these values divided by the time interval.

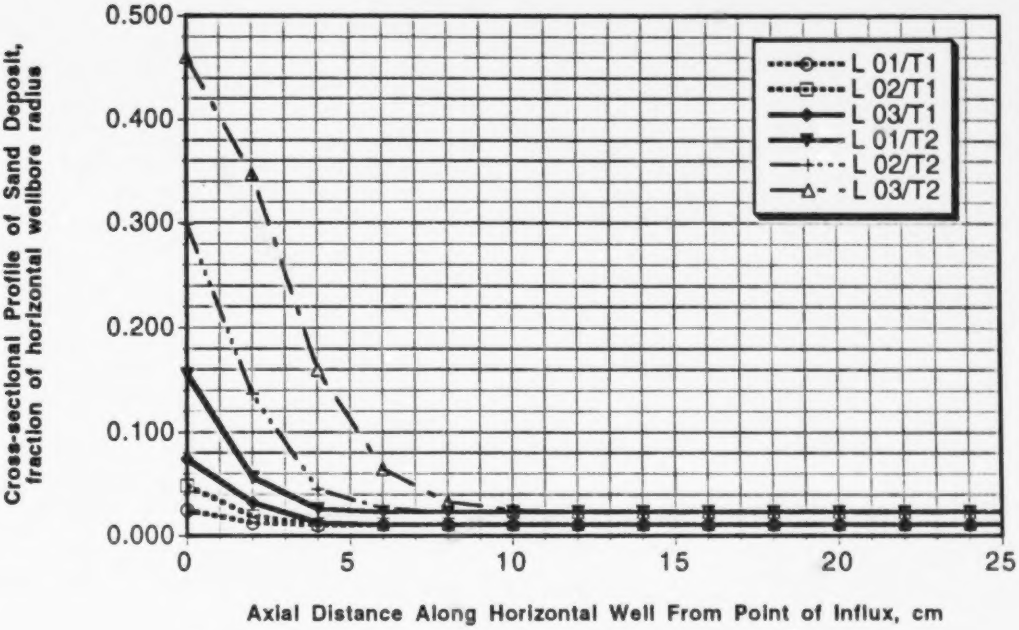

a) Profiles at time T 1 (t = 0.09 s), and at time T 2 (t = 0.38 s)

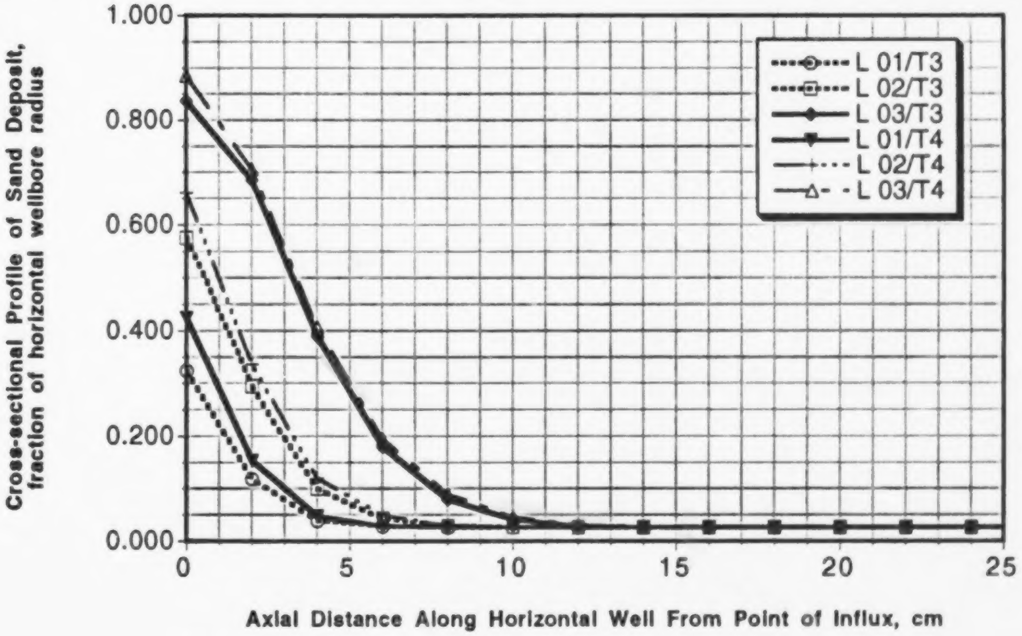

b) Profiles at time T 3 (t = 0.80 s), and at time T 4 (t = 1.15 s)

Figure 6. 31: Light Oil/Effect of flow velocity – Profile of sand deposit at different times for three velocities, Run L 01 (W_f = 6.825 cm/s), Run L 02 (W_f = 13.65 cm/s) and Run L 03 (W_f = 27.3 cm/s), ρ_o = 0.90 g/cm^3, μ = 25 mPa.s, d = 0.5 cm .

Table 6.5: Values of height of deposit bed at different positions, Gravity Deposition Model {between T2 (t=0.38 second) and T3 (t=0.80 second)}

	Well inlet				5 cm downstream			
	@T2	@T3	Diff.	Rate	@T2	@T3	Diff.	Rate
L 01	0.16	0.33	0.17	0.41	0.03	0.05	0.02	0.05
L 02	0.30	0.58	0.28	0.67	0.05	0.08	0.03	0.07
L 03	0.46	0.84	0.38	0.91	0.08	0.30	0.22	0.52

As seen in this table, between T2 and T3 the profile for Run L 03 (highest flow velocity) undergoes the largest expansion – not just at the well inlet, but also at a distance 5 cm downstream. Indeed, it is seen that the expansion is, compared to that for the other two velocities, even more pronounced downstream than at the well inlet for Run L 03. The second highest velocity (Run L 02) also has a high expansion rate at the well inlet; but, there is virtually no sand deposition, and hence, no expansion of the deposit bed downstream. This expansion behaviour for Run L 02 is similar, not necessarily in terms of magnitude, to that observed for Run L 01 which has the lowest flow velocity. The net result of these expansion behaviours, as reflected by the numbers presented in Table 6.5, is a more spread-out, gradual deposition profile for the higher flow velocity. Between T3 and T4, the small gaps seen between the profiles for all three flow velocities seem to indicate that their deposition processes reach a steady/pseudo-steady state.

b) Oil viscosity = 25 mPa.s, particle diameter = 0.1 cm

The flow velocities for the three runs whose results are illustrated in Figure 6.32 are as follows: 6.825 cm/s in Run L 04, 13.65 cm/s in Run L 05, and 27.30 cm/s in Run L 06. The general trend of a more spread-out deposition for a higher flow velocity, seen in sub-case a) above, is repeated. As above, Table 6.6 is given to facilitate the following discussion on the expansion of the deposit bed with time, as a function of the flow velocity.

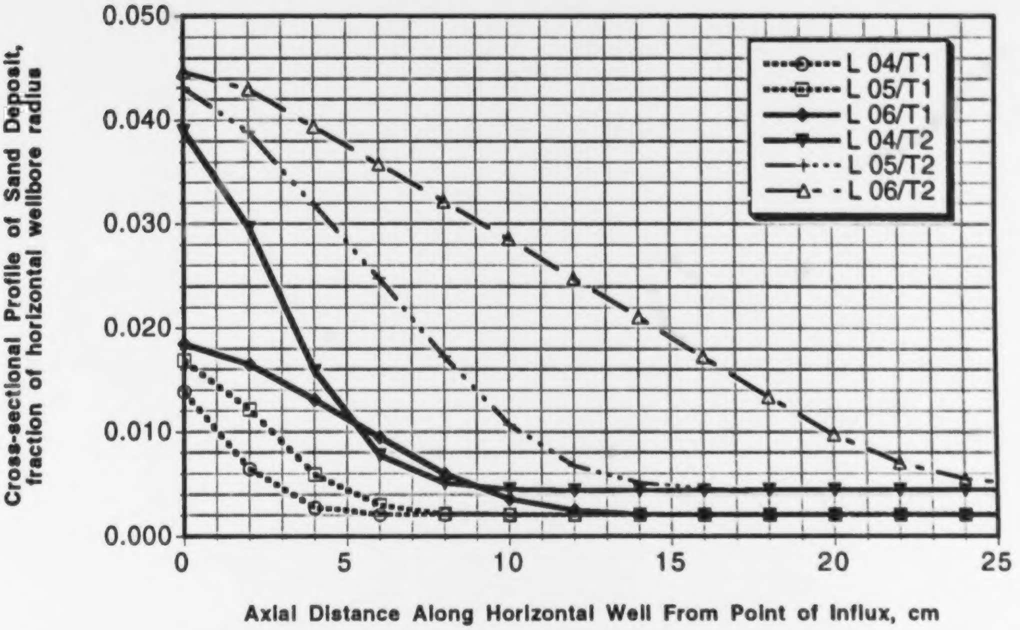

a) Profiles at time T 1 (t = 0.39 s), and at time T 2 (t = 0.85 s)

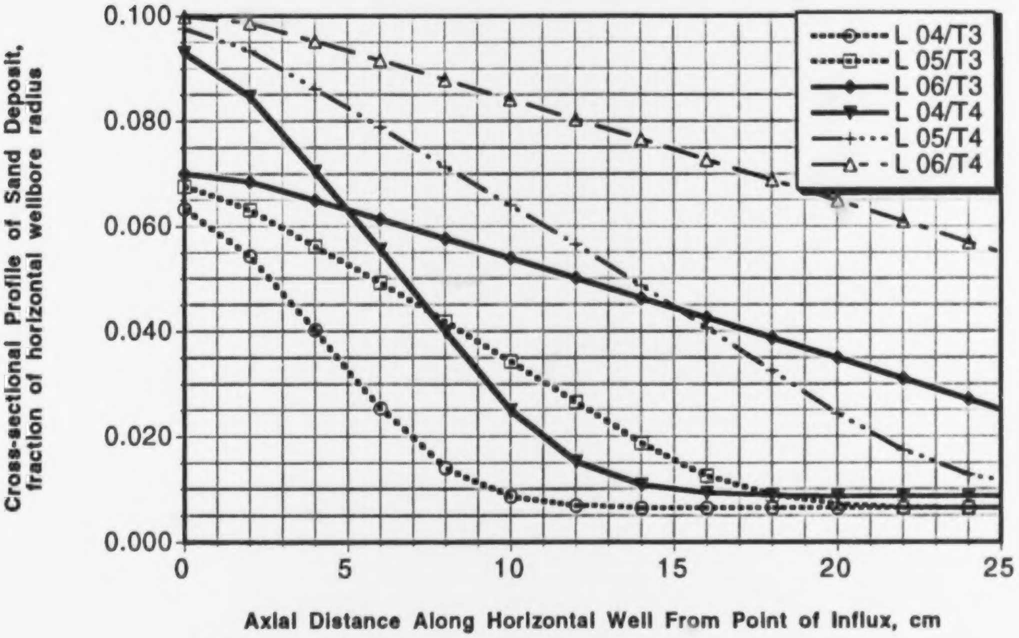

b) Profiles at time T 3 (t = 1.30 s), and at time T 4 (t = 1.85 s)

Figure 6. 32: Light Oil/Effect of flow velocity – Profile of sand deposit at different times for three velocities, Run L 04 (W_f = 6.825 cm/s), Run L 05 (W_f = 13.65 cm/s) and Run L 06 (W_f = 27.3 cm/s), ρ_o = 0.90 g/cm^3, μ = 25 mPa.s, d = 0.1 cm .

Table 6.6: Values of height of deposit bed at different positions, Gravity Deposition Model

* Between T2 (t=0.85 second) and T3 (t=1.30 seconds)

	Well inlet				5 cm downstream			
	@T2	@T3	Diff.	Rate	@T2	@T3	Diff.	Rate
L 04	0.033	0.063	0.030	0.07	0.012	0.033	0.021	0.04
L 05	0.042	0.068	0.026	0.06	0.028	0.053	0.025	0.05
L 06	0.045	0.070	0.025	0.05	0.038	0.065	0.027	0.06

* Between T3 (t=1.30 seconds) and T4 (t=1.85 seconds)

	@T3	@T4	Diff.	Rate
L 04	0.063	0.093	0.030	0.05
L 05	0.068	0.098	0.030	0.05
L 06	0.070	0.100	0.030	0.05

The changes between T3 and T4 at 5 cm downstream are negligible, and not included in Table 6.6. As can be seen, the expansion rates for all three flow velocities are very comparable between T2 and T3 – both at the well inlet, and at a distance of 5 cm downstream – and identical between T3 and T4. The deposit bed, for all three runs, expands very slowly. As seen clearly in Figure 6.32 the wide gaps between the profiles for all three flow velocities suggest that the deposition process is continuing, and not about to reach steady/pseudo-steady state.

A general conclusion is made, here, on the effect of particle size on the deposition process. Comparing the magnitude of the deposit bed peaks at various points along the horizontal well, as illustrated in Figure 6.32 (this sub-case) with those illustrated in Figure 6.31 (sub-case a) it is seen that the deposition process is much slower when the solid particle size changes from 0.5 cm to 0.1 cm.

c) Oil viscosity = 100 mPa.s, particle diameter = 0.5 cm

As seen in Figure 6.33, there is more deposition for Run L 09 (velocity = 27.30 cm/s) than for Run L 08 (velocity = 13.65 cm/s) and for Run L 07 (velocity = 6.825 cm/s) at the end of T2 (t=0.52 second). Its deposition profile is also more spread out. Data for the expansion rates for the three flow velocities are given in Table 6.7.

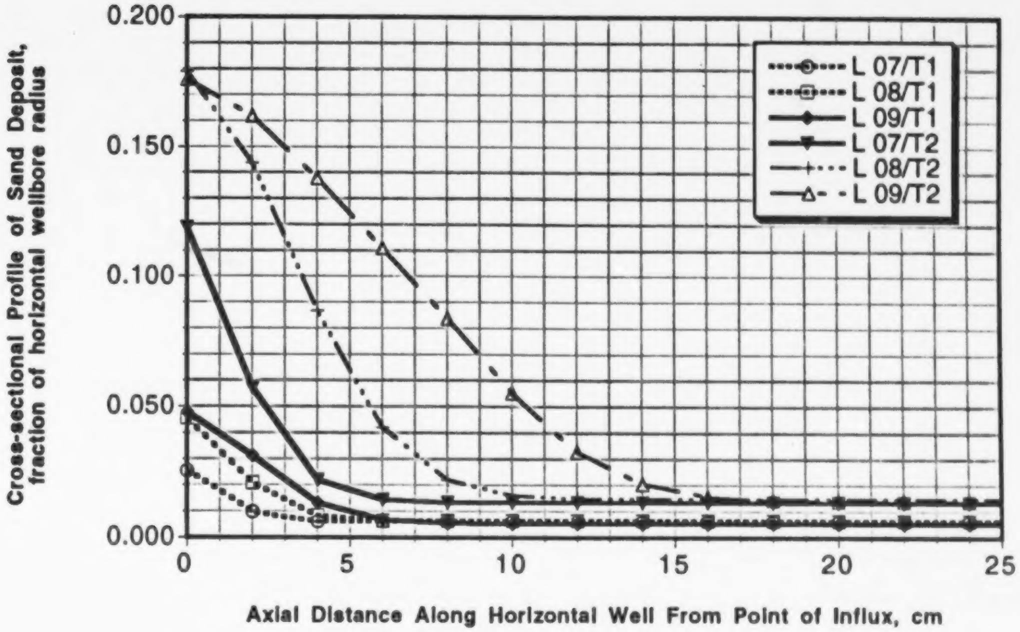

a) Profiles at time T 1 (t = 0.20 s), and at time T 2 (t = 0.52 s)

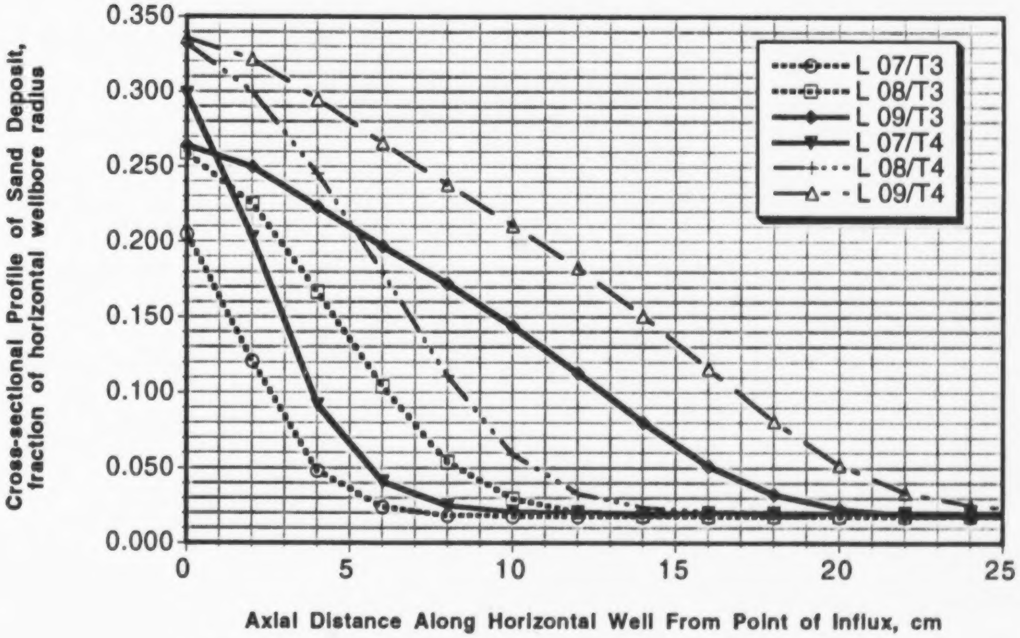

b) Profiles at time T 3 (t = 0.78 s), and at time T 4 (t = 1.05 s)

Figure 6. 33: Light Oil/Effect of flow velocity – Profile of sand deposit at different times for three velocities, Run L 07 (W_f = 6.825 cm/s), Run L 08 (W_f = 13.65 cm/s) and Run L 09 (W_f = 27.3 cm/s), ρ_o = 0.90 g/cm^3, μ = 100 mPa.s, d = 0.5 cm .

Table 6.7: Values of height of deposit bed at different positions, Gravity Deposition Model

	Well inlet				5 cm downstream			
* Between T2 (t=0.52 second) and T3 (t=0.78 second)								
	@T2	@T3	Diff.	Rate	@T2	@T3	Diff.	Rate
L 07	0.120	0.205	0.085	0.33	0.020	0.035	0.015	0.06
L 08	0.177	0.260	0.083	0.32	0.067	0.135	0.068	0.26
L 09	0.175	0.265	0.090	0.35	0.124	0.215	0.091	0.35
* Between T3 (t=0.78 second) and T4 (t=1.05 seconds)								
	@T3	@T4	Diff.	Rate	@T3	@T4	Diff.	Rate
L 07	0.205	0.300	0.095	0.35	0.035	0.070	0.035	0.13
L 08	0.260	0.335	0.075	0.28	0.135	0.215	0.080	0.30
L 09	0.265	0.337	0.068	0.25	0.215	0.280	0.065	0.24

Between T2 and T3 the expansion rate is relatively similar for all three flow velocities at the well inlet. However, the rate becomes quite different at 5 cm downstream from the well inlet: 0.06 fraction of well radius for Run L 07 (lowest velocity), 0.26 for Run L 08, and 0.35 for Run L 09 (highest velocity). For Run L 09, the solid particles are deposited at the same rate at the well inlet, and at 5 cm downstream – as suggested by the results in Table 6.7.

Between T3 and T4, the profile for Run L 07 achieves the highest expansion rate at the well inlet, and the lowest expansion rate downstream. This behaviour results in it having the most abrupt deposit bed profile among the three velocities. The expansion rate at the well inlet and 5 cm downstream are comparable for Run L 08, as well as for Run L 09 – giving them spread out, gradual deposition profiles. The expansion rates calculated at a distance 10 cm downstream from the well inlet (not included in Table 6.7 above, due to lack of room) show highest expansion rate for Run L 09, and smallest expansion rate for Run L 07. These results again support the observation that high flow velocity, not only results in more deposition, but also produces a more spread-out, gradual deposition profile.

The deposition process for the above three runs (L 07, L 08, and L 09) occurs at a relatively high rate, as shown by Figure 6.35. At the end of 1.05 seconds, there is a deposit forming at the well inlet, for all three runs. The peak of these deposit beds already reaches approximately one-sixth of the full height of the horizontal well.

d) Oil viscosity = 100 mPa.s, particle diameter = 0.1 cm

As seen in Figure 6.34, the trends for this sub-case are very similar to those observed for sub-case c). There is more deposition for Run L 12 (velocity = 27.30 cm/s) than for Run L 11 (velocity = 13.65 cm/s) and for Run L 10 (velocity = 6.825 cm/s) at all times. The deposition profile is also more spread out when the flow velocity is higher. Table 6.8 illustrates data for the expansion rates for these flow velocities.

Table 6.8: Values of height of deposit bed at different positions, Gravity Deposition Model

	Well inlet				10 cm downstream			
* Between T2 (t=1.27 seconds) and T3 (t=2.24 seconds)								
	@T2	@T3	Diff.	Rate	@T2	@T3	Diff.	Rate
L 10	0.016	0.028	0.022	0.02	0.002	0.013	0.011	0.01
L 11	0.017	0.029	0.022	0.02	0.009	0.023	0.014	0.01
L 12	0.017	0.030	0.023	0.02	0.013	0.027	0.014	0.01
* Between T3 (t=2.24 seconds) and T4 (t=3.25 seconds)								
	@T3	@T4	Diff.	Rate	@T3	@T4	Diff.	Rate
L 10	0.028	0.043	0.015	0.02	0.013	0.027	0.014	0.02
L 11	0.029	0.043	0.014	0.02	0.023	0.036	0.013	0.02
L 12	0.030	0.045	0.015	0.02	0.027	0.041	0.014	0.02

It is seen that all three runs have similar expansion rates. Furthermore, the expansion rates at the well inlet are almost identical to those at a distance of 10 cm away downstream. As such, the deposit bed expands at a uniform rate at different times, for all three flow velocities. The expansion rate is, however, very low – indicating a very slow deposition process under these hydrodynamic conditions.

6.4.1.3. Effect of Particle Size

The effect of particle size on the gravity deposition of sand in a horizontal well is examined below, for the Light Oil case. Two particle sizes are used: 1 000 microns and 5 000 microns.

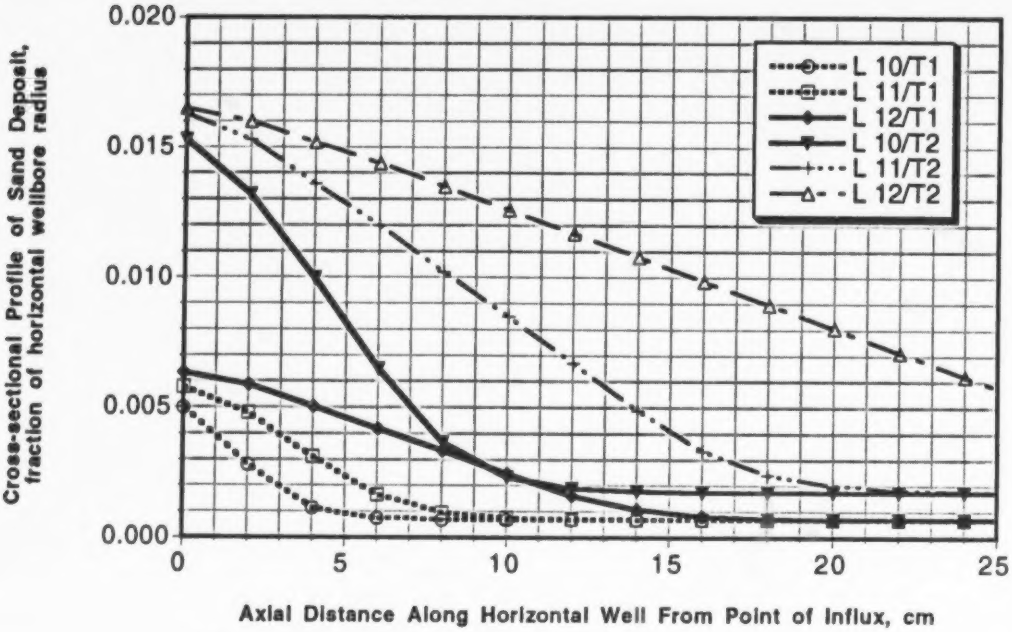

a) Profiles at time T 1 (t = 0.49 s), and at time T 2 (t = 1.27 s)

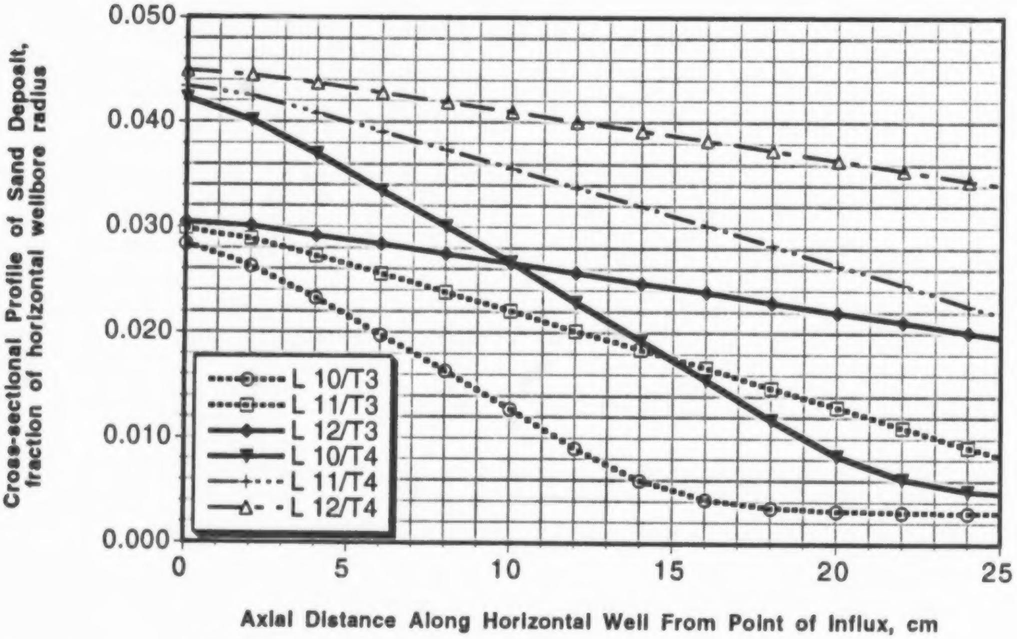

b) Profiles at time T 3 (t = 2.24 s), and at time T 4 (t = 3.25 s)

Figure 6. 34: Light Oil/Effect of flow velocity – Profile of sand deposit at different times for three velocities, Run L 10 (W_f = 6.825 cm/s), Run L 11 (W_f = 13.65 cm/s) and Run L 12 (W_f = 27.3 cm/s), ρ_o = 0.90 g/cm^3, μ = 100 mPa.s, d = 0.1 cm .

a) Well production rate = 150.0 m³/day, oil viscosity = 25 mPa.s

It is seen from Figure 6.35 that there is more deposition for the larger particle size (Run L 01) than for the smaller particle size (Run L 04). This observation is true at the end of T1 (t=0.52 second), T2 (t=1.00 second), T3 (t=1.45 seconds), and T4 (t=1.85 seconds). The larger particle results in a relatively high deposition and expansion rate, with the peak of the deposit bed reaching 0.23 fraction of the well radius at the end of 0.52 second, and after 1.00 second 0.39 fraction of the well radius. The values are at the well inlet. The corresponding values for the smaller-particle-size profile are 0.02 and approximately 0.05 fraction of the well radius. Thus, it is seen that a five-fold increase in the particle size results in 9-fold increase, approximately, in the deposition rate at the inlet at the end of 1.00 second. There is no noticeable evidence of smaller particles being kept in suspension longer, and deposited further downstream.

During the 0.45-second interval between T2 and T3 the larger-particle-size profile continues to expand. It increases from 0.39 to 0.49 fraction of the well radius at the well inlet, and from 0.04 to 0.05 fraction of the well radius at 5 cm downstream. The corresponding changes for the smaller-particle-size profile are from 0.05 to 0.08 fraction of the well radius at the well inlet, and from 0.02 to 0.05 at 5 cm downstream. As such, the uniform increases in the smaller-particle-size profile make it expand more uniformly; for the larger-particle-size profile the uneven increases result in much higher expansion at the well inlet than away from it.

Between T3 and T4 it can be seen that there is little change in the shape of the deposition profile for the larger particle size. This, coupled with the small gap between the two curves, suggests that the deposition process reaches a steady/pseudo-steady state. For the smaller particle run the gap between the T3 and T4 curves is noticeable, but also constant between the well inlet and up to 8-9 cm downstream. This observation suggests a rather uniform, and constant – albeit very slow – expansion. Another observation worth pointing out is that the deposition process occurs very slowly for the smaller particle, even when the flow rate – at 150.0 m³/day – is relatively slow. At the end of 1.85 second the peak of its deposition profile reaches only 0.10 fraction of the horizontal well radius. On the other hand, the peak of the larger-particle-size profile reaches 0.55 fraction of the well radius.

b) Well production rate = 300.0 m³/day, oil viscosity = 25 mPa.s

From Figure 6.36 it is observed that the trends in this sub-case follow closely those in sub-case a). Again, there is much more deposition for the larger particle (Run L 02, dia.=0.5 cm) at all times, from T1 (t=0.10 second), to T2 (t=0.53 second), to T3 (t=0.94 second) to finally T4 (t=1.20 seconds). Comparing the results for the larger-particle-size profile in this sub-case (flow rate = 300.0 m³/day) with those in the previous sub-case (flow rate = 150.0 m³/day) an interesting result is ob-

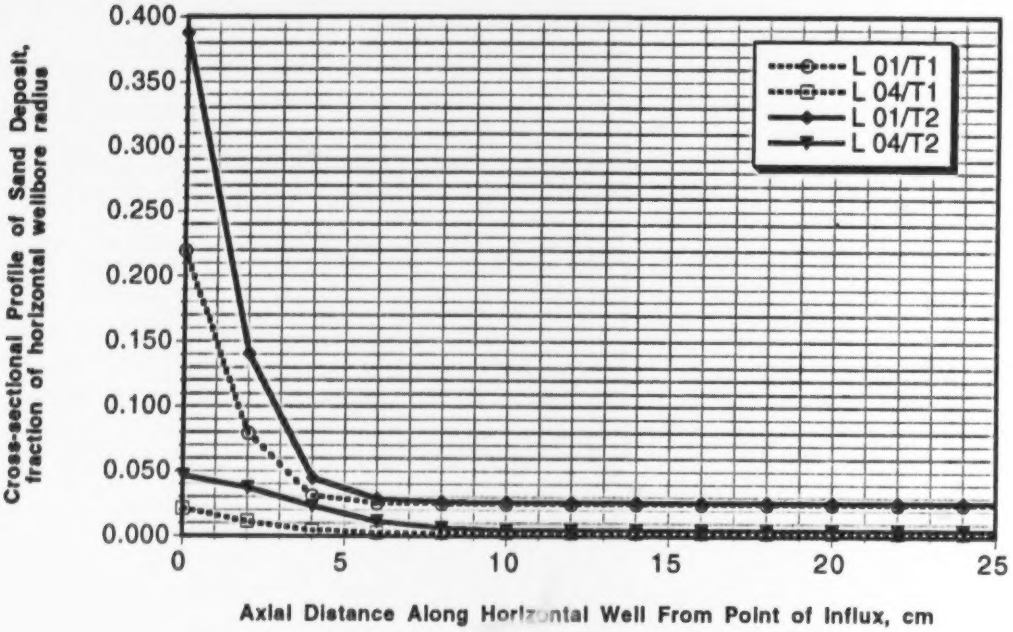

a) Profiles at time T 1 (t = 0.52 s), and at time T 2 (t = 1.00 s)

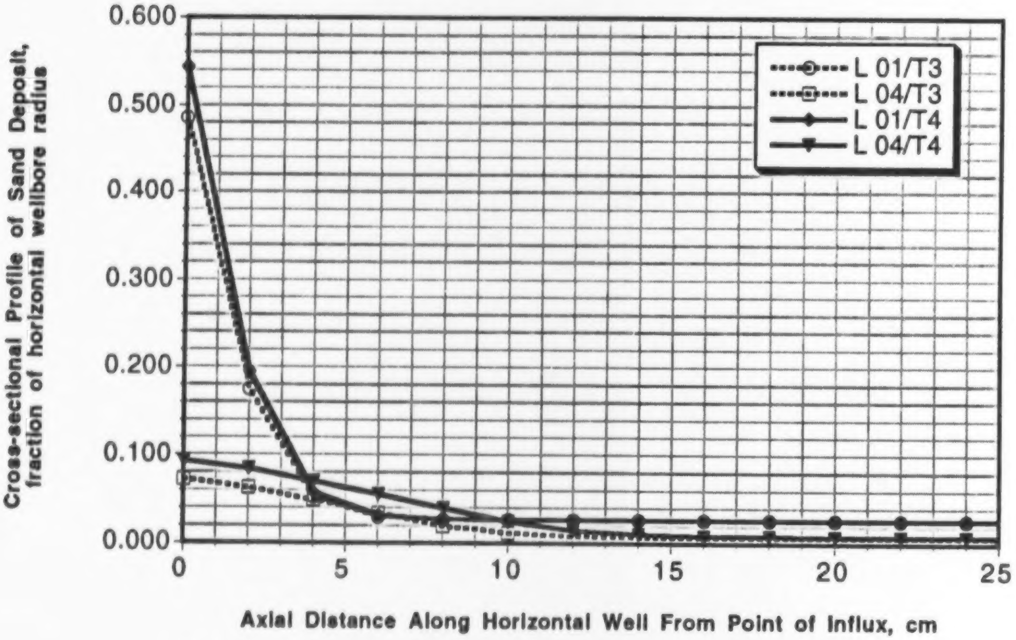

b) Profiles at time T 3 (t = 1.45 s), and at time T 4 (t = 1.85 s)

Figure 6. 35: Light oil/Effect of particle size – Profile of sand deposit at different times for two sand sizes, Run L 01 (d = 0.5 cm) and Run L 04 (d = 0.1 cm), W_t = 6.825 cm/s, ρ_o = 0.90 g/cm^3, μ = 25 mPa.s .

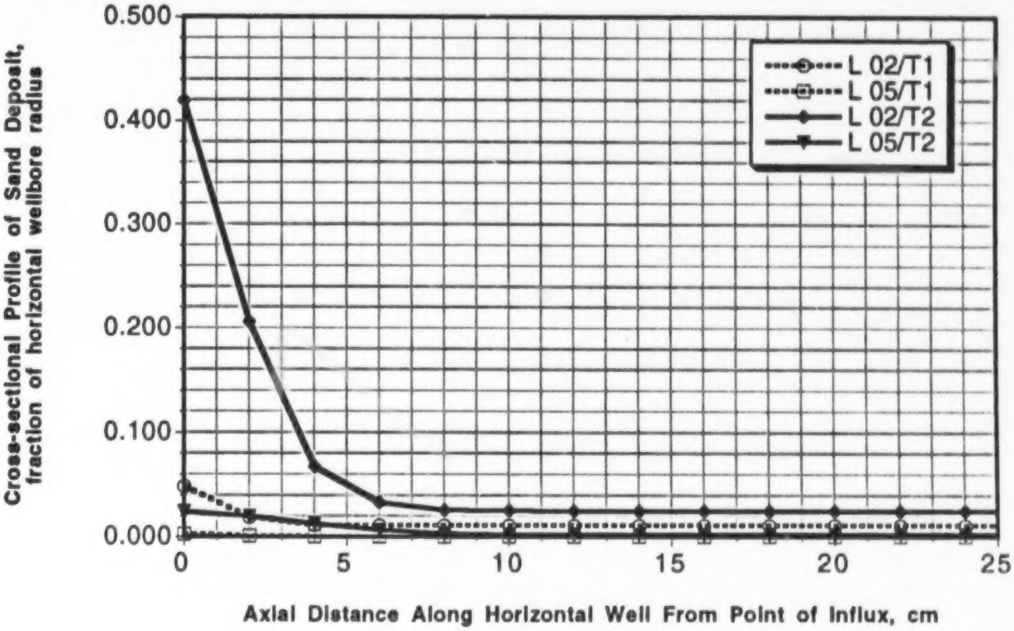

a) Profiles at time T 1 (t = 0.10 s), and at time T 2 (t = 0.53 s)

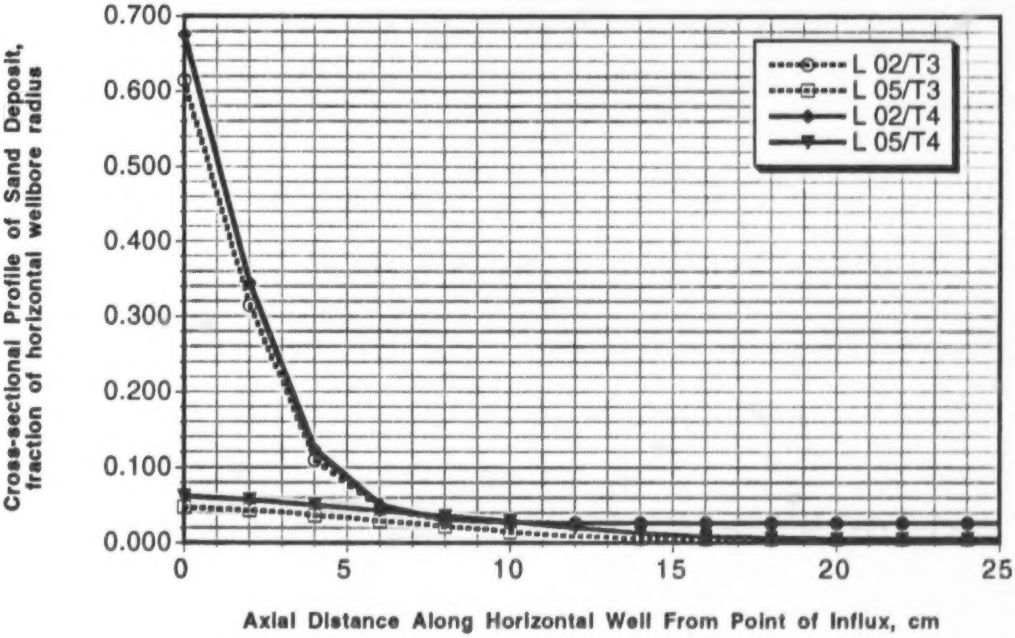

b) Profiles at time T 3 (t = 0.94 s), and at time T 4 (t = 1.20 s)

Figure 6. 36: Light oil/Effect of particle size – Profile of sand deposit at different times for two sand sizes, Run L 02 (d = 0.5 cm) and Run L 05 (d = 0.1 cm), W_i = 13.65 cm/s, ρ_o = 0.90 g/cm^3, μ = 25 mPa.s .

served. At the end of T4 (t=1.20 seconds) for this sub-case the peak of the deposit profile at the well inlet is 0.68 fraction of the well radius. For the previous sub-case this value is 0.55 fraction of the well radius, at the end of a considerably longer time (t=1.85 seconds). These results contradict the conventional belief that a higher flow velocity means less deposition, and particles are kept longer in suspension before they settle.

Performing the same comparison for the smaller-particle-size (Run L 05, dia.=0.1 cm) profiles an opposite observation is obtained. The lower flow rate in sub-case a) results in a higher peak value for the deposi tion profile, i.e. faster and more deposition. These results for the smaller particle size support intuition in that a slower fluid flow leads to more deposition.

c) Well production rate = 600.0 m^3/day, oil viscosity = 25 mPa.s

The results given in Figure 6.37 follow the same trends seen in sub-case b). Again, the results for this sub-case and sub-case b) are compared to determine indirectly the effect of flow velocity on the deposition process. In comparing these results it is noted that the time intervals T1, T2, T3, and T4 for sub-case b) are reasonably close to their counterparts for the present sub-case. As such, the results are compared on a much more contemporary basis. A higher flow rate in this case (600.0 m^3/day) results in more deposition for the larger particle (Run L 03, dia.=0.5 cm) than lower flow rate in the previous sub-case (300.0 m^3/day). For example, the profile peak at the well inlet is 0.66 and 0.88 fraction of the well radius after 0.53 second and 1.15 seconds, respectively, for the higher flow rate. Their equivalent values for sub-case b) are 0.42 and 0.68 fraction of the well radius after 0.53 second and 1.20 seconds, respectively. This behaviour, similar to that observed for sub-case b), contradicts the conventional belief that a higher fluid velocity (or flow rate) results in less deposition. Unlike what is observed between sub-cases a) and b), the results for the smaller particle (Run L 06, dia.=0.1 cm) are less conclusive, however.

d) Well production rate = 150.0 m^3/day, oil viscosity = 100 mPa.s

It can be seen from Figure 6.38, as well as Figures 6.39–6.40, that to a large extent the results seen for the three sub-cases d), e) and f) – which involve a more viscous oil (viscosity = 100 mPa.s) than the oil (viscosity = 25 mPa.s) in sub-cases a), b) and c) – follow the same general trend of faster, and greater deposition for the larger particle as compared to those in Figures 6.37–6.39. The big difference between the three less-viscous-oil sub-cases and the three more-viscous-oil sub-cases is that the peaks of the deposition profile are lower for the more viscous oil.

As for this particular sub-case it can be seen from Figure 6.38 that there is much more deposition, particularly in the vicinity of the well inlet, for the larger particle (Run L 07, dia.=0.5 cm). The deposition profile peak values at the well inlet at the end of T2 (t=0.92 second), T3 (t=1.47

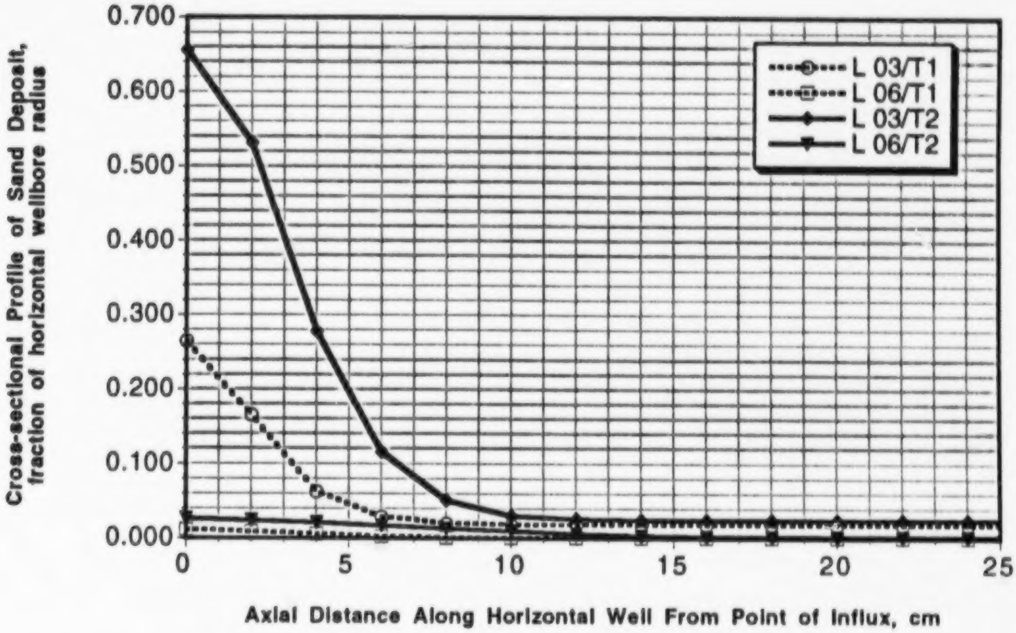

a) Profiles at time T 1 (t = 0.25 s), and at time T 2 (t = 0.53 s)

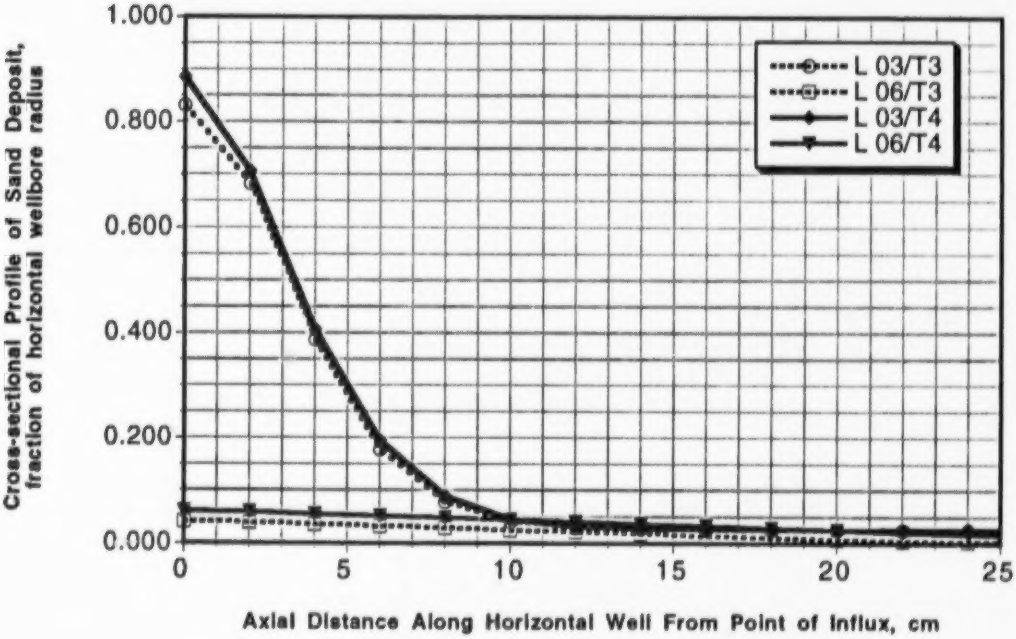

b) Profiles at time T 3 (t = 0.80 s), and at time T 4 (t = 1.15 s)

Figure 6. 37: Light oil/Effect of particle size – Profile of sand deposit at different times for two sand sizes, Run L 03 (d = 0.5 cm) and Run L 06 (d = 0.1 cm), W_f = 27.3 cm/s, ρ_o = 0.90 g/cm^3, μ = 25 mPa.s .

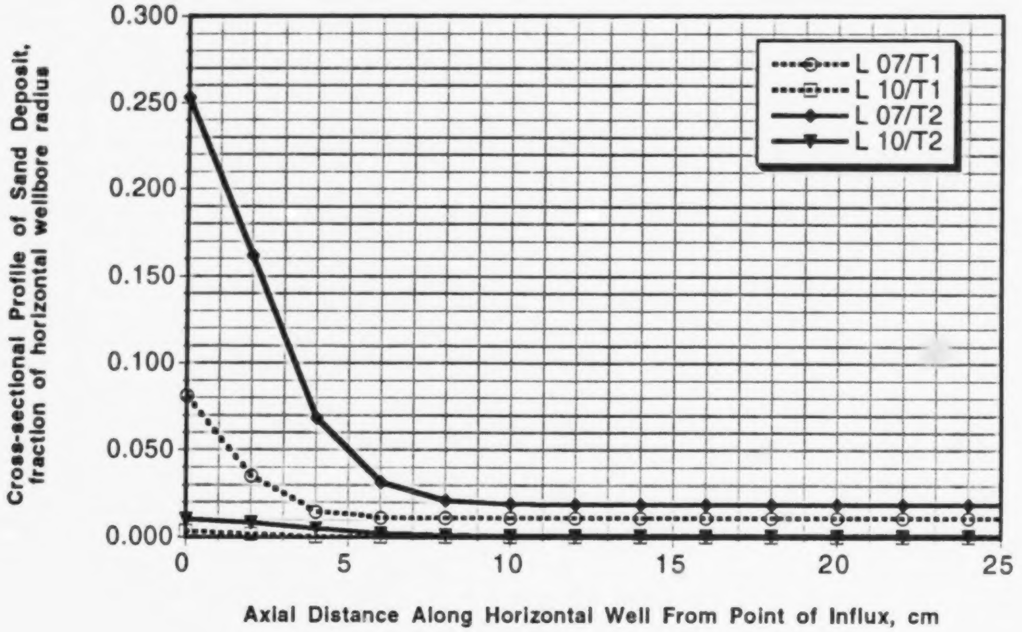

a) Profiles at time T 1 (t = 0.41 s), and at time T 2 (t = 0.92 s)

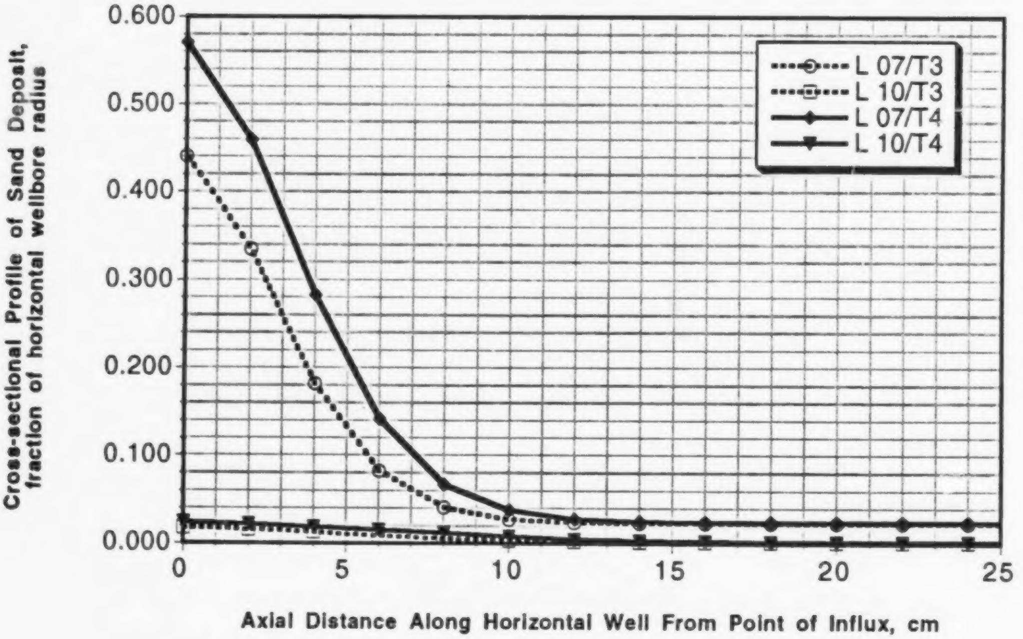

b) Profiles at time T 3 (t = 1.47 s), and at time T 4 (t = 1.95 s)

Figure 6. 38: Light oil/Effect of particle size – Profile of sand deposit at different times for two sand sizes, Run L 07 (d = 0.5 cm) and Run L 10 (d = 0.1 cm), W_t = 6.825 cm/s, ρ_o = 0.90 g/cm^3, μ = 100 mPa.s .

seconds), and T4 (t=1.95 seconds) are 0.25, 0.44 and 0.57 fraction of the well radius, respectively. At 5 cm downstream the values are 0.03, 0.14, and 0.22 fraction of the well radius. As can be inferred from these numbers, the expansion rate is seen to be quite high between T2 and T3, at both positions. It starts to slow down, however, between T3 and T4. There is hardly any deposition for the smaller particle (Run L 10, dia.=0.1 cm), with the deposit profile reaching only 0.03 fraction of the well radius at the well inlet after 1.95 seconds. This is in large contrast to the value for the larger-particle-size profile (0.57 fraction of the well radius).

e) Well production rate = 300.0 m^3/day, oil viscosity = 100 mPa.s

Again, as seen in Figure 6.39, there is more deposition for the larger particle (Run L 08, dia.=0.5 cm) than for the smaller particle (Run L 11, dia.=0.1 cm). Actually, there is hardly any deposition for the smaller particle. Whatever the amount of deposition for the smaller particle, the deposit bed profile is seen to remain mostly static with time.

f) Well production rate = 600.0 m^3/day, oil viscosity = 100 mPa.s

Figure 6.40 presents results which, again, follow the same trend of more deposition for the larger particle (Run L 09, dia.=0.5 cm) as observed previously. The deposition occurs at a relatively fast rate, as evidenced by the fact that after 1.00 second the deposit bed, at the well inlet, is already reaching a height one-third the horizontal well radius. At a distance of 10 cm downstream this height is one-fifth of the well radius. This trend remains true for all the time intervals. There is hardly any deposition for the smaller particle (Run L 12, dia.=0.1 cm).

Given the different time intervals when snapshots of the deposition profiles are taken, only a general comparison of Figures 6.38–6.40 is performed to evaluate the indirect influence of flow velocity on the deposition process. It is seen that a higher flow velocity generally results in a more spread-out deposition pattern. This is manifested in terms of the deposit bed having lower peak(s) and a wider base, as evidenced by the fact that the deposit bed peak located 10 cm downstream of the well inlet is 0.21 fraction of the well radius for a flow velocity of 27.30 cm/s, 0.10 for a flow velocity of 13.65 cm/s, and only 0.03 for a velocity of 6.825 cm/s. A similar situation exists at 15 cm downstream. This trend of a more spread-out deposition pattern, and a more gradual deposition profile with higher flow velocity agrees logically with intuition.

In brief, the following conclusions are drawn from the above results. On the basis of individual variables, there is more deposition when the fluid (oil) is less viscous and the solid particles are larger. The deposition pattern is more spread out, and the deposit bed profile more gradual when the flow velocity is higher. These results agree closely with conventional theory. However, the results – albeit derived from indirect comparison – are less conforming to intuition when sev-

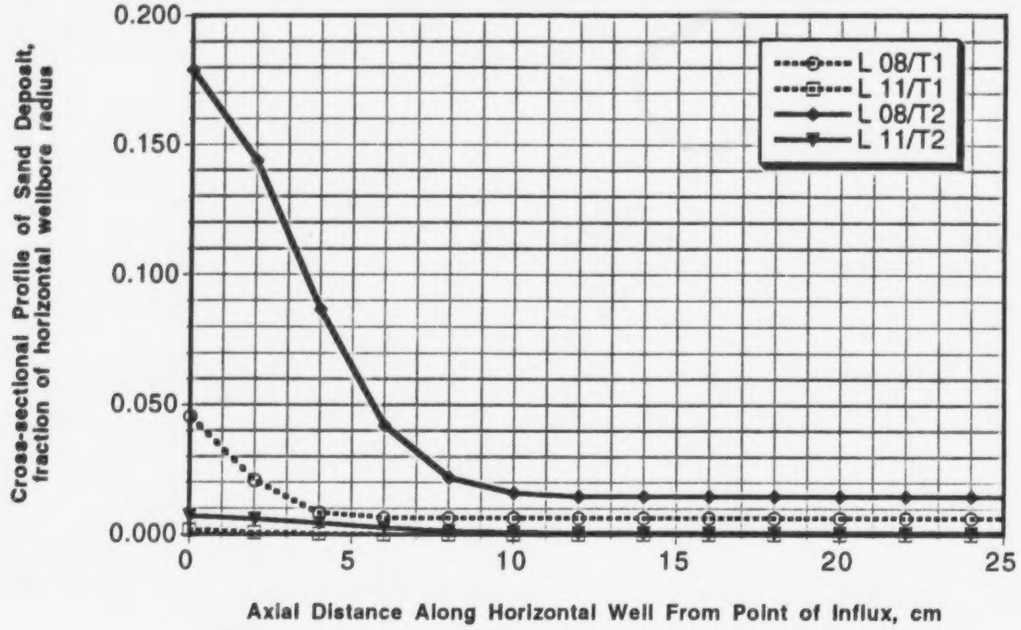

a) Profiles at time T 1 (t = 0.20 s), and at time T 2 (t = 0.60 s)

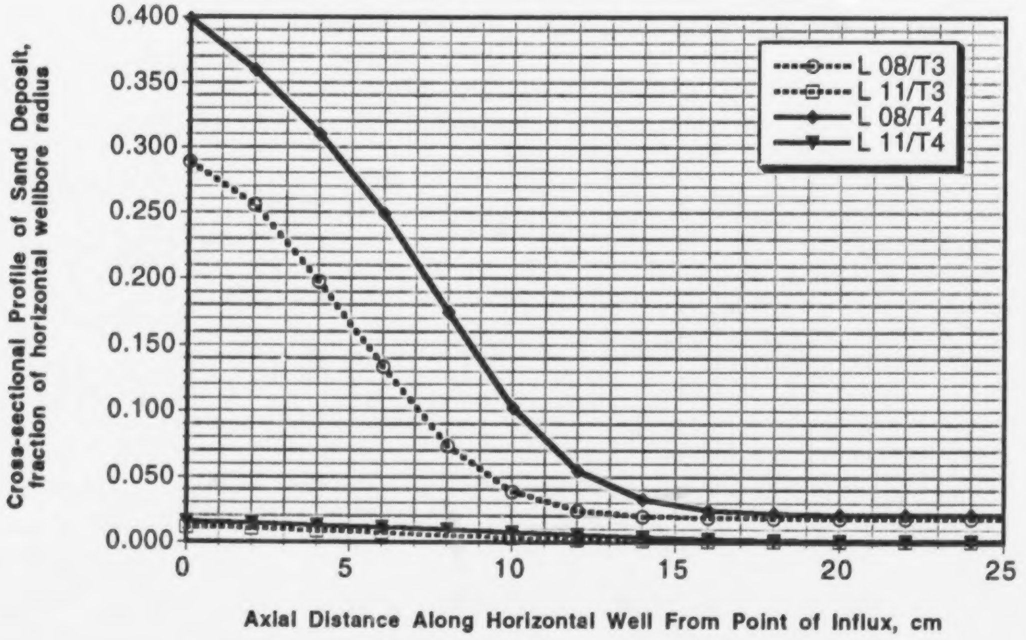

b) Profiles at time T 3 (t = 0.92 s), and at time T 4 (t = 1.24 s)

Figure 6. 39: Light oil/Effect of particle size – Profile of sand deposit at different times for two sand sizes, Run L 08 (d = 0.5 cm) and Run L 11 (d = 0.1 cm), W_t = 13.65 cm/s, ρ_o = 0.90 g/cm^3, μ = 100 mPa.s .

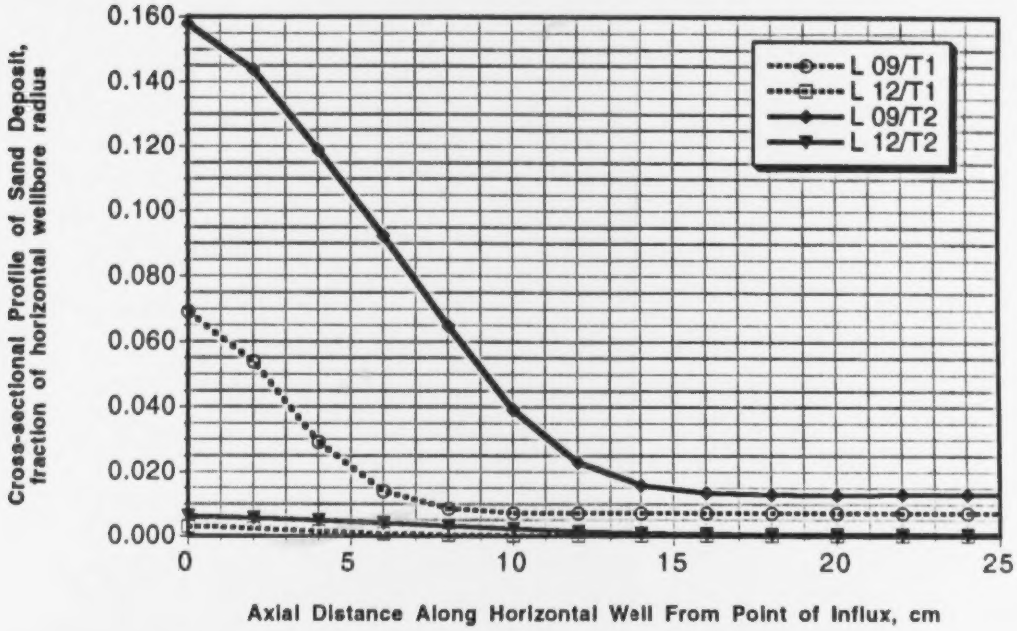

a) Profiles at time T 1 (t = 0.24 s), and at time T 2 (t = 0.50 s)

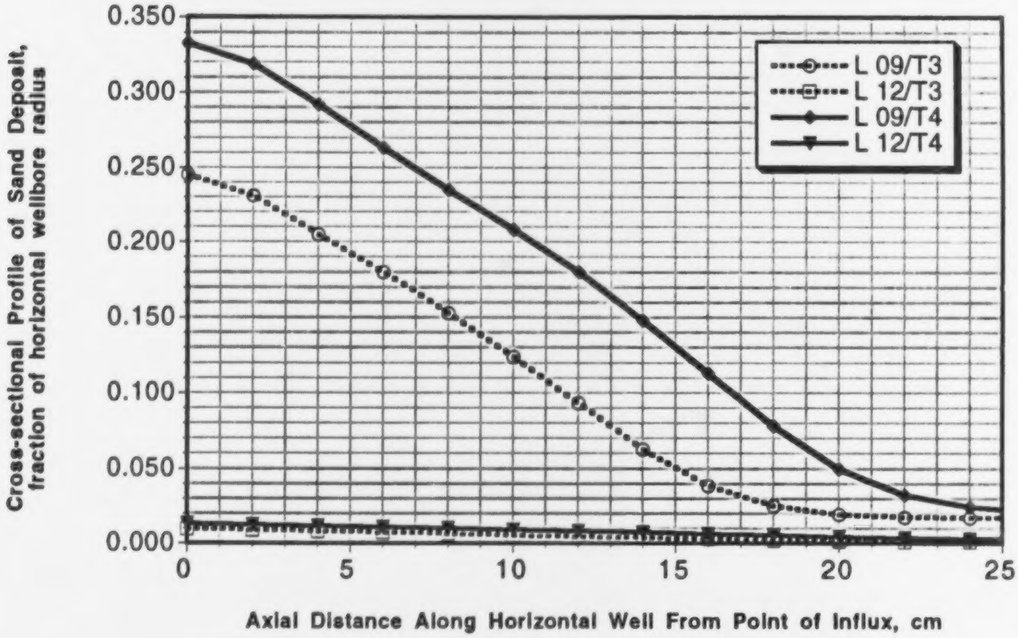

b) Profiles at time T 3 (t = 0.75 s), and at time T 4 (t = 1.00 s)

Figure 6. 40: Light oil/Effect of particle size – Profile of sand deposit at different times for two sand sizes, Run L 09 (d = 0.5 cm) and Run L 12 (d = 0.1 cm), W_l = 27.3 cm/s, ρ_o = 0.90 g/cm^3, μ = 100 mPa.s .

eral variables are considered together. This finding reinforces the logic behind the strategy of determining first the influence of an individual variable on the transport process before examining the interaction between the variables, and their influences.

6.4.2. Heavy Oil

For the Heavy Oil case, the two oil viscosities examined are 1 500 mPa.s and 10 000 mPa.s; the solid phase velocities are 2.0 cm/s, 4.0 cm/s, and 5.46 cm/s; again, the two particle sizes are 0.1 cm and 0.5 cm. The solid phase velocities are chosen, in all three cases, to be eight-tenths of the fluid phase velocities. The corresponding fluid phase velocities are 2.5 cm/s, 5.0 cm/s, and 6.825 cm/s. These fluid velocities are equivalent to average flow rates of 55.0 m^3/day, 110.0 m^3/day, and 150.0 m^3/day, approximately. These flow rates are judged to be reasonable horizontal well production rates for heavy oils. In all cases, snapshots of the profiles of the deposit bed for different cases are taken. They are then cross-compared to evaluate the influence of the isolated variable.

Two pressure gradients are used. For Runs H 01 – H 06, there is a pressure differential of 1 000 g/cm.s^2 (100 Pa) across the 50-cm long segment of the horizontal well. For Runs H 07 – H 12, which involve the smaller particle size, the above pressure gradient results in the sand particles being accelerated and moved *ahead* of the fluid phase. To eliminate this aphysical behaviour the pressure differential is adjusted downward to 10 Pa (i.e. 100 g/cm.s^2). Recalling the discussion in Section 6.2.3., the viscosity values used in this case prove to be most important as they show the applicability of the Gravity Deposition model to study the field-scale sand deposition problem.

It is important to point out that in many of the following figures the deposition profiles are shown to be less than the size of a single sand particle. Physically, this is impossible. The explanation for this observation is, however, rather simple. The results are calculated, and graphically displayed, from the gravity deposition mathematical model which invokes the continuum assumption for both the solid phase and the fluid phase. The continuum treatment for the solid phase, as such, eliminates completely the actual, physical size of the solid particles. As far as the mathematical model is concerned, the solid particles are of the same size as the surrounding fluid molecules (very small). Indeed, the actual particle size only enters into consideration in the calculation of the particle Reynolds Number, drag coefficient, and interaction coefficient. {Results for the Light Oil case are, mostly, not affected by this mathematical artifact.}

6.4.2.1. Effect of Oil Viscosity

Five different graphs are presented to examine the effect of oil viscosity in the Heavy Oil case. They are given in Figures 6.41 – 6.45. Each of these figures is studied individually below.

a) Well production rate = 110.0 m^3/day, particle diameter = 0.5 cm

As seen in Figure 6.41, the less viscous oil (Run H 02, viscosity=1 500 mPa.s) results in more deposition, and has a more abrupt deposition profile. These observations are true at the end of 0.99 second (T1), 2.01 seconds (T2), 3.00 seconds (T3), and 4.00 seconds (T4). The large gaps between the less-viscous-oil profiles at different times indicate continuing deposition of solid particles. The expansion rate is relatively appreciable – with the peak of the deposition profile at the well inlet increasing from 0.04 fraction of the well radius at the end of T2 to 0.06 at the end of T3, and 0.08 (approximately) at the end of T4. Considering these magnitudes, and the equal size of the time intervals, the deposition process is seen to proceed at a constant rate at the well inlet. At distances downstream it is also seen that the deposit bed is expanding rather uniformly.

Comparing the results seen here (Figure 6.41) with those seen previously, the deposition process is occurring relatively slowly. At the end of 4.00 seconds the peak of the deposit bed reaches only 0.08 fraction of the well radius at the well inlet. As for the more viscous oil (Run H 05, viscosity=10 000 mPa.s), there is deposition; but it is proceeding at rate much reduced as compared to that seen for the less viscous oil.

b) Well production rate = 150.0 m^3/day, particle diameter = 0.5 cm

The results in Figure 6.42 reveal more deposition for the less viscous oil (Run H 03, viscosity=1 500 mPa.s) at all times. There is negligible deposition for the more viscous oil (Run H 06, viscosity=10 000 mPa.s). Between T1 (t=0.12 second) and T2 (t=1.01 seconds) the less-viscous-oil deposition profile has a higher expansion rate at the well inlet, than downstream from it. As a result, the deposition profile becomes much more abrupt in going from T1 to T2. Between T2 and T3 (t=2.01 seconds) the expansion rate downstream starts to increase, and becomes more or less equal to the expansion rate at the well inlet. This uniform expansion rate results in a more gradual deposition profile for up to 15 cm downstream of the well inlet. The uniform expansion rate continues between T3 and T4 (t=3.12 seconds), thus maintaining the gradual deposition profile. At the end of T4, there starts to be more deposition at a distance of 20 cm downstream.

The results in Figure 6.42 (flow rate = 150.0 m^3/day) are compared with those in Figure 6.43 (flow rate = 110.0 m^3/day) to evaluate, indirectly, the influence of flow velocity on the deposition process. It is seen that at the end of 1.0 second the lower-flow-rate profile is more spread out and gradual than the profile for the present sub-case. At the end of 2.0 seconds the two profiles are, up to 5 cm downstream from the well inlet, identical to one another. There is a small difference between the two profiles beyond this distance. As such, a higher flow rate seems to have little effect on the deposition profile in these two sub-cases.

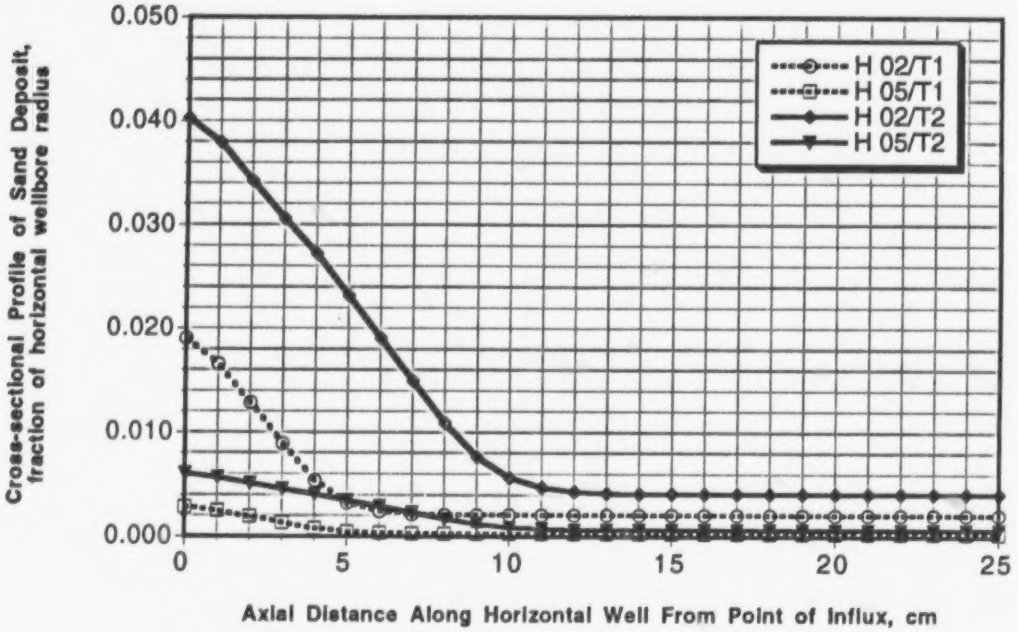

a) Profiles at time T 1 (t = 0.99 s), and at time T 2 (t = 2.01 s)

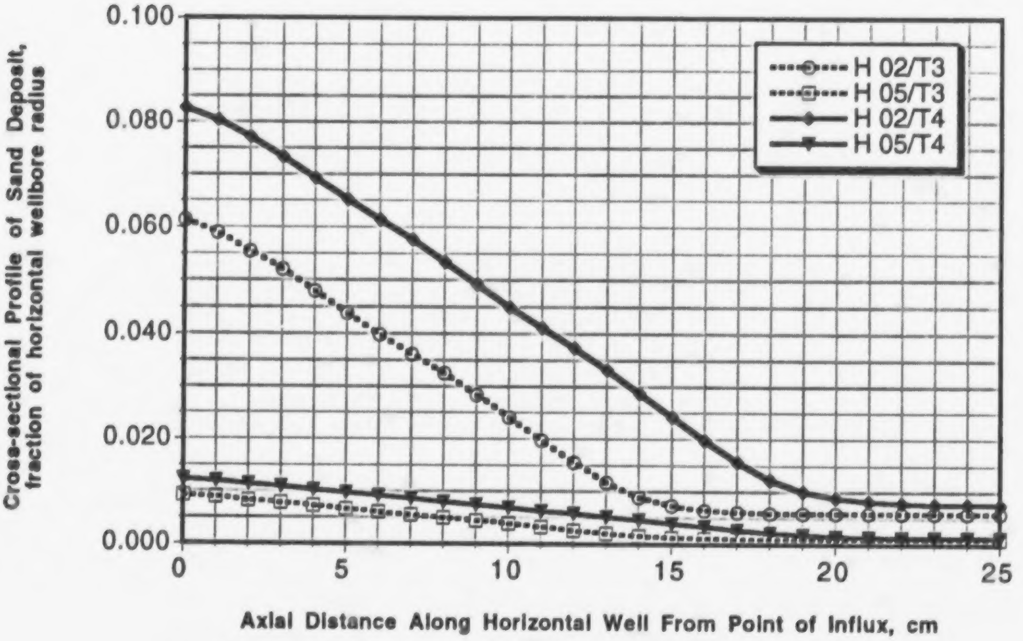

b) Profiles at time T 3 (t = 3.00 s), and at time T 4 (t = 4.00 s)

Figure 6. 41: Heavy Oil/Effect of oil viscosity – Profile of sand deposit at different times for two heavy oils, Run H 02 (μ = 1 500 mPa.s) and Run H 05 (μ = 10 000 mPa.s), W_f = 5.0 cm/s, ρ_o = 1.00 g/cm^3, d = 0.5 cm .

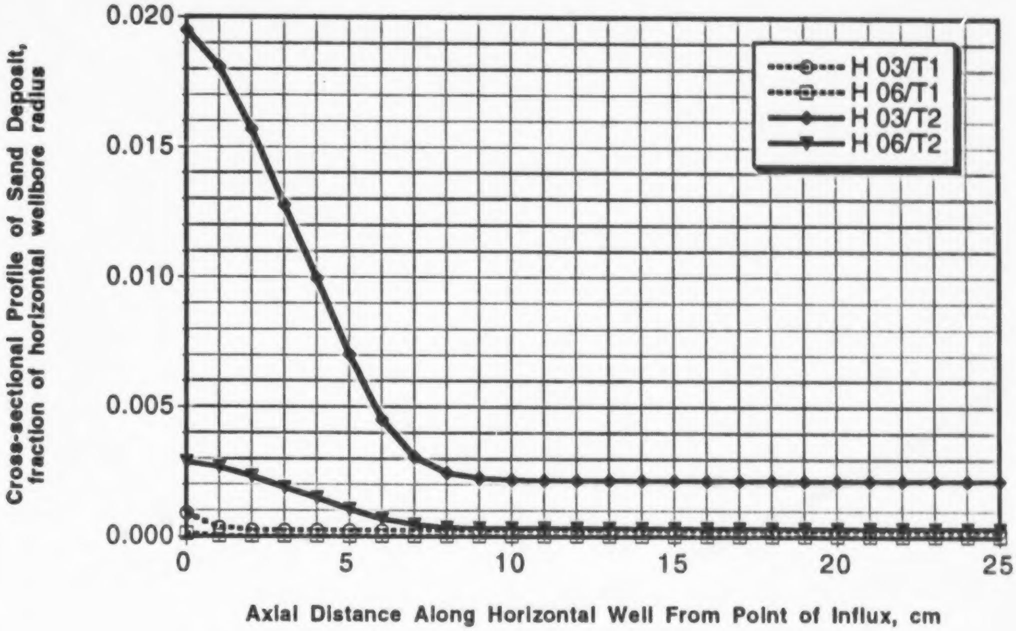

a) Profiles at time T 1 (t = 0.12 s), and at time T 2 (t = 1.01 s)

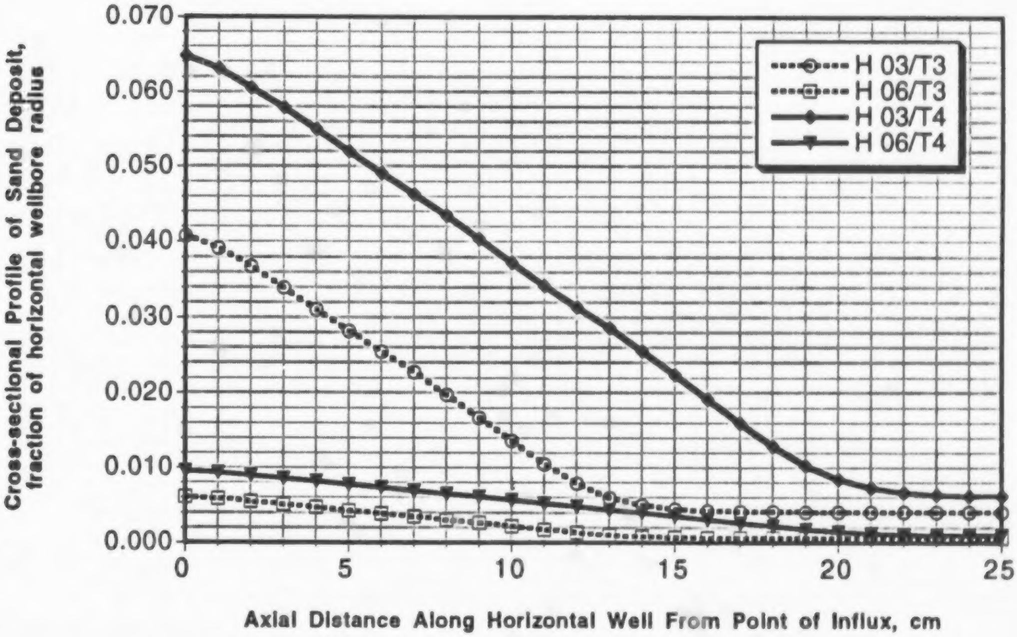

b) Profiles at time T 3 (t = 2.01 s), and at time T 4 (t = 3.12 s)

Figure 6. 42: Heavy Oil/Effect of oil viscosity – Profile of sand deposit at different times for two heavy oils, Run H 03 (μ = 1 500 mPa.s) and Run H 06 (μ = 10 000 mPa.s), W_f = 6.825 cm/s, ρ_o = 1.00 g/cm^3, d = 0.5 cm .

c) Well production rate = 55.0 m³/day, particle diameter = 0.1 cm

As seen in Figure 6.43, the trend of more deposition for the less viscous oil (Run H 07, viscosity=1 500 mPa.s) – seen in previous sub-cases – is again observed for this sub-case. There is hardly any deposition for the more viscous oil (Run H 10, viscosity=10 000 mPa.s). Taking into account the magnitude of the vertical scale at the end of all four time intervals, it is easily seen that there is – in absolute terms – practically no sand deposition, even for the less viscous oil.

d) Well production rate = 110.0 m³/day, particle diameter = 0.1 cm

The results in Figure 6.44 follow the same trend as that seen in Figure 6.45. The "relative" deposition rate for this sub-case, which has a higher flow rate than sub-case c), is less than that for sub-case c). Again, there is hardly any deposition in absolute terms.

e) Well production rate = 150.0 m³/day, particle diameter = 0.1 cm

Results in Figure 6.45 are similar to those seen in Figures 6.43 and 6.44. As such, the comments for these two sub-cases also apply to this sub-case.

Collectively, the results in Figures 6.43–6.45 show that when the solid particles are very small (relative scale) they are kept in suspension for a much longer time, before deposition occurs. On the other hand, the results in Figures 6.43 and 6.44 show noticeable deposition when the particles are larger (dia.=0.5 cm).

6.4.2.2. Effect of Velocity

Three different graphs are presented to examine the effect of velocity on the gravity deposition process in the Heavy Oil case. Three flow velocities are used in the simulation runs. They are: 2.5 cm/s for Run H 01, 5.0 cm/s for Run H 02, and 6.825 cm/s for Run H 03.

a) Oil viscosity = 1 500 mPa.s, particle diameter = 0.5 cm

Figure 6.46 illustrates the deposition profiles for Runs H 01 – H 03 at different times. There is, in absolute terms, very little deposition – the highest peak of the three profiles (that of Run H 03) at the end of 3.00 seconds is only 0.06 fraction of the well radius. Also, it is seen that for all three runs their profile peaks, at the well inlet, cluster together. This occurs at the end of T2 (t=1.04 seconds), T3 (t=2.01 seconds), as well as T4 (t=3.00 seconds). The three profiles separate from one another away from the well inlet, and then converge again far downstream where there is hardly any expansion for any of the three profiles. This behaviour is reflected in the data in Table 6.9.

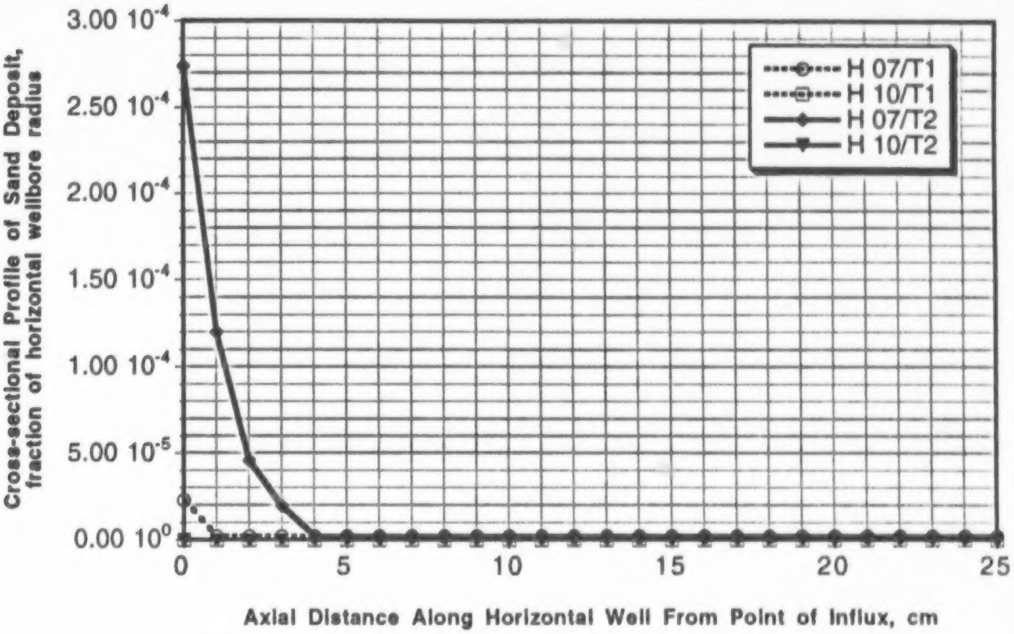

a) Profiles at time T 1 (t = 0.11 s), and at time T 2 (t = 0.52 s)

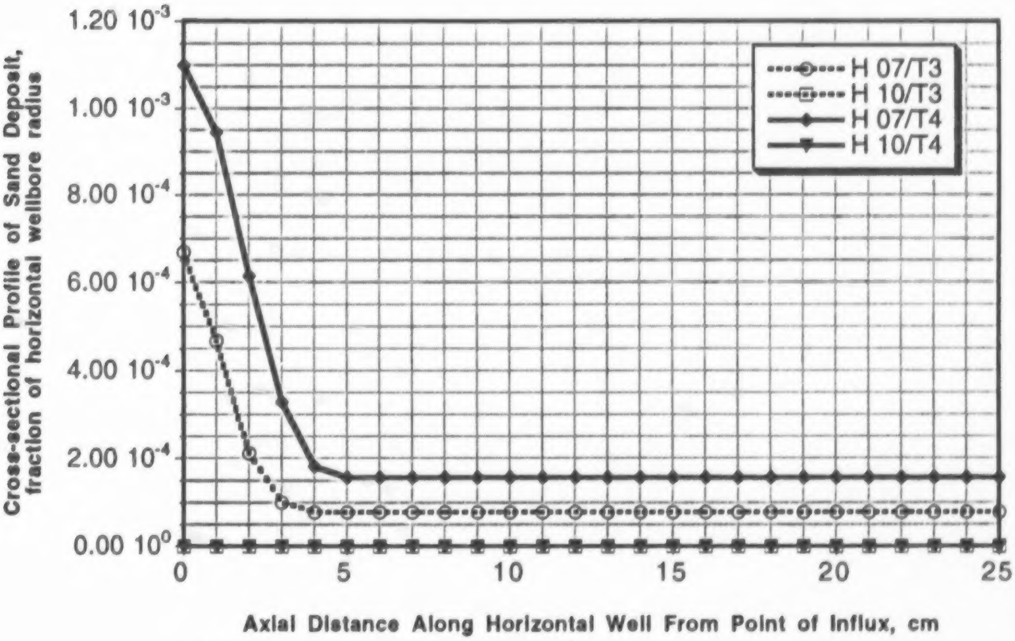

b) Profiles at time T 3 (t = 0.99 s), and at time T 4 (t = 1.50 s)

Figure 6. 43: Heavy Oil/Effect of oil viscosity – Profile of sand deposit at different times for two heavy oils, Run H 07 (μ = 1 500 mPa.s) and Run H 10 (μ = 10 000 mPa.s), W_f = 2.5 cm/s, ρ_o = 1.00 g/cm^3, d = 0.1 cm .

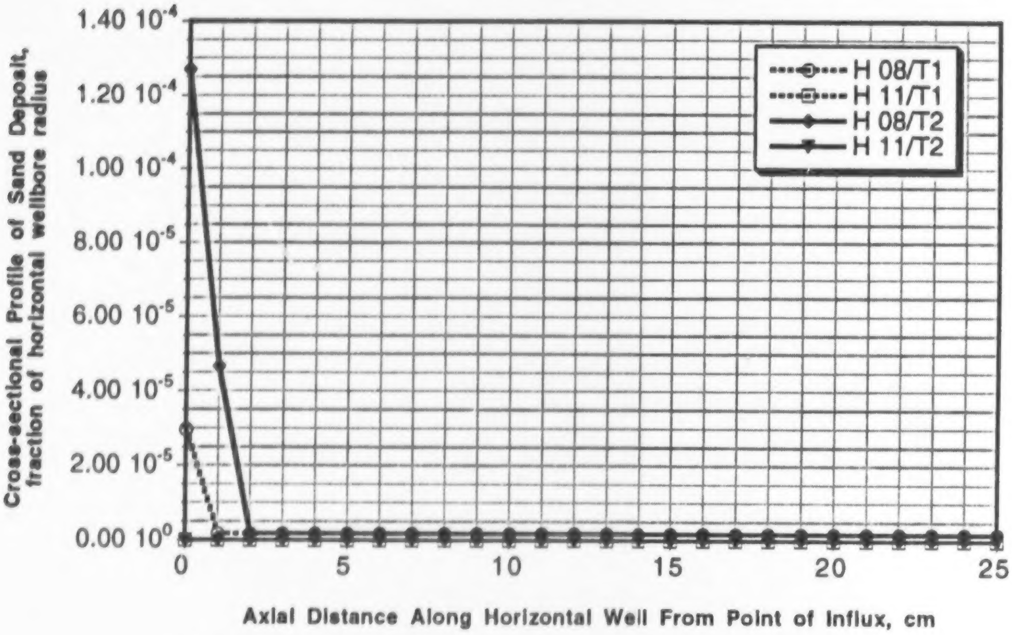

a) Profiles at time T 1 (t = 0.10 s), and at time T 2 (t = 0.25 s)

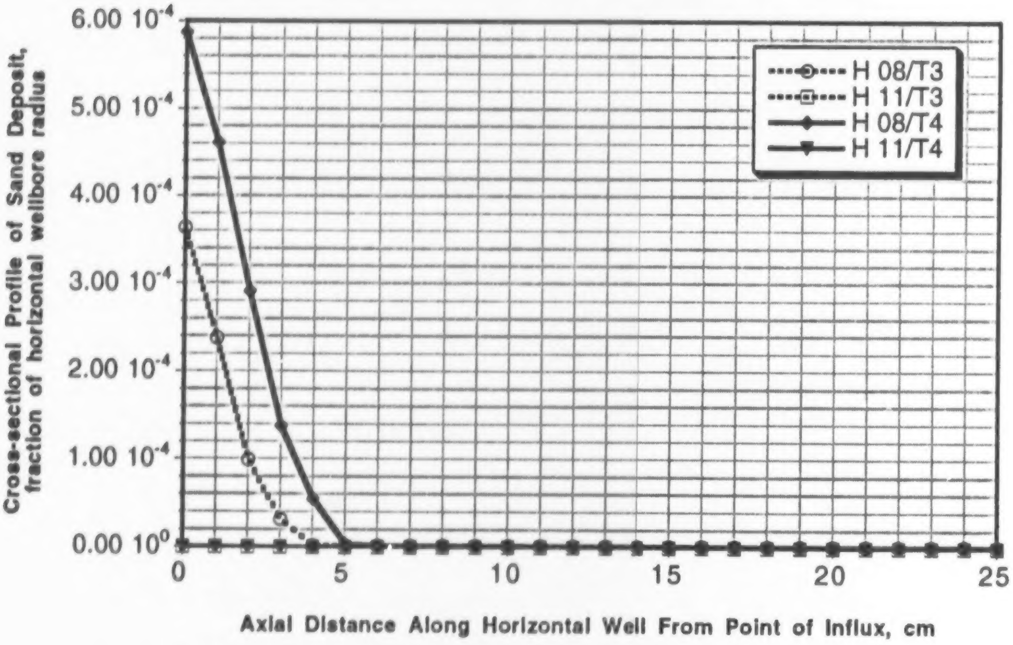

b) Profiles at time T 3 (t = 0.50 s), and at time T 4 (t = 0.74 s)

Figure 6. 44: Heavy Oil/Effect of oil viscosity – Profile of sand deposit at different times for two heavy oils, Run H 08 (μ = 1 500 mPa.s) and Run H 11 (μ = 10 000 mPa.s), W_f = 5.0 cm/s, ρ_o = 1.00 g/cm^3, d = 0.1 cm .

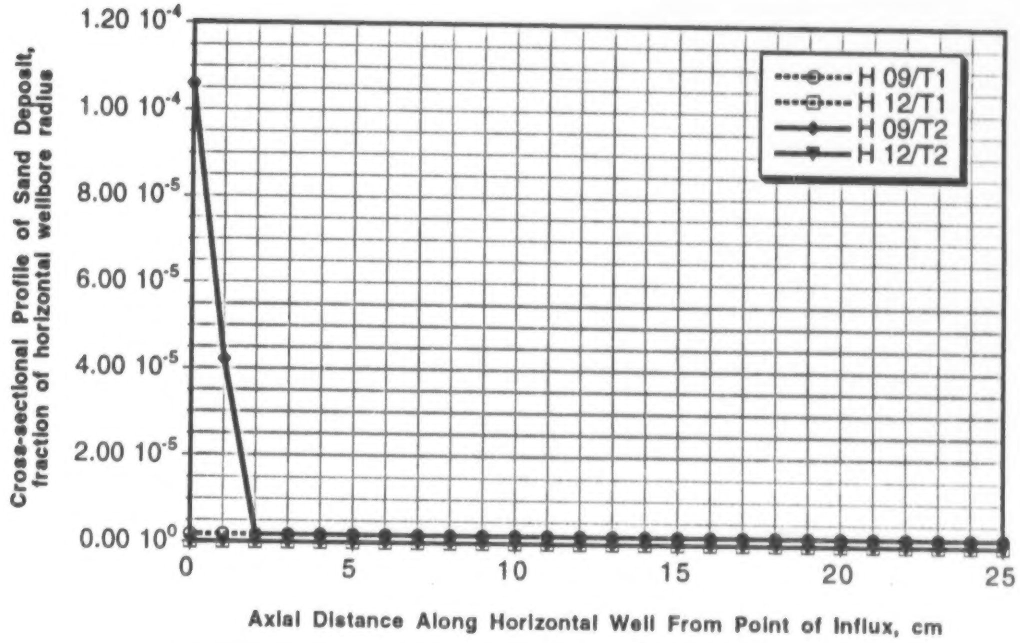

a) Profiles at time T 1 (t = 0.05 s), and at time T 2 (t = 0.20 s)

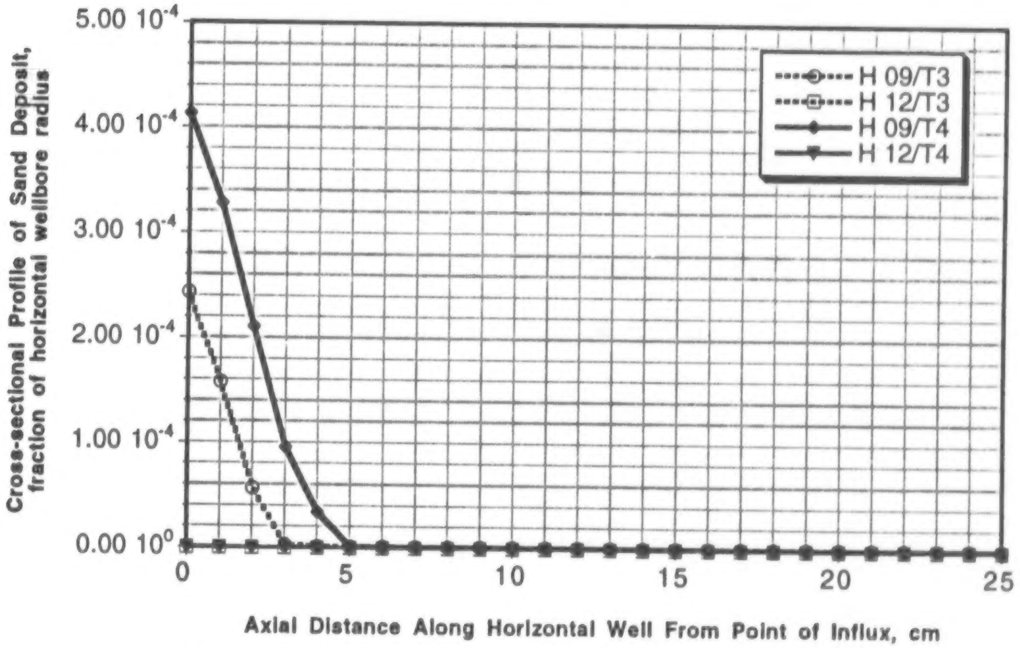

b) Profiles at time T 3 (t = 0.35 s), and at time T 4 (t = 0.55 s)

Figure 6. 45: Heavy Oil/Effect of oil viscosity – Profile of sand deposit at different times for two heavy oils, Run H 09 (μ = 1 500 mPa.s) and Run H 12 (μ = 10 000 mPa.s), W_f = 6.825 cm/s, ρ_o = 1.00 g/cm^3, d = 0.1 cm .

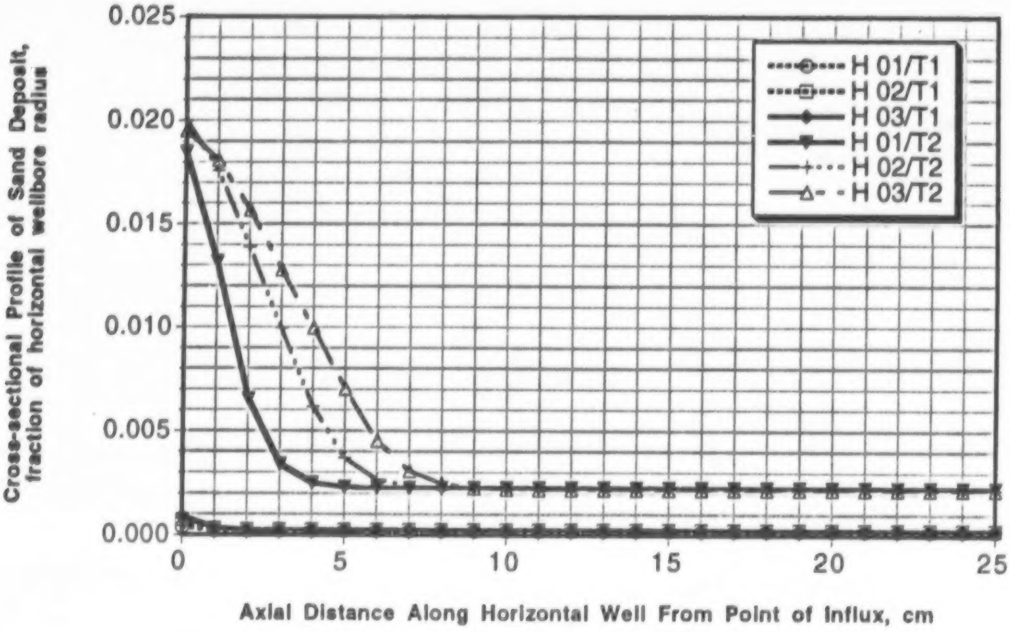

a) Profiles at time T 1 (t = 0.15 s), and at time T 2 (t = 1.04 s)

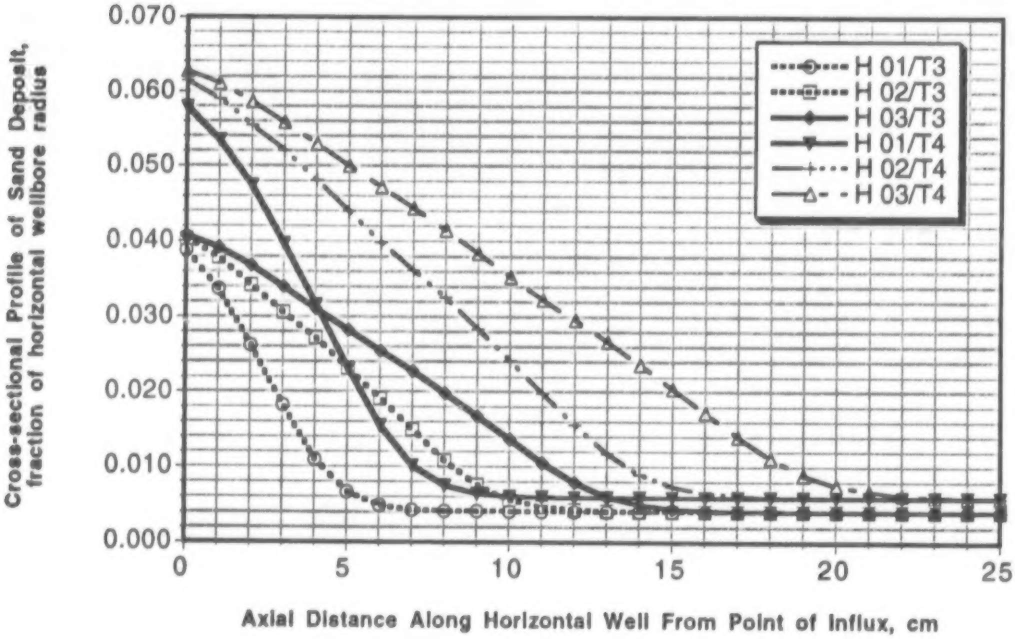

b) Profiles at time T 3 (t = 2.01 s), and at time T 4 (t = 3.00 s)

Figure 6. 46: Heavy Oil/Effect of flow velocity – Profile of sand deposit at different times for three velocities, Run H 01 (W_f = 2.5 cm/s), Run H 02 (W_f = 5.0 cm/s) and Run H 03 (W_f = 6.825 cm/s), ρ_o = 1.00 g/cm^3, μ = 1 500 mPa.s, d = 0.5 cm .

Table 6.9: Values of height of deposit bed at different positions, Gravity Deposition Model

* Between T2 (t=1.04 seconds) and T3 (t=2.01 seconds)

	Well inlet				5 cm downstream			
	@T2	@T3	Diff.	Rate	@T2	@T3	Diff.	Rate
H 01	0.019	0.039	0.020	0.021	0.003	0.007	0.004	0.004
H 02	0.020	0.041	0.021	0.022	0.004	0.024	0.020	0.021
H 03	0.019	0.041	0.022	0.023	0.007	0.028	0.021	0.022

* Between T3 (t=2.01 seconds) and T4 (t=3.00 seconds)

	Well inlet				5 cm downstream			
	@T3	@T4	Diff.	Rate	@T3	@T4	Diff.	Rate
H 01	0.039	0.058	0.019	0.019	0.007	0.029	0.022	0.022
H 02	0.041	0.062	0.021	0.021	0.024	0.044	0.020	0.020
H 03	0.041	0.063	0.022	0.022	0.028	0.050	0.022	0.022

There is, virtually, no difference in the rates of expansion – both at the well inlet, and at 5 cm downstream – at the end of 3.00 seconds. This uniform expansion is reflected readily in Figure 6.48. The deposition profiles are basically shifted upward and sideways in going from T3 to T4, and the difference between individual profiles reflects the volume of deposition laid down during the intervening period.

b) Oil viscosity = 1 500 mPa.s, particle diameter = 0.1 cm

The deposition profiles seen in Figure 6.47 in many ways mirror those seen in Figure 6.46, with one noticeable difference. The rate of deposition is even smaller here than in sub-case a), as seen in the magnitude of the vertical axis in the graphs. There is hardly any deposition.

c) Oil viscosity = 10 000 mPa.s, particle diameter = 0.1 cm

It is very clear from Figure 6.48 that there is no deposition of solid particles for the relatively small time period considered. *Of all the figures presented for the Gravity Deposition model, this figure (alone) provides the most definitive showing of absolutely no deposition of solid particles due to gravity.* The particles are kept in suspension, and the magnitude of the drag force – due to a combination of small particle size and high fluid viscosity – is much larger than the gravity force.

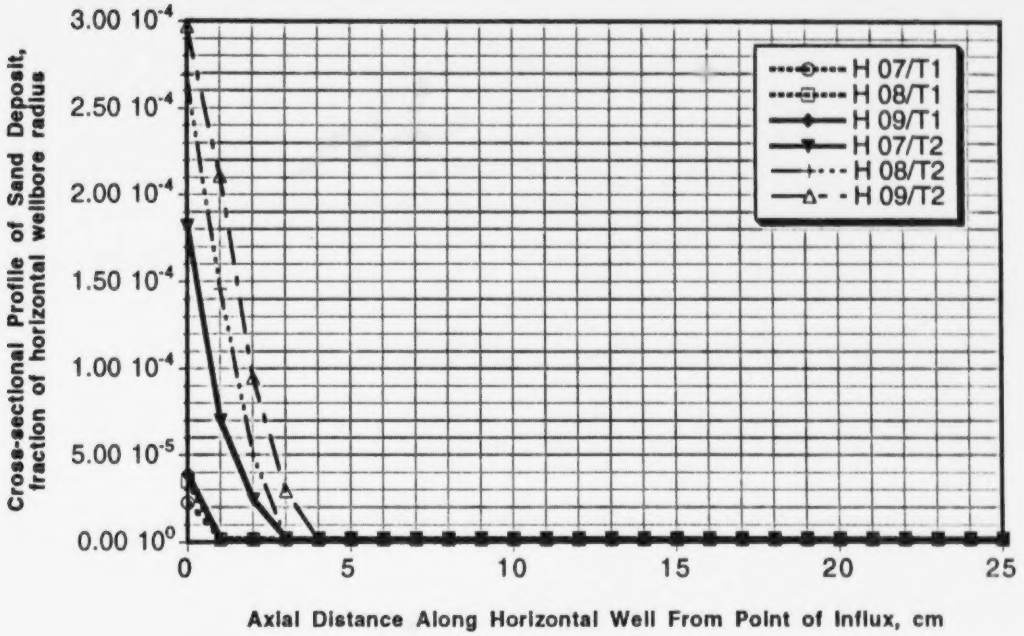

a) Profiles at time T 1 ($t = 0.11$ s), and at time T 2 ($t = 0.40$ s)

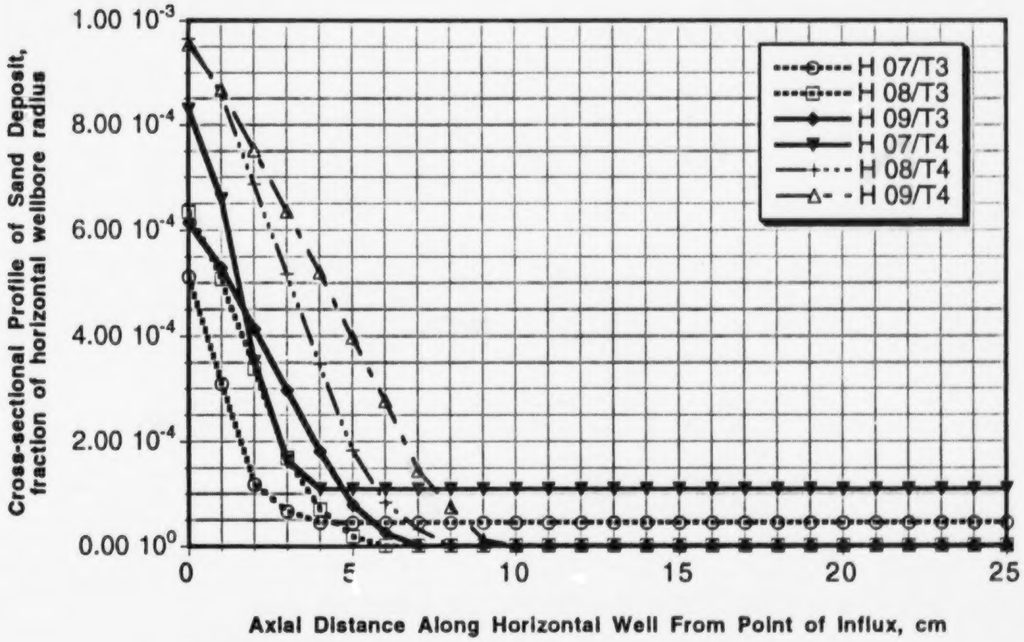

b) Profiles at time T 3 ($t = 0.80$ s), and at time T 4 ($t = 1.19$ s)

Figure 6. 47: Heavy Oil/Effect of flow velocity – Profile of sand deposit at different times for three velocities, Run H 07 ($W_f = 2.5$ cm/s), Run H 08 ($W_f = 5.0$ cm/s) and Run H 09 ($W_f = 6.825$ cm/s), $\rho_o = 1.00$ g/cm^3, $\mu = 1\,500$ mPa.s, $d = 0.1$ cm .

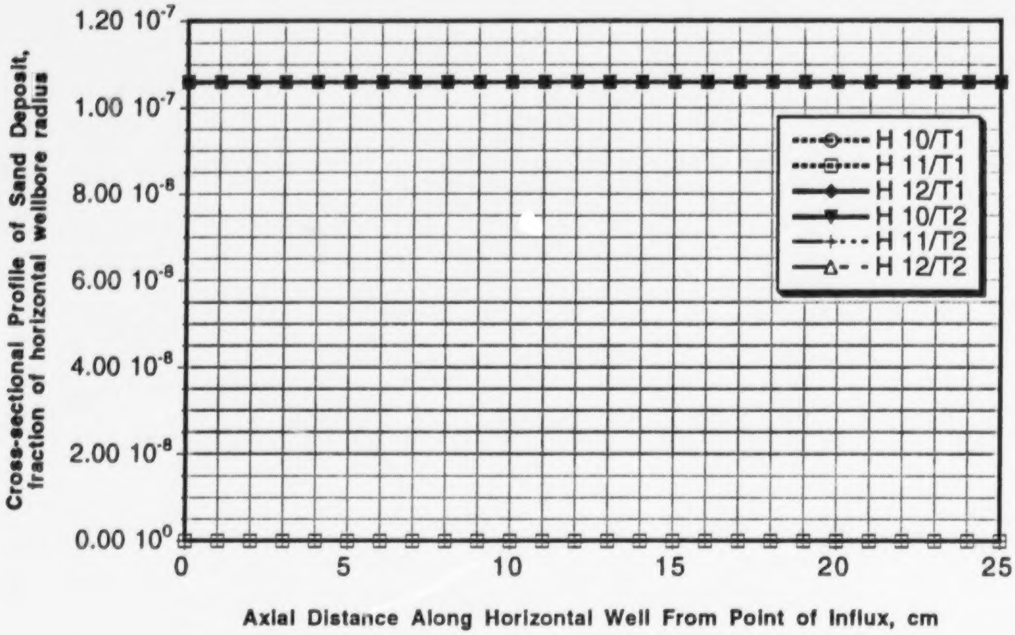

a) Profiles at time T 1 (t = 0.05 s), and at time T 2 (t = 0.20 s)

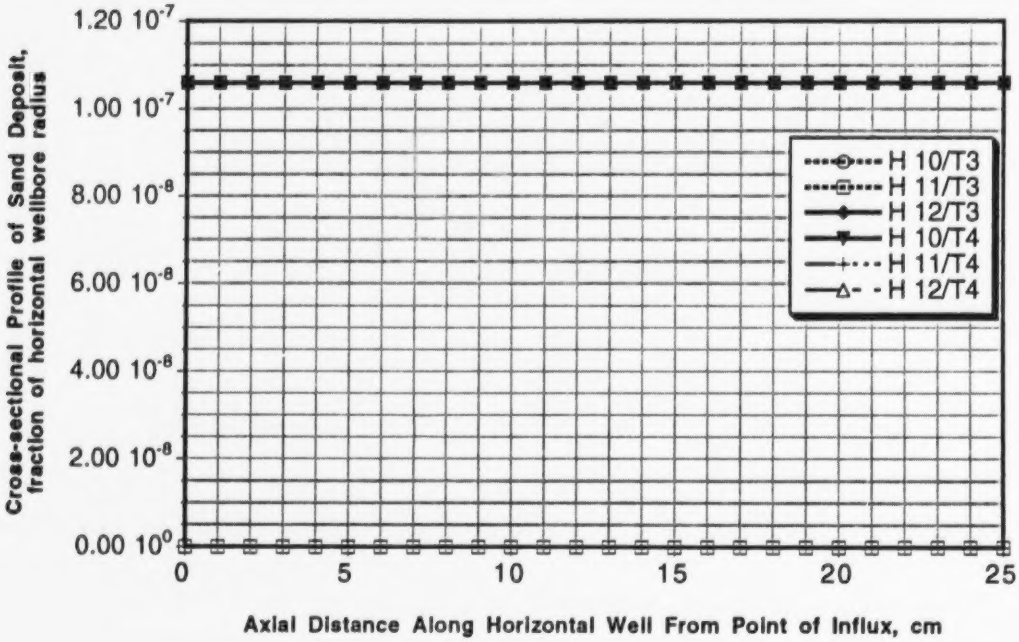

b) Profiles at time T 3 (t = 0.35 s), and at time T 4 (t = 0.54 s)

Figure 6. 48: Heavy Oil/Effect of flow velocity – Profile of sand deposit at different times for three velocities, Run H 10 (W_f = 2.5 cm/s), Run H 11 (W_f = 5.0 cm/s) and Run H 12 (W_f = 6.825 cm/s), ρ_o = 1.00 g/cm^3, μ = 10 000 mPa.s, d = 0.1 cm .

6.4.2.3. Effect of Particle Size

The effect of particle size on the gravity deposition process in the Heavy Oil case is examined in the following sub-cases.

a) Well production rate = 55.0 m^3/day, oil viscosity = 1 500 mPa.s

Keeping in view the previous discussion about actual scale of the deposition process (Section 6.4.2), it is seen from Figure 6.49 that there is more deposition for the larger particle. The deposition process continues from T1 (t=1.06 seconds), to T2 (t=1.74 seconds), to T3 (t=2.51 seconds), to T4 (t=3.22 seconds). At earlier times the deposition occurs almost exclusively at the well inlet. However, as time goes on more deposition also takes place downstream – resulting in a more gradual deposition profile. There is hardly any deposition for the smaller particle, and its profile remains more or less static with time.

b) Well production rate = 110.0 m^3/day, oil viscosity = 1 500 mPa.s

The results contained in Figure 6.50 follow the same trends of a very slow deposition process for the larger particle (Run H 02, dia.=0.5 cm), and a much slower still deposition process for the smaller particle (Run H 08, dia.=0.1 cm). In comparing Figure 6.50 with Figure 6.49 two interesting features are noted. The deposition profile peaks at the inlet for this sub-case and sub-case a) are about the same at the end of about 1.75 seconds. At a distance of 5 cm downstream, the profile peak for this case is 0.015 fraction of the well radius. This value is approximately three times that of sub-case a) which has a flow velocity half that of the present sub-case. As such, a higher flow velocity results in a more spread-out deposition profile.

c) Well production rate = 150.0 m^3/day, oil viscosity = 1 500 mPa.s

The biggest difference between the results contained in Figure 6.51 and those in Figure 6.50 is the larger rate of increase in the deposition profile peak at the well inlet initially for sub-case b). Otherwise, the profiles for the larger particle are very similar between the two sub-cases.

d) Well production rate = 110.0 m^3/day, oil viscosity = 10 000 mPa.s

As seen from Figure 6.52 there is no deposition for the smaller particle (Run H 11, dia.=0.1 cm). The deposition process is extremely slow for the larger particle (Run 05, dia.=0.5 cm), and is negligible in absolute terms.

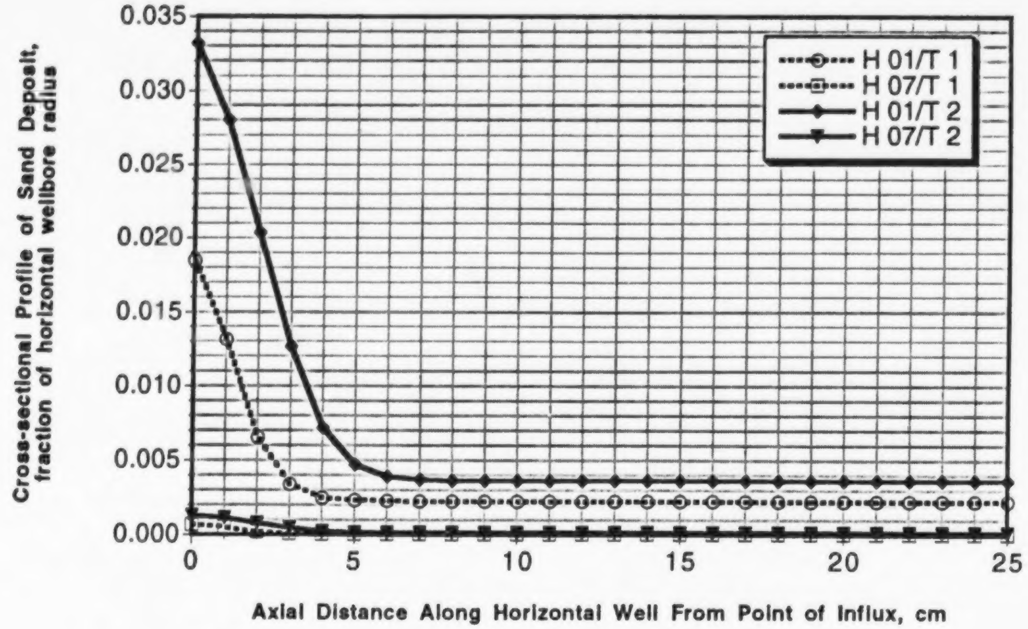

a) Profiles at time T 1 (t = 1.06 s), and at time T 2 (t = 1.74 s)

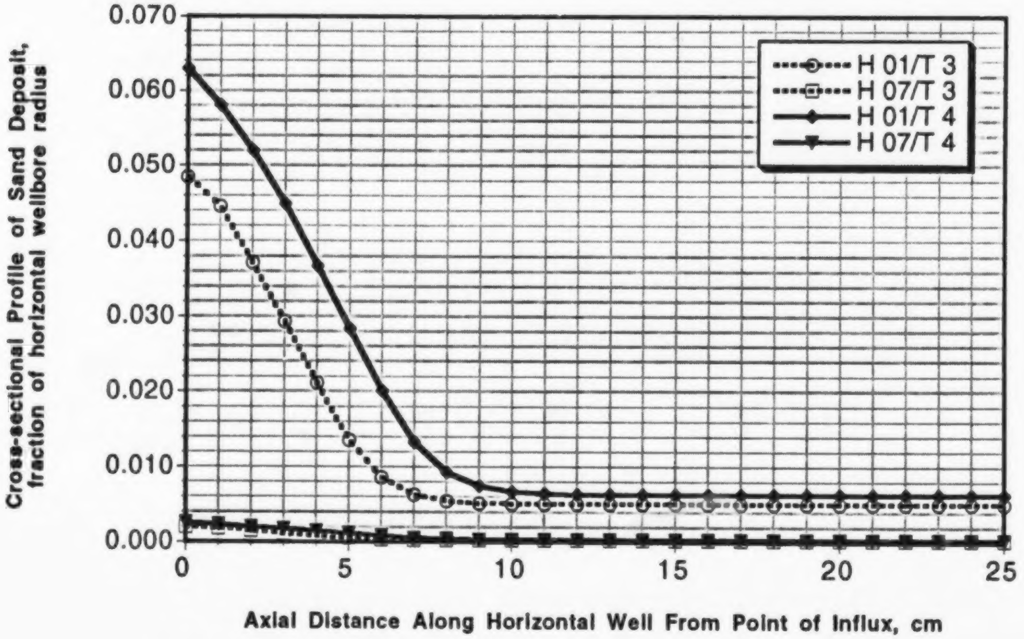

b) Profiles at time T 3 (t = 2.51 s), and at time T 4 (t = 3.22 s)

Figure 6. 49: Heavy oil/Effect of particle size – Profile of sand deposit at different times for two sand sizes, Run H 01 (d = 0.5 cm) and Run H 07 (d = 0.1 cm), W_t = 2.5 cm/s, ρ_o = 1.00 g/cm^3, μ = 1 500 mPa.s .

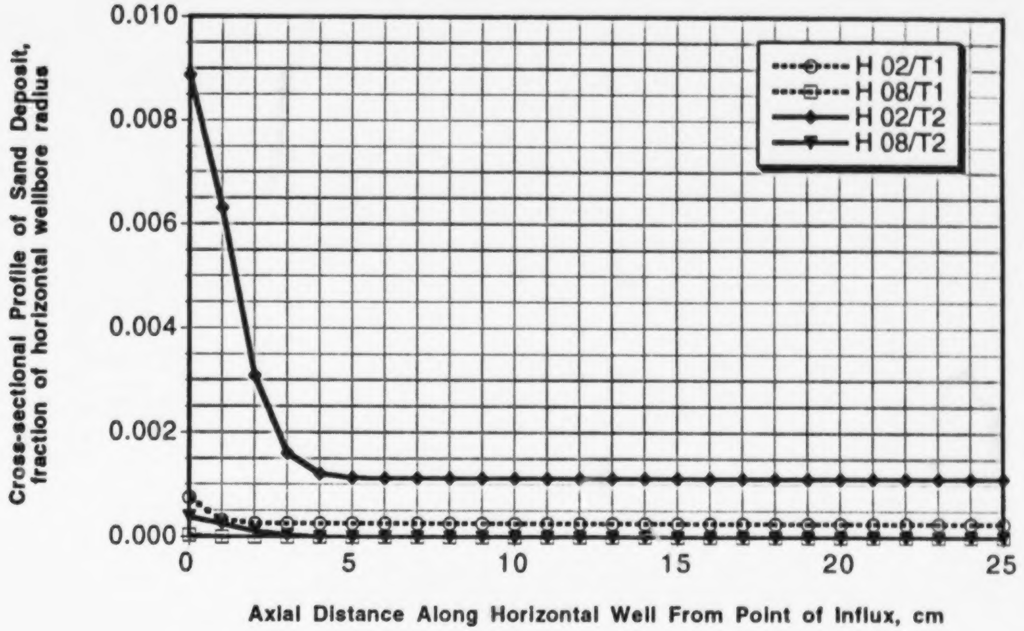

a) Profiles at time T 1 (t = 0.12 s), and at time T 2 (t = 0.52 s)

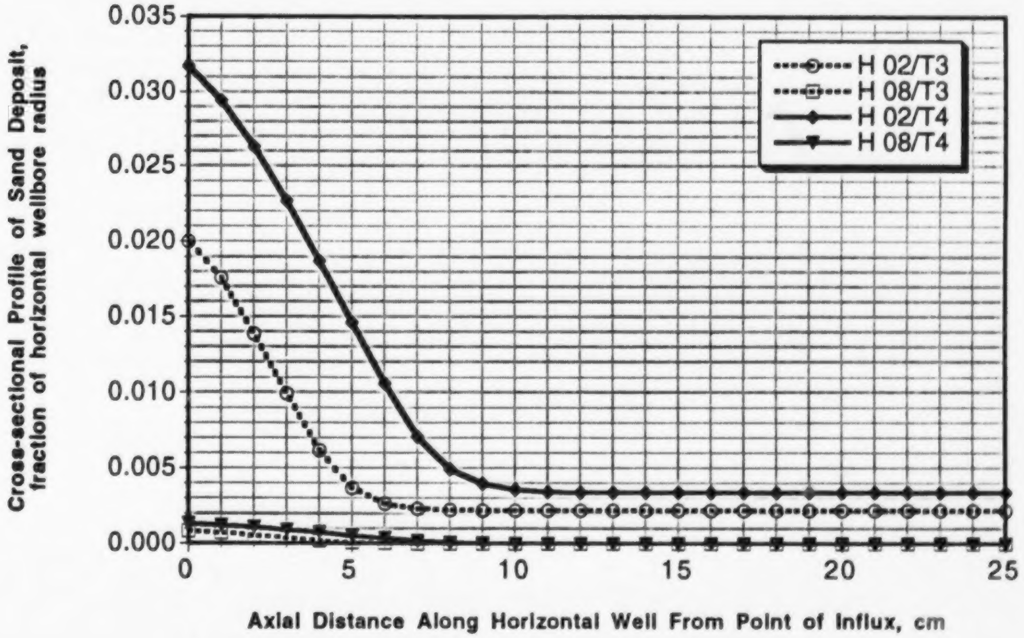

b) Profiles at time T 3 (t = 1.03 s), and at time T 4 (t = 1.62 s)

Figure 6. 50: Heavy oil/Effect of particle size – Profile of sand deposit at different times for two sand sizes, Run H 02 (d = 0.5 cm) and Run H 08 (d = 0.1 cm), W_f = 5.0 cm/s, ρ_o = 1.00 g/cm^3, μ = 1 500 mPa.s .

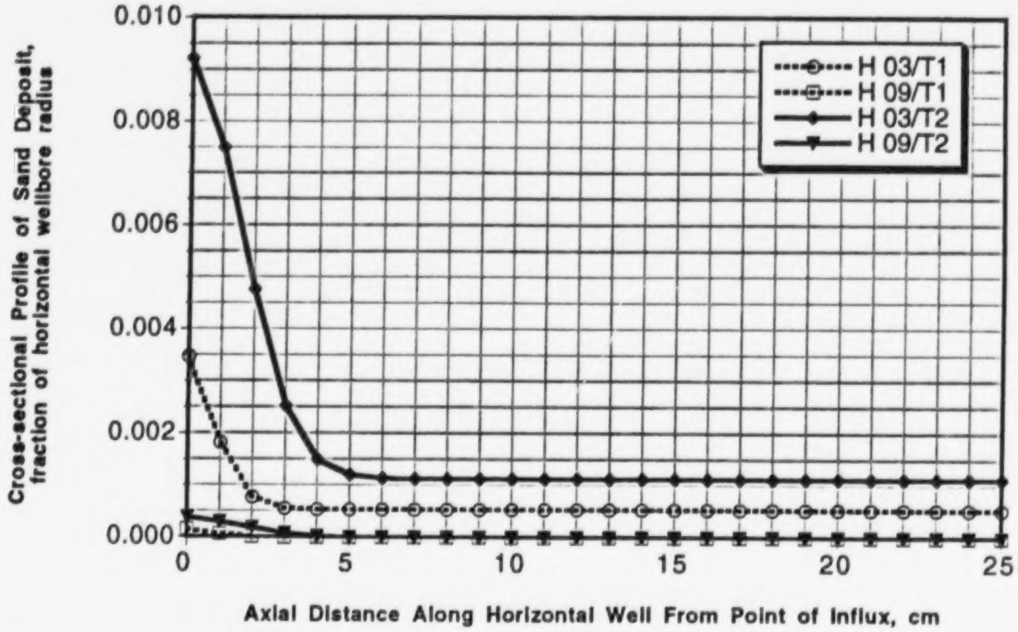

a) Profiles at time T 1 (t = 0.24 s), and at time T 2 (t = 0.51 s)

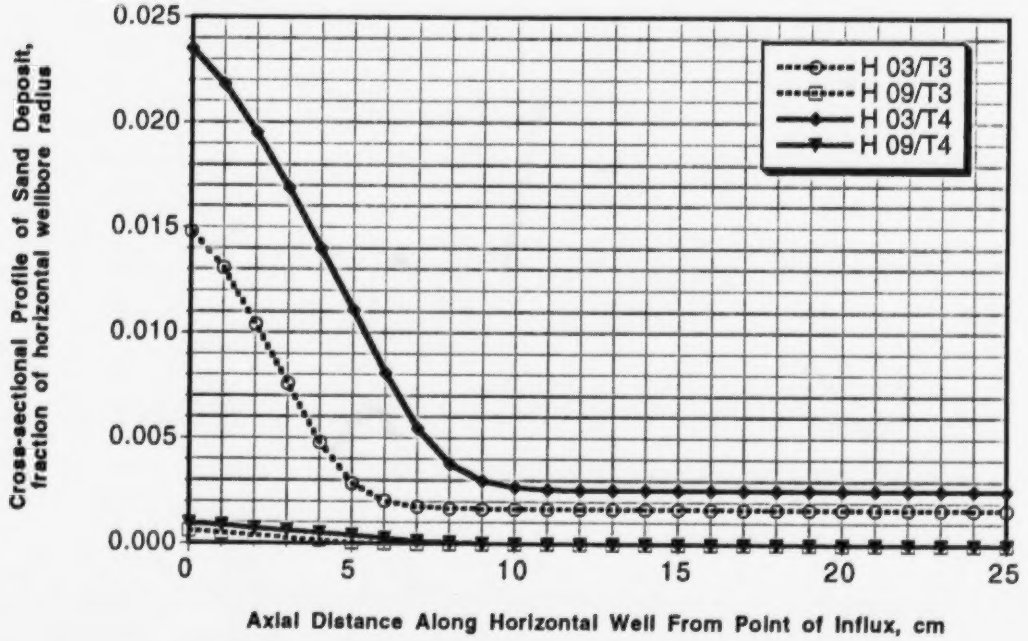

b) Profiles at time T 3 (t = 0.77 s), and at time T 4 (t = 1.20 s)

Figure 6. 51: Heavy oil/Effect of particle size – Profile of sand deposit at different times for two sand sizes, Run H 03 (d = 0.5 cm) and Run H 09 (d = 0.1 cm), W_t = 6.825 cm/s, ρ_o = 1.00 g/cm^3, μ = 1 500 mPa.s .

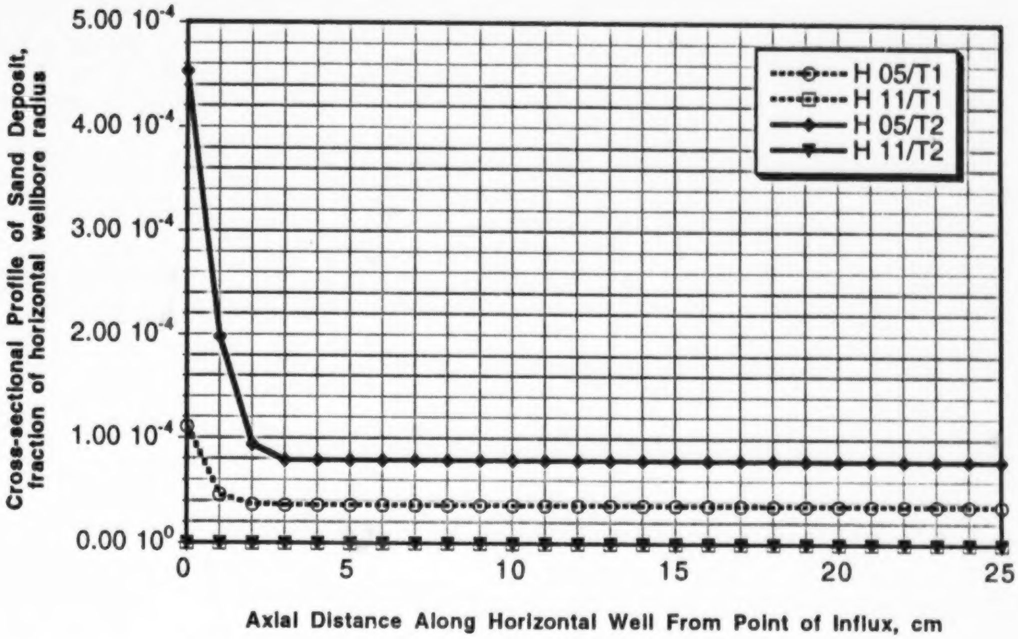

a) Profiles at time T 1 (t = 0.11 s), and at time T 2 (t = 0.24 s)

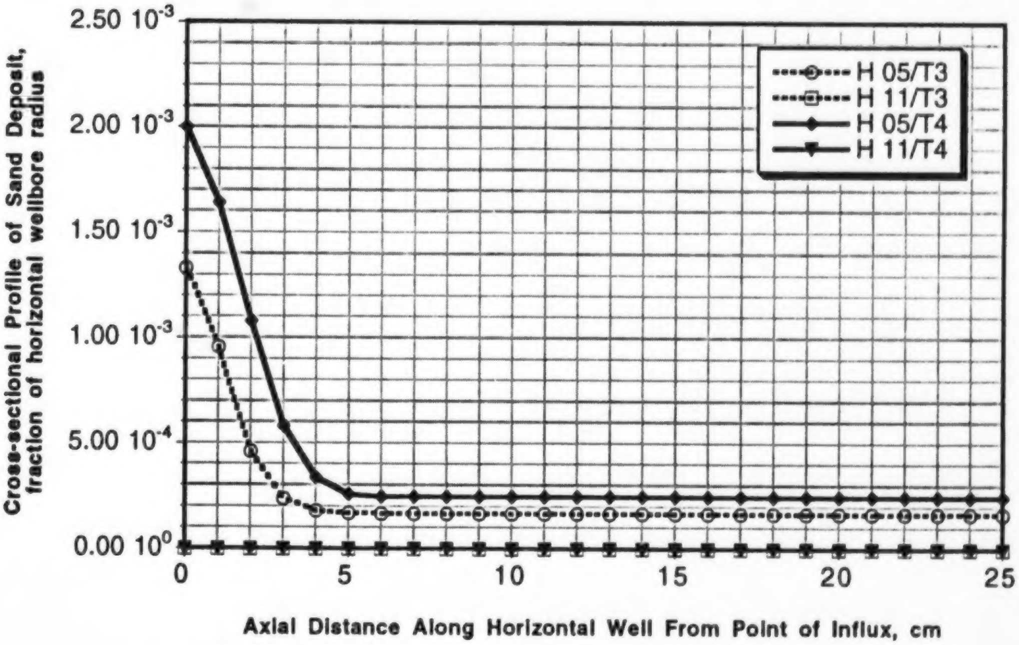

b) Profiles at time T 3 (t = 0.52 s), and at time T 4 (t = 0.73 s)

Figure 6. 52: Heavy oil/Effect of particle size – Profile of sand deposit at different times for two sand sizes, Run H 05 (d = 0.5 cm) and Run H 11 (d = 0.1 cm), $W_t = 5.0$ cm/s, $\rho_o = 1.00$ g/cm³, $\mu = 10\,000$ mPa.s .

e) Well production rate = 150.0 m³/day, oil viscosity = 10 000 mPa.s

There is practically no deposition for the larger particle (Run H 06, dia.=0.5 cm), and no deposition for the smaller particle (Run H 12, dia.=0.1 cm), as shown in Figure 6.53.

The following conclusions are drawn from the above results for the Heavy Oil case. On the basis of an individual variable, there is more deposition for less viscous fluid and larger particle size. A higher flow velocity results in a more spread-out deposition pattern, and a more gradual deposition profile. The most noticeable difference in comparing the results for the Light Oil case and the Heavy Oil case is the larger rate of deposition, and the expansion rate for the deposit once it forms in the Light Oil sub-cases.

6.5. Implication of Simulation Results for Field Conditions

It is important to keep a proper perspective of the simulation results before examining their implication for field conditions. As stated above, limitations in the storage memory capacity of the personal computer used in this study (Macintosh Quadra 800) play an important role in the types, and in the number of simulation runs performed. The duration of the deposition process (from initial homogeneous condition), in most of the simulation runs, was less than 10 seconds. Even under hydrodynamic conditions designed to facilitate and expedite particle deposition (i.e. relatively low oil viscosity, larger-than-average particle size) the simulated durations are still rather short, and represent only the early stage of the transport process. In addition, only one point of influx for oil and sand is allowed. Under these combined conditions certain phenomena of the particles deposition process are observed. The most common result seen in the various cases (and sub-cases) considered is the formation of a solid deposit bed at the bottom of a horizontal well (near the point of influx), and its subsequent expansion – vertically, as well as laterally. The initial rate of particles deposition and the subsequent expansion rate of the deposit bed vary for different cases, depending on the prevailing hydrodynamic conditions.

However, the simulation runs are definitely not long enough in duration to obtain pictures of the whole transport process, i.e. from initial homogeneous condition to some 'final' condition. This final condition could range from steady state flow of the oil-sand suspension with no particle deposition, to the horizontal well being completely plugged with sand deposits at some point(s). The final condition could also be the formation of a series of stationary sand deposits along the entire length of the horizontal well. These late-stage phenomena are not, unfortunately, observed in the results for the reason given above. Additionally, this final condition depends to a large extent – not only on the prevailing hydrodynamic conditions – but more importantly on the features incorporated into the mathematical model. For example, given the fact that saltatory mo-

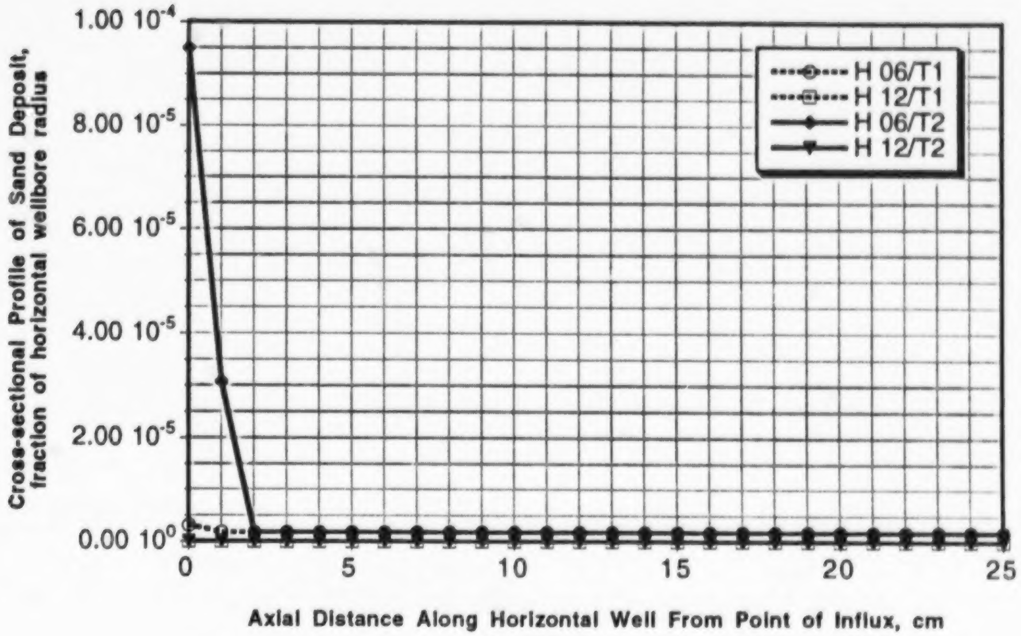

a) Profiles at time T 1 (t = 0.05 s), and at time T 2 (t = 0.21 s)

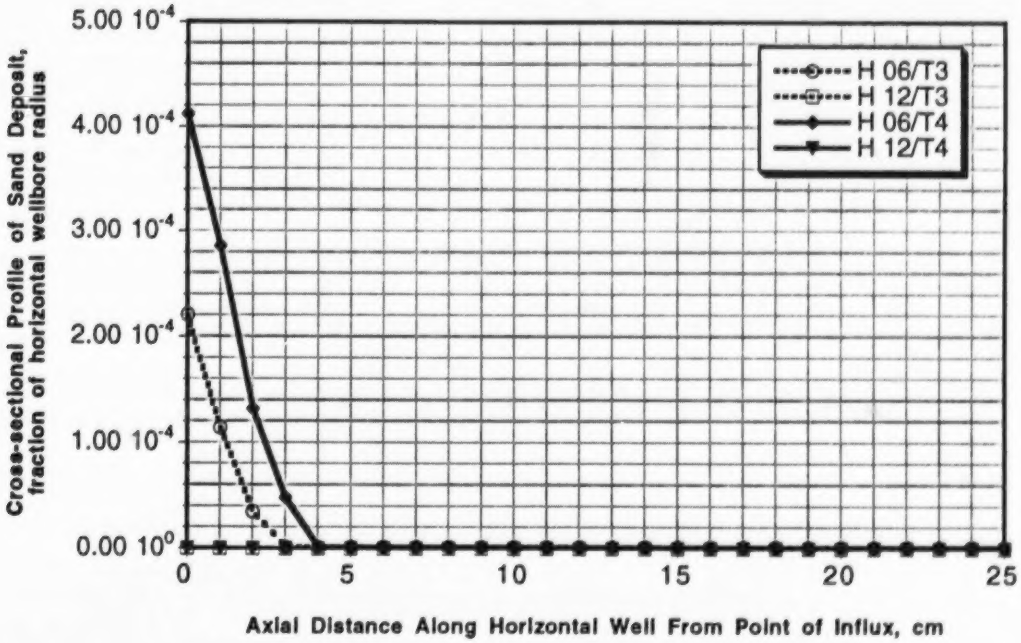

b) Profiles at time T 3 (t = 0.36 s), and at time T 4 (t = 0.55 s)

Figure 6. 53: Heavy oil/Effect of particle size – Profile of sand deposit at different times for two sand sizes, Run H 06 (d = 0.5 cm) and Run H 12 (d = 0.1 cm), $W_f = 6.825$ cm/s, $\rho_o = 1.00$ g/cm^3, $\mu = 10\,000$ mPa.s .

tion of particles is excluded from the Gravity Deposition model it is not possible to expect a final condition of moving sand dunes to be obtained.

Nevertheless, certain conclusions can be advanced on the basis of the short-duration results obtained in this study. Revisiting the results illustrated in Figures 6.20 – 6.24, it is seen that the simulation results for the Gravity Deposition model agree with the experimental observations made by Bagnold for the formation of sand ripples and depositions in a shallow-water environment [144]. These results are also logically explainable, in terms of the variations in the pressure distribution and the velocity distribution for the fluid phase and solid phase as a result of sand deposition and accumulation at the bottom of the horizontal well. It is also important to remember that the simulation runs carried out in this study model what is essentially an element of symmetry of the horizontal well, with one point of influx. On the basis of the agreement between the numerical results obtained in this study and Bagnold's experimental observations, it is believed that longer simulation runs, coupled with multiple points of influx for oil and sand will enable a final condition of a series of stationary deposit beds forming along the horizontal well length.

Given the above discussion, it is seen from the results presented above that the Gravity Deposition model is capable of modelling the gravity deposition of sand from an initial condition of homogeneous suspension. The deposition process occurs naturally, and as a result of the hydrodynamic conditions inside the horizontal well, including fluid viscosity and velocity, particle size, and pressure gradient. In the majority of cases studied deposition occurs quickly (soon after the introduction of sand into the horizontal well), and the resulting deposit bed expands at a relatively fast rate. Conditions conducive to the formation of a sand deposit bed at the bottom of a horizontal well include low oil (fluid) viscosity and large sand particles. However, as the oil viscosity increases and the sand particles become smaller the deposition process slows down considerably. In addition, the expansion rate for the deposit bed also is reduced appreciably by the conditions of high oil (fluid) viscosity and smaller particle size. In one of the cases studied, there is absolutely no sand deposition, as the sand particles are kept in suspension. The oil viscosity is 10 000 mPa.s, and the diameter of the sand particles is 1 000 microns, for this case of no deposition. Flow rates ranging from 55.0 m^3/day to 150.0 m^3/day do not seem to have any effect on the outcome of no sand deposition. Also, there is extremely limited deposition of sand in other cases of reasonably high oil (fluid) viscosity, and larger particles.

A view of the features incorporated into the Gravity Deposition model also provides some insights into the deposition process, as shown by the numerical results. The omission of Saffman's lift force from the Gravity Deposition model tends to enhance gravity deposition. It is postulated that there is more (particle) deposition in the cases studied here than would have been if Saffman's lift force had been included in the equation of motion for the fluid phase and solid phase. On the other hand, the assumption of instantaneous acceleration of the influx mass (for both the fluid and solid phases) to the prevailing stream velocities tends to have the opposite effect. What this statement means is that had this assumption not been invoked, and some momentum was lost to accelerate the influx mass there would have been more solid deposition at the bottom of the horizontal well – especially close to the point of influx.

In the context of heavy oil reservoirs in eastern Alberta and Saskatchewan these simulation results, as analyzed, indicate that there would be little or no deposition of sand at the bottom of a horizontal well. Sand particles that are produced and introduced into a horizontal well, depending on their velocities, tend to be kept in suspension and carried along with the fluid to the wellhead, mostly unaffected by fluid production rates. The high drag force, due to the high oil (fluid) viscosity, ensures that the sand particles are kept in suspension, and not deposited out. This type of behaviour, as predicted by the simulation results here, is also observed by field operators who have found repeatedly that the best production strategy is to produce the sand with the fluid(s), and not to try to stop sand production [136]. This is not to say that there is no sand deposition forming and accumulating at the bottom of a horizontal well. It is important to remember the following. As stated previously, many of these heavy oil reservoirs are underlain by bottom water. As such, water – given its high mobility (i.e. low viscosity) – tends to be quickly produced into and through the horizontal well, either as a separate phase or in an emulsified form. A slug of water produced into the horizontal well will no doubt deposit sand particles which might have been produced/introduced with it into the wellbore. Continuing production of water and sand into the wellbore provides hydrodynamic conditions very conducive not only to the initial formation of a deposit bed, but also to the expansion of this accumulation. It is believed that it is within this context of water production that sand deposition takes place in a horizontal well recovering oil from these heavy oil reservoirs.

6.6. Concluding Remarks

In summary, numerical results for two one-dimensional models simulating the transport of oil and sand in a horizontal well are presented in this chapter. The first model *a priori* and arbitrarily fixes the geometry and expansion rate of a constriction inside the flow channel, and examines the transport process as a result of the presence of this constriction. Results for two cases are obtained, and analyzed. In the first case, the transport process is dominated by pressure forces. It is seen that the hydrodynamic conditions in this case result in a large amount of slip between the two phases. This large discrepancy in the solid phase and fluid phase velocities, together with the increased collisions among the solid particles, gives rise to a large increase in the kinematic pressure. In the second case, the interfacial drag force dominates the flow. A high fluid viscosity and a small particle size together give rise to a high drag force between the solid and fluid phases, the result being a very small amount of slip between their velocities. The kinematic pressure is negligible in this case. Discussion of the physical meanings of values assigned for several variables in the simulation runs is provided. A previously reported (the Constriction) model [83], despite numerous attempts to adapt and modify it, cannot be used to study sand deposition under field conditions.

The Gravity Deposition model, developed from the Constriction model, takes the transport process to the next level. It actually simulates the gravity deposition of solid particles as a result of the prevailing hydrodynamic conditions. It does not *a priori* and arbitrarily fix the geometry and expansion rate of a deposit (i.e. constriction). It was run for many cases of different fluid viscosity, particle size, and flow rates. The values assigned for various hydrodynamic variables and parameters are field-scale, and representative of values obtained for an actual Saskatchewan (Lloykdminster) heavy oil reservoir. The effects of three transport variables (oil viscosity, flow rate, and particle size) on the gravity deposition process are studied, individually. From the results obtained, it is seen that conditions conducive to the formation of a deposit at the bottom of a horizontal well and its subsequent expansion include low oil (fluid) viscosity and large particle sizes. These results follow remarkably closely to the behaviour predicted by (the much simpler) Stokes's law for the terminal settling velocity. A general discussion is provided regarding the problem of sand deposition for heavy oil reservoirs in eastern Alberta and Saskatchewan on the basis of these results. The gravity deposition model is suitable as a tool to be used in the study of sand deposition in a horizontal well, and its effect on well productivity.

Chapter 7. Conclusions

This investigation has been carried out as a result of an increasingly common problem of sand deposition and accumulation in many horizontal wells recovering oil from heavy oil reservoirs in Alberta and Saskatchewan. On the basis of the work performed, and the results obtained, the following conclusions are offered:

1. First and foremost, this study has to a large degree achieved the objective set out in Chapter 3. Mathematical models have been formulated to describe mechanistically the transport of oil and sand inside a horizontal well. These models have been developed for different cases, ranging from two-dimensional transport to one-dimensional transport of oil and sand in a constricted channel to finally a one-dimensional model describing the gravity deposition of solid particles from initial homogeneous conditions.

2. Numerical results have been obtained for two one-dimensional models. In the case of suspension flow in a constricted channel, results have been generated which agree with results reported in a previous study. Explanations are offered for the behaviour observed for the two cases considered, on the basis of the kinematic pressure theory. When there is a large amount of slippage between the solid phase and the fluid phase, and intense intraphase interaction in the form of particle-particle collisions there is a significant difference between the fluid phase and solid phase pressures. When the fluid viscosity is high, little slippage between the two phases occurs, and the solid particles are largely carried in the fluid stream. An attempt to apply the Constriction model to study sand deposition and accumulation under field conditions was not successful.

3. The Gravity Deposition model was developed to describe the gravity deposition of solid particles as a result of prevailing hydrodynamic conditions inside a horizontal well, without having to resort to fixing the profile and expansion rate of the constriction arbitrarily. Results generated by this model are consistent with experimental observation of the formation and expansion of sand ripples at the bottom of shallow water bodies.

4. For the Gravity Deposition model, results have been obtained to examine the influence of three variables – fluid (oil) viscosity, solid particle size, and flow velocity – on the deposition and expansion of solid particles at the bottom of a horizontal well. Using field data, it is determined that hydrodynamic conditions conducive to fast particles deposition and to a high expansion rate of the deposit bed include low fluid viscosity and large particle size. There is little or no deposition when

the fluid viscosity is high and/or the solid particle is small. The observed behaviour agrees with Stokes' law for terminal settling velocity

5. Scaling criteria are derived using both Inspectional Analysis and Dimensional Analysis. Physical meanings of the derived scaling criteria are determined to provide some insight into the interaction between different variables and parameters involved in the transport process.

The principal contributions of this study are as follows.

1. A systematic survey of relevant two-phase flow literature has been performed. The problem of sand production and deposition in a wellbore, and its subsequent impact on well productivity is not new. However, a theoretical treatment of the transport of oil and sand in a wellbore in general and a horizontal well in particular has been, in many respects, lacking. Nor have there been many experimental investigations of this problem. Other experimental studies are restricted mostly to the flow *after* sand deposition and accumulation. As far as it is known by the author, this study is one of the first (and few) attempts to examine the transport process mechanistically.

2. A theoretical framework is developed for the transport of oil and sand in a horizontal well. Of particular interest is the formulation employed for the Gravity Deposition model, which allows the deposition and bed expansion process to occur naturally, as functions of the prevailing hydrodynamic conditions inside the horizontal well. As such, the model is not dependent on artificially and/or arbitrarily assigned parameters to be able to model sand deposition and accumulation in a horizontal well. The combination of these two factors is believed to provide a solid foundation for more comprehensive research into this problem in the future, both in terms of physical modelling and numerical modelling.

These contributions are pointed out in full recognition of the many features and mechanisms not incorporated into the present study. As pointed out many times previously, multiphase flow processes are highly complex, and many flow mechanisms remain far from being understood fully. It is not possible to gain insight into a particular multiphase flow process in just a few (whatever the number might be !) studies. What is required is a systematic, multi-staged, multi-faceted approach including investigation of the process at both the microscopic and macroscopic levels. It is within this spirit that this discussion is provided.

Chapter 8. Recommendations

On the basis of the work performed, the results obtained, and the discussion provided, the following recommendations are offered:

1. First, the Gravity Deposition model should be tested for longer time durations. This is to examine its capability in generating late-time phenomena of the transport of oil and sand in a horizontal well. The influence of other parameters including slippage velocity and pressure drop should also be investigated.

2. Mechanisms such as Saffman's lift force and the pressure loss required to accelerate influx mass to stream velocities should be incorporated into the model. As pointed out previously, many of the mechanisms not considered in this study have complementary and/or competing influence on the deposition and bed expansion processes. As such, these mechanisms have to be incorporated and investigated individually first, and jointly subsequently.

3. Once the influence of individual parameters and mechanisms are understood, scaling criteria similar to those derived in this work should be incorporated into the numerical simulation runs. This is to provide insight into the role and influence of combined parameters and mechanisms on the overall transport process.

4. Of equal importance is the need to perform physical experiments to study the transport process. A scaled physical model should be designed, and operated taking advantage of the scaling criteria obtained in this study. The scaled model experiments should proceed in a similar fashion of investigating first the influence of individual parameters prior to investigating the influence of grouped/combined parameters and mechanisms.

5. Saltatory motion of solid particles should be incorporated into the model(s). This feature enables the study of dynamic growth, including expansion and contraction, of the deposit bed with time.

REFERENCES

1) Soo, SL: Fluid Dynamics of Multiphase Systems, Blaisdell Publishing Company, 1967.

2) Bird, R.B., Stewart, W.E. and Lightfoot, E.N.: Transport Phenomena, Wiley, 1960, Chapter 3, pp. 71-122..

3) Segré, G. and Silberberg, A.: Behaviour of Macroscopic Rigid Spheres in Poiseuille Flow, Part 1 – Determination of Local Concentration by Statistical Analysis of Particle Passages Through Cross Light Beams, *Jour. of Fluid Mechanics*, **14**, 1962, pp. 115-135.

4) Segré, G. and Silberberg, A.: Behaviour of Macroscopic Rigid Spheres in Poiseuille Flow, Part 2 – Experimental Results and Interpretation, *Jour. of Fluid Mechanics*, **14**, 1962, pp. 136-157.

5) Saffman, P.G.: The Lift on a Small Sphere in a Slow Shear Flow, *Jour. of Fluid Mechanics*, **22**, 1965, Part 2, pp. 385-400.

6) Rouhiainen, P.O. and Stachiewicz, J.W.: On the Deposition of Small Particles from Turbulent Streams, *Jour. of Heat Transfer, Trans.* of **ASME**, February, 1970, pp.169-177.

7) Lee, SL: A Further Discussion of "Particle Drag in a Dilute Turbulent Two-Phase Suspension Flow", *Intl. Jour. of Multiphase Flow*, **17**, 3, 1991, pp. 421-424.

8) Moreland, C.: Settling Velocities of Coal Particles, *Can. Jour. of Chemical Engineering*, June 1963, pp. 108-110.

9) Blumberg, P.N. and Mohr, M.C.: Effect of Orientation on the Settling Characteristics of Cylindrical Particles, *AIChE Jour.*, **14**, 2, March 1968, pp. 331-334.

10) O' Brien, V.: Form Factors for Deformed Spheroids in Stokes Flow, *AIChE Jour.*,**14**, 6, November 1968, pp. 870-875.

11) Peden, J.M. and Luo, Y.: Settling Velocity of Variously Shaped Particles in Drilling and Fracturing Fluids, *SPE Drilling Engineering*, December 1987, pp. 337-343.

12) Clark, N.N., Gabrielle, P., Shuker, S. and Turton, R.: Drag Coefficient of Irregular Particles in Newton' s Settling Regime, *Jour. of Powder Technology*, **59** (1989), pp. 69-72.

13) Hedstrom, B.O.A.: Flow of Plastic Materials in Pipes, *Industrial and Engineering Chemistry*, **44**, 3, March 1952, pp. 651-656.

14) Ansley, R.W. and Smith, T.N.: Motion of Spherical Particles in a Bingham Plastic, *AIChE Jour.*, **13**, 6, November 1967, pp. 1193-1196.

15) Shah, S.N.: Proppant Settling Correlations for Non-Newtonian Fluids Under Static and Dynamic Conditions, *Soc. of Petroleum Engineers Jour.*, April 1982, pp. 164-170.

16) Meyer, B.R.: Generalized Drag Coefficient Applicable for All Flow Regimes, *Oil & Gas Jour.*, May 26/1986, pp. 71-77.

17) Dedegil, M.Y.: Drag Coefficient and Settling Velocity of Particles in Non-Newtonian Suspensions, Intl. Symposium on Slurry Flows, Winter Ann. Meeting of the American Soc. of Mechanical Engineers, Anaheim, CA, December 7-12, 1986.

18) Mena, B., Manero, O. and Leal, L.G.: The Influence of Rheological Properties on the Slow Flow Past Spheres, *Jour. of Non-Newtonian Fluid Mechanics*, **26**, 1987, pp. 247-275.

19) McMechan, DE and Shah, S.N.: Static Proppant-Settling Characteristics of Non-Newtonian Fracturing Fluids in a Large-Scale Test Model, *SPE Production Engineering*, August 1991, pp. 305-312.

20) Steinour, H.H.: Rate of Sedimentation – Nonflocculated Suspensions of Uniform Spheres, *Industrial and Engineering Chemistry*, **36**, 7, July 1944, pp. 618-624.

21) Ergun, S. and Orning, A.A.: Fluid Flow Through Randomly Packed Columns and Fluidized Beds, *Industrial and Engineering Chemistry*, **41**, 6, June 1949, pp. 1179-1184.

22) Ergun, S.: Fluid Flow Through Packed Columns, *Chemical Engineering Progress*, **48**, 1952, pp. 89-94.

23) Richardson, J.F. and Zaki, W.N.: Sedimentation and Fluidisation: Part I, *Trans. Institute of Chemical Engineers*, **32**, 1954, pp. 35-52.

24) Maude, A.D. and Whitmore, R.L.: A Generalized Theory of Sedimentation, *British Jour. of Applied Physics*, **9**, 1958, pp. 477-482.

25) Fan, L.-T., Lee, C.J. and Bailie, R.C.: Axial Solid Distribution in Gas-Solid Fluidized Beds, *AIChE Jour.*, **8**, 2, May 1962, pp. 239-244.

26) Round, G.F. and Kruyer, J.: Experiments on the Suspension of Spheres in Inclined Tubes – I.Suspension by Water in Turbulent Flow, *Chemical Engineering Science*, **22**, 1967, pp. 1133-1145.

27) Batchelor, G.K.: Sedimentation in a Dilute Dispersion of Spheres, *Jour. of Fluid Mechanics*, **52**, part 2, 1972, pp. 245-263.

28) Glendinning, A.B. and Russell, W.B.: Sedimentation and Diffusion in Concentrated Colloidal Dispersions, *Jour. of Colloid Interface Science*, **89**, 1982, pp. 124-141.

29) Tadros, Th.F.: Chapter 11. Settling of Suspensions and Prevention of Formation of Dilatant Sediments, Solid/Liquid Dispersions, edited by Th.F. Tadros, Academic Press, 1987, pp. 225-274.

30) Bagnold, R.A.: The Movement of a Cohesionless Granular Bed by Fluid Flow Over It, *British Jour. of Applied Physics*, **2**, February 1951, pp. 29-34.

31) Shook, C.A. and Daniel, S.M.: Flow of Suspensions of Solids in Pipelines, Part I. Flow with a Stable Stationary Deposit, *Can. Jour. of Chemical Engineering*, April 1965, pp. 56-61.

32) Shook, C.A., Daniel, S.M., Scott, J.A. and Holgate, J.P.: Flow of Suspensions in Pipelines, Part 2. Two Mechanisms of Particle Suspension, *Can. Jour. of Chemical Engineering*, **46**, August 1968, pp. 238-244.

33) Noda, K., Kawashima, T. and Masuyama, T.: Studies on Three-Phase Flow in an Inclined Pipe: Determination of Entrance Region of Pipe and Measurement of Pressure Loss, paper D5, Proc. of the Second Intl. Conference on the Hydraulic Transport of Solids in Pipes, Warwick, England, September 20-22, 1972.

34) Yan, Y., Pal, R. and Masliyah, J.: Rheology of Oil-in-Water Emulsions with Added Solids, *Chemical Engineering Science*, **46**, 4, 1991, pp. 985-994.

35) Yan, Y., Pal, R. and Masliyah, J.: Viscosity Correlations for Emulsion-Solids Mixtures as Bimodal Systems, *Chemical Engineering Science*, **46**, 7, 1991, pp. 1823-1828.

36) Shah, S.N.: Rheological Characterization of Hydraulic Fracturing Slurries, *SPE Production & Facilities*, May 1993, pp. 123-130.

37) Graf, W.H. and Acaroglu, E.R.: Sediment Transport in Conveyance Systems, Part 1. A Physical Model for Sediment Transport in Conveyance Systems, *Bulletin of the Intl. Association of Scientific Hydrology*, **2**, 13, June 1968, pp. 20-39.

38) Acaroglu, E.R. and Graf, W.H.: Sediment Transport in Conveyance Systems, Part 2. The Modes of Sediment Transport and Their Related Bed Forms in Conveyance Systems, *Bulletin of the Intl. Association of Scientific Hydrology*, **3**, 13, September 1968, pp. 123-135.

39) Alves, G.E., Boucher, D.F. and Pigford, R.L.: Pipeline Design for Non-Newtonian Solutions and Suspensions, *Chemical Engineering Progress*, **48**, 8, August 1952, pp. 385-393.

40) Durand, R.: Basic Relationships of the Transportation of Solids in Pipes – Experimental Research, Proc. of the 5th Congress, Intl. Association of Hydraulic Research, Minneapolis, Minnesota, 1953.

41) Newitt, D.M., Richardson, J.F. and Shook, C.A.: Hydraulic Conveying of Solids in Horizontal Pipes, Part II: Distribution of Particles and Slip Velocities, Proc. of Symposium on Interaction Between Fluids & Particles, *Institute of Chemical Engineers*, London, UK, 1962, pp. 87-100.

42) Thomas, D.G.: Non-Newtonian Suspensions, Part I: Physical Properties and Laminar Transport Characteristics, *Industrial and Engineering Chemistry*, **55**, 11, November 1963, pp. 18-29.

43) Thomas, D.G.: Non-Newtonian Suspensions, Part II: Turbulent Transport Characteristics, *Industrial & Engineering Chemistry*, **55**, 12, December 1963, pp. 27-35.

44) Thomas, D.G.: Transport Characteristics of Suspensions: II. Transport Velocity for Flocculated Suspensions in Horizontal Pipes, *AIChE Jour.*, **7**, 3, September 1961, pp. 423-430.

45) Thomas, D.G.: III. Laminar-Flow Properties of Flocculated Suspensions, *AIChE Jour.*, **7**, 3, September 1961, pp. 431-437.

46) Thomas, D.G.: Transport Characteristics of Suspensions: Part IV. Friction Loss of Concentrated-Flocculated Suspensions in Turbulent Flow, *AIChE Jour.*, **8**, 2, May 1962, pp. 266-271.

47) Thomas, D.G.: Transport Characteristics of Suspensions: Part VI. Minimum Transport Velocity for Large Particle Size Suspensions in Round Horizontal Pipes, *AIChE Jour.*, **8**, 3, July 1962, pp. 373-378.

48) Thomas, D.G.: Transport Characteristics of Suspensions: Part VII. Relation of Hindered-Settling Floc Characteristics to Rheological Parameters, *AIChE Jour.*, **9**, 3, May 1963, pp. 310-316.

49) Thomas, D.G.: Transport Characteristics of Suspensions: Part IX. Representation of Periodic Phenomena on a Flow Regime Diagram for Dilute Suspension Transport, *AIChE Jour.*, **10**, 3, May 1964, pp. 303-308.

50) Soo, SL, Trezek, G.J., Dimick, R.C. and Hohnstreiter, G.F.: Concentration and Mass Flow Distribution in a Gas-Solid Suspension, *Industrial & Engineering Chemistry Fundamentals*, **3**, 2, May 1964, pp. 98-106.

51) Soo., SL and Trezek, G.J.: Turbulent Pipe Flow of Magnesia Particles in Air, *Industrial & Engineering Chemistry Fundamentals*, **5**, 3, August 1966, pp. 388-392.

52) Wasp, E.J., Aude, T.C., Seiter, R.H. and Thompson, T.L.: Hetero-Homogeneous Solids/Liquid Flow in the Turbulent Regime, paper 13, Proc. of American Soc. of Civil Engineers Intl. Symposium on Solid-Liquid Flow, University of Pennsylvania, March 1968, pp. 199-210.

53) Rose, H.E. and Duckworth, R.A.: Transport of Solid Particles in Liquids and Gases, *The Engineer*, March 14, 1969, pp. 392-396; March 21, 1969, pp. 430-433; March 28, 1969, pp. 478-483.

54) Gay, E.C., Nelson, P.A. and Armstrong, W.P.: Flow Properties of Suspensions with High Solids Concentration, *AIChE Jour.*, **15**, 6, November 1969, pp. 815-822.

55) Kaskas, A.: Swarm Velocities in Sedimentation of Polydisperse Suspensions, Proc.of Particle Technology Seminar, edited by D. Venkateswarlu & A. Prabhakara Rao, Indian Institute of Technology, Madras, January 1971, pp. 441-454.

56) Hanks, R.W. and Dadia, B.H.: Theoretical Analysis of the Turbulent Flow of Non-Newtonian Slurries in Pipes, *AIChE Jour.*, **17**, 3, May 1971, pp. 554-557.

57) Turian, R.M., Yuan, T.-F. and Mauri, G.: Pressure Drop Correlation for Pipeline Flow of Solid-Liquid Suspension, *AIChE Jour.*, **17**, 4, July 1971, pp. 809-817.

58) Hsu, S.T., van der Beken, A., Landweber, L. and Kennedy, J.F.: The Distribution of Suspended Sediment in Turbulent Flows in Circular Pipes, paper 15d, Proc. of AIChE Meeting on Solids Transport in Slurries, August 29-September 01, 1971, Atlantic City, New Jersey, pp. 1-20.

59) Freshwater, D.C. and Goodacre, C.: Settling Suspension Flow in a Horizontal Pipe, Proc. of 1973 Intl. Conference on Particle Technology, ITT Research Institute, Chicago, Illinois, August 21-24, 1973, pp. 67-76.

60) Masuyama, T., Kawashima, T. and Noda, K.: Pressure Loss of Pseudo-plastic Fluid Flow Containing Coarse Particles in a Pipe, paper D1, Proc. of the Fifth Intl.Conference on the Hydraulic Transport of Solids in Pipes, Hanover, Germany, May 8-11, 1978.

61) Thomas, A.D.: Coarse Particles in a Heavy Medium – Turbulent Pressure Drop Reduction and Deposition Under Laminar Flow, paper D5, Proc. of the Fifth Intl. Conference on the Hydraulic Transport of Solids in Pipes, Hanover, Germany, May 8-11, 1978.

62) Hashimoto, H., Noda, K., Masuyama, T. and Kawashima, T.: Influence of Pipe Inclination on Deposit Velocity, paper F2, Proc. of the Seventh Intl. Conference on the Hydraulic Transport of Solids in Pipes, Sendai, Japan, November 4-6,1980.

63) Kao, D.T., Nosrati, A. and Schaefer, J.L.: Flow Behaviour of Solid-Liquid Mixtures in Pipes on Positive and Negative Grades, paper F1, Proc. of the Seventh Intl. Conference on the Hydraulic Transport of Solids in Pipes, Sendai, Japan, November 4-6, 1980.

64) Weber, M.: Improved Durand Equation for Multiple Application, Proc. of Intl.Symposium on Slurry Flows, Winter Ann. Meeting of the American Soc. of Mechanical Engineers, Anaheim, CA, December 7-12, 1986, pp. 61-66.

65) Hauge, H. and Sharma, M.P.: An Investigation of Coarse Particle Transport in Inclined Pipes, Proc. of Intl. Symposium on Slurry Flows, Winter Ann. Meeting of the American Soc. of Mechanical Engineers, Anaheim, CA, December 7-12, 1986, pp. 113-118.

66) Ponce-Campos, C.D. and Motan, E.S.: Critical Friction Factors During Pipe Blockage Dislodgement in Slurry Flow, Proc. of Intl. Symposium of Slurry Flow, Winter Ann. Meeting of the American Soc. of Mechanical Engineers, Anaheim, CA, December 7-12, 1986, pp. 119-124.

67) Nasr-El-Din, H., Shook, C.A. and Colwell, J.: The Lateral Variation of Solids Concentration in Horizontal Slurry Pipeline Flow, Proc. of Intl. Symposium of Slurry Flow, Winter Ann. Meeting of the American Soc. of Mechanical Engineers, Anaheim, CA, December 7-12, 1986, pp. 175-180.

68) Thomas, J.W. and Knuth, R.H.: Patterns of Aerosol Particles Settling in Streamline Flow in a Straight Horizontal Tube, *Air & Water Pollution Intl. Jour.*, **10**, 1966, pp. 569-572.

69) Pich, J.: Theory of Gravitation Deposition of Particles from Laminar Flows in Channels, *Aerosol Science*, **3**, 1972, pp. 351-361.

70) Tomren, P.H., Iyoho, A.W. and Azar, J.J.: Experimental Study of Cuttings Transport in Directional Wells, *SPE Drilling Engineering*, February 1986, pp. 43-56.

71) Okrajni, S. and Azar, J.J.: The Effects of Mud Rheology on Annular Hole Cleaning in Directional Wells, *SPE Drilling Engineering*, August 1986, pp. 297-308.

72) Becker, T.E., Azar, J.J. and Okrajni, S.S.: Correlations of Mud Rheological Properties with Cuttings Transport Performance in Directional Drilling,*SPE Drilling Engineering*, March 1991, pp. 16-24.

73) Van Deemter, J.J. and Van der Laan, E.T.: Momentum and Energy Balances for Dispersed Two-Phase Flow, *Applied Science Research*, Section A, **10**, 1961, pp. 102-108.

74) Hinze, J.O.: Momentum and Mechanical-Energy Balance Equations for a Flowing Homogeneous Suspension with Slip Between the Two Phases, *Applied Science Research*, Section A, **11**, 1963, pp. 33-46.

75) Hershey, D. and Song, G.: Friction Factors and Pressure Drop for Sinusoidal Laminar Flow of Water and Blood in Rigid Tubes, *AIChE Jour.*, **13**, 3, May 1967, pp. 491-496.

76) Soo, SL: Pipe Flow of Suspensions, *Applied Science Research*, **21**, August 1969, pp. 68-84.

77) Soo, SL: Slurry Flow Modelling and Effect of Concentration, Proc. of Intl. Symposium of Slurry Flow, Winter Ann. Meeting of the American Soc. of Mechanical Engineers, Anaheim, CA, December 7-12, 1986, pp. 1-8.

78) Roco, M.C.: Diagram to Classify Liquid-Solid Flows by Their Microstructure, paper B3, Proc. of the Eleventh Intl. Conference on the Hydraulic Transport of Solids in Pipes, Stratford-upon-Avon, UK, October 19-21, 1988, pp. 81-106.

79) Murthy, V.R.K. and Zandi, I.: Turbulent Flow of Non-Newtonian Suspensions in Pipes, *Jour. of the Engineering Mechanics Division*, EM1, Proc. of American Soc. of Civil Engineers, February 1969, pp. 271-288.

80) Soo, SL: Correlation of States of Hydraulic Transport of Solids in Pipes, paper A1, Proc. of First Intl. Conference on the Hydraulic Transport of Solids in Pipes,University of Warwick, England, September 1-4, 1970.

81) Soo, SL and Tung, S.K.: Pipe Flow of Suspensions in Turbulent Fluid. Electrostatic and Gravity Effects, *Applied Science Research*, **24**, June 1971, pp. 83-97.

82) Soo, SL and Tung, S.K.: Deposition and Entrainment in Pipe Flow of a Suspension, *Powder Technology*, **6**, 1972, pp. 283-294.

83) Givler, R.C. and Mikatarian, R.R.: Numerical Simulation of Fluid-Particle Flows: Geothermal Drilling Applications, Trans of ASME, *Jour. of Fluids Engg.*, **109**, September 1987, pp. 324-331.

84) Lee, SL and Wiesler, M.A.: Theory on Transverse Migration of Particles in a Turbulent Two-Phase Suspension Flow Due to Turbulent Diffusion – I, *Intl. Jour. of Multiphase Flow*, **13**, 1, 1987, pp. 99-111.

85) Rasteiro, M.G. and Rebola, M.M.: Simulation of Solid/Liquid Transport in Pipes, paper B1, Proc. of the Eleventh Intl. Conference on the Hydraulic Transport of Solids in Pipes, Stratford-upon-Avon, UK, October 19-21, 1988, pp. 49-61.

86) Toda, M., Konno, H. and Saito, S.: Simulation of Limit-Deposit Velocity in Horizontal Liquid-Solid Flow, paper J2, Proc. of the Seventh Intl. Conference on the Hydraulic Transport of Solids in Pipes, Sendai, Japan, November 4-6, 1980.

87) Roco, M.C. and Shook, C.A.: Modelling of Slurry Flow: The Effect of Particle Size, *Can. Jour. of Chemical Engineering*, **61**, August 1983, pp. 494-503.

88) Roco, M.C. and Shook, C.A.: Critical Deposit Velocity in Slurry Flow, *AIChE Jour.*, **31**, 8, August 1985, pp. 1401-1404.

89) Murray, J.D.: On the Mathematics of Fluidization, Part 1. Fundamental Equations and Wave Propagation, *Jour. of Fluid Mechanics*, **21**, 3, 1965, pp. 465-493.

90) Standart,G.: The Mass, Momentum and Energy Equations for Heterogeneous Flow Systems, *Chemical Engg. Science*, **19**, 1964, pp. 227-236.

91) Rudinger, G. and Chang, A.: Analysis of Nonsteady Two-phase Flow, *Physics of Fluid*, **7**, 11, November 1964, pp. 1747-1754.

92) Harlow, F.H. and Amsden, A.A.: Numerical Calculation of Multiphase Fluid Flow, *Jour. of Computational Physics*, **17**, 1975, pp. 19-52.

93) Stewart, H.B.: Stability of Two-phase Flow Calculation Using Two-fluid Models, *Jour. of Computational Physics*, **33**, 1979, pp. 259-270.

94) Ettehadieh, B., Gidaspow, D. and Lyczkowski, R.W.: Hydrodynamics of Fluidization in a Semi-circular Bed with a Jet, *AIChE Jour.*, **30**, 4, July 1984, pp.529-536.

95) Jones, A.V.: Numerical Treatment of the Momentum Equations for Two-phase Flow, Transient Phenomena in Multiphase Flow, Ed. N.H. Afgan, Hemisphere Publishing Corporation, 1988, pp. 853-869.

96) Murray, J.D.: On the Mathematics of Fluidization, Part 2. Steady Motion of Fully Developed Bubbles, *Jour. of Fluid Mechanics*, **22**, 1, 1965, pp. 57-80.

97) Stuhmiller, J.H.: The Influence of Interfacial Pressure Forces on the Character of Two- phase Flow Model Equations, *Intl. Jour. of Multiphase*, **3**, 1977, pp. 551-560.

98) Nunziato, J.W.: A Multiphase Mixture Theory for Fluid-Particle Flows, Theory of Dispersed Multiphase Flow, Ed. R.E. Meyer, Academic Press, 1983, pp. 191-226.

99) Stewart, H.B. and Wendroff, B.: Two-phase Flow: Models and Methods, *Jour. of Computational Physics*, **56**, 1984, pp. 363-409.

100) Prosperetti, A. and Jones, A.V.: Pressure Forces in Disperse Two-phase Flow, *Intl. Jour. of Multiphase Flow*, **10**, 4, 1984, pp. 425-440.

101) McTigue, D.F., Givler, R.C. and Nunziato, J.W.: Rheological Effects of Nonuniform Particle Distributions in Dilute Suspensions, *Jour. of Rheology*, 30, 5, October 1986, pp. 1053-1076.

102) Hwang, G.J. and Shen, H.H.: Modeling the Phase Interaction in the Momentum Equations of a Fluid-Solid Mixture, *Intl. Jour. of Multiphase Flow*, 17, 1, 1991, pp. 45-57.

103) Borisov, Ju. P.: Oil Field Production Using Horizontal and Multiple-Deviation Wells, Moskva, Nedra, 1964. *Translated from Russian to English by J. Strauss.*

104) Giger, F.M., Reiss, L.H. and Jourdan, A.P.: The Reservoir Engineering Aspects of Horizontal Drilling, SPE 15430, 61st Ann. Tech. Conf. and Exhibition, New Orleans, October 5-8, 1986.

105) Joshi, S.D.: Augmentation of Well Productivity Using Slant and Horizontal Wells, *Jour. of Petroleum Engg.*, June 1988, pp. 729-739.

106) Babu, D.K. and Odeh, A.S.: Productivity of a Horizontal Well, *SPE Reservoir Engineering*, November 1989, pp. 417-421.

107) Peaceman, D.W.: Discussion of Productivity of a Horizontal Well, *SPE Reservoir Engineering*, May 1990, pp. 252-253.

108) Dikken, B.J.: Pressure Drop in Horizontal Wells and Its Effect on Their Production Performance, *Jour. of Petroleum Engg.*, November 1990, pp. 1426-1433.

109) Asheim, H., Kolnes, J. and Oudeman, P.: A Flow Resistance Correlation for Completed Wellbore, *Jour. of Petroleum Science & Engineering*, **8**, 1992, pp. 97-104.

110) Landman, M.: Analytical Modelling of Selectively Perforated Horizontal Wells, *Jour. of Petroleum Science & Engineering*, **10**, 1994, pp. 179-188.

111) Plaxton, W.L.: Pipe Flow Experiments for the Analysis of Two-phase Liquid-liquid Pressure Drop in Horizontal Wells, M.Sc. Thesis, U. of Alberta, Canada, 1995.

112) Bratli, R.K. and Risnes, R.: Stability and Failure of Sand Arches, *SPE Journal*, April 1981, pp. 236-248.

113) Morita, N., Whitfill, D.L., Fedde, ø.P. and Løvik, T.H.: Parametric Study of Sand- Production Prediction: Analytical Approach, *SPE Production Engg.*, February 1989, pp. 25-33.

114) Kirkwood, J.G., Maun, E.K. and Adler, B.J.: Radial Distribution Functions and the Equation of State for a Fluid Composed of Rigid Spherical Particles, *Jour. of Chemistry & Physics*, **18**, 1950, pp. 1040-1047.

115) Harlow, F.H. and Welch, J.E.: Numerical Calculation of Time-Dependent Viscous Incompressible Flow of Fluid with Free Surface, *Physics of Fluids*, **8**, 12, December 1965, pp. 2182-2189.

116) Harlow, F.H. and Shannon, J.P.: The Splash of a Liquid Drop, *Jour. of Applied Physics*, **38**, 10, September 1967, pp. 3855-3866.

117) Hirt, C.W. and Shannon, J.P.: Free-Surface Stress Conditions for Incompressible-Flow Calculations, *Jour. of Computational Physics*, **2**, 1968, pp. 403-411.

118) Daly, B.J.: A Technique for Including Surface Tension Effects in Hydrodynamic Calculations, *Jour. of Computational Physics*, **4**, 1969, pp. 97-117.

119) Pracht, W.E.: A Numerical Method for Calculating Transient Creep Flows, *Jour. of Computational Physics*, **7**, 1971, pp. 46-60.

120) Easton, C.R.: Homogeneous Boundary Conditions for Pressure in the MAC Method, *Jour. of Computational Physics*, **9**, 1972, pp. 375-379.

121) Hirt, C.W. and Cook, J.L.: Calculating Three-Dimensional Flows around Structures and over Rough Terrain, *Jour. of Computational Physics*, **10**, 1972, pp. 324-340.

122) Deville, M.O.: Numerical Experiments on the MAC Code for a Slow Flow, *Jour. of Computational Physics*, **15**, 1974, pp. 362-374.

123) Ghia, K.N., Hankey, W.L., Jr. and Hodge, J.K.: Use of Primitive Variables in the Solution of Incompressible Navier-Stokes Equations, *AIAA Journal*, **17**, 3, 1979, pp. 298-301.

124) Sakamoto, Y. and Matsuo, Y.: Numerical Predictions of Three-dimensional Flow in a Ventilated Room Using Turbulence Models, *Applied Mathematical Modelling*, **4**, February 1980, pp. 67-72.

125) Patel, N.R. and Briggs, D.G.: A MAC Scheme in Boundary-Fitted Curvilinear Coordinates, *Jour. of Numerical Heat Transfer*, **6**, 1983, pp. 383-394.

126) Farouq Ali, S.M.: Personal communications, September-December 1994.

127) Issa, R.I. and Lockwood, F.C.: On the Prediction of Two-Dimensional Supersonic Viscous Interactions Near Walls, *AIAA Journal*, **15**, 2, 1977, pp. 182-188.

128) Carver, M.B.: Some Continuity Considerations in Multidimensional Two Fluid Computation, Transient Two-Phase Flow, Proc. of Third CSNI Specialist Meeting, Ed. by M.S. Plesset, N. Zuber, and I. Catton, Hemisphere Publishing Corporation, 1983, p. 341-352.

129) Boris, J.P. and Book, D.L.: Flux-Corrected Transport. I. SHASTA, A Fluid Transport Algorithm That Works, *Jour. of Computational Physics*, **11**, 1973, pp. 38-69.

130) Liles, D.R. and Reed, W.M.: A Semi-Implicit Method for Two-Phase Fluid Dynamics, *Jour. of Computational Physics*, **26**, 1978, pp. 390-407.

131) Issa, R.I.: Solution of the Implicitly Discretised Fluid Flow Equations by Operator-Splitting, *Jour. of Computational Physics*, **62**, 1985, pp. 40-65.

132) Issa, R.I., Gosman, A.D. and Watkins, A.P.: The Computation of Compressible and Incompressible Recirculating Flows by a Non-interative Implicit Scheme, *Jour. of Computational Physics*, **62**, 1986, pp. 66-82.

133) Fletcher, C.A.J.: Computational Techniques for Fluid Dynamics, Volume II. Specific Techniques for Different Flow Categories, Springer-Verlag, 1988, Chapter 17.

134) Leverett, M.C., Lewis, W.B. and True, M.E.: Dimensional Model Studies of Oil Field Behaviour, *Petroleum Transaction*, **AIME** Vol. **146**, 1942, 175.

135) Rapoport, L.A. and Leas, W.J.: Properties of Linear Waterflood, *Petroleum Transaction*, **AIME** Vol. **198**, 1953, 139.

136) Croes, G.A. and Schwarz, N.:Dimensionally Scaled Experiments and the Theories in the Water Drive Process, *Petroleum Transaction*, **AIME** Vol. **204**, 1955, 35.

137) Offeringa, J. and van der Poel, C.: *Petroleum Transaction*, **AIME** Vol. **201**, 1954, 310.

138) Geertsma, J., Croes, G.A. and Schwarz, N.: Theory of Dimensionally Scaled Models of Petroleum Reservoirs, *Petroleum Transaction*, **AIME** Vol. **207**, 1956, pp. 118-127.

139) Pujol, L. and Boberg, T.C.: Scaling Accuracy of Laboratory Steam Flooding Models, SPE 4191, presented at California Regional Meeting of Soc. of Petroleum Engineers, Bakersfield, CA, November 8-10, 1972.

140) Rojas, G.A., Zhu, T., Dyer, S.B., Thomas, S. and Farouq Ali, S.M.: Scaled Model Studies of CO_2 Floods, *SPE Reservoir Engineering*, May 1991, pp. 169-178.

141) Stegemeier, G.L., Laumbach, D.D. and Volek, C.W.: Representing Steam Processes with Vacuum Models, *Society of Petroleum Engineers Jour.*, June 1980, pp. 151-174.

142) Farouq Ali, S.M. and Redford, D.A.: Physical Modelling of In-situ Recovery Methods for Oil Sands, proc. Canada-Venezuela Oil Sands Symposium, Edmonton, Canada, CIM Special Volume No. 17, 1977, pp. 319-326.

143) Kimber, K., Farouq Ali, S.M. and Puttagunta, V.R.: Verification of Scaling Approaches for Steam Injection Experiments, paper 88-39-17, presented at 39th Ann. Tech. Meeting of Petroleum Society of CIM, Calgary, June 12-16, 1988.

144) Bagnold, R.A.: Motion of Waves in Shallow Water Interaction Between Waves and Sand Bottoms, The Physics of Sediment Transport by Wind and Water – A Collection of Hallmark Papers by R.A. Bagnold, Ed. by C.R. Thorne, R.C. MacArthur, and J.B. Bradley, American Society of Civil Engineers, 1988, pp. 91-107.

145) Farouq Ali, S.M.: Personal communications, June 1995.

Appendix A

Soo's Model for Deposition of Particulate Phase due to Gravity Force [80-82]

In this model, the flow is assumed to be fully developed, and steady state. External forces acting on the solid particles (i.e. particulate phase), beside the drag force exerted by the fluid phase, include Saffman' s lift force [5] , and gravity field force. In the following an equation describing the distribution of the density (i.e. concentration) of the particulate phase under the influence of the gravity field force is derived from the continuity equation of the particulate phase and a diffusion-type equation. The system of governing equations include the mass conservation equations for the fluid phase and particulate phase, and the equation of motion for the particulate phase along the radial and axial directions, i.e.

* Fluid phase mass conservation equation

$$\frac{\partial w_f}{\partial z} = 0 \tag{A.1}$$

* Particulate phase mass conservation equation

$$\frac{1}{r}\frac{\partial}{\partial r}(r\rho_s u_s) + \frac{\partial}{\partial z}(\rho_s w_s) = 0 \tag{A.2}$$

The momentum conservation equation for the particulate phase includes

* the radial-component

$$u_s = -\frac{1}{\Im}\left(1 - \frac{\overline{\rho_f}}{\rho_s}\right) g \sin\theta \cos\varphi \tag{A.3}$$

* the axial-component

$$-\rho_s\left(1 - \frac{\overline{\rho_f}}{\rho_s}\right) g \cos\theta + \frac{1}{r}\frac{\partial}{\partial r}\left(r\tau_{s,zr}\right) + \frac{1}{r}\frac{\partial}{\partial \varphi}\left(r\tau_{s,z\varphi}\right) + \Im\rho_s\left(w_f - w_s\right) = 0 \tag{A.4}$$

The diffusivity equation for the particulate phase under the influence of the field force is now derived from its mass conservation equation, as shown in the following,

$$\frac{1}{r}\frac{\partial}{\partial r}(r\rho_s u_s) + \frac{\partial}{\partial z}(\rho_s w_s) = 0 \Rightarrow \frac{\partial}{\partial r}(r\rho_s u_s) + \frac{\partial}{\partial z}(r\rho_s w_s) = 0 \tag{A.5}$$

$$\Rightarrow \frac{\partial}{\partial r}\left[r\rho_s u_s\right] + \frac{\partial}{\partial z}\left[r\rho_s\left\{(w_s - w_f) + w_f\right\}\right] = 0 \tag{A.6}$$

$$\frac{\partial}{\partial r}\left[r\rho_s u_s\right] + \frac{\partial}{\partial z}\left[r\rho_s(w_s - w_f)\right] + \frac{\partial}{\partial z}\left(r\rho_s w_f\right) = 0 \tag{A.7}$$

$$\Rightarrow \frac{\partial}{\partial r}\left[r\rho_s u_s\right]+\frac{\partial}{\partial z}\left[r\rho_s(w_s-w_f)\right]+r\frac{\partial}{\partial z}\left(\rho_s w_f\right)=0 \qquad \text{(A.8)}$$

$$\frac{\partial}{\partial r}\left[r\rho_s u_s\right]+\frac{\partial}{\partial z}\left[r\rho_s(w_s-w_f)\right]+r\left[\rho_s\frac{\partial w_f}{\partial z}+w_f\frac{\partial \rho_s}{\partial z}\right]=0 \qquad \text{(A.9)}$$

Recalling Equation A.1, Equation (A.9) becomes

$$\frac{\partial}{\partial r}\left[r\rho_s u_s\right]+\frac{\partial}{\partial z}\left[r\rho_s(w_s-w_f)\right]+rw_f\frac{\partial \rho_s}{\partial z}=0 \qquad \text{(A.10)}$$

$$\frac{1}{r}\frac{\partial}{\partial r}\left[r\rho_s u_s\right]+\frac{\partial}{\partial z}\left[\rho_s(w_s-w_f)\right]+w_f\frac{\partial \rho_s}{\partial z}=0 \qquad \text{(A.11)}$$

$$\therefore w_f\frac{\partial \rho_s}{\partial z}=-\frac{1}{r}\frac{\partial}{\partial r}\left[r\rho_s u_s\right]-\frac{\partial}{\partial z}\left[\rho_s(w_s-w_f)\right] \qquad \text{(A.12)}$$

Equation A.12 describes the distribution of the particulate phase density along the axis of the pipe as a function of the radial and axial momentum fluxes.

Defining $J_{sr}=\rho_s u_s$, and $J_{sz}=\rho_s\left(w_s-w_f\right)$, Equation A.12 becomes,

$$w_f\frac{\partial \rho_s}{\partial z}=-\frac{1}{r}\frac{\partial}{\partial r}\left(rJ_{sr}\right)-\frac{\partial}{\partial z}J_{sz}\ , \qquad \text{(A.13)}$$

for small or negligible axial diffusion flux, i.e. $\frac{\partial}{\partial z}J_{sz}\approx 0$, the above equation becomes

$$w_f\frac{\partial \rho_s}{\partial z}=-\frac{1}{r}\frac{\partial}{\partial r}\left(rJ_{sr}\right). \qquad \text{(A.14)}$$

If the radial diffusion flux is defined as,

$$J_{sr}=-D_s\frac{\partial \rho_s}{\partial r}+\frac{F_{sr}\rho_s}{m\Im} \qquad \text{(A.15)}$$

then,

$$w_f\frac{\partial \rho_s}{\partial z}=-\frac{1}{r}\frac{\partial}{\partial r}\left[-rD_s\frac{\partial \rho_s}{\partial r}+r\frac{F_{sr}\rho_s}{m\Im}\right]\Rightarrow w_f\frac{\partial \rho_s}{\partial z}=-\frac{1}{r}\left[-D_s\frac{\partial \rho_s}{\partial r}-rD_s\frac{\partial^2 \rho_s}{\partial r^2}\right]-\frac{1}{r}\frac{\partial}{\partial r}\left(r\frac{F_{sr}\rho_s}{m\Im}\right) \qquad \text{(A.16)}$$

$$\Rightarrow w_f\frac{\partial \rho_s}{\partial z}=+\frac{1}{r}D_s\frac{\partial \rho_s}{\partial r}+D_s\frac{\partial^2 \rho_s}{\partial r^2}-\frac{1}{r}\frac{\partial}{\partial r}\left(r\frac{F_{sr}\rho_s}{m\Im}\right). \qquad \text{(A.17)}$$

In the above equations,

$$\Im = \left(\frac{C_D}{24}\right)\left(\frac{2a\overline{\rho_f}}{\mu_f}\left|w_f - w_s\right|\right)\left(\frac{9\mu_f}{2a^2\overline{\rho_s}}\right)\frac{1}{\left[1 + \left(\overline{\rho_f}/2\overline{\rho_s}\right)\right]} \tag{A.18}$$

is the inverse of the relaxation time, and m is the mass of a particle.

For a horizontal well making an angle θ with the true direction of gravity, the gravity field force is given as follows,

$$F_g = mg\left(1 - \frac{\overline{\rho_f}}{\overline{\rho_s}}\right)\left[-\sin\theta\cos\varphi \cdot \hat{r} + \sin\theta\sin\varphi \cdot \hat{\varphi} - \cos\theta \cdot \hat{z}\right], \tag{A.19}$$

with $\hat{r}, \hat{\varphi}, \hat{z}$ being the unit vectors along the r, φ, z directions. As such, the equation describing particulate phase density distribution along the axis of the pipe (i.e. Equation A.19) becomes,

$$\begin{aligned} w_f\frac{\partial\rho_s}{\partial z} = {} & D_s\left[\frac{1}{r}\frac{\partial}{\partial r}\left(r\frac{\partial\rho_s}{\partial r}\right) + \frac{1}{r^2}\frac{\partial^2\rho_s}{\partial\varphi^2} + \frac{\partial^2\rho_s}{\partial z^2}\right] + \frac{g}{\Im}\left(1 - \frac{\overline{\rho_f}}{\overline{\rho_s}}\right)\left[\frac{1}{r}\frac{\partial}{\partial r}(r\rho_s\sin\theta\cos\varphi)\right. \\ & \left. - \frac{1}{r}\frac{\partial}{\partial\varphi}(\rho_s\sin\theta\sin\varphi) + \frac{\partial}{\partial z}(\rho_s\cos\theta)\right] \end{aligned} \tag{A.20}$$

Simultaneous solution of the momentum conservation equation for the particulate phase along the radial and axial directions (Equations A.3, A.4), along with the diffusivity equation for the particulate phase due to the gravity field force (Equation A.20) gives the velocity distribution and density distribution for the particulate phase. The fluid phase velocity distribution is given by the assumption of either laminar or turbulent flow.

Appendix B

Dimensionless Numbers Governing Flow of Dilute Oil-Sand Suspensions

In this appendix Dimensional Analysis is used to construct a parametric model to describe the hydrodynamic transport of sand by oil inside a horizontal well. The sand-oil suspension is assumed to be dilute, with the collective volume of the sand particles in the suspension occupying no more than 8% of the total suspension volume (i.e. $\phi \leq 0.08$). Hence, particle-particle interaction is considered to be negligible when compared to particle-fluid interaction. The sand particles making up the particulate phase are assumed to be spherical in shape, and uniform in size. The particles are homogeneously and uniformly dispersed in the fluid phase.

The fluid phase (oil) is assumed to be incompressible and Newtonian. Its motion is controlled by a pressure gradient along the horizontal well axis. The motion of the sand particles is controlled primarily by two mechanisms: fluid phase motion which transfers part of its momentum to the particulate phase through various forces (drag, lift and added mass), and gravity force which affects particle diffusion. Both fluid phase flow and particulate phase flow are assumed to be symmetrical in the azimuthal direction of the horizontal well. For the influx from the reservoir into the horizontal well through the perforations it is assumed that the volumetric flow rate per unit well length as well as the overall density are specified, and that its solid volume fraction is also less than 0.08. The sand particles, once settled out of the fluid stream and deposited in the sediment bed, are assumed to be cohesionless. The added mass effect (or fluid inertia effect) and the Basset force are assumed to be negligible. Mathematically, this transport process is expressed as follows,

$$f = f\Big(r, z, u_f, u_s, w_f, w_s, \mu_f, D_s, a, \delta, L_s, F_D, \Delta u, \Delta w, L, R, \Im, \Delta p, g, \overline{\rho_f}, \overline{\rho_s}, q^{\bullet}_{in.},$$
$$A, m, C_D, \dot{m}, \rho_{mixture}, \rho^{\bullet}_{f,in.}, \rho^{\bullet}_{s,in.} t\Big) \tag{B.1}$$

There are 30 parameters altogether. Three of these variables, the axial slip velocity, the radial coordinate, and the material density of the particulate phase are selected to represent the three fundamental dimensions of mass, length, and time. The Buckingham π-theorem is applied to obtain the expected 27 dimensionless π-groups (using a procedure similar to that illustrated in Section 5.2.2. of Chapter 5). These dimensionless similarity groups, along with their meaning, are given in Table B.1.

Table B.1: Dimensionless Similarity Groups for Flow of Dilute Suspensions

$\pi_1 = r / z$	ratio of radial dimension to axial dimension
$\pi_2 = u_f / \Delta u$	ratio of radial fluid phase velocity to axial slip velocity
$\pi_3 = u_s / \Delta w$	ratio of radial particulate phase velocity to axial slip velocity
$\pi_4 = w_f / \Delta w$	ratio of axial fluid phase velocity to axial slip velocity
$\pi_5 = w_s / \Delta w$	ratio of axial particulate phase velocity to axial slip velocity
$\pi_6 = a\rho_s(\Delta w) / \mu_f$	ratio of inertia force to viscous force (particle Reynolds Number)
$\pi_7 = D_s / r(\Delta w)$	ratio of particulate phase diffusivity to inertia motion along radial direction
$\pi_8 = a / r$	ratio of solid particle size (radius) to well size
$\pi_9 = \delta / r$	ratio of deposit bed thickness to radial coordinate
$\pi_{10} = L_s / r$	ratio of particle-fluid interaction to radial coordinate
$\pi_{11} = F_D / \left[r^2(\Delta w)^2 \rho_s\right]$	ratio of drag force to particulate phase inertia force
$\pi_{12} = \Delta u / \Delta w$	ratio of slip velocity in radial direction to slip velocity in axial direction
$\pi_{13} = L / r$	ratio of horizontal well length to radial dimension
$\pi_{14} = R / r$	ratio of horizontal well radius to radial dimension

Table B.1: Dimensionless Similarity Groups for Flow of Dilute Suspensions (continued)

$\pi_{15} = r\Im / \Delta w$	ratio of momentum transfer due to relaxation mechanism to axial slip velocity
$\pi_{16} = \Delta p / \rho_s (\Delta w)^2$	ratio of pressure drop to particulate phase kinetic energy
$\pi_{17} = rg / (\Delta w)^2$	ratio of velocity due to gravitational force to kinetic energy along axial direction
$\pi_{18} = \rho_f / \rho_s$	ratio of fluid phase density to particulate phase density
$\pi_{19} = \dot{q}_{in.} / r(\Delta w)$	ratio of volumetric influx to radial flux
A / r^2	ratio of cross-sectional area open to flow to area at a particular radial coordinate
$m / \left(r^3 \rho_s\right)$	ratio of mass of single particle to mass of particulate phase
C_D	drag coefficient
$\dot{m} / \left(r^2 (\Delta w) \rho_s\right)$	ratio of total mass flow rate to axial mass flux of particulate phase
$\rho_{mixture} / \rho_s$	ratio of mixture density to particulate phase density
$\dot{\rho}_{f,in.} / \rho_s$	ratio of influx fluid phase density to particulate phase density
$\dot{\rho}_{s,in.} / \rho_s$	ratio of influx particulate phase density to particulate phase density
$r / (t(\Delta w))$	ratio of radial dimension to axial distance traversed during time t

Soo [76,80-81] derived six dimensionless numbers correlating different variables and parameters involved in the flow of dilute suspensions. The numbers include the Reynolds Number (N_{Re}), Froude Number (N_{Fr}), Diffusion Response Number (N_{DF}), Momentum Transfer Number (N_{M}), particle Knudsen Number ($N_{Kn,p}$), and Pressure Coefficient. Table B.2 illustrates how these numbers are obtained from the dimensionless similarity groups derived by the Dimensional Analysis in this study.

Table B.2: Dimensionless Groups Characterizing Flow of Dilute Suspensions

Reynolds Number:

$$N_{Re} = \frac{2a\rho_f(\Delta w)}{\mu_f} = \frac{2r\rho_s(\Delta w)}{\mu_f}\cdot\frac{a}{r}\cdot\frac{\rho_f}{\rho_s} = 2\pi_6\cdot\pi_8\cdot\pi_{18} \tag{B.2}$$

Froude Number:

$$N_{Fr} = \frac{w_f^2}{Rg} = \left(\frac{w_f}{\Delta w}\right)^2\cdot\frac{(\Delta w)^2}{rg}\cdot\frac{r}{R} = \pi_4^2\cdot\pi_{17}^{-1}\cdot\pi_{14}^{-1} \tag{B.3}$$

Diffusion Response Number:

$$N_{DF} = \frac{D_s}{R^2\Im} = \left[\frac{D_s}{r(\Delta w)}\cdot\frac{\Delta w}{r\Im}\cdot\left(\frac{r}{R}\right)^2\right]^{1/2} = \left(\pi_7\cdot\pi_{15}^{-1}\cdot\pi_{14}^{-2}\right)^{1/2} \tag{B.4}$$

Momentum Transfer Number:

$$N_M = \frac{w_f}{R\Im} = \frac{w_f}{\Delta w}\cdot\frac{r}{R}\cdot\frac{\Delta w}{r\Im} = \pi_4\cdot\pi_{14}^{-1}\cdot\pi_{15}^{-1} \tag{B.5}$$

Particle Knudsen Number:

$$N_{Kn,p} = \frac{L_s}{R} = \frac{L_s}{r}\cdot\frac{r}{R} = \pi_{10}\cdot\pi_{14}^{-1} \tag{B.6}$$

Pressure Coefficient:

$$\frac{\Delta p}{\rho_f w_f^2} = \frac{\Delta p}{\rho_s(\Delta w)^2}\cdot\frac{(\Delta w)^2}{w_f^2}\cdot\frac{\rho_s}{\rho_f} = \pi_{16}\cdot\pi_{14}^{-2}\cdot\pi_{18}^{-1} \tag{B.7}$$

Of the above six dimensionless numbers, the Diffusion Response Number (N_{DF}) correlates the relaxation time for the momentum transfer between the fluid phase and the particulate phase to the diffusion time for the particulate phase. The Momentum Transfer Number (N_{M}) correlates the relaxation time to the transport time, while the particle Knudsen Number ($N_{Kn,p}$) controls the particle-fluid interaction. The Froude Number (N_{Fr}) correlates the magnitude of the inertia force to that of the gravity force. The Reynolds Number (N_{Re}) correlates the inertia and the viscous forces in pipe flow, and the Pressure Coefficient relates the pressure drop to the kinetic energy of fluid flow.

Appendix C

Derivation of Conservation Equations for 2-D Model

Continuity equation

The general statement of material balance is as follows,

$$\{\text{Rate of mass accumulation}\} = \{\text{Rate of mass in}\} - \{\text{Rate of mass out}\} \tag{C.1}$$

This conservation law holds true for an element of arbitrary size of the system.

Referring to Figure 4.1, which is a schematic representation of a control volume element of the horizontal well, it is seen that the flow along the radial direction is opposite to that of the positive radial-coordinate axis. The flow along the azimuthal direction is assumed to be negligible. For the flow from the reservoir into the horizontal well (i.e. influx) the normal convention of assigning a positive sign for mass going into the system, and a negative sign for mass going out of the system is followed. As such, the following equations are obtained

* Mass rate going into the control volume:

$$= -(r + \Delta r) \cdot \Delta\theta \cdot \Delta z \cdot (\rho u)|_{r+\Delta r} + \Delta r \cdot (r\Delta\theta) \cdot (\rho w)|_{z} + \{(r\Delta\theta) \cdot \Delta r \cdot \Delta z\}(\rho q)^{*}_{in.}$$

* Mass rate going out of the control volume:

$$= -r \cdot \Delta\theta \cdot \Delta z \cdot (\rho u)|_{r} + \Delta r \cdot (r\Delta\theta) \cdot (\rho w)|_{z+\Delta z}$$

* Net mass accumulation in the control volume element is equal to the time rate of change of the density multiplied by the element volume which is fixed according to the Eulerian formulation chosen for this formulation, i.e., the net rate mass of accumulation is equal to

$$= (\Delta r \cdot r\Delta\theta \cdot \Delta z)\frac{\partial}{\partial t}(\rho)$$

Putting all these terms together leads to the following expression,

$$-\left\{(r+\Delta r)\cdot\Delta\theta\cdot\Delta z\cdot(\rho u)|_{r+\Delta r}-r\Delta\theta\cdot\Delta z\cdot(\rho u)|_{r}\right\}+\left\{\Delta r\cdot(r\Delta\theta)\cdot(\rho w)|_{z}-\Delta r\cdot(r\Delta\theta)\cdot(\rho w)|_{z}\right\}$$

$$+\{(r\Delta\theta)\cdot\Delta r\cdot\Delta z\}(\rho q)^{*}_{in.}=(\Delta r\cdot r\Delta\theta\cdot\Delta z)\frac{\partial}{\partial t}(\rho) \tag{C.2}$$

Dividing through by $(\Delta r\cdot r\Delta\theta\cdot\Delta z)$, and taking limit as $\Delta r,\Delta z\rightarrow 0$, the following equation is obtained,

$$+\frac{\partial}{\partial r}(\rho u)+\frac{1}{r}((\rho u))-\frac{\partial}{\partial z}(\rho w)+(\rho q)^{*}_{in.}=\frac{\partial}{\partial t}(\rho) \tag{C.3}$$

$$\therefore +\frac{1}{r}\frac{\partial}{\partial r}(\rho u)-\frac{\partial}{\partial z}(\rho w)+(\rho q)^{*}_{in.}=\frac{\partial}{\partial t}(\rho) \tag{C.4}$$

The derivation up to this point has been generic. For two-phase flow of oil and sand, with the oil being the continuous fluid phase, and the sand particles being the disperse solid phase the above mass conservation equation is modified appropriately for each of these two phases. This is done by introducing the subscripts f and s to the variables in the continuity equation for the fluid phase and solid phase, respectively. The results are illustrated below,

*for the Fluid phase,

$$\frac{1}{r}\frac{\partial}{\partial r}(\rho_f u_f)-\frac{\partial}{\partial z}(\rho_f w_f)+(\rho_f q)^{*}_{in.}=\frac{\partial}{\partial t}(\rho_f) \tag{C.5}$$

*for the Solid phase,

$$\frac{1}{r}\frac{\partial}{\partial r}(\rho_s u_s)-\frac{\partial}{\partial z}(\rho_s w_s)+(\rho_s q)^{*}_{in.}=\frac{\partial}{\partial t}(\rho_s) \tag{C.6}$$

Equation of motion

The general statement of momentum balance is as follows,

$$\left\{\begin{matrix}\text{Rate of momentum}\\ \text{accumulation}\end{matrix}\right\}=\left\{\begin{matrix}\text{Rate of}\\ \text{momentum in}\end{matrix}\right\}-\left\{\begin{matrix}\text{Rate of}\\ \text{momentum out}\end{matrix}\right\}+\left\{\begin{matrix}\text{Sum of forces}\\ \text{acting on system}\end{matrix}\right\} \tag{C.7}$$

For two-dimensional flow (negligible flow in the azimuthal direction) with cylindrical co-ordinates the following general equations are modified from those equations in Table 3.4-3 of Bird, Stewart and Lightfoot' s book [146], *r-component*

$$\left[\frac{\partial}{\partial t}(\rho u) - \frac{\partial}{\partial r}(\rho uu) + \frac{\partial}{\partial z}(\rho wu)\right] = -\frac{\partial p}{\partial r} - \left[\frac{1}{r}\frac{\partial}{\partial r}(r\tau_{rr}) + \frac{\partial \tau_{zr}}{\partial z}\right] + \rho g_r \tag{C.8}$$

z-component

$$\left[\frac{\partial}{\partial t}(\rho w) - \frac{\partial}{\partial r}(\rho uw) + \frac{\partial}{\partial z}(\rho ww)\right] = -\frac{\partial p}{\partial z} - \left[\frac{1}{r}\frac{\partial}{\partial r}(r\tau_{rz}) + \frac{\partial \tau_{zz}}{\partial z}\right] + \rho g_z \tag{C.9}$$

Again, as in the continuity equation case, Equations C.7 and C.8 are for generic flow. They are now modified to describe the conservation of momentum for the fluid phase and solid phase of the transport process being studied.

* Fluid phase

For a Newtonian fluid, Equation C.7 becomes

$$\frac{\partial}{\partial t}(\rho_f u_f) - \frac{\partial}{\partial r}(\rho_f u_f u_f) + \frac{\partial}{\partial z}(\rho_f w_f u_f) = -\varepsilon\frac{\partial p_f}{\partial r} - \mu_f\left[\frac{\partial}{\partial r}\left(\frac{1}{r}\frac{\partial}{\partial r}(ru_f)\right)\right] + \mu_f\frac{\partial^2 u_f}{\partial z^2}$$
$$-\rho_f g - (\rho_f q)^{\bullet}_{in.} u_f \tag{C.10}$$

The pressure gradient in Equation C.9 is adjusted for the fluid phase concentration. In addition, it is assumed that the influx mass for the fluid phase is instantaneously accelerated to the local radial velocity. Saffman' s lift force acting on the solid phase due to fluid shear, and the interphase momentum transfer are now incorporated into the above equation as follows,

$$\frac{\partial}{\partial t}(\rho_f u_f) - \frac{\partial}{\partial r}(\rho_f u_f u_f) + \frac{\partial}{\partial z}(\rho_f w_f u_f) = -\varepsilon\frac{\partial p_f}{\partial r} + \mu_f\left[\frac{\partial}{\partial r}\left(\frac{1}{r}\frac{\partial}{\partial r}(-ru_f)\right) + \frac{\partial^2 u_f}{\partial z^2}\right] - (\rho_f q)^{\bullet}_{in.} u_f$$
$$-\rho_f g - \frac{3}{8}C_L\rho_S\frac{\overline{\rho_f}}{\rho_s}\frac{(u_s - u_f + \Delta v)^2}{a} + \beta_r(u_f - u_s) \tag{C.11}$$

For the flow in the axial direction, Equation C.8 is similarly modified except for the following. It is assumed that the lift force and gravity force act only in the radial direction. The result is,

$$\frac{\partial}{\partial t}\left(\rho_f w_f\right) - \frac{\partial}{\partial r}\left(\rho_f u_f w_f\right) + \frac{\partial}{\partial z}\left(\rho_f w_f w_f\right) = -\varepsilon \frac{\partial p_f}{\partial z} + \mu_f\left[\frac{1}{r}\frac{\partial}{\partial r}\left(r\frac{\partial w_f}{\partial r}\right) + \frac{\partial^2 w_f}{\partial z^2}\right]$$
$$-\left(\rho_f q\right)^{*}_{in.} w_f + \beta_z\left(w_f - w_s\right)$$

(C.12)

* Solid phase

Incorporating modifications similar to those for the fluid phase equation results in the following equations for the conservation of momentum along the radial and axial directions for the solid phase.

Along the radial (r-) direction

$$\frac{\partial}{\partial t}(\rho_s u_s) - \frac{\partial}{\partial r}(\rho_s u_s u_s) + \frac{\partial}{\partial z}(\rho_s w_s u_s) = -\phi\frac{\partial p_s}{\partial r} + \left[\frac{1}{r}\frac{\partial}{\partial r}\left(-r\mu_s\frac{\partial u_s}{\partial r}\right) + \frac{\partial}{\partial z}\left(\mu_s\frac{\partial u_s}{\partial z}\right)\right] - p_{k,r}\frac{\partial \phi}{\partial r} - \rho_s g$$
$$-(\rho_s q)^{*}_{in.} u_s + \frac{3}{8}C_L\rho_s\frac{\overline{\rho_f}}{\rho_s}\frac{\left(u_s - u_f + \Delta u\right)^2}{a} - \beta_r\left(u_f - u_s\right)$$

(C.13)

Along the axial (z-) direction

$$\frac{\partial}{\partial t}(\rho_s w_s) - \frac{\partial}{\partial r}(\rho_s u_s w_s) + \frac{\partial}{\partial z}(\rho_s w_s w_s) = -\phi\frac{\partial p_s}{\partial z} + \left[\frac{1}{r}\frac{\partial}{\partial r}\left(-r\mu_s\frac{\partial w_s}{\partial r}\right) + \frac{\partial}{\partial z}\left(\mu_s\frac{\partial w_s}{\partial z}\right)\right]$$
$$-p_{k,z}\frac{\partial \phi}{\partial z} - (\rho_s q)^{*}_{in.} w_s - \beta_z\left(w_f - w_s\right)$$

(C.14)

Equations C.5, C.6, C.11, C.12, C.13 and C.14 are identical to Equations 4.1, 4.2, 4.3, 4.4, 4.5 and 4.6, respectively.

Appendix D

Solid-phase Pressure Equation for 2-D Model

- Continuity equation

* Mass conservation for the fluid phase

$$\frac{\partial \varepsilon}{\partial t} - \frac{1}{r}\frac{\partial}{\partial r}\left(r\varepsilon u_f\right) + \frac{\partial}{\partial z}\left(\varepsilon w_f\right) - (\varepsilon q)^{\bullet}_{in.} = 0 \tag{D.1}$$

* Mass conservation for the solid phase

$$\frac{\partial \phi}{\partial t} - \frac{1}{r}\frac{\partial}{\partial r}\left(r\phi u_s\right) + \frac{\partial}{\partial z}\left(\phi w_s\right) - (\phi q)^{\bullet}_{in.} = 0 \tag{D.2}$$

- Equation of motion

* Conservation of momentum for the fluid phase

Along the radial (r-) direction

Ignoring lift force from the equation,

$$\frac{\partial}{\partial t}\left(\varepsilon u_f\right) - \frac{\partial}{\partial r}\left(\varepsilon u_f u_f\right) + \frac{\partial}{\partial z}\left(\varepsilon w_f u_f\right) = -\frac{\varepsilon}{\rho_f}\frac{\partial p_f}{\partial r} + \frac{\mu_f}{\rho_f}\left[\frac{\partial}{\partial r}\left(\frac{1}{r}\frac{\partial}{\partial r}\left(-ru_f\right)\right) + \frac{\partial^2 u_f}{\partial z^2}\right] - (\varepsilon q)^{\bullet}_{in.} u_f - \varepsilon g + \frac{\beta_r}{\rho_f}\left(u_f - u_s\right) \tag{D.3}$$

Along the axial (z-) direction

$$\frac{\partial}{\partial t}\left(\varepsilon w_f\right) - \frac{\partial}{\partial r}\left(\varepsilon u_f w_f\right) + \frac{\partial}{\partial z}\left(\varepsilon w_f u_f\right) = -\frac{\varepsilon}{\rho_f}\frac{\partial p_f}{\partial z} + \frac{\mu_f}{\rho_f}\left[\frac{1}{r}\frac{\partial}{\partial r}\left(r\frac{\partial w_f}{\partial r}\right) + \frac{\partial^2 w_f}{\partial z^2}\right] - (\varepsilon q)^{\bullet}_{in.} w_f + \frac{\beta_z}{\rho_f}\left(w_f - w_s\right) \tag{D.4}$$

* Conservation of momentum for the solid phase

Along the radial (r-) direction

$$\frac{\partial}{\partial t}(\phi u_s) - \frac{\partial}{\partial r}(\phi u_s u_s) + \frac{\partial}{\partial z}(\phi w_s u_s) = -\frac{\phi}{\overline{\rho_s}}\frac{\partial p_s}{\partial r} + \left[\frac{1}{r}\frac{\partial}{\partial r}\left(-r\mu_s \frac{\partial u_s}{\partial r}\right) + \frac{\partial}{\partial z}\left(\mu_s \frac{\partial u_s}{\partial z}\right)\right] - \frac{p_{k,r}}{\overline{\rho_s}}\frac{\partial \phi}{\partial r} - \phi g$$

$$-(\phi q)^{\bullet}_{in.} u_s - \frac{\beta_r}{\overline{\rho_s}}\left(u_f - u_s\right) \qquad \text{(D.5)}$$

Along the axial (z-) direction

$$\frac{\partial}{\partial t}(\phi w_s) - \frac{\partial}{\partial r}(\phi u_s w_s) + \frac{\partial}{\partial z}(\phi w_s w_s) = -\frac{\phi}{\overline{\rho_s}}\frac{\partial p_s}{\partial z} + \frac{1}{\overline{\rho_s}}\left[\frac{1}{r}\frac{\partial}{\partial r}\left(-r\mu_s \frac{\partial w_s}{\partial r}\right) + \frac{\partial}{\partial z}\left(\mu_s \frac{\partial w_s}{\partial z}\right)\right]$$

$$-\frac{p_{k,z}}{\overline{\rho_s}}\frac{\partial \phi}{\partial z} - (\phi q)^{\bullet}_{in.} w_s - \frac{\beta_z}{\overline{\rho_s}}\left(w_f - w_s\right) \qquad \text{(D.6)}$$

In finite difference form the above equations become,

* Mass conservation for the fluid phase

$$\frac{\left(\varepsilon^{n+1}_{i,k} - \varepsilon^{n}_{i,k}\right)}{\Delta t} = \frac{1}{r_{i,k}} \cdot \frac{1}{\Delta r}\left[\left(r\varepsilon u_f\right)^{n+1}_{i+1/2,k} - \left(r\varepsilon u_f\right)^{n+1}_{i-1/2,k}\right] + \frac{1}{\Delta z}\left[\left(\varepsilon w_f\right)^{n+1}_{i,k+1/2} - \left(\varepsilon w_f\right)^{n+1}_{i,k-1/2}\right]$$

$$-\left[(\varepsilon q)^{\bullet}_{in.}\right]^{n+1}_{i,k} \qquad \text{(D.7)}$$

* Mass conservation for the solid phase

$$\frac{\left(\phi^{n+1}_{i,k} - \phi^{n}_{i,k}\right)}{\Delta t} = \frac{1}{r_{i,k}} \cdot \frac{1}{\Delta r}\left[\left(r\phi u_s\right)^{n+1}_{i+1/2,k} - \left(r\phi u_s\right)^{n+1}_{i-1/2,k}\right] + \frac{1}{\Delta z}\left[\left(\phi w_s\right)^{n+1}_{i,k+1/2} - \left(\phi w_s\right)^{n+1}_{i,k-1/2}\right]$$

$$-\left[(\phi q)^{\bullet}_{in.}\right]^{n+1}_{i,k} \qquad \text{(D.8)}$$

* Momentum conservation for the solid phase

Along the radial direction,

considering the equation of motion for the solid phase about the point (i+1/2,k)

$$(\phi u_s)^{n+1}_{i+1/2,k} = \frac{\Delta t}{\Delta r}\left\{\phi^n + \left.\frac{d\phi}{dp_s}\right|^n \cdot \left(p_s^{n+1} - p_s^n\right)\right\}_{i+1/2,k}\left[p^{n+1}_{si+1,k} - p^{n+1}_{si,k}\right] + F_{si+1/2,k} \tag{D.9}$$

where,

$$\begin{aligned}
F_{si+1/2,k} = \Delta t\Bigg\{&\left[\frac{(\phi u_s u_s)_{i+1,k} - (\phi u_s u_s)_{i,k}}{\Delta r}\right]^{n+1} + \left[\frac{(\phi w_s u_s)_{i+1/2,k+1/2} - (\phi w_s u_s)_{i+1/2,k-1/2}}{\Delta z}\right]^{n+1} \\
&+\left[\left(\left(p^n_{kr} + \frac{\partial p_{kr}}{\partial \phi}\right)\right|^n (\phi^{n+1} - \phi^n)\right)_{i+1/2,k} * \left(\frac{\phi^{n+1}_{i+1,k} - \phi^{n+1}_{i,k}}{\Delta r}\right)\right] - \left[g(\phi)^{n+1}_{i+1/2,k}\right] \\
&+\frac{1}{\bar{\rho}_s}\frac{1}{r_{i+1/2,k}}\frac{1}{\Delta r}\left[\left\{r_{i+1,k}\left(\mu^n_s + \left.\frac{d\mu_s}{d\phi}\right|^n (\phi^{n+1} - \phi^n)\right)_{i+1,k} * \left(\frac{u^{n+1}_{si+3/2,k} - u^{n+1}_{si+1/2,k}}{\Delta r}\right)\right\}\right. \\
&\left.-\left\{r_{i,k}\left(\mu^n_s + \left.\frac{d\mu_s}{d\phi}\right|^n (\phi^{n+1} - \phi^n)\right)_{i,k} * \left(\frac{u^{n+1}_{si+1/2,k} - u^{n+1}_{si-1/2,k}}{\Delta r}\right)\right\}\right] + \left[(\phi q)^*_{in.} u_s\right]^{n+1}_{i+1/2,k} \\
&+\frac{1}{\bar{\rho}_s}\frac{1}{\Delta z}\left[\left\{\left(\mu^n_s + \left.\frac{d\mu_s}{d\phi}\right|^n (\phi^{n+1} - \phi^n)\right)_{i+1/2,k+1/2} * \left(\frac{u^{n+1}_{si+1/2,k+1} - u^{n+1}_{si+1/2,k}}{\Delta z}\right)\right\}\right. \\
&\left.-\left\{\left(\mu^n_s + \left.\frac{d\mu_s}{d\phi}\right|^n (\phi^{n+1} - \phi^n)\right)_{i+1/2,k-1/2} * \left(\frac{u^{n+1}_{si+1/2,k} - u^{n+1}_{si+1/2,k-1}}{\Delta z}\right)\right\}\right] \\
&-\frac{1}{\bar{\rho}_s}\left[\left(\beta^n_r + \left.\frac{\partial \beta_r}{\partial \phi}\right|^n (\phi^{n+1} - \phi^n)\right)_{i+1/2,k}(u^{n+1}_{fi+1/2,k} - u^{n+1}_{si+1/2,k})\right]\Bigg\} + (\phi u_s)^n_{i+1/2,k}
\end{aligned} \tag{D.10}$$

Similarly, considering the equation of motion for the solid phase about the point (i-1/2,k)

$$(\phi u_s)^{n+1}_{i-1/2,k} = \frac{\Delta t}{\Delta r}\left\{\phi^n + \left.\frac{d\phi}{dp_s}\right|^n \cdot \left(p_s^{n+1} - p_s^n\right)\right\}_{i-1/2,k}\left[p^{n+1}_{si,k} - p^{n+1}_{si-1,k}\right] + F_{si-1/2,k} \tag{D.11}$$

where,

$$\begin{aligned}
F_{si-1/2,k} = \Delta t \Bigg\{ & \left[\frac{(\phi u_s u_s)_{i,k} - (\phi u_s u_s)_{i-1,k}}{\Delta r}\right]^{n+1} + \left[\frac{(\phi w_s u_s)_{i-1/2,k+1/2} - (\phi w_s u_s)_{i-1/2,k-1/2}}{\Delta z}\right]^{n+1} \\
& + \Bigg[\left(\left(p_{kr}^{n} + \frac{\partial p_{kr}}{\partial \phi}\right|^{n} (\phi^{n+1} - \phi^{n})\right)_{i-1/2,k} * \left(\frac{\phi_{i,k}^{n+1} - \phi_{i-1,k}^{n+1}}{\Delta r}\right)\Bigg] - [g(\phi)_{i-1/2,k}^{n+1}] \\
& + \frac{1}{\bar{\bar{\rho}}_s} \frac{1}{r_{i-1/2,k}} \frac{1}{\Delta r} \Bigg[\Bigg\{ r_{i,k}\left(\mu_s^{n} + \frac{d\mu_s}{d\phi}\right|^{n} (\phi^{n+1} - \phi^{n})\Bigg)_{i,k} * \left(\frac{u_{si+1/2,k}^{n+1} - u_{si-1/2,k}^{n+1}}{\Delta r}\right)\Bigg\} \\
& - \Bigg\{ r_{i-1,k}\left(\mu_s^{n} + \frac{d\mu_s}{d\phi}\right|^{n} (\phi^{n+1} - \phi^{n})\Bigg)_{i-1,k} * \left(\frac{u_{si-1/2,k}^{n+1} - u_{si-3/2,k}^{n+1}}{\Delta r}\right)\Bigg\}\Bigg] + [(\phi q)_{in.}^{*} u_s]_{i-1/2,k}^{n+1} \\
& + \frac{1}{\bar{\bar{\rho}}_s} \frac{1}{\Delta z} \Bigg[\Bigg\{\left(\mu_s^{n} + \frac{d\mu_s}{d\phi}\right|^{n} (\phi^{n+1} - \phi^{n})\Bigg)_{i-1/2,k+1/2} * \left(\frac{u_{si-1/2,k+1}^{n+1} - u_{si-1/2,k}^{n+1}}{\Delta z}\right)\Bigg\} \\
& - \Bigg\{\left(\mu_s^{n} + \frac{d\mu_s}{d\phi}\right|^{n} (\phi^{n+1} - \phi^{n})\Bigg)_{i-1/2,k-1/2} * \left(\frac{u_{si-1/2,k}^{n+1} - u_{si-1/2,k-1}^{n+1}}{\Delta z}\right)\Bigg\}\Bigg] \\
& - \frac{1}{\bar{\bar{\rho}}_s} \Bigg[\left(\beta_r^{n} + \frac{\partial \beta_r}{\partial \phi}\right|^{n} (\phi^{n+1} - \phi^{n})\Bigg)_{i-1/2,k} (u_{fi-1/2,k}^{n+1} - u_{si-1/2,k}^{n+1})\Bigg]\Bigg\} + (\phi u_s)_{i-1/2,k}^{n}
\end{aligned}$$

(D.12)

Along the axial direction,

considering the equation of motion for solid phase about the point (i,k+1/2)

$$(\phi w_s)_{i,k+1/2}^{n+1} = \frac{\Delta t}{\Delta z} \left\{ \phi^{n} + \frac{d\phi}{dp_s}\right|^{n} \cdot \left(p_s^{n+1} - p_s^{n}\right)\Bigg\}_{i,k+1/2} \left[p_{si,k+1}^{n+1} - p_{si,k}^{n+1}\right] + G_{si,k+1/2} \qquad \text{(D.13)}$$

where,

$$
\begin{aligned}
G_{si,k+1/2} = \Delta t \Bigg\{ & \left[\frac{\langle\phi u_s w_s\rangle_{i+1/2,k+1/2} - \langle\phi u_s w_s\rangle_{i-1/2,k+1/2}}{\Delta r}\right]^{n+1} + \left[\frac{\langle\phi w_s w_s\rangle_{i,k+1} - \langle\phi w_s w_s\rangle_{i,k}}{\Delta z}\right]^{n+1} \\
& + \Bigg[\left(\left(p_{kz}^{n} + \frac{\partial p_{kz}}{\partial \phi}\right)\Bigg|^{n} (\phi^{n+1} - \phi^{n})\right)_{i,k+1/2} * \left(\frac{\phi_{i,k+1}^{n+1} - \phi_{i,k}^{n+1}}{\Delta z}\right)\Bigg] + \frac{1}{\bar{\rho}_s}\frac{1}{\Delta r}\frac{1}{r_{i,k+1/2}} * \\
& \Bigg[\Bigg\{ r_{i+1/2,k+1/2}\left(\mu_s^{n} + \frac{d\mu_s}{d\phi}\Bigg|^{n} (\phi^{n+1} - \phi^{n})\right)_{i+1/2,k+1/2} * \left(\frac{w_{si+1,k+1/2}^{n+1} - w_{si,k+1/2}^{n+1}}{\Delta r}\right)\Bigg\} \\
& - \Bigg\{ r_{i-1/2,k+1/2}\left(\mu_s^{n} + \frac{d\mu_s}{d\phi}\Bigg|^{n} (\phi^{n+1} - \phi^{n})\right)_{i-1/2,k+1/2} * \left(\frac{w_{si,k+1/2}^{n+1} - w_{si-1,k+1/2}^{n+1}}{\Delta r}\right)\Bigg\}\Bigg] \\
& + \frac{1}{\bar{\rho}_s}\frac{1}{\Delta z}\Bigg[\Bigg\{\left(\mu_s^{n} + \frac{d\mu_s}{d\phi}\Bigg|^{n} (\phi^{n+1} - \phi^{n})\right)_{i,k+1} * \left(\frac{w_{si,k+3/2}^{n+1} - w_{si,k+1/2}^{n+1}}{\Delta z}\right)\Bigg\} \\
& - \Bigg\{\left(\mu_s^{n} + \frac{d\mu_s}{d\phi}\Bigg|^{n} (\phi^{n+1} - \phi^{n})\right)_{i,k} * \left(\frac{w_{si,k+1/2}^{n+1} - w_{si,k-1/2}^{n+1}}{\Delta z}\right)\Bigg\}\Bigg] + [\langle\phi q\rangle_{in.}^{*} w_s]_{i,k+1/2}^{n+1} \\
& - \frac{1}{\bar{\rho}_s}\Bigg[\left(\beta_z^{n} + \frac{\partial \beta_z}{\partial \phi}\Bigg|^{n} (\phi^{n+1} - \phi^{n})\right)_{i,k+1/2} (w_{fi,k+1/2}^{n+1} - w_{si,k+1/2}^{n+1})\Bigg]\Bigg\} + \langle\phi w_s\rangle_{i,k+1/2}^{n}
\end{aligned}
$$

(D.14)

considering the equation of motion for solid phase about the point (i,k-1/2)

$$
(\phi w_s)_{i,k-1/2}^{n+1} = \frac{\Delta t}{\Delta z}\left\{\phi^{n} + \frac{d\phi}{dp_s}\Bigg|^{n} \cdot \left(p_s^{n+1} - p_s^{n}\right)\right\}_{i,k-1/2} \left[p_{si,k}^{n+1} - p_{si,k-1}^{n+1}\right] + G_{si,k-1/2} \qquad \text{(D.15)}
$$

where,

$$
\begin{aligned}
G_{si,k-1/2} = \Delta t \Bigg\{ & \left[\frac{\langle\phi u_s w_s\rangle_{i+1/2,k-1/2} - \langle\phi u_s w_s\rangle_{i-1/2,k-1/2}}{\Delta r}\right]^{n+1} + \left[\frac{\langle\phi w_s w_s\rangle_{i,k} - \langle\phi w_s w_s\rangle_{i,k-1}}{\Delta z}\right]^{n+1} \\
& + \Bigg[\left(\left(p_{kz}^{n} + \frac{\partial p_{kz}}{\partial \phi}\right)\Bigg|^{n} (\phi^{n+1} - \phi^{n})\right)_{i,k-1/2} * \left(\frac{\phi_{i,k}^{n+1} - \phi_{i,k-1}^{n+1}}{\Delta z}\right)\Bigg] + \frac{1}{\bar{\rho}_s}\frac{1}{\Delta r}\frac{1}{r_{i,k-1/2}} * \\
& \Bigg[\Bigg\{ r_{i+1/2,k-1/2}\left(\mu_s^{n} + \frac{d\mu_s}{d\phi}\Bigg|^{n} (\phi^{n+1} - \phi^{n})\right)_{i+1/2,k-1/2} * \left(\frac{w_{si+1,k-1/2}^{n+1} - w_{si,k-1/2}^{n+1}}{\Delta r}\right)\Bigg\} \\
& - \Bigg\{ r_{i-1/2,k-1/2}\left(\mu_s^{n} + \frac{d\mu_s}{d\phi}\Bigg|^{n} (\phi^{n+1} - \phi^{n})\right)_{i-1/2,k-1/2} * \left(\frac{w_{si,k-1/2}^{n+1} - w_{si-1,k-1/2}^{n+1}}{\Delta r}\right)\Bigg\}\Bigg] \\
& + \frac{1}{\bar{\rho}_s}\frac{1}{\Delta z}\Bigg[\Bigg\{\left(\mu_s^{n} + \frac{d\mu_s}{d\phi}\Bigg|^{n} (\phi^{n+1} - \phi^{n})\right)_{i,k} * \left(\frac{w_{si,k+1/2}^{n+1} - w_{si,k-1/2}^{n+1}}{\Delta z}\right)\Bigg\} \\
& - \Bigg\{\left(\mu_s^{n} + \frac{d\mu_s}{d\phi}\Bigg|^{n} (\phi^{n+1} - \phi^{n})\right)_{i,k-1} * \left(\frac{w_{si,k-1/2}^{n+1} - w_{si,k-3/2}^{n+1}}{\Delta z}\right)\Bigg\}\Bigg] + [\langle\phi q\rangle_{in.}^{*} w_s]_{i,k-1/2}^{n+1} \\
& - \frac{1}{\bar{\rho}_s}\Bigg[\left(\beta_z^{n} + \frac{\partial \beta_z}{\partial \phi}\Bigg|^{n} (\phi^{n+1} - \phi^{n})\right)_{i,k-1/2} (w_{fi,k-1/2}^{n+1} - w_{si,k-1/2}^{n+1})\Bigg]\Bigg\} + \langle\phi w_s\rangle_{i,k-1/2}^{n}
\end{aligned}
$$

(D.16)

Substituting the above expressions back into the mass conservation equation for the solid phase,

$$\begin{aligned}
&\frac{1}{r_{i,k}}\cdot\frac{1}{\Delta r}\left[r_{i+1/2,k}\left\{\frac{\Delta t}{\Delta r}\left(\phi^n + \left.\frac{d\phi}{dp_s}\right|^n \cdot \left(p_s^{n+1}-p_s^n\right)\right)_{i+1/2,k}\left[p_{si+1,k}^{n+1}-p_{si,k}^{n+1}\right]\right\}\right.\\
&\left.-r_{i-1/2,k}\left\{\frac{\Delta t}{\Delta r}\left(\phi^n + \left.\frac{d\phi}{dp_s}\right|^n \cdot \left(p_s^{n+1}-p_s^n\right)\right)_{i-1/2,k}\left[p_{si,k}^{n+1}-p_{si-1,k}^{n+1}\right]\right\}\right]\\
&+\frac{1}{\Delta z}\left[\frac{\Delta t}{\Delta z}\left\{\phi^n + \left.\frac{d\phi}{dp_s}\right|^n \cdot \left(p_s^{n+1}-p_s^n\right)\right\}_{i,k+1/2}\left[p_{si,k+1}^{n+1}-p_{si,k}^{n+1}\right]\right.\\
&\left.-\frac{\Delta t}{\Delta z}\left\{\phi^n + \left.\frac{d\phi}{dp_s}\right|^n \cdot \left(p_s^{n+1}-p_s^n\right)\right\}_{i,k-1/2}\left[p_{si,k}^{n+1}-p_{si,k-1}^{n+1}\right]\right]\\
&+\left[r_{i+1/2,k}F_{si+1/2,k}-r_{i-1/2,k}F_{si-1/2,k}+G_{si,k+1/2}-G_{si,k-1/2}\right]-\left[(\phi q)^{*}_{in.}\right]^{n+1}_{i,k}=\frac{\left(\phi^{n+1}_{i,k}-\phi^{n}_{i,k}\right)}{\Delta t}
\end{aligned}$$

(D.17)

Defining the following,

$$A_{i+1/2,k}=\left(\phi^n+\left.\frac{\partial\phi}{\partial p_s}\right|^n\left(p_s^{n+1}-p_s^n\right)\right)_{i+1/2,k} \tag{D.18a}$$

$$A_{i-1/2,k}=\left(\phi^n+\left.\frac{\partial\phi}{\partial p_s}\right|^n\left(p_s^{n+1}-p_s^n\right)\right)_{i-1/2,k} \tag{D.18b}$$

$$B_{i,k+1/2}=\left(\phi^n+\left.\frac{\partial\phi}{\partial p_s}\right|^n\left(p_s^{n+1}-p_s^n\right)\right)_{i,k+1/2} \tag{D.18c}$$

$$B_{i,k-1/2}=\left(\phi^n+\left.\frac{\partial\phi}{\partial p_s}\right|^n\left(p_s^{n+1}-p_s^n\right)\right)_{i,k-1/2} \tag{D.18d}$$

and substituting them into Equation D.17 leads to,

$$
\begin{aligned}
&\frac{1}{r_{i,k}}\left[\frac{(rA)_{i-1/2,k}\,p^{n+1}_{si-1,k}-\left[(rA)_{i-1/2,k}+(rA)_{i+1/2,k}\right]p^{n+1}_{si,k}+(rA)_{i+1/2,k}\,p^{n+1}_{si+1,k}}{(\Delta r)^2}\right]\\
&+\left[\frac{B_{i,k-1/2}\,p^{n+1}_{si,k-1}-\left[B_{i,k-1/2}+B_{i,k+1/2}\right]p^{n+1}_{si,k}+B_{i,k+1/2}\,p^{n+1}_{si,k+1}}{(\Delta z)^2}\right]\\
&=\frac{1}{\Delta t}\left[\left(\frac{r_{i-1/2,k}}{r_{i,k}}\,\frac{F_{si-1/2,k}}{\Delta r}\right)-\left(\frac{r_{i+1/2,k}}{r_{i,k}}\,\frac{F_{si+1/2,k}}{\Delta r}\right)+\frac{1}{\Delta z}(G_{si,k-1/2}-G_{si,k+1/2})\right.\\
&\left.-\{(\phi q)^{*}_{in.}\}^{n+1}_{i,k}\right]+\frac{1}{(\Delta t)^2}(\phi^{n+1}_{i,k}-\phi^{n}_{i,k})
\end{aligned}
\tag{D.19}
$$

Equation D.19 describes the pressure distribution for the solid phase. It is identical to Equation 4.24.

Appendix E

Solid-phase Pressure Equation for the Constriction Model

Given the following conversation equations for the one-dimensional constriction model

* mass conservation for the fluid phase

$$\frac{\partial \varepsilon}{\partial t} + \frac{\partial}{\partial z}\left(\varepsilon w_f\right) = 0 \qquad \text{(E.1)}$$

* mass conservation for the solid phase

$$\frac{\partial \phi}{\partial t} + \frac{\partial}{\partial z}\left(\phi w_s\right) = 0 \qquad \text{(E.2)}$$

* conservation of momentum for the fluid phase

$$\frac{\partial}{\partial t}\left(\varepsilon w_f\right) + \frac{\partial}{\partial z}\left(\varepsilon w_f w_f\right) = -\frac{\varepsilon}{\bar{\rho}_f}\frac{\partial p_f}{\partial z} - (\varepsilon g) + \frac{\beta}{\bar{\rho}_f}\left(w_f - w_s\right) \qquad \text{(E.3)}$$

* conservation of momentum for the solid phase

$$\frac{\partial}{\partial t}\left(\phi w_s\right) + \frac{\partial}{\partial z}\left(\phi w_s w_s\right) = -\frac{\phi}{\bar{\rho}_s}\frac{\partial p_s}{\partial z} - \frac{p_{k,z}}{\bar{\rho}_s}\frac{\partial \phi}{\partial z} - (\phi g) - \frac{\beta}{\bar{\rho}_s}\left(w_f - w_s\right) \qquad \text{(E.4)}$$

Adding the equations of motion for the fluid phase and the solid phase together results in the following,

$$\frac{\partial}{\partial t}\left[\phi w_s + \varepsilon w_f\right] + \frac{\partial}{\partial z}\left[(\phi w_s)w_s + \left(\varepsilon w_f\right)w_f\right] = -\frac{\phi}{\bar{\rho}_s}\frac{\partial p_s}{\partial z} - \frac{\varepsilon}{\bar{\rho}_f}\frac{\partial p_f}{\partial z} - g + \left(\frac{\left(\bar{\rho}_f - \bar{\rho}_s\right)}{\bar{\rho}_f \cdot \bar{\rho}_s}\right)\beta\left(w_f - w_s\right) \qquad \text{(E.5)}$$

Substituting the definition for the kinematic pressure $(p_s = p_f + p_k)$ into Equation E.5 leads to,

$$\frac{\partial}{\partial t}\left[\phi w_s + \varepsilon w_f\right] + \frac{\partial}{\partial z}\left[(\phi w_s)w_s + \left(\varepsilon w_f\right)w_f\right] = -\left(\frac{1}{\overline{\rho_f}} - \phi\left(\frac{1}{\overline{\rho_f}} + \frac{1}{\overline{\rho_s}}\right)\right)\frac{\partial p_s}{\partial z} - \frac{p_k}{\overline{\rho_s}}\frac{\partial \phi}{\partial z} - \frac{\varepsilon}{\overline{\rho_f}}\frac{\partial p_k}{\partial z}$$
$$-g + \left(\frac{\left(\overline{\rho_f} - \overline{\rho_s}\right)}{\overline{\rho_f} \cdot \overline{\rho_s}}\right)\beta\left(w_f - w_s\right)$$

(E.6)

Taking the divergence of the above equation, and considering that $\frac{\partial}{\partial z}\left(\phi w_s + \varepsilon w_f\right) = 0$, the following expression is obtained,

$$\frac{\partial}{\partial z}\left\{\frac{\partial}{\partial z}\left[(\phi w_s)w_s + (\varepsilon w_f)w_f\right]\right\} = \left[-\frac{(1-\phi)}{\overline{\rho_f}} + \frac{\phi}{\overline{\rho_s}}\right]\frac{\partial^2 p_s}{\partial z^2} - \left[\frac{\left(\overline{\rho_f} - \overline{\rho_s}\right)}{\overline{\rho_f} \cdot \overline{\rho_s}}\right]\frac{\partial \phi}{\partial z}\frac{\partial p_s}{\partial z} + \frac{\partial}{\partial z}\left\{-\frac{p_k}{\overline{\rho_s}}\frac{\partial \phi}{\partial z} + \frac{\varepsilon}{\overline{\rho_f}}\frac{\partial p_k}{\partial z}\right.$$
$$\left. -g + \left(\frac{\left(\overline{\rho_f} - \overline{\rho_s}\right)}{\overline{\rho_f} \cdot \overline{\rho_s}}\right)\beta\left(w_f - w_s\right)\right\}$$

(E.7)

Rearranging Equation C.7 leads to,

$$\frac{\partial}{\partial z}\left\{\frac{\partial}{\partial z}\left[(\phi w_s)w_s + (\varepsilon w_f)w_f\right]\right\} = \left[-\frac{\phi\left(\overline{\rho_s} - \overline{\rho_f}\right) - \overline{\rho_s}}{\overline{\rho_f} \cdot \overline{\rho_s}}\right]\frac{\partial^2 p_s}{\partial z^2} - \left[\frac{\left(\overline{\rho_f} - \overline{\rho_s}\right)}{\overline{\rho_f} \cdot \overline{\rho_s}}\right]\frac{\partial \phi}{\partial z}\frac{\partial p_s}{\partial z} + \frac{\partial}{\partial z}\left\{-\frac{p_k}{\overline{\rho_s}}\frac{\partial \phi}{\partial z} + \frac{\varepsilon}{\overline{\rho_f}}\frac{\partial p_k}{\partial z}\right.$$
$$\left. -g + \left(\frac{\left(\overline{\rho_f} - \overline{\rho_s}\right)}{\overline{\rho_f} \cdot \overline{\rho_s}}\right)\beta\left(w_f - w_s\right)\right\}$$

(E.8)

Moving the pressure distribution to one side, the following is obtained

$$\frac{\partial^2 p_s}{\partial z^2} + \left(\frac{\left(\overline{\rho_s} - \overline{\rho_f}\right)}{\phi\left(\overline{\rho_s} - \overline{\rho_f}\right) - \overline{\rho_s}} \cdot \frac{\partial \phi}{\partial z}\right)\frac{\partial p_s}{\partial z} = \left[\frac{\overline{\rho_f} \cdot \overline{\rho_s}}{\phi\left(\overline{\rho_s} - \overline{\rho_f}\right) - \overline{\rho_s}}\right]\frac{\partial}{\partial z}\left\{-\frac{\varepsilon}{\overline{\rho_f}}\frac{\partial p_k}{\partial z} + \frac{p_k}{\overline{\rho_s}}\frac{\partial \phi}{\partial z}\right.$$
$$\left. -\frac{\left(\overline{\rho_s} - \overline{\rho_f}\right)}{\overline{\rho_f} \cdot \overline{\rho_s}}\beta\left(w_f - w_s\right) + \frac{\partial}{\partial z}\left[(\phi w_s)w_s + \left(\varepsilon w_f\right)w_f\right]\right\}$$

(E.9)

Equation E.9 is identical to Equation 4.35; as well, it is identical to Equation 29 of Reference [83].